

Tests of the Data Acquisition System and Detector Control System for the Muon Chambers of the CMS Experiment at the LHC

Von der Fakultät für Mathematik, Informatik und Naturwissenschaften der RWTH Aachen University zur Erlangung des akademischen Grades eines Doktors der Naturwissenschaften genehmigte Dissertation

vorgelegt von

Diplom-Physiker
Michael Christian Sowa
aus Groß Strehlitz (PL)

Berichter:
Universitätsprofessor Dr. T. Hebbeker
Universitätsprofessor Dr. A. Stahl

Tag der mündlichen Prüfung: 27.02.2009

Diese Dissertation ist auf den Internetseiten der Hochschulbibliothek online verfügbar.

Abstract

The Phys. Inst. III A of RWTH Aachen University is involved in the development, production and tests of the Drift Tube (DT) muon chambers for the barrel muon system of the CMS detector at the LHC at CERN (Geneva). The present thesis describes some test procedures which were developed and performed for the chamber local Data Acquisition (DAQ) system, as well as for parts of the Detector Control System (DCS). The test results were analyzed and discussed.

Two main kinds of DAQ tests were done. On the one hand, to compare two different DAQ systems, the chamber signals were split and read out by both systems. This method allowed to validate them by demonstrating, that there were no relevant differences in the measured drift times, generated by the same muon event in the same chamber cells. On the other hand, after the systems were validated, the quality of the data was checked. For this purpose extensive noise studies were performed. The noise dependence on various parameters (threshold, HV) was investigated quantitatively. Also detailed studies on single cells, qualified as "dead" and "noisy" were done.

For the DAQ tests a flexible hardware and software environment was needed. The organization and installation of the supplied electronics, as well as the software development was realized within the scope of this thesis.

The DCS tests were focused on the local gas pressure read-out components, attached directly to the chamber: pressure sensor, manifolds and the pressure ADC (PADC). At first it was crucial to proof, that the calibration of the mentioned chamber components for the gas pressure measurement is valid. The sensor calibration data were checked and possible differences in their response to the same pressure were studied. The analysis of the results indicated that the sensor output depends also on the ambient temperature, a new experience which implied an additional pedestal measurement of the chamber gas pressure sensors at CMS.

The second test sequence considered the gas pressure read-out quality. This kind of test used data obtained during the CMS Magnet Test and Cosmic Challenge (MTCC). The signal of two sensor types measuring the same gas pressure at the same time were compared. Also the stability of the sensor output, as well as of the sensor supply voltage were analyzed at different magnetic field values.

To perform the mentioned DCS tests a complex software system was developed. This system merges the sensor and calibration data to obtain the final pressure values for each possible sensor/PADC/chamber combination. This proceeds fully automatically by connecting to the diverse internal and external databases, by finding proper data, performing calculations and creating the Look Up Tables (LUT).

Zusammenfassung

Das III. Physikalische Institut A der RWTH Aachen beteiligt sich an der Entwicklung, Fertigung und Testdurchführung der Myonkammern, die ein Bestandteil des Myonsystems im Zentralbereich des CMS-Detektors im LHC-Speicherring am CERN (Genf) sind. Die vorliegende Arbeit beschreibt einige Testprozeduren, die für das lokale Datennahmesystem (*Data Acquisition*, DAQ) wie auch für einen Teil des Kontroll- und Steuerungssystems des Detektors (*Detector Control System*, DCS) vorgenommen wurden. Anschließend wurden die Testergebnisse analysiert und diskutiert.

Grundsätzlich führte man zwei Typen von DAQ-Tests durch. Einerseits wurden die Kammer-signale geteilt und von zwei verschiedenen DAQ-Systemen ausgelesen. Diese Methode erlaubte es, die beiden Systeme zu vergleichen und sie zu validieren, da man keine nennenswerten Unterschiede in den gemessenen Driftzeiten fand, die von dem selben Myonereignis stammten. Andererseits, nach der Validierung beider Systeme, wurde die Qualität der DAQ-Daten geprüft. Zu diesem Zweck wurden umfangreiche Studien bzgl. des Rauschverhaltens vorgenommen. Es wurde die Abhängigkeit des Rauschens von verschiedenen Parametern (Schwelle, Hochspannung) quantitativ untersucht. Darüber hinaus wurden detaillierte Studien über das Verhalten der einzelnen Zellen vorgenommen, die zuvor als "rauschend" bzw. "tot" eingestuft worden waren.

Für die DAQ-Tests wurde eine breite Hardware- und Softwareumgebung benötigt. Im Rahmen dieser Arbeit wurde die Organisation und Inbetriebnahme der DAQ-Elektronik bewerkstelligt, sowie die erforderlichen Softwarepakete entwickelt.

Bei den DCS-Tests konzentrierte man sich auf die lokalen Komponenten für die Auslese der Gasdruckwerte, die direkt an den Myonkammern angebracht wurden: Drucksensoren, Druckverteiler und Druck-Analog-Digital-Wandler (*Pressure Analog to Digital Converter*, PADC). Zunächst war es unabdingbar, sich über die Korrektheit der Kalibrationen dieser Komponenten zu vergewissern. Zu diesem Zweck wurden die Kalibrationsdaten der Sensoren analysiert und die eventuellen Differenzen ihrer analogen Ausgangssignale studiert. Die Analyse der Resultate zeigte, dass die Pulshöhe der Signale auch von der Umgebungstemperatur abhängt. Diese neue Erfahrung impliziert eine zusätzliche Druckbasismessung im CMS-Detektorbetrieb.

Bei der anderen Testreihe wurde die Qualität der Gasdruckauslese untersucht. Für diese Tests verwendete man die Daten vom CMS *Magnet Test and Cosmic Challenge* (MTCC). Es wurden die Signale von zwei Sensortypen verglichen, die denselben Druck zur selben Zeit gemessen hatten. Auch die Stabilität der Sensormessung, wie auch der Sensorversorgungsspannung, wurde bei verschiedenen Magnetfeldwerten untersucht.

Um die erwähnten DCS-Tests durchzuführen, musste ein komplexes Softwaresystem entwickelt werden. Dieses System verknüpft die Sensor- und PADC-Kalibrationsdaten um endgültige Druckwerte für jede mögliche Sensor/PADC/Kammer-Kombination zu erhalten. Diese Prozedur verläuft völlig automatisch, bei Anschluss an verschiedene interne und externe Datenbanken. Dabei werden die benötigten Daten den Datenbanken entnommen, umgerechnet, und schließlich für die Erstellung der Konversionstabellen (*Look Up Tables*, LUT) des DCS verwendet.

Contents

Abstract	iii
Zusammenfassung	v
1. Introduction	1
2. Theoretical framework of Particle Physics	3
2.1. Gauge principle	3
2.2. The Standard Model	5
2.2.1. Main features	5
2.2.2. Quantum Chromodynamics	7
2.2.3. Electroweak interactions	9
2.2.4. The Higgs mechanism	11
2.3. Beyond the Standard Model	15
2.3.1. Supersymmetry	15
2.3.2. Other models	19
3. New experiments for new particle search	23
3.1. The Large Hadron Collider (LHC)	23
3.1.1. General description	23
3.1.2. LHC physics	25
3.1.3. The LHC experiments	28
3.2. The Compact Muon Solenoid (CMS)	30
3.2.1. Detector design	30
3.2.2. The CMS muon system	34
3.3. The Drift Tube muon chambers	38
3.3.1. Chamber layout	39
3.3.2. Chamber working principle	41
3.3.3. Chamber production and tests	43
4. Data taking with the CMS DT muon chambers	45
4.1. Detector triggering and data taking systems	45
4.1.1. CMS trigger system	45
4.1.2. Data Acquisition System (DAQ)	49
4.2. The local DAQ system for the CMS DT muon chambers	52
4.2.1. Chamber output signals	52
4.2.2. Drift time measurement	54
4.2.3. Data transfer and storage	56
4.3. The Aachen CMS DT muon chamber test facility	59
4.3.1. Chamber function tests with cosmic muons	60
4.3.2. The Aachen DAQ system	62

4.3.3.	The MiniCrate DAQ system	62
4.3.4.	DAQ data	65
4.4.	Tests of the local DAQ system	68
4.4.1.	Comparison of two different DAQ systems	68
4.4.2.	Noise analysis	79
4.4.3.	Conclusions on DAQ tests	90
5.	Measurement of the gas pressure in the CMS DT muon chambers	93
5.1.	Detector control and monitoring systems	93
5.1.1.	Run Control and Monitor System (RCMS)	93
5.1.2.	Detector Control System	95
5.2.	Local DCS gas pressure monitoring and control for the CMS DT muon chambers	99
5.3.	Calibrated hardware components	102
5.3.1.	Why calibration?	102
5.3.2.	Pressure sensors	102
5.3.3.	Pressure Analog to Digital Converter (PADC)	113
5.4.	Look Up Tables (LUTs)	118
5.4.1.	Data for the LUTs	119
5.4.2.	LUT creation	121
5.5.	Gas pressure system tests	122
5.5.1.	Verification of the sensor calibration	123
5.5.2.	Gas pressure read-out tests.	134
5.5.3.	Conclusions on gas pressure tests	139
6.	Summary	143
A.	MiniCrate DAQ configuration and readout software	145
A.1.	<i>MiniCrate_MB1_TDC_configuration_setup_ac.vi</i>	145
A.2.	<i>Read_out_ROS-8_DG535_ac.vi</i>	147
A.3.	Event data block	149
B.	DCS gas pressure sensor calibration and LUT software	151
B.1.	<i>SensCalV2.0.vi</i>	151
B.2.	<i>Select_Manifold.vi</i>	153
B.3.	<i>LUT_PADC.vi</i>	154
B.4.	<i>MB_item_for_LUT_PADC.vi</i>	155
B.5.	<i>Read_mbID_mbposition_URL.vi</i> and <i>Read_mbtype_mbID_padcID_manifoldID_URL.vi</i>	155
C.	DCS gas pressure sensor calibration and LUT files and databases	159
	Bibliography	163
	Acknowledgments	171

1. Introduction

In first years of the 20th century two milestones were set in physics: the quantum mechanics (Planck, Schrödinger, Heisenberg et al.) and the relativity theories (Einstein). The dynamic development of the physics in the 20th century showed that these two disciplines are quite useful in order to describe the material and antimaterial world. The physics of the elementary particle is based on these two concepts and supplies a handful of answers concerning the particles as basic modules of the matter and describing the interactions between them.

Just the simplest and the most understood model of the elementary particle physics, the Standard Model (Glashow, Salam, Weinberg) can impress by its simplicity and structure and finds its confirmation in a large number of particle discoveries achieved in the last century in laboratories like Fermilab (USA), CERN (Swiss) and others. Excepting the only one particle of the Standard Model – the Higgs boson – all matter and antimatter particle and interaction bosons were discovered. Thus one is sure that if the Standard Model is valid, the discovery of the Higgs boson is only a question of time. As a consequence a couple of questions should be then clarified. For example: why the elementary particles of the matter and anti-matter appear symmetrical in the only three duplex generations or why they have so different masses which are extended over ten magnitude orders (Chapter 2).

Even if other questions will remain still open, the discovery of the Higgs boson would provide us an interesting view over the constitutive properties of the massive particles. Therefore it is not amazing that the particle physicists in the whole world regard the discovery of the Higgs boson as one of the most important challenges, maybe even the most important challenge anyway of today's time. For this purpose there are leptons or/and hadrons – particle described by the Standard Model – accelerated onto high energies in huge linear and ring accelerators and brought to the collisions with each other. However, the offensive remained without intended success. The analysis of the earlier CERN data (LEP) could not point to an existence of the Higgs bosons; only a lower exclusion limit of 114.4 GeV was estimated for its mass [1]. Likewise the CDF and D0-experiments at the Tevatron did not detect any Higgs boson, however the data evaluation is here not yet finished.

Therefore the aim is to generate much larger energies in the particle collisions and to search for dedicated collision products like Higgs boson. Among others one hopes it for the Large Hadron Collider (LHC) at CERN. In a storage ring with a circumference of 27 km, 100 m below ground, there are proton bunches accelerated in two opposite directions and brought under control to the collisions with each other. The energy 14 TeV released at those points would be enough to detect the Higgs boson and/or other sorts of particles which are not described in the Standard Model. For this purpose four detectors – ATLAS, CMS, LHC-b and ALICE – are installed on LHC subterrestrial points. Whereas the first two of them are designed predominantly for detecting the Higgs boson, the main focus of LHC-b and ALICE is the study of the B-physics and heavy ions, respectively, which are further aspects of the modern particle physics (Chapter 3).

The III. Physics Institute A of the RWTH Aachen participates in one of the LHC experiments (CMS). Especially for the CMS detector muon system drift chambers (muon chambers)

1. Introduction

were here produced and tested. They consist of multiple gas-filled drift cells, which are positioned parallel to each other and form by this means together a super-layer; each muon chamber consists of mostly three such super-layers. Now, if a Higgs boson is produced with a mass of ca. 150 GeV, it then decays into muons $H \rightarrow ZZ^* \rightarrow 4\mu$. The simultaneous detection of four muons by the muon chambers will thus get direct evidence to the existence of the searched Higgs boson (Chapter 3).

To ensure that these informations are not missed, a complex data acquisition (DAQ) and trigger system was developed, whose local units (MiniCrate) were mounted directly on the chambers. Here the drift times are locally digitized and Level-1 (L1) trigger informations are stored. In order to ensure the correct function of this system for the duration of the LHC, the local DAQ system have to undergo a large number of diverse test and check procedures. These procedures are mainly performed on the chambers already commissioned and installed in the CMS detector. Independently on this it is important that the chamber DAQ system undergoes its own studies, even long termed, as described in this thesis, for better understanding its behavior. For this purpose a completely assembled and instrumented chamber, which was produced as spare unit and in the first instance not declared to be installed in the CMS detector, was ideally qualified. It was placed in the Aachen test facility which was designed for the tests with the cosmic muons on the muon chambers produced in Aachen. Such studies, performed on the MiniCrate and its environment, were then compared to the work and to the test results obtained by use of the previous DAQ system, which was developed and had been operated for the function tests on the Aachen chambers during the assembling period (Chapter 4).

The DAQ provides reliable data only if the detector and its environment work perfectly. The Detector Control System (DCS), containing a large number of the hardware and software components, is developed for monitoring and control of the work of the entire detector and its subsystems. In Aachen a system responsible for the monitoring of the gas pressure at each muon chamber in the CMS detector was conceived, developed and manufactured. The control over this system is also performed via MiniCrate. The gas pressure information is transferred from pressure sensors via an ADC to the final data storage and interpreted by the so-called Look Up Tables (LUTs), created for each muon chamber and using the sensor and ADC calibration data. The application and tests of this part of the DCS, particularly during the Magnet Test Cosmic Challenge (MTCC) in 2006 were the subject of another study, which is described in this thesis (Chapter 5).

The procedure and the performing of the tests at the DAQ and DCS system, which are described in this thesis, represents only a small fraction of the entirety of the applied validation and test methods which must be executed on the muon chambers, in order to ensure unimpeachable and undisturbed functioning of the CMS detector for the duration of the LHC. This complexity shows additionally that one sets great value upon the CMS detector to classify it as an extremely reliable and ideally suited instrument for the detection of some possible, but yet not discovered particles. Thus we should hope that the data, which will soon be provided to us from the detector, even if maybe would not allow to get the full response to all questions, however would give us a possibility for a better understanding of our world.

2. Theoretical framework of Particle Physics

The CMS experiment at the LHC has the potential to detect new particles, which were not discovered until now. On the basis of such discoveries usual models of elementary particle physics can be confirmed, extended but also rejected. Therefore it is useful in order to understand the purpose and the goal of this thesis, to represent the theoretical principles of elementary particle physics in a compact outline.

The present chapter deals particularly with the usual, today generally accepted concept of elementary particle physics: the Standard Model (SM). Its main features are emphasized, the agreement of its theoretical predictions with the experiment is presented, as well as its weakness and open questions. Then also Supersymmetry is presented in an outline, which could be treated as a promising extension of the SM. Also some other theoretical approaches beyond the SM are briefly described.

Because the whole present chapter is only a short theoretical representation, we refer to the extensive literature on this topic, in order to delve into the subject being treated here. As an example, the references [2] and [3] are mentioned, on which this chapter is based.

2.1. Gauge principle

Symmetries play an important role in describing physical processes and systems. A system is called "symmetric" if it remains invariant under some group of transformations. A symmetry transformation implies the existence of one or more conserved quantities, which are associated with these operations (Noether's Theorem, [4]). The applications of this theorem are known from classical physics. For example the invariance of the systems with respect to the spatial translations is associated with the conservation of linear momentum; the invariance with respect to time translations gives the well known law of conservation of energy.

This principle can be generalized. For example let us regard a particle represented by a wave function $\psi(x, t)$ with the mass m and charge q in electric and magnetic fields

$$\vec{E} = -\vec{\nabla}\phi - \frac{\partial\vec{A}}{\partial t}, \quad \vec{B} = \vec{\nabla} \times \vec{A} \quad (2.1)$$

in terms of the potential $A^\mu = (\phi, \vec{A})$. The dynamics of that particle is expressed by the Schrödinger equation

$$\frac{1}{2m}[(-i\vec{\nabla} - q\vec{A})^2 + q\phi]\psi(x, t) = i\frac{\partial\psi(x, t)}{\partial t} \quad (2.2)$$

or in compact form

$$\frac{1}{2m}(-i\vec{D})^2\psi(x, t) = iD_0\psi(x, t) \quad (2.3)$$

2. Theoretical framework of Particle Physics

obtained by substitutions

$$\vec{\nabla} \rightarrow \vec{D} = \vec{\nabla} - iq\vec{A}, \quad \frac{\partial}{\partial t} \rightarrow D_0 = \frac{\partial}{\partial t} + iq\phi. \quad (2.4)$$

The fields \vec{E} and \vec{B} remain the same after the following *gauge* transformations $(\phi, A) \xrightarrow{G} (\phi', \vec{A}')$:

$$\phi \rightarrow \phi' = \phi - \frac{\partial\chi}{\partial t}, \quad \vec{A} \rightarrow \vec{A}' = \vec{A} + \vec{\nabla}\chi. \quad (2.5)$$

The Schrödinger equation has now the form

$$\frac{1}{2m}(-i\vec{D}')^2\psi'(x, t) = iD'_0\psi'(x, t) \quad (2.6)$$

where D' and D'_0 are the derivatives in Equation 2.4 with the transformed potentials in Equation 2.5 and $\psi'(x, t)$ is its new solution. Equation 2.6 describes the same physics as Equation 2.3 only if $\psi'(x, t)$ is transformed

$$\psi(x, t) \rightarrow \psi'(x, t) = \exp(iq\chi)\psi(x, t). \quad (2.7)$$

The physics of ψ and ψ' becomes gauge invariant because of $|\psi|^2 = |\psi'|^2$. Also the current $J \propto \psi^*(\vec{\nabla}\psi) - (\vec{\nabla}\psi)^*\psi$ remains the same for ψ or ψ' .

Very important is the reverse argument: to demand a specific dynamics of a system under the spacetime dependent phase transformation. Considering the free Dirac Lagrangian

$$\mathcal{L}_\psi = \bar{\psi}(i\gamma_\mu\partial^\mu - m)\psi \quad (2.8)$$

one can see, that it is invariant under a *local* gauge transformation

$$\psi \rightarrow \psi' = \exp[i\alpha(x)]\psi. \quad (2.9)$$

only by introduction of a new gauge field A_μ through minimal coupling

$$D_\mu = \partial_\mu + ieA_\mu \quad (2.10)$$

and simultaneous transformation of A_μ

$$A_\mu \rightarrow A'_\mu = A_\mu + \frac{1}{e}\partial_\mu\alpha. \quad (2.11)$$

e is the electric elementary charge and A_μ is identified with the photon field. The Lagrangian is now transformed as

$$\mathcal{L}_\psi \rightarrow \mathcal{L}'_\psi = \mathcal{L}_\psi - e\bar{\psi}\gamma_\mu\psi A^\mu \quad (2.12)$$

The last term describes the coupling between electron and photon. One makes the point that the electromagnetic strength tensor

$$F_{\mu\nu} = \partial_\mu A_\nu - \partial_\nu A_\mu \quad (2.13)$$

is also invariant under the gauge transformation (Equation 2.11).

The complete Lagrangian describing Quantum Electrodynamics is expressed by means of three terms

$$\mathcal{L}_{QED} = \mathcal{L}_\psi - e\bar{\psi}\gamma_\mu\psi A^\mu - \frac{1}{4}F_{\mu\nu}F^{\mu\nu} \quad (2.14)$$

meaning the free Lagrangian, photon-electron coupling and photon kinetic energy, respectively. A term $\mathcal{L}_A^m = -\frac{1}{2}\mu_\gamma A_\mu A^\mu$ characterizing the photon mass μ_γ is not invariant under the gauge transformation (Equation 2.11), thus $\mu_\gamma = 0$.

The mentioned considerations can be generalized for all elements ψ which undergo unitary transformations

$$\psi \rightarrow \psi' = U\psi, \quad U^\dagger U = U^{-1}U = 1. \quad (2.15)$$

The unitarity is required to ensure the normalization. The simplest representant for a unitary operator U is

$$U = \exp[-iT^a\alpha(x)] \quad (2.16)$$

with their hermitian generators T^a and spacetime dependent gauge parameters $\alpha(x)$. With $\det|U|=+1$ the T^a form a semi-simple compact Lie group and satisfy therefore the Lie algebra. The Lagrangian is then invariant under the matter field transformations (Equation 2.15) by introducing the gauge field for each generator.

2.2. The Standard Model

The Standard Model (SM) is nowadays the most understood and generally accepted theory of the elementary particles. It describes them as fundamental constituents of matter and the interactions between them. Each particle interaction described in the SM can be explained by means of an appropriate gauge theory. In this way it explains three of four basic interactions: electromagnetic, strong and weak. However, gravity is not included in the SM; until today there does not exist any satisfying quantum theory of gravity. Nevertheless, the gravity effects are negligible at the energy scales of particle physics and can be – temporarily – ignored.

2.2.1. Main features

The basic aim of the Standard Model is to present the fundamental constituents of matter and antimatter, as well as the fundamental interactions (or forces) between them (see Figure 2.1). The particles of which the entire matter is made up are fermions. There are 12 fermions in the SM, grouped in 6 quarks and 6 leptons. The quarks and leptons undergo the electric (if charged) and weak interactions, the quarks experience additionally the strong one. The quarks and leptons are arranged in three generations, each containing two leptons and two quarks. Within a generation the fermions have different masses but the same electric charge pattern: in a generation the charges of the two quarks are $+\frac{2}{3}$ and $-\frac{1}{3}$, the charges of the two leptons -1 and 0 . Each fermion is accompanied by its own "mirror image", the antifermion, which is constituent of the antimatter (not presented in the Figure 2.1). These antiparticles differ from the matter particles in the opposite electric charge. For example the antiup and positron (i.e. antielectron) have then the electric charge $-\frac{2}{3}$ and $+1$, respectively. Apart from the electric charge, the quarks have an additional charge, the color, formally expressed for the

2. Theoretical framework of Particle Physics

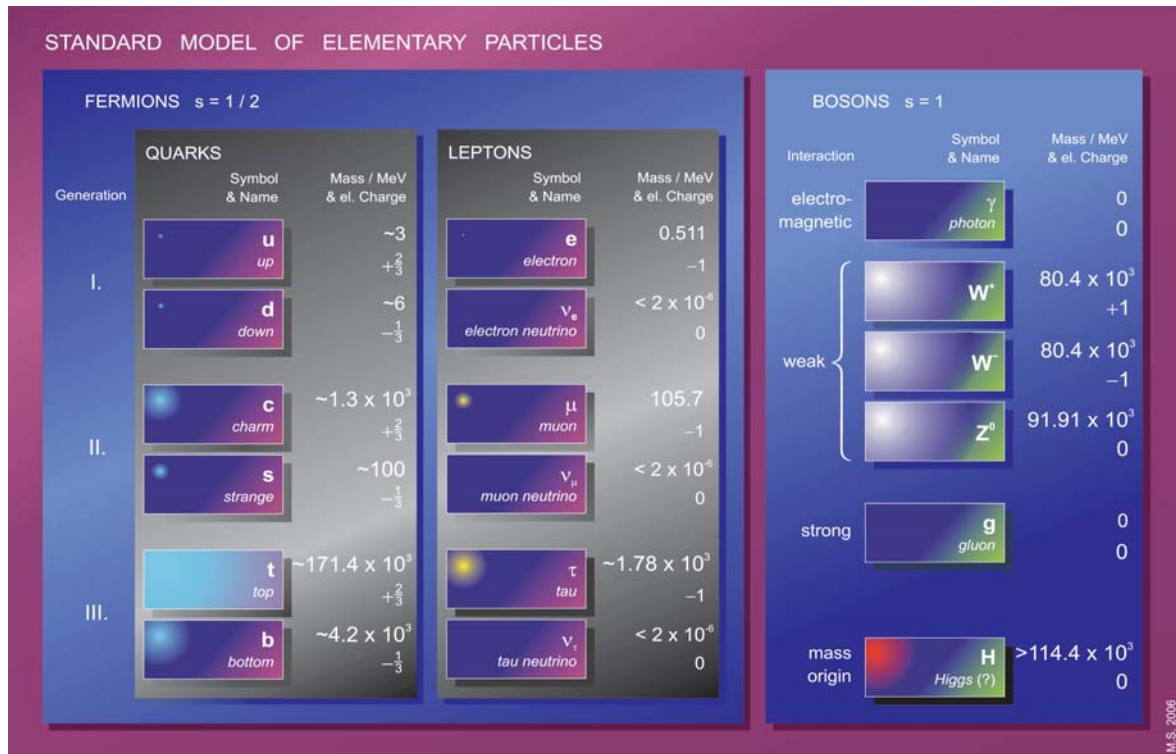


Figure 2.1.: The concept of the Standard Model is to interpret the fundamental constituents of matter and fundamental forces between them as particles. The constituents of matter are represented by 12 fermions: 6 quarks and 6 leptons; the forces (or interactions) are carried out by 5 gauge bosons. The sixth non-gauge boson, the Higgs, would explain the origin of mass of the SM particles and is the only particle in this model which is not discovered to date. The mass values of the particles (for the quarks only the approximated ones due to the mass measurement inability based on the quark confinement) are quoted from Reference [5].

three possible quark states experiencing the strong interaction: red, green and blue (see also Section 2.2.2).

The masses of the fermions (and the corresponding antifermions) are different but generally one can realize that the particle mass increases from lower to the higher quark and lepton generation number. The particles with low masses were discovered earlier than the heavier ones, so the allocating in the specific generations was performed well-nigh chronologically. The neutrinos in the lepton generations were assumed for a long time to be massless. Only in the last decade a couple of experiments provided direct indication for their non-zero masses [6]. The masses of the quarks in the SM can be only given approximately because of the phenomenon called *quark confinement*: the strong interaction between quarks increases as the distance between them is increased, so it is impossible to obtain isolated quarks. The quarks can only exist in groups forming hadrons; there are several methods in theoretical physics (sum rules, lattice QCD) to determine the quark masses on the basis of the phenomenological observations.

Only three of the fermions – up and down on the quark side and electron on the lepton side – are the components of the stable matter in the universe. All other ones are created through different strong and weak interactions. Apart from neutrinos the heavier charged leptons and

the hadrons other than neutron and proton – bound in the atomic nuclei – are instable and decay into lighter particles. The mean life times vary from μs (muon) to 10^{-24} s (ρ mesons) [5].

The function of the bosons contained in the Standard Model is to transmit the force (interactions) between the fermions. For each kind of the interactions specified bosons are responsible.

The photon is a particle which acts as interchange quantum for the electromagnetic force. Its mass and electric charge is zero; therefore the electrically charged fermions participating in the electromagnetic interactions conserve their charge and the force between them can act at infinite distances.

The carriers of the weak interaction are massive bosons W^+ , W^- and Z^0 (see Figure 2.2). Because of their masses the weak interaction can be experienced only for very short distances ($\sim 10^{-18}$ m). The weak interactions where the W^+ and W^- participate change the flavor of the quarks (for example $u \rightarrow d$) but do not change their color charge. It was possible to unify the two forces, electromagnetic and weak, into one electroweak interaction ([7], see also Section 2.2.3).

The gluons with their zero-mass and zero-charge are the carriers of the third fundamental force: the strong interaction. They carry color charge by themselves, so the quarks being involved in the strong interactions do not change the flavor but the color charge. Because of the quark confinement the strong force can act only for small distances ($\sim 10^{-15}$ m). The strong interactions change the color of the quarks but conserve their flavor.

2.2.2. Quantum Chromodynamics

Quantum Chromodynamics (QCD) is a non-abelian quantum field theory which describes the strong interactions of the quarks and gluons, both being constituents of hadrons. The QCD is featured by two important properties:

- **Asymptotic freedom:** the interactions between quarks and gluons become arbitrarily weak at very short distances (i. e. in very high-energy reactions).
- **Confinement:** the force between quarks increases as the distance between them becomes longer. As a result the existence of free quarks is not possible.

QCD postulates a new degree of freedom: the color charge (or simply: color). This expression is formally chosen to characterize the three possible different quantum states of the quarks having the same flavor and included in a baryon. According to the Pauli exclusion principle fermions may not occupy the same quantum state simultaneously. Following this three colors *red* (r), *blue* (b) and *green* (g) are names for the new charge type. Each baryon includes one red, one green and one blue quark and remains thereby color-neutral (or *white*). Corresponding to the electric charge the anticolors are also defined: *antired* (\bar{r}), *antiblue* (\bar{b}) and *antigreen* (\bar{g}). The antibaryons contains analogically three antiquarks with the mentioned anticolors. Each meson contains a pair quark/antiquark with the colors r/\bar{r} , b/\bar{b} and g/\bar{g} , so the outer color of the mesons is also white. Further combinations of more quarks in a bound state remaining completely color neutral are at least theoretically possible (e.g. penta-quarks: four quarks and one antiquark).

The color, which is a new internal degree of freedom, means that the quark field is associated with a state vector q^i in a complex three dimensional color space $C(3)$. The rotations of q^i

2. Theoretical framework of Particle Physics

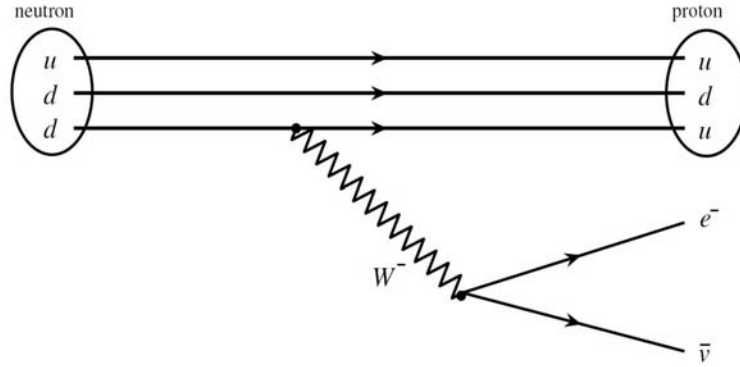


Figure 2.2.: A typical example to demonstrate the Standard Model interaction is the free neutron decay $n \rightarrow p^+ + e^- + \bar{\nu}_e$. A down quark contained in the neutron becomes an up quark by emitting a massive W^- boson which then forms the new lepton pair, electron and electron neutrino. With this flavor transformation of the quark the neutron is converted into a proton.

in $C(3)$, which are linear transformations conserving the length of q^i , form the group $SU(3)$, whose dimension is equal $3^2 - 1 = 8$. According to the Equations 2.15 and 2.16 any rotation in $C(3)$ can be presented in exponential form¹

$$U = \exp[iT^a c_a] \quad (2.17)$$

where T^a ($a = 1, 2, \dots, 8$) are the 3×3 Gell-Mann matrices and represent the generators as introduced in Equation 2.16.

The free Lagrangian (Equation 2.8) is invariant under the *global* gauge transformations of the quark and antiquark fields (with constant c_a):

$$\begin{aligned} q &\rightarrow q' = \exp[ic_a t^a] q \\ \bar{q} &\rightarrow \bar{q}' = \exp[-ic_a t^a] \bar{q}. \end{aligned} \quad (2.18)$$

Also the postulation of the local invariancy ($c_a(x_\mu)$) is satisfied by introducing a new auxiliary field A_μ^a . The result is the Lagrangian

$$\mathcal{L}_{QCD} = \bar{q}(i\gamma_\mu \partial^\mu + g_s A^\mu - m)q - \frac{1}{2} \text{Tr} G_{\mu\nu} G^{\mu\nu} \quad (2.19)$$

where

$$G_{\mu\nu} = \partial_\mu A_\nu - \partial_\nu A_\mu - ig_s [A_\mu, A_\nu] \quad (2.20)$$

is the tensor of the field A_μ , which is associated with the gluon field

$$A_\mu = \sum_{a=1}^8 A_\mu^a t^a. \quad (2.21)$$

The coupling of the strong interaction g_s is related to the QCD coupling constant $\alpha_s = (g_s^2/4\pi)$. This coupling depends on the momentum transfer Q in the particle reactions and goes towards zero for large value of Q^2 . This is the reason for the two phenomena *confinement* and *asymptotic freedom*, mentioned in the beginning of this section.

¹Note, that in this and the following equations q means the quark field, and not the electric charge as presented in the formulas in Section 2.1.

2.2.3. Electroweak interactions

The first evidence for a new interaction type was the observed free neutron decay, also called β decay (Figure 2.2)

$$n \rightarrow p + e^- + \bar{\nu}.$$

In this reaction, as mentioned and presented in the previous sections, the quarks contained in the nucleus change their flavor. Neither the electromagnetic nor the strong forces are able to cause this behavior, so a new interaction type was needed and implemented for the explanation of the observed scenario. This new force had been called *weak*, because of the fact, that its strength is about 10^{13} times less than that of the strong interaction. According to this, the weak interaction is induced by massive bosons W^+ , W^- and Z^0 whose masses are about 90 GeV (see Section 2.2.1) and their mean life is about $3 \cdot 10^{-25}$ s. Therefore they can act for only distances to about 10^{-18} m (1000 times smaller than the diameter of atomic nucleus).

It was observed for the β decay that the charged weak currents (W^+ , W^-) couple exclusively to left-handed fermions. Therefore the left-handed fermions are arranged in the doublets of the electroweak isospin T . The right-handed fermions being not involved in the W^\pm -coupling form isospin singlets. For the weak interactions one postulates the invariance under the rotation in the isospin space. The corresponding symmetry group is here SU(2).

The SU(2) gauge group includes three gauge bosons W_μ^1 , W_μ^2 and W_μ^3 . These bosons couple with the same strength g to the left-handed fermions. The two physical charged bosons W^+ and W^- are linear combinations of W_μ^1 and W_μ^2 . W_μ^3 is a neutral boson coupling also only to the left-handed fermions. However, there have been found no experimental evidences for existence of a neutral current which couples only to the left-handed fermions. Thus the SU(2) have to be extended with an U(1) symmetry group of a new quantity called *weak hypercharge* Y . There exist interrelations between the three values electric charge Q , weak hypercharge Y and the third component of the isospin T_3 expressed in the Gell-Mann-Nishijima formula

$$Q = T_3 + \frac{Y}{2}. \quad (2.22)$$

The gauge field B_μ from the U(1) $_Y$ symmetry couples to the left-handed as well as to the right-handed fermions. The resulting SU(2) $_L \otimes$ U(1) $_Y$ structure includes the U(1) $_{EM}$ group as its subgroup. This way both forces, weak and electromagnetic, could be unified into one *electroweak* interaction. The theory describing this interaction is also called *GSW-Theory* (after its developer's names: Glashow, Salam and Weinberg). The postulation of the local gauge invariance in the entire SU(2) $_L \otimes$ U(1) $_Y$ group is fulfilled with the covariant derivative

$$\partial \rightarrow D_\mu = \partial_\mu + igT_j W_\mu^j + i\frac{g'}{2}YB_\mu \quad (2.23)$$

with the gauge fields $\vec{W}_\mu = \{W_\mu^1, W_\mu^2, W_\mu^3\}$ of SU(2) $_L$ and B_μ of U(1) $_Y$. The Lagrangian extension for the bosons is

$$\mathcal{L}_{Yang-Mills} = \frac{1}{4}\vec{W}^{\mu\nu}\vec{W}_{\mu\nu} - \frac{1}{4}B^{\mu\nu}B_{\mu\nu} \quad (2.24)$$

2. Theoretical framework of Particle Physics

with the field strength tensors of the *Yang-Mills* theory [8].

The classification of the fermions with their associated quantum numbers is presented in Table (2.1). Note, that the quark weak eigenstates d' , s' and b' are not identical with their mass eigenstate d , s , and b (Figure 2.1). Both quark representations can transform into each other:

$$\begin{pmatrix} d' \\ s' \\ b' \end{pmatrix} = V_{CKM} \begin{pmatrix} d \\ s \\ b \end{pmatrix}$$

where V_{CKM} is the *Cabibbo-Kobayashi-Maskawa mixing matrix*. Also the neutrino eigenstates ν_e, ν_μ and ν_τ are not identical to the observed mass eigenstates ν_1, ν_2 and ν_3 . Due to the non-zero mass of the neutrinos the existence of right-handed neutrinos is conceivable.

	Generation			Quantum Number			
	1	2	3	Q	T	T_3	Y
Leptons	$\begin{pmatrix} \nu_e \\ e \end{pmatrix}_L$	$\begin{pmatrix} \nu_\mu \\ \mu \end{pmatrix}_L$	$\begin{pmatrix} \nu_\tau \\ \tau \end{pmatrix}_L$	0	1/2	+1/2	-1
	e_R	μ_R	τ_R	-1	1/2	-1/2	-1
				-1	0	0	-2
Quarks	$\begin{pmatrix} u \\ d' \end{pmatrix}_L$	$\begin{pmatrix} c \\ s' \end{pmatrix}_L$	$\begin{pmatrix} t \\ b' \end{pmatrix}_L$	+2/3	1/2	+1/2	+1/3
	u_R	c_R	t_R	-1/3	1/2	-1/2	+1/3
	d_R	s_R	b_R	+2/3	0	0	+4/3
				-1/3	0	0	-2/3

Table 2.1.: The order of the left-handed (L) and right-handed (R) fermions in multiplets in the GSW theory. The prime values mean the weak eigenstates of the quarks to distinguish them from the signed mass eigenstates.

The mass eigenstate of the bosons W_μ^1, W_μ^2 and W_μ^3 and B_μ belonging to $SU(2)_L \otimes U(1)_Y$ are obtained by linear combinations

$$W_\mu^\pm = \frac{1}{\sqrt{2}}(W_\mu^1 \mp iW_\mu^2) \quad (2.25)$$

$$A_\mu = B_\mu \cos \theta_W + W_\mu^3 \sin \theta_W \quad (2.26)$$

$$Z_\mu = -B_\mu \sin \theta_W + W_\mu^3 \cos \theta_W. \quad (2.27)$$

W_μ^\pm represents the charged bosons, which are carrier of the charged weak currents, A_μ is the photon field, Z_μ is the neutral boson being carrier of the neutral weak current. θ_W is called weak mixing angle and is dependent on the coupling constants g and g' :

$$\cos \theta_W = \frac{g}{\sqrt{g^2 + g'^2}}, \quad \sin \theta_W = \frac{g'}{\sqrt{g^2 + g'^2}}. \quad (2.28)$$

The photon field A_μ should have the same coupling strength as in the QED. For this purpose one requires that the weak couplings g and g' are proportional to the electric elementary charge e

$$g = \frac{e}{\sin \theta_W}, \quad g' = \frac{e}{\cos \theta_W}. \quad (2.29)$$

Boson field	Coupling term
γ (photon)	$-ie\gamma_\mu$
W^\pm	$-i\frac{e}{\sqrt{2}\sin\theta_W}\gamma^\mu\frac{1}{2}(1-\gamma^5)$
Z^0	$-i\frac{e}{\sqrt{2}\sin\theta_W\cos\theta_W}\gamma^\mu\frac{1}{2}(g_V - g_A\gamma^5)$

Table 2.2.: The three electroweak coupling terms. The photon field photon couples via vector coupling to the fermions, the W^\pm bosons couple only to the left-handed fermions and right-handed antifermions, the strength of the neutral current (Z^0) coupling to the fermions depends on the fermion electric charge and is expressed in the vector and axial vector couplings, g_V and g_A , respectively.

In Table (2.2) all three electroweak coupling terms are listed. The first term, representing the photon field, couples via vector coupling to the fermions. The second term representing the W^\pm bosons has a vector-minus axial vector structure. This means that the W^\pm bosons couple only to the left-handed fermions and right-handed antifermions. Also the third term for the neutral charged current (Z^0) contains both parts for vector and axial vector coupling. However, they are generally not equal; the strength of the Z^0 coupling to the fermions depends on their electric charge

$$g_V = T_3 - 2Q \sin^2 \theta_W, \quad g_A = T_3. \quad (2.30)$$

2.2.4. The Higgs mechanism

The theory invariance under $SU(2)_L \otimes U(1)_Y$ transformations implies the existence of the mentioned four gauge bosons. But in the GSW the masses are predicted to be zero, which contradicts the experimental facts (see Figure 2.1). The local gauge invariance forbids to insert artificially massive bosons into the theory (mass terms like $\frac{1}{2}m^2 B_\mu B^\mu$). Also the fermion mass terms $m\bar{\psi}\psi = m(\bar{\psi}_R\psi_L + \bar{\psi}_L\psi_R)$ are not allowed, since they would be transformed like doublets (and not singlets) under $SU(2)_L$ symmetry because of the different transformation behavior of the ψ_L and ψ_R , and would destroy the gauge invariance. The GSW theory is therefore extended by an additional principle of the dynamic generation of the particle mass – the Higgs mechanism.

In 1964 the first version of this mechanism was presented by P. Higgs, F. Englert and R. Brout [9]. Here a complex scalar field Φ was postulated. It interacts with a potential $V(\Phi)$, which is invariant under $SU(2)_L \otimes U(1)_Y$ transformations.

In consequence Φ can be presented as a isospin doublet

$$\Phi = \begin{pmatrix} \phi^+ \\ \phi^0 \end{pmatrix} = \frac{1}{\sqrt{2}} \begin{pmatrix} \phi_1 + i\phi_2 \\ \phi_3 + i\phi_4 \end{pmatrix} \quad (2.31)$$

with the corresponding potential

2. Theoretical framework of Particle Physics

$$V(\Phi) = \mu^2 \Phi^\dagger \Phi + \lambda(\Phi^\dagger \Phi)^2. \quad (2.32)$$

(see Figure 2.3, presented as function of the fields ϕ_3 and ϕ_4 only).

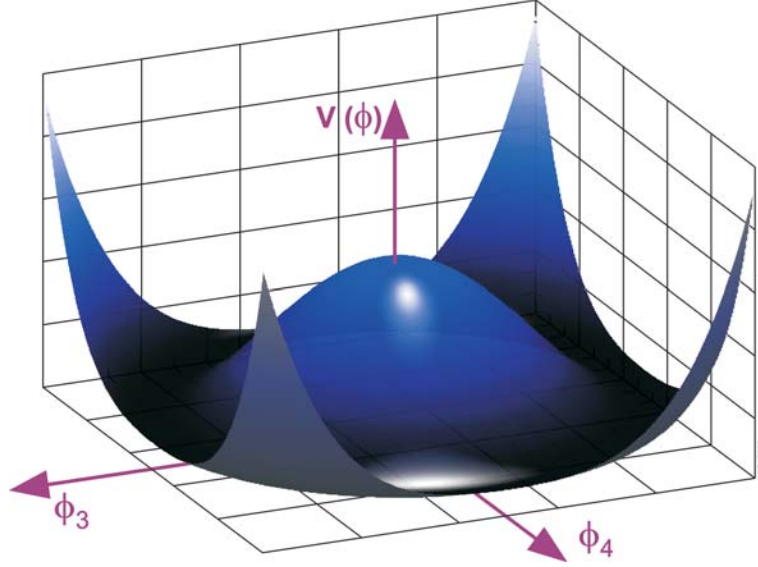


Figure 2.3.: The Higgs potential. The choice for the minimum at $V_{min} = v/\sqrt{2}$ implies the spontaneous symmetry breaking of $SU(2)_L \otimes U(1)_Y$.

The invariance under the $U(1)_{EM}$ group implies a non-zero *vacuum expectation value* (vev) $\frac{v}{\sqrt{2}} = \frac{\mu^2}{2\lambda}$ of the ϕ^0 field. It means that the ground state is

$$\Phi(x) = \frac{1}{\sqrt{2}} \begin{pmatrix} 0 \\ v + h(x) \end{pmatrix}, \quad (2.33)$$

where $h(x)$ is a real scalar field in radial direction ϕ_3 and represents fluctuations around the expected value $v/\sqrt{2}$. The expansion around $v/\sqrt{2}$ breaks the symmetry of $SU(2)_L \otimes U(1)_Y$; the Lagrangian and the ground state have no more the same symmetry.

The Goldstone theorem [10] says, that in the case of a global symmetry breaking massless fields always appear: the *Goldstone bosons*. The effect of the vacuum fluctuation of $\Phi(x)$ in the directions ϕ_1 , ϕ_2 and ϕ_4 is the creation of three Goldstone bosons θ_1 , θ_2 and θ_3 , respectively². The mentioned field $h(x)$ is identified with a new scalar field, the *Higgs boson*. The fluctuation of the field $\Phi(x)$ can be parametrized as expression in the terms of θ_1 , θ_2 , θ_3 and $h(x)$:

$$\Phi(x) = \exp \left[i \sum_{j=1}^3 \theta_j(x) \frac{\tau_j}{v} \right] \frac{1}{\sqrt{2}} \begin{pmatrix} 0 \\ v + h(x) \end{pmatrix} \quad (2.34)$$

²Look here to the indices denoting $3 \rightarrow 4$

with the usual Pauli matrices τ_1 , τ_2 and τ_3 .

Because the four fields θ_1 , θ_2 , θ_3 and $h(x)$ are in fact independent of each other, the Higgs Lagrangian

$$\mathcal{L}_{Higgs} = (D_\mu \Phi)^\dagger D^\mu \Phi - V(\Phi) \quad (2.35)$$

is locally invariant under SU(2) transformations. The former isospin doublet can be transformed onto a Higgs isospinor Φ . The Goldstone bosons can be removed hereby. Into the form of the Higgs Lagrangian (2.35) the fields (2.25), (2.26) and (2.27) are now inserted:

$$\begin{aligned} \mathcal{L}_{Higgs} &= \frac{1}{2} \partial_\mu h \partial^\mu h & (a) \\ &+ \frac{1}{4} g^2 v^2 W_\mu^+ W^{-\mu} + \frac{1}{8} (g^2 + g'^2) v^2 Z_\mu Z^\mu - \lambda v^2 h^2 & (b) \\ &+ \frac{1}{2} g^2 v h W_\mu^+ W^{-\mu} + \frac{1}{4} (g^2 + g'^2) v h Z_\mu Z^\mu & (c) \\ &+ \frac{1}{4} g^2 h^2 W_\mu^+ W^{-\mu} + \frac{1}{8} (g^2 + g'^2) h^2 Z_\mu Z^\mu & (d) \\ &- \lambda v h^3 - \frac{1}{4} \lambda h^4 & (e) \\ &+ \text{const} & (f) \end{aligned} \quad (2.36)$$

The interpretation of the individual non-constant terms in Equation 2.36 is following:

- (a): kinetic term of the Higgs boson field;
- (b): mass terms for W^+ , W^- , Z^0 and Higgs bosons;

$$m_W = \frac{1}{2} v g, \quad (2.37)$$

$$m_Z = \frac{1}{2} v \sqrt{g^2 + g'^2}, \quad (2.38)$$

$$m_H = v \sqrt{2\lambda} = \sqrt{-2\mu^2}; \quad (2.39)$$

- (c): trilinear coupling terms HW^+W^- and HZ^0Z^0 ;
- (d): quadrilinear coupling terms HHW^+W^- and HHZ^0Z^0 ;
- (e): Higgs self-coupling terms HHH and $HHHH$.

The photon field γ must remain massless after the symmetry breaking; it does not appear in the Equation 2.36. This was realized by choice of the $U(1)_{EM}$ symmetrical vacuum, which caused the breaking of the $SU(2)_L \otimes U(1)_Y$ symmetry in the way, that the $U(1)_{EM}$ symmetry of QED remained not affected: the photon is the gauge boson of $U(1)_{EM}$. In case of the spontaneous symmetry breaking of the vacuum symmetry, the W^\pm s and Z^0 s become massive whilst the gauge symmetry of \mathcal{L}_{Higgs} was maintained. The three bosons being now massive have the three theoretical Goldstone bosons absorbed by use of an additional longitudinal degree of freedom.

It is possible to give mass to the fermions as well as to the W^\pm and Z^0 bosons. For this purpose new coupling modes – the *Yukawa coupling* for left and right handed fermions – are connected to the Higgs doublet (as well as to its charge conjugated doublet)

$$\Phi_C = i\tau_2 \Phi^* \begin{pmatrix} \bar{\phi}^0 \\ -\phi^- \end{pmatrix}. \quad (2.40)$$

2. Theoretical framework of Particle Physics

This is performed by extending the Higgs Lagrangian by the Yukawa term (here only presented for the 1. quark and lepton generation):

$$\begin{aligned}
\mathcal{L}_{Yukawa} = & -g_e \left[(\bar{\nu}_e, \bar{e})_L \begin{pmatrix} \phi^+ \\ \phi^0 \end{pmatrix} e_R + \bar{e}_R(\phi^-, \bar{\phi}^0) \begin{pmatrix} \nu_e \\ e \end{pmatrix}_L \right] \\
& -g_d \left[(\bar{u}, \bar{d})_L \begin{pmatrix} \phi^+ \\ \phi^0 \end{pmatrix} d_R + \bar{d}_R(\phi^-, \bar{\phi}^0) \begin{pmatrix} u \\ d \end{pmatrix}_L \right] \\
& -g_u \left[(\bar{u}, \bar{d})_L \begin{pmatrix} \bar{\phi}^0 \\ -\phi^- \end{pmatrix} u_R + \bar{u}_R(\phi^0, -\phi^+) \begin{pmatrix} u \\ d \end{pmatrix}_L \right].
\end{aligned} \tag{2.41}$$

The vev expansion yields

$$\begin{aligned}
\mathcal{L}_{Yukawa} = & -\frac{1}{\sqrt{2}}g_e v \bar{e}e - \frac{1}{\sqrt{2}}g_d v \bar{d}d - \frac{1}{\sqrt{2}}g_u v \bar{u}u & (a) \\
& -\frac{1}{\sqrt{2}}g_e \bar{e}eh - \frac{1}{\sqrt{2}}g_d \bar{d}dh - \frac{1}{\sqrt{2}}g_u \bar{u}uh. & (b)
\end{aligned} \tag{2.42}$$

The line (a) in Equation 2.42 contains the fermion masses

$$m_e = \frac{1}{\sqrt{2}}g_e v, \quad m_d = \frac{1}{\sqrt{2}}g_d v, \quad m_u = \frac{1}{\sqrt{2}}g_u v. \tag{2.43}$$

In line (b) the couplings of the Higgs boson field to the fermions are presented, which are proportional to their masses (see Equation 2.43). The construction of the Yukawa terms for the fermions of the 2nd and 3rd generation proceeds analogously. Unfortunately, the fermion masses cannot be calculated theoretically in the SM due to the fact, that the coupling constants g_f are here free parameters.

The complete Lagrangian of the GSW theory can now be assembled from the parts:

$$\begin{aligned}
\mathcal{L}_{GSW} = & -\frac{1}{4} \sum_{j=1}^3 W_{\mu\nu}^j W_j^{\mu\nu} - \frac{1}{4} B_{\mu\nu} B^{\mu\nu} & (a) \\
& + \bar{L} \gamma^\mu \left(i\partial_\mu - g \sum_{j=1}^3 \frac{\tau_j}{2} W_\mu^j - g' \frac{Y}{2} B_\mu \right) L + \bar{R} \gamma^\mu \left(i\partial_\mu - g' \frac{Y}{2} B_\mu \right) R & (b) \\
& + \left| \left(i\partial_\mu - g \sum_{j=1}^3 \frac{\tau_j}{2} W_\mu^j - g' \frac{Y}{2} B_\mu \right) \Phi \right|^2 - V(\Phi) & (c) \\
& + g_f \left[\bar{L} \Phi R + \bar{R} \Phi^\dagger L \right]. & (d)
\end{aligned} \tag{2.44}$$

where L and R indicate a left-handed fermion doublet and right handed fermion singlet, respectively. The parts in Equation 2.44 have following meanings:

- (a): kinetic term of photons, self interaction of W^\pm and Z^0 bosons;
- (b): kinetic term of fermions and their interaction with the gauge bosons;
- (c): masses of gauge and Higgs bosons, coupling of gauge bosons to the Higgs bosons, self interaction of the Higgs boson;
- (d): fermion masses and their coupling to the Higgs boson.

2.3. Beyond the Standard Model

The SM comprehensibly explains the world of the particles and antiparticles. The strength of SM is expressed particularly by the fact, that particles predicted by the SM, were discovered after a search period in diverse laboratories of particle physics; for example the detection of τ (SLAC 1975), W^\pm , Z^0 (CERN 1983) and top (FNAL 1995) [2].

Although the theoretical stand of the SM has found its confirmation in the experimental range, since a long time one is convinced of the fact, that it could not be the complete model of elementary particle physics. The mostly presented argument for it is, that the SM does not explain the various parameters contained in itself, such like the masses of the fermions and bosons, which are free parameters in the SM. However, one can recognize mass patterns in the SM generations, which suggest, that the particle masses are not completely random. Also the complete exclusion of the gravity in the SM demands its further extensions in form of more developed theoretical particle models [11].

2.3.1. Supersymmetry

The most famous theory being a candidate for extending the SM by giving an answer on its open question is Supersymmetry (SUSY). It is up to date the mainstream theory for collider experiments of the last years and we hope to explain the new physics at the TeV scale, which could be observed there soon.

General description

Two important SM problems can be solved by SUSY:

- SUSY is able to unify the coupling constants of all fundamental interactions at one scale point Λ_{GUT} (see Figure 2.4). Introducing a new symmetry group SU(5) in the SM, it satisfies this demand only partially, in addition the gauge bosons X and Y of SU(5) violate the baryon number, which implies proton decay. This fact is not observed to date ($\tau_{proton} > 10^{33}$ a).
- Based on the SM, for the theoretical treatment of the particle mass some terms of higher order are required which become infinite and cannot be experimentally proved. The problem seems to be mathematically solved within the SM by application of integral regulation resulting in finite scales, but a physical interpretation is difficult. For instance, one can find in the correction graphs for the Higgs mass m_H terms like

$$\Delta m_H^2(f) = \frac{|\lambda_f|^2}{16\pi^2} \left(-2\Lambda_{UV}^2 + 6m_f^2 \ln \frac{\Lambda_{UV}}{m_f} + \dots \right), \quad (2.45)$$

$$\Delta m_H^2(S) = \frac{\lambda_S}{16\pi^2} \left(\Lambda_{UV}^2 - 2m_S^2 \ln \frac{\Lambda_{UV}}{m_S} + \dots \right), \quad (2.46)$$

where Λ_{UV} is the implemented ultra-violet (UV) cut scale for fermions f and scalars F [3].

2. Theoretical framework of Particle Physics

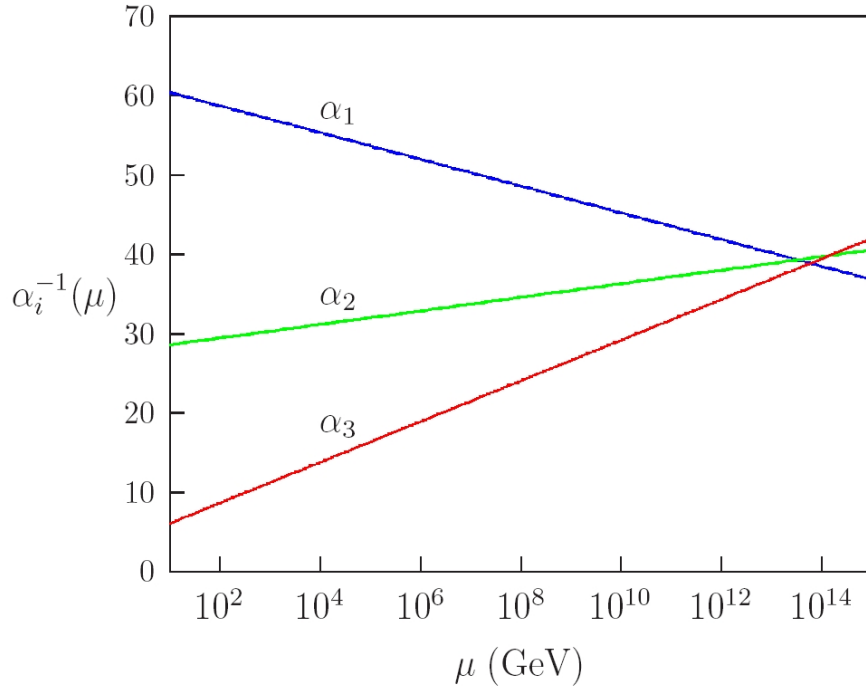


Figure 2.4.: Gauge-coupling unification in a supersymmetric model. The couplings α_i representing the three fundamental interactions meet approximately at one point (here ca. 10^{14} GeV) [12].

The different signs in Equations 2.45 and 2.46 predict a new solution for given problems, which can be found in a new symmetry between fermions and bosons. In this case, i.e. if each of the SM fermions is accompanied by two complex scalars with $\lambda_S = |\lambda_f|^2$, the respective corrections cancel each other. This must be also validated for the terms of higher order. These considerations lead to a Supersymmetry, in which each fermion state can be transformed into a boson and vice versa:

$$\mathcal{Q}|fermion\rangle = |boson\rangle, \quad \mathcal{Q}|boson\rangle = |fermion\rangle. \quad (2.47)$$

The generating operator \mathcal{Q} – *supercharge* – is a complex spinor

$$\mathcal{Q} = \begin{pmatrix} Q_\alpha \\ Q_{\dot{\alpha}}^\dagger \end{pmatrix}. \quad (2.48)$$

with following properties:

$$\begin{aligned} [Q_\alpha, Q_{\dot{\alpha}}^\dagger]_- &= 2\sigma_{\alpha,\dot{\alpha}}^\mu P_\mu, \\ [Q_\alpha, Q_\beta]_- &= [Q_{\dot{\alpha}}^\dagger, Q_{\dot{\beta}}^\dagger]_- = 0, \\ [Q_\alpha, P_\mu]_- &= [P^\mu, Q_{\dot{\alpha}}^\dagger]_- = 0. \end{aligned} \quad (2.49)$$

σ_μ mean the usual Pauli Matrices, P_μ the momentum operator.

Thus the supercharge \mathcal{Q} is of fermion origin and SUSY is a space-time and spin symmetry. Moreover, P^2 also commutate with Q and Q^\dagger ; therefore the spinors have the same eigenvalues under these transformations. This implies the same mass and quantum numbers of the superpartners.

A general property appearing by implementation of a gauge theory within SUSY are terms that violate the lepton (L) and baryon (B) numbers. A possible proton decay could be then explained by means of SUSY. Further discrete symmetries can suppress these terms by implementing the so-called R -parity

$$R = (-1)^{3(B-L)+2S}. \quad (2.50)$$

Here the conservation numbers L and B are related to the spin S of the particles. R is positive for all known SM particles $R_{SM} = +1$. In the SM it is impossible to observe vertices violating L or B .

The main phenomenological consequence of the R parity conservation is the fact, that the SUSY particles are produced only by even number and may not be mixed with the known SM particles. The *Lightest Supersymmetric Particle* (LSP) with $R_{LSP} = -1$ is stable. In case of its possible electrical neutrality it is therefore a possible candidate for the non-baryonic dark matter in cosmological models, because of its merely weak interaction with matter [13].

Minimal Supersymmetric Standard Model

The number of the maximal possible supersymmetric generators \mathcal{Q} is determined by $N_{\mathcal{Q}} \leq 4J$, where J is the highest particle spin. The *Minimal Supersymmetric Standard Model* (MSSM) is the minimal extension of the SM that operates with only one generator, so that each SM particle is associated with one new super partner. The list of the MSSM particles is given in Figure (2.5). In the MSSM one can find five classes of SM super partner particles: squarks, gluinos, charginos, neutralinos and sleptons³.

In addition, the R parity is postulated, the LSP of the MSSM is therefore stable. The R parity is also needed to explain the stability of the proton. Nevertheless the MSSM must undergo a break mechanism, due to the fact that the super partners of the SM particles have not been discovered yet, although they have the same masses. These soft symmetry breaking is communicated to the Lagrangian by some unknown dynamics. The result are 120 new parameters in the MSSM. A large number of those parameters lead to unacceptable processes like flavor changing neutral currents or electric dipole moments of neutron and electron.

The motivation for introducing the MSSM was stabilization of the Higgs mass to radiative corrections, being divergent in the SM. The scalars in the supersymmetric models are related to the fermions and have the same masses, therefore the scalar masses should have the same radiative stability as the fermion masses. The mass of the superpartners of the SM particles should then be about the Higgs vev, roughly 100 GeV. If the superpartners are at the TeV scale then the couplings of the three SM gauge groups SU(3), SU(2) and U(1) are unified (see Figure 2.4).

The SM Higgs boson has more than one superpartner in the MSSM, in opposition to the most of the SM particles. A single SM Higgs superpartner – Higgissino – would lead to a gauge anomaly and the theory would be inconsistent. Only if the theory contains pairs of

³In order to the convention the super partner are named by addition of prefix "s-" (SM fermions) or suffix "-ino" (SM bosons).

2. Theoretical framework of Particle Physics

MINIMAL SUPERSYMMETRIC STANDARD MODEL (MSSM) OF ELEMENTARY PARTICLES					
MSSM PARTICLE		SUPERPARTNER		MASS EIGENSTATE	
Symbol	N	Symbol & Name	N	Symbol & Name	N
ν	3	$\tilde{\nu}$ sneutrino	3	$\tilde{\nu}$ sneutrino	3
$\ell_L(e, \mu, \tau)$	3	$\tilde{\ell}_L$ slepton	3	$\tilde{\ell}_1, \tilde{\ell}_2$ slepton	6
$\ell_R(e, \mu, \tau)$	3	$\tilde{\ell}_R$ slepton	3		
q_L	6	\tilde{q}_L squark	6		
$u_R(u, c, t)$	3	\tilde{u}_R squark	3	\tilde{q}_1, \tilde{q}_2 squark	12
$d_R(d, s, b)$	3	\tilde{d}_R squark	3		
g	8	\tilde{g} gluino	8	\tilde{g} gluino	8
W^\pm	2	\tilde{W}^\pm wino	2		
H_1^-	1	\tilde{H}_1^- Higgsino	1	$\tilde{\chi}_{1,2}^\pm$ chargino	4
H_2^+	1	\tilde{H}_2^+ Higgsino	1		
W^3	1	\tilde{W}^3 wino	1		
B	1	\tilde{B} bino	1	$\tilde{\chi}_{1,4}^0$ neutralino	4
H_1^0	1	\tilde{H}_1^0 Higgsino	1		
H_2^0	1	\tilde{H}_2^0 Higgsino	1		

Figure 2.5.: The Minimal Supersymmetric Standard Model (MSSM) extends minimally the SM by associating only one additional supersymmetric partner to each of the SM particle. These new particle classes are squarks, gluinos, charginos, neutralinos and sleptons. Analogically to the SM the states \tilde{W}^3 and \tilde{B} mixes into the *zino* \tilde{Z} and *photino* $\tilde{\gamma}$.

Higgsinos the gauge anomaly does not exist. The simplest supposition is a theory with one Higgsino pair and therefore one pair of scalar Higgs doublet

$$H_u = \begin{pmatrix} H_u^+ \\ H_u^0 \end{pmatrix}, \quad H_d = \begin{pmatrix} H_d^0 \\ H_d^- \end{pmatrix}. \quad (2.51)$$

This Higgs doublet (called *up type* Higgs and *down type* Higgs) is demanded in order to have renormalizable Yukawa couplings between Higgs and SM fermions. In opposition to the SM there are no charge conjugated fields with chiral potential in the supersymmetrical models. The MSSM contains vector superfields that are related to the SM gauge groups and include the vector bosons and associated gauginos. Also it contains chiral superfields with SM fermions, Higgs bosons and their superpartners.

MSSM Symmetry Breaking and Higgs Bosons

The MSSM Lagrangian consist of several parts, like Kahler potential, which describes particle masses and Higgs fields (kinetic terms for the fields), gauge field superpotential (kinetic terms for the gauge bosons and gauginos) and the superpotential for matter and Higgs fields (Yukawa couplings for the SM fermions and mass term for Higgsinos). Interesting is the last Lagrangian part that represents the soft symmetry breaking

$$\mathcal{L}_{breaking} = m_{\frac{1}{2}}\tilde{\lambda}\tilde{\lambda} + m_0\phi^+\phi + Ah_u\tilde{q}\tilde{u}^c + Ah_d\tilde{q}\tilde{d}^c + Ah_d\tilde{l}\tilde{e}^c + \text{h.c.} \quad (2.52)$$

The first term, where $\tilde{\lambda}$ are the gauginos and $m_{\frac{1}{2}}$ depends on gaugino type (wino, bino and gluino), produces gaugino masses. The second term represents the soft masses for the MSSM scalar fields ϕ . m_0 are 3×3 hermitian matrices for the squarks and sleptons. The rest non-constant terms in the Lagrangian 2.52 describes diverse coupling of the Higgs fields with each other and chiral fields \tilde{u}^c , \tilde{d}^c and \tilde{e}^c .

The symmetry should be broken by a mechanism, which postulates zero vev for the charged Higgs fields in Equation 2.51. This is demanded due to the conserving the $U(1)_{EM}$ group. The postulates lead to $\partial V / \partial H_u^+ = 0$, so that for the V_{min} also $H_d^- = 0$. The resulting potential is then

$$\begin{aligned} V &= (|\mu|^2 + M_{H_u}^2)|H_1|^2 + (|\mu|^2 + M_{H_d}^2)|H_2|^2 - b(H_1H_2 + H_2^+H_1^+) \\ &+ \frac{1}{8}(g^2 + g'^2)(|H_1|^2 - |H_2|^2)^2 \end{aligned} \quad (2.53)$$

with the Higgs mass parameter μ and the bilinear coupling b . After the symmetry is broken the eight scalars of the isospin doublets transform themselves into the three well known Goldstone bosons and five Higgs bosons. The Goldstone bosons G^0 and G^\pm become a longitudinal degree of freedom of the W^\pm and Z^0 bosons. The mass eigenvalues of the remaining Higgs fields include a new pseudo-scalar A , two charged Higgs bosons H^\pm and two neutral Higgs bosons h and H .

In the lower order one can find for the masses of the MSSM Higgs bosons (with $m_{1,2}^2 = |\mu|^2 + M_{H_{u,d}}^2$ and β as one of the mixing angle being a parameter at the symmetry breaking)

$$\begin{aligned} m_A^2 &= m_1^2 + m_2^2 \\ m_{H^\pm}^2 &= m_A^2 + m_W^2 \\ m_{h,H}^2 &= \frac{1}{2} \left(m_A^2 + m_Z^2 \mp \sqrt{(m_A^2 + m_Z^2)^2 - 4m_A^2m_Z^2 \cos 2\beta} \right) \end{aligned} \quad (2.54)$$

with the relations

$$m_W \leq m_{H^\pm}, \quad m_h \leq m_A \leq m_H. \quad (2.55)$$

2.3.2. Other models

Other than the Supersymmetry there exist a couple more of alternative models to the SM. Some of them are in fact its extensions and one can recognize as same basic approach in them as in the SM. The most well-known problem included in these theories is the attempt to unify

2. Theoretical framework of Particle Physics

the three interactions occurred in the SM in a *Grand Unified Theory* (GUT). The problem of the missing connection of the gravity to the other interaction is attempted to be solved in some quantum gravity theories, which is involved e.g. in diverse *String Theories*. Some another theories like e.g. *Technicolor* try to explain the dynamical electroweak symmetry breaking. In following an overview of these three models as representations of SM alternatives is given. For more informations see the References [14], [15], [16], [17], and [18].

Grand Unification Theory (GUT)

The *Grand Unification Theory* (GUT) unifies the fundamental gauge symmetries: hypercharge, weak force and quantum chromodynamics. The basic idea of GUT is that at extremely high energies above 10^{14} GeV all gauge symmetries have only one coupling strength and thus the electromagnetic, weak and strong forces become a single unified field.

The motivation for searching for any GUT theory was the demand for a simply aesthetic in the particle models. The more symmetrical a theory is the more elegant it is. This is to date not satisfied by regarding the SM, which is a direct product of three groups. Reasoning with the unification of electricity and magnetism, as well as of electromagnetism and weak interaction, one tries to unify these three groups in an analogical manner. These circumstances mean that the three couplings in common with a large number of Yukawa couplings cause too many free parameters. Thereby the SM chiral fermions fields unify into only three generations with two representations in SU(5) and three generations in SO(10). The generic combination of chiral fermions are then free of gauge anomalies and will be unified representing some large Lie groups with additional matter fields. SO(10) predicts additionally a right-handed neutrino.

Both SU(5) and SO(10) predicts relations within the fermion masses such as electron and down quark, muon and strange quarks, tau and bottom quark (Georgi-Jarlskog mass relation [19]). Since other Lie groups lead to different normalizations, the renormalization group running of the three gauge couplings is common for them at one point if the hypercharge is normalized and is consistent with SU(5) or SO(10) GUTs. However, it becomes more accurate if MSSM is used than SM.

The GUT models contain among others a compact Lie group. A Higgs sector of GUT consists of a number of scalar fields and chiral Weyl fermions within real or complex representations of the Lie group. This Lie group contains the SM and Higgs fields with their vevs leading to a spontaneous symmetry breaking. The matter is represented by the Weyl fermions. The SO(10) being the most promising candidate of GUTs does not contain any exotic fermions like fermions beyond SM or right-handed neutrinos. Each generation in SO(10) is unified into a simple irreducible representation.

The existence of some topological defects such as monopoles, cosmic strings and others are predicted by the GUT models. None of them has been observed to date, like for example the proton decay that is also generally predicted by GUTs. Both SU(5) and SO(10) are affected by so-called doublet-triplet problem: for each electroweak Higgs doublet a new colored Higgs triplet is postulated with mass being many orders of magnitude below the GUT scale. After unifying quarks with leptons the Higgs doublet is also unified with the Higgs triplet. However these triplets, which would cause a very rapid proton decay, are not discovered yet.

Finally most GUTs require a threefold replication of the matter fields and can not explain the three generations of fermions. Also the little hierarchy between the fermion masses in different generations cannot be explained by using the most GUT models.

String Theory

In contrast to other elementary particle theories, in which the constituents of matter are represented as zero-dimensional point particles, the string theory is a fundamental model describing the particles as one-dimensional extended objects – strings. The transition from point-like to string particles makes it possible to involve the quantum theory of gravity into the usual particle models. Moreover, it seems to be possible in the string theory to unify all known natural forces – gravitational, electromagnetic, weak and strong – using the same equation set for their description (*Theory Of Everything*, TOE).

Basically all string theories formulate the matter constituents as strings of very slight size, in order of the Planck length $\sim 10^{-35}$ m. These strings vibrate with specific frequencies in different modes. The difference in the modes appears as different particle (electron, photon etc.). The mass of the particle and the interaction kind are determined by the vibration state of the strings. Splitting and combining of the strings would appear as emitting and absorbing particles, respectively. The strings included in the string theories can be open with two distinct endpoints, and/or closed with joined endpoints forming a string loop. These two string types yield different spectra within the theory.

The string theory was at first formulated for bosons, later also for fermions. These two different models were then successfully tried to be joined within a new comprehensive theory which include the string Supersymmetry between bosons and fermions. An attempt to explain the strong interaction by means of strings demands 26 dimensions in boson theory and "only" 10 dimensions in the superstring theory. Nevertheless, it was evident that the superstrings were an excellent candidate for a model unifying theory of all natural forces including the gravity. The gravity represented in closed strings is then a massless spin-2 excitation and the remaining forces spin-1 boson excitations. The additional dimensions have to be compacted (rolled up) to provide a realistic elementary particle model.

Technicolor

The Technicolor models are theories with no scalar Higgs field but with a large number of fermion fields. They also use a larger gauge group than the SM. The SM is then an effect of a spontaneous breaking of the gauge group.

The reason for implementation of the Technicolor was the absence of dynamical explanation in many aspects in diverse other particle models, including the SM. The answer for the dynamical origin of the electroweak symmetry breaking $SU(2)_L \otimes U(1)_Y \rightarrow U(1)_{EM}$ (see Section 2.2.3) would be provided by Technicolor. The SM Higgs potential gives no dynamical explanation for that problem; i.e. one have no satisfying response for the question, why the energy scale of the electroweak symmetry breaking, expressed by $\frac{v}{\sqrt{2}} = \frac{\mu^2}{2\lambda}$ in Equation 2.32 have non-zero value. Also the dynamical origin of the SM masses is not known, as well as the origin of the quark and lepton flavors. The fact that the quarks and leptons build three identical generations is not explained by any other elementary particle model.

The main idea in Technicolor is to obtain a model, in which the same kind of dynamics seen in the QCD is used for explaining the origin of the W^\pm and Z^0 boson masses. The quarks in the QCD experience both the strong and weak interactions. They are bound together by the strong interaction in condensates and thereby the electroweak symmetry is broken. Indeed the QCD causes the masses of W^\pm and Z^0 , however they are too small, compared to the experimental mass measurements. Analogously to the QCD Technicolor uses a similar method at a higher energy to explain the observed masses of W^\pm and Z^0 .

2. Theoretical framework of Particle Physics

The general concept of electroweak symmetry breaking in different Technicolor models is the assumption of a gauge group $G \otimes H$ at high energies, where G contains the SM gauge group. By running the renormalization group the strong coupling strength for H increases, what causes chiral symmetry breaking. An H -invariant composite field being the representation of the $G \otimes H$ obtains vev dynamically. In the case, that this vev is not G -invariant, the G is spontaneously broken without any Higgs field. If G is the SM group itself, this mechanism breaks the electroweak symmetry dynamically. H becomes then confined and disappears at low energies.

The extended Technicolor models assumes a unified gauge group K , which is broken spontaneously to $G \otimes H$ at energies higher than the Technicolor scale. This would lead to the gauge-mediated couplings between the SM fermions and Techniquarks which can provide masses to the SM fermions. Additionally, the Technibosons decay in the same way into SM particles.

3. New experiments for new particle search

The previous particle physics experiments were insufficient for the observation of expected new particle physics: neither the Higgs boson, nor the superpartner nor any "exotic" particles have been discovered at the diverse accelerator and cosmic ray experiments. On the other hand, theory requires new physics to solve inconsistencies. Therefore new experimental concepts are required, which are able to provide new findings in this sector. The needed energy scale for this purpose is, at least, in the TeV range. The Large Hadron Collider (LHC) fulfills this requirement by colliding proton-proton packets of 7 TeV each at a high luminosity. It is complemented by performant detectors permitting an extremely rapid detection and analysis of the collision products.

The present chapter describes the LHC design, its detectors and presents its potential for particle physics research. Afterwards the CMS experiment, the focus of this thesis, is presented with special consideration of its muon system. Finally, the design, function and production of the drift tube chambers, which are crucial for detection of muons, constituting a clear signature for the Higgs particle, are also described here.

3.1. The Large Hadron Collider (LHC)

3.1.1. General description

The *Large Hadron Collider* (LHC) [20] is a circular particle accelerator and collider located at CERN (Geneva), which will become the largest machine of such type and reaches the highest energy in the world. It is housed in a circular tunnel with a circumference of about 27 km at a depth of up to 175 m underground (Figure 3.1). The tunnel was formerly used for the LHC precursor, the LEP accelerator, an electron/positron collider, with a maximal collision energy of about 208 GeV. The LHC accelerates protons to their center of mass energy $\sqrt{s} = 14$ TeV. The main reason to avoid the difficult use of antiprotons was the fact that the reaction yield obtained by such collisions could not have been high enough, because the production and storage of a large amount of protons is simpler than of the antiprotons. In addition, at the mentioned high energy scale it is irrelevant whether the charge of the initial state is 0 or +2. The general layout of the LHC allows also its operation with heavy ion beams.

The proton injection in the LHC occurs stepwise using the existing upgraded and modified pre-accelerators. So the first acceleration takes place at *Linac 2*. From here the 50 MeV protons are delivered to the *Proton Synchrotron* (PS) and then, with an energy of 26 GeV and the final bunch spacing of 25 ns, to the *Super Proton Synchrotron* (SPS). Finally the proton bunches are injected from the SPS into the LHC in two beams circulating in opposite directions with an initial energy of 450 GeV.

Therefore two separate pipes are used for two separate proton beams accelerated in two opposite directions. For keeping the protons in such a way, two sets of deflecting magnets are installed within the pipes with opposite magnetic fields each. However, to reduce the amount of magnets it was decided to use "twin magnets" to be able to obtain a field in both directions. These magnets, developed specifically for the LHC, are superconducting (NbTi). They are

3. New experiments for new particle search

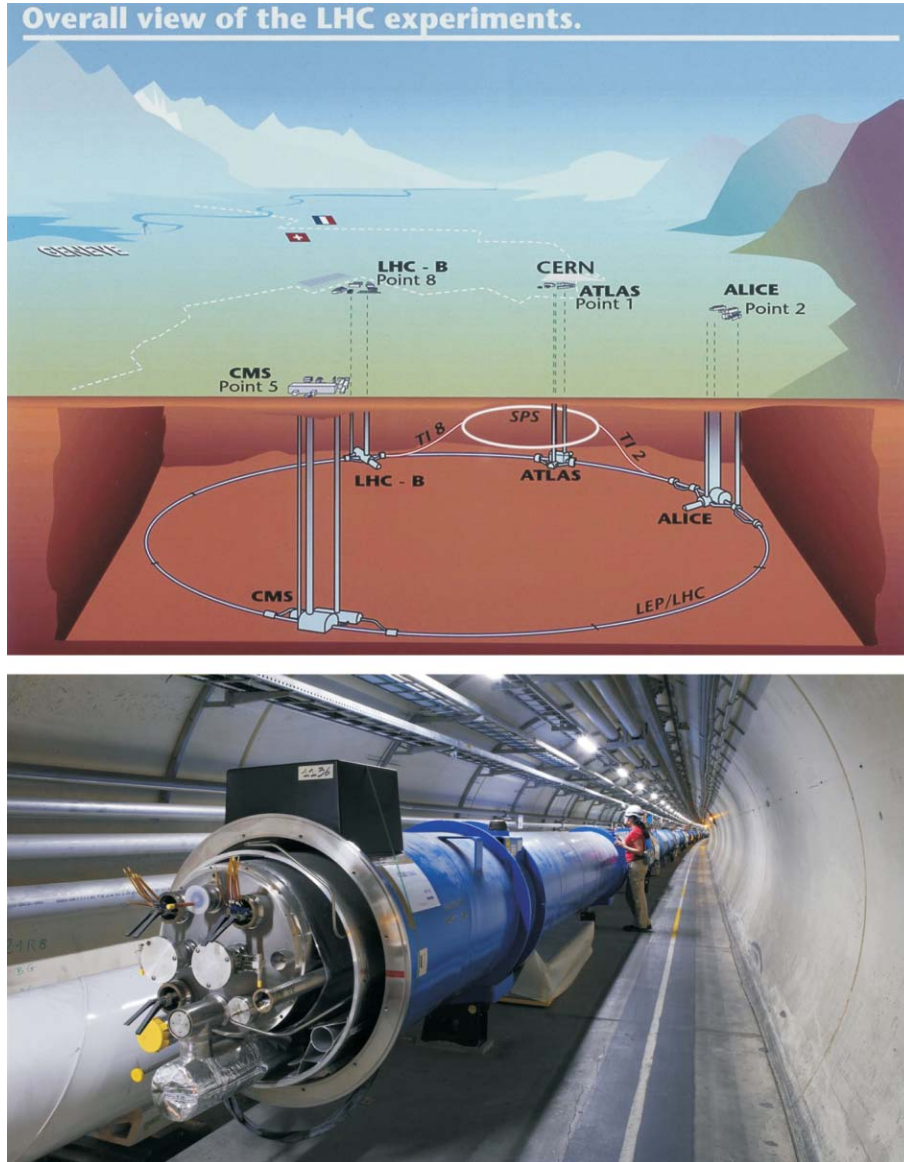


Figure 3.1.: The Large Hadron Collider (LHC) is a proton ring accelerator with a center of mass energy $\sqrt{s} = 14$ TeV (top). It was installed inside a 27 km long underground circular tunnel, where four main LHC detectors – ATLAS, CMS, ALICE and LHCb – are located at bunch crossing points. The two opposite proton beams are kept on track by superconducting magnets (bottom, during installation) [21].

cooled with superfluid Helium to a temperature of 1.9 K. The 1232 main magnet dipoles are 14.3 m long. The magnetic field obtained is about 8.33 T. A system of quadrupol magnets is used for beam focusing, guaranteeing the proper LHC operation.

At the moment of bunch crossing only few protons included in the accelerated bunches really collide with each other and produce the expected events. The other particles could also be deflected by the electromagnetic field of the opposite beam and vice versa. This can lead to appreciable particle loss for bunches with high particle density. The luminosity L , being a

measure for the number of all interactions per time unit t

$$\frac{dN}{dt} = \sigma L, \quad N = \sigma \int L dt = \sigma \mathcal{L} \quad (3.1)$$

must be as high as possible, especially for the search for rare particles like Higgs bosons. Here σ is the cross section, \mathcal{L} is the integrated luminosity for all interactions in the given period. The LHC's aim is to obtain $L = 10^{34} \text{ cm}^{-2}\text{s}^{-1}$. For this purpose the proton bunches must rapidly follow each other; the bunch distance in time is only 25 ns. Each of the 2808 bunches has about $1.1 \cdot 10^{11}$ protons, which implies an average beam current of 0.53 A. The lifetime of the bunches is about 10 hours. During this time the bunches execute about 400 millions cycles in the LHC.

3.1.2. LHC physics

To enlarge the particle interaction rate in Equation 3.1 it is important to obtain \mathcal{L} as high as possible. The luminosity is approximately

$$L = \frac{n_b \cdot N_b \cdot f}{4\pi \cdot \sigma_x \cdot \sigma_y}. \quad (3.2)$$

n_b represents the number of bunches per beam, N_b the number of particles in a bunch, f the bunch frequency, σ_x and σ_y are the widths of the proton distribution (Gaussian) in the beam. The cross section for a given partonic process in a pp-collision between two particles (protons) depends on the cross section of the proton partons $\hat{\sigma}$ and proton's parton densities, represented by their *parton density function* (pdf) $f(x_i, Q^2)$

$$\sigma = \int dx_1 \int dx_2 f_1(x_1, Q^2) f_2(x_2, Q^2) \hat{\sigma}. \quad (3.3)$$

The pdf expresses the probability for the existence of a parton inside the proton with momentum fraction x_i at the energy scale Q . Figure 3.2 presents the event rate at the LHC for nominal luminosity of $10^{34} \text{ cm}^{-2}\text{s}^{-1}$ as a function of \sqrt{s} for various processes. The total cross section is dominated by QCD events $qq \rightarrow qq$, $qq \rightarrow gg$ and $qg \rightarrow qg$. Events like Higgs production are rare, less than a factor of about 10^{-10} . Such rare particles decay very fast, mostly in partons again, manifest in hadronic showers (jets). But for new particle searches the leptonic and semi-leptonic decay processes are preferred to the QCD reactions due to their lower background. Therefore the identification and measurement of leptons is a crucial task of the LHC experiments.

For the interesting processes leading to Higgs production only few mechanisms have a measurable cross section. This is due to the property of the Higgs boson to couple preferentially to a particle with high mass, like massive vector bosons (W^\pm and Z^0) or massive quarks (particularly bottom and top quarks). Especially the following reactions, concerning Higgs physics, are of interest:

- gluon-gluon fusion $gg \rightarrow H$;
- WW and ZZ fusion $qq \rightarrow qqH$;
- associated Higgs production with W^\pm or Z^0 bosons $q\bar{q}' \rightarrow WH$, $q\bar{q} \rightarrow ZH$;

3. New experiments for new particle search

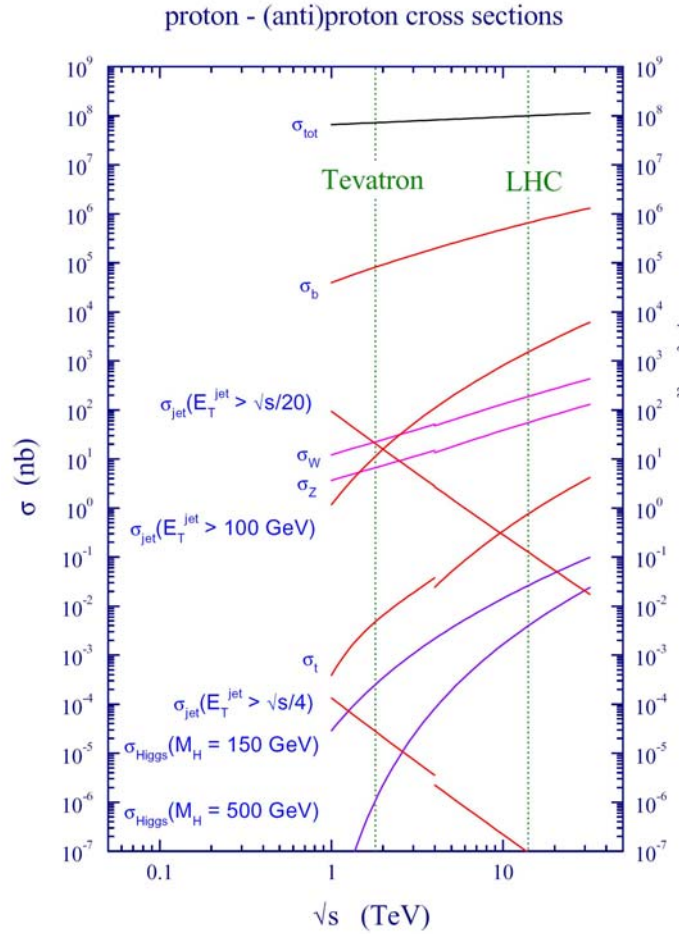


Figure 3.2.: The cross section and event rates at pp-colliders for various processes as function of \sqrt{s} [22]. The dominant processes are $b\bar{b}$ and jet production, while rare events, like Higgs production, are suppressed by a factor of about 10^{10} with respect to the total cross section σ_{tot} .

- associated Higgs production with $t\bar{t}$ pairs $gg, q\bar{q} \rightarrow t\bar{t}H$.

Of course, there are some uncertainties in the calculation of cross sections. Most significantly are the insufficient information about gluon distribution at low x and the unknown effect of QCD corrections at higher order. As far as it is possible to calculate them at next-to-leading order (NLO), the cross sections for Higgs production at the LHC are presented in Figure 3.3 (top). The dominant process over the entire Higgs mass range is the gluon-gluon fusion. The Higgs mass is limited by former LEP experiments. The combined data of ALEPH, DELPHI, L3 and OPAL provide a lower limit for the Higgs mass [1]

$$m_H > 114.4 \text{ GeV (95\% CL)}.$$

Due to its high mass, the Higgs boson decays in various channels. Interesting are the Higgs decays in fermion pairs $f\bar{f}$ for $m_H \simeq 135 \text{ GeV}$ and $2m_f < m_H$, calculated to lowest order [24]

3.1. The Large Hadron Collider (LHC)

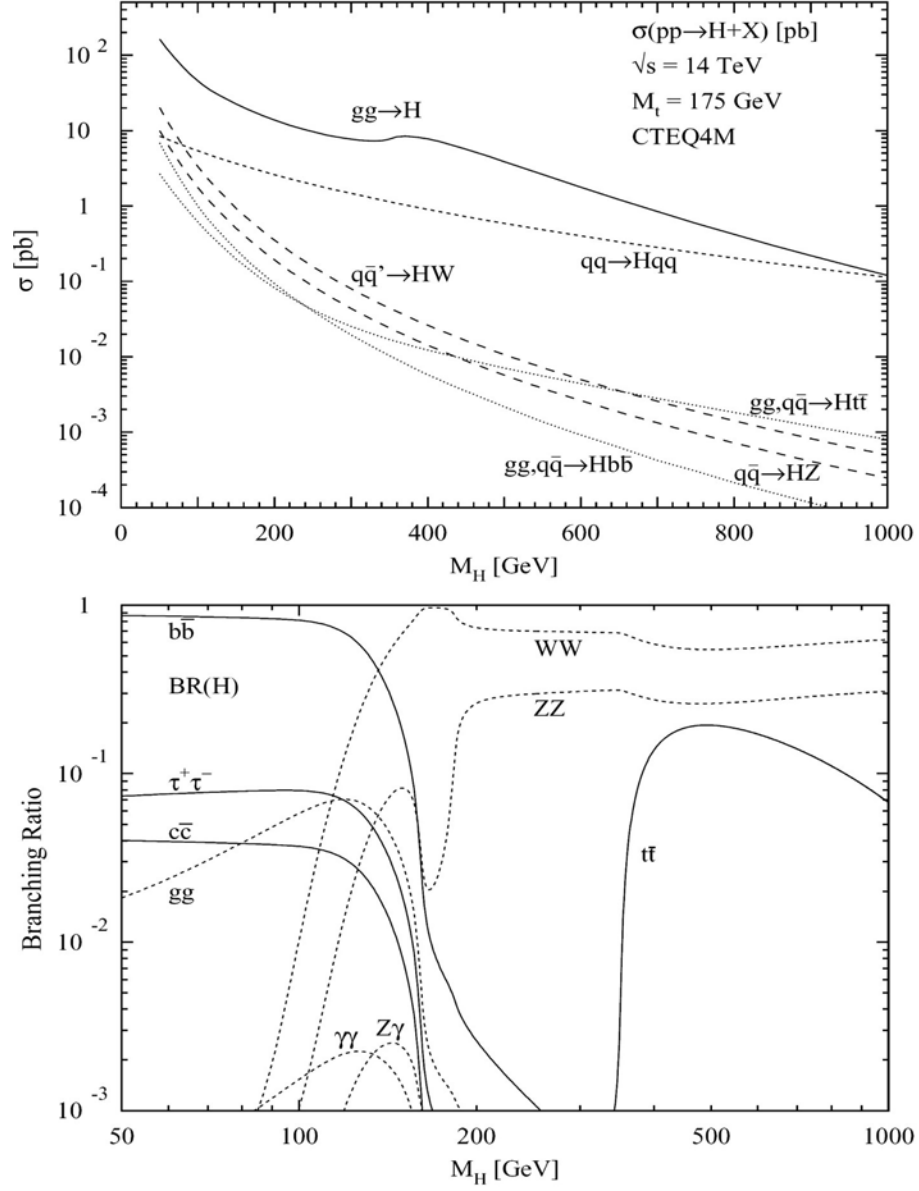


Figure 3.3.: Production (top) and decay (bottom) of a Higgs boson at the LHC [23]. The dominant production channel is $gg \rightarrow H$. For detection of the Higgs boson especially the decay mode $H \rightarrow ZZ \rightarrow \mu^+\mu^-\mu^+\mu^-$ is interesting, due to its very clear signature.

$$\Gamma(H \rightarrow f\bar{f}) = \frac{G_F N_C}{4\sqrt{2}\pi} m_f^2 m_H \left(1 - \frac{4m_f^2}{m_H^2}\right)^{\frac{3}{2}} \quad (3.4)$$

as well as in the vector bosons V (i.e. W^\pm or Z^0) [24]

$$\Gamma(H \rightarrow VV) = \frac{G_F m_H^3}{64\sqrt{2}\pi} \delta_V \left(4 - 4\frac{4m_V^2}{m_H^2} + 3\left(\frac{4m_V^2}{m_H^2}\right)^2\right) \left(1 - \frac{4m_V^2}{m_H^2}\right)^{\frac{1}{2}}. \quad (3.5)$$

3. New experiments for new particle search

N_C is the color factor (1 for leptons and 3 for quarks) and G_F is the Fermi constant; $\delta_V = 1$ for Z^0 and $\delta_V = 2$ for W^\pm .

Figure 3.3 (bottom) presents the branching ratios for various decays as a function of m_H . Up to $m_H \simeq 135$ GeV the decay $H \rightarrow b\bar{b}$ is dominant. Beginning at the mass of about $m_H \simeq 2m_W$ up to the $t\bar{t}$ decays the Higgs boson predominantly decays into W^+W^- and ZZ pairs since the Higgs boson couples preferentially to the heaviest particles. Also decays in virtual W^\pm and Z^0 bosons below the threshold are possible.

Generally the most promising signatures for the Higgs detection are:

- $gg \rightarrow H \rightarrow \gamma\gamma$;
- $q\bar{q}' \rightarrow WH \rightarrow l\nu_l\gamma\gamma$ and $gg, q\bar{q} \rightarrow t\bar{t}H \rightarrow l\nu_l\gamma\gamma X$;
- $q\bar{q}' \rightarrow WH \rightarrow l\nu_l b\bar{b}$ and $gg, q\bar{q} \rightarrow t\bar{t}H \rightarrow b\bar{b}b\bar{b}WW \rightarrow b\bar{b}bl\nu_l X$;
- $gg \rightarrow H \rightarrow Z^{(*)}Z^{(*)} \rightarrow l^+l^-l'^+l'^-$ ($l, l' = e$ or μ);
- $gg \rightarrow H \rightarrow W^{(*)}W^{(*)} \rightarrow l^+\nu_l l'^-\bar{\nu}_{l'}$ ($l, l' = e$ or μ);
- $gg \rightarrow H \rightarrow ZZ \rightarrow l^+l^-\nu_{l'}\bar{\nu}_{l'}$ ($l = e$ or μ ; $l' = e, \mu$ or τ).

The fourth reaction in the list is particularly important. If all produced leptons are muons, a good separation from background is possible because muons easily traverse the massive detector components and can be detected in its outer muon system. This "golden channel" is characterized by a small cross section but very clear signature. The LHC experiments, which are mainly dedicated to detect the Higgs boson, use this property and thus must have a reliable muon system.

3.1.3. The LHC experiments

The detection of the particles created at the bunch crossing points is the main goal of seven detectors constructed for the LHC. Six of them – ATLAS, CMS (both general purpose detectors), ALICE (heavy ions), LHCb (B-physics), TOTEM (total cross section, elastic scattering) [25] and LHCf (forward particles) [26] – are located directly in the excavated caverns at the intersection points of the LHC. The seventh experiment FP420 (forward proton physics) [27] contains four similar detectors which are positioned at a distance 420 m from the ATLAS and CMS detectors. The four main LHC experiments (Figure 3.4, for the CMS see also Figure 3.5) are:

- **ATLAS (A Toroidal LHC ApparatuS)** [28]: A general purpose detector, which was designed to investigate a large spectrum of physics detectable in the LHC collisions. Its main goal is to detect the Higgs boson. Also it is designed to investigate the CP violation. Furthermore ATLAS is able to make precise measurements of top-quark and its physics. As well as the SM physics, the models of physics beyond the SM can also be investigated by detecting possible new particles.

The ATLAS detector structure is based on a series of concentric cylinders around the bunch crossing point and can be divided in four complementary main parts:

1. The Inner Detector:
 - Pixel Detector, 1744 silicon modules 250 μm thick with over 80 million read-out channels;



Figure 3.4.: The four main LHC detectors. The aim of the two largest experiments ATLAS and CMS is primarily the search for the Higgs boson, ALICE is particularly designed for the study of heavy ion collisions and LHCb investigates the B-physics (Photographs from [21]).

- Semi-Conductor-Track, 80 μm wide silicon strips, with 6.2 million channels;
 - Transition Radiation Tracker, 351000 straws of 4 mm diameter.
2. Calorimeters:
 - The electromagnetic calorimeter, with lead and steel absorber components and liquid argon as sampler;
 - The hadron calorimeter, with steel as absorber and scintillation tiles as sampling material.
 3. Muon Spectrometer: a large tracking system consisting of pressurized cylindrical drift tubes (called MDT) and of resistive plate chambers (RPC), with several hundred thousand read-out channels.
 4. Magnet system:
 - The Solenoid, with 2 T magnetic field, surrounding the Inner Detector;
 - The Toroid, eight superconducting coils, making up the barrel system and placed in the muon system, and two end-cap coils.

The entire ATLAS detector is with its 46 m length and 25 m height the world biggest particle detector at accelerators that was ever built.

3. *New experiments for new particle search*

- **CMS (Compact Muon Solenoid)**: Similar to the ATLAS experiment, the CMS is also designed to investigate the large number of physics aspects at 14 TeV. The detailed description of the detector and its components can be found in Section 3.2.
- **ALICE (A Large Ion Collider Experiment)** [29]: Generally constructed to investigate the heavy Pb-Pb ion collisions at $\sqrt{s} = 5.5$ TeV per nucleon. This energy density is able to generate a quark-gluon plasma in which the quark confinement is abolished. The main detector parts are:
 1. Inner Tracking System, six cylindrical silicon layers surrounding the interaction point;
 2. Time Projection Chamber, being the main particle tracking component of ALICE;
 3. Time Of Flight, about 1600 Multigap Resistive Plate Chambers;
 4. Photon Spectrometer, lead tungstate crystals for measurement of the collision temperature;
 5. High Momentum Particle Identification Detector, a cesium iodide RICH detector for measurement of particle momentum up to 5 GeV (kaon/proton determination);
 6. Forward Multiplicity Detector, consisting of five silicon discs;
 7. Electromagnetic Calorimeter;
 8. Muon Spectrometer, for measurement of muon pairs.
- **LHCb (Large Hadron Collider for beauty studies)** [30]: Specifically developed for b-physics studies. Particularly the CP violation in the interaction of b-hadrons is investigated. It is a single arm forward spectrometer. Its asymmetric layout is determined by the fact, that the b-hadrons are predominantly produced in the same direction as the b-mesons. The LHCb main components are:
 1. Vertex locator, used for precisely separation of primary and secondary vertices for B-tagging;
 2. RICH-1, for low momentum particle detection;
 3. Main tracking system;
 4. RICH-2, for high momentum particle detection;
 5. High Momentum Particle Identification Detector, a cesium iodide RICH detector for measurement of particle momentum up to 5 GeV (kaon/proton determination);
 6. Electromagnetic and Hadron Calorimeter;
 7. Muon system, used as trigger.

3.2. The Compact Muon Solenoid (CMS)

3.2.1. Detector design

The *Compact Muon Solenoid* (CMS, see Figure 3.5) is one of two detectors developed for universal investigations in particle physics at the LHC [31]. Its most emerging property is – as the name indicates – the compactness: the CMS structure is dominated by the solid iron yoke, giving the detector its ultimate stature. The main function of the compact yoke is to return the

magnetic field, generated by the very large detector solenoid, which is the other remarkable CMS feature: particles, produced by proton-proton collisions are to be detected and their transverse momenta p_T are to be calculated by measuring their bending in the magnetic field inside and outside the coil. This occurs by means of several subdetectors surrounding the beam pipe in cylindrical layers (*barrel region*), which are divided in five movable ring parts (*wheels*, numbered by -2 , -1 , 0 , $+1$ and $+2$). Additionally, for particle detection in both forward directions, some detector subsystems are positioned on end discs (*endcap region*). The entire CMS detector has a length of 21.6 m, a diameter of 14.6 m and a weight of about 12,500 t.

The CMS convention for a coordinate system, to be used by all subsystems is to have an origin at the interaction point at the center of the detector. The x axis is pointing towards the LHC, the y axis upwards in the vertical direction, the z axis is identical with the beam line. In the x - y plane the azimuthal angle ϕ and in the y - z plane the polar angle θ are measured. θ determines the *pseudorapidity*

$$\eta = -\ln \left[\tan \left(\frac{\theta}{2} \right) \right], \quad (3.6)$$

which is a spatial coordinate generally used in particle physics when dealing with hadron colliders.

In the following the subdetector systems are described. The muon system, which is crucial to understand the subject of this thesis, is presented explicitly in Section 3.2.2.

The inner tracker [32]

The subdetector closest to the interaction point is the *inner tracker*. Its active detection material is exclusively silicon. It has about 80 million read-out channels within a cylindrical form with 5.4 m length and 2.4 m diameter. Effort was made to minimize the amount of absorber material and hence energy losses in the inner tracker. The inner tracker consists of the following two main components:

- **The Silicon Pixel Detector.** Some particles created by the proton-proton collisions, like b -quarks, c -quarks and τ -leptons, decay after traveling only a few millimeters, forming secondary vertices. The pixel detector, mounted as close as possible to the interaction point, allows an efficient detection of these particles due to its high granularity. It consists of two barrel layers, which are positioned at a distance of about 40 mm and 70 mm from the beam line, and two pairs of endcap discs with radius of 60-150 mm, positioned, in opposite directions, at a distance of 32.5 cm and 46.5 cm from the interaction point. For at least two pixel hits the pixel detector covers the detection area up to $|\eta| = 2.4$. The pixel dimensions of $100 \mu\text{m} \times 150 \mu\text{m}$ provide a good hit resolution of about $10 \mu\text{m}$ in the r - ϕ plane and of about $17 \mu\text{m}$ in the r - z plane (charge collection on pixels). A higher hit resolution is possible by using charge interpolation among several pixels. The pixel detector is operated at a temperature of about $-10 \text{ }^\circ\text{C}$ to minimize the impact of damage caused by high radiation.
- **The Silicon Strip Tracker.** Starting from the pixel detector, the reconstructed particle tracks are then extrapolated into the silicon strip tracker, where the precise measurement of transverse momentum is performed. This performance is made possible by a very high resolution in the measurement of the track bending, caused by the magnetic field. The total active detection area of more than 200 m^2 is made up by ten barrel

3. New experiments for new particle search

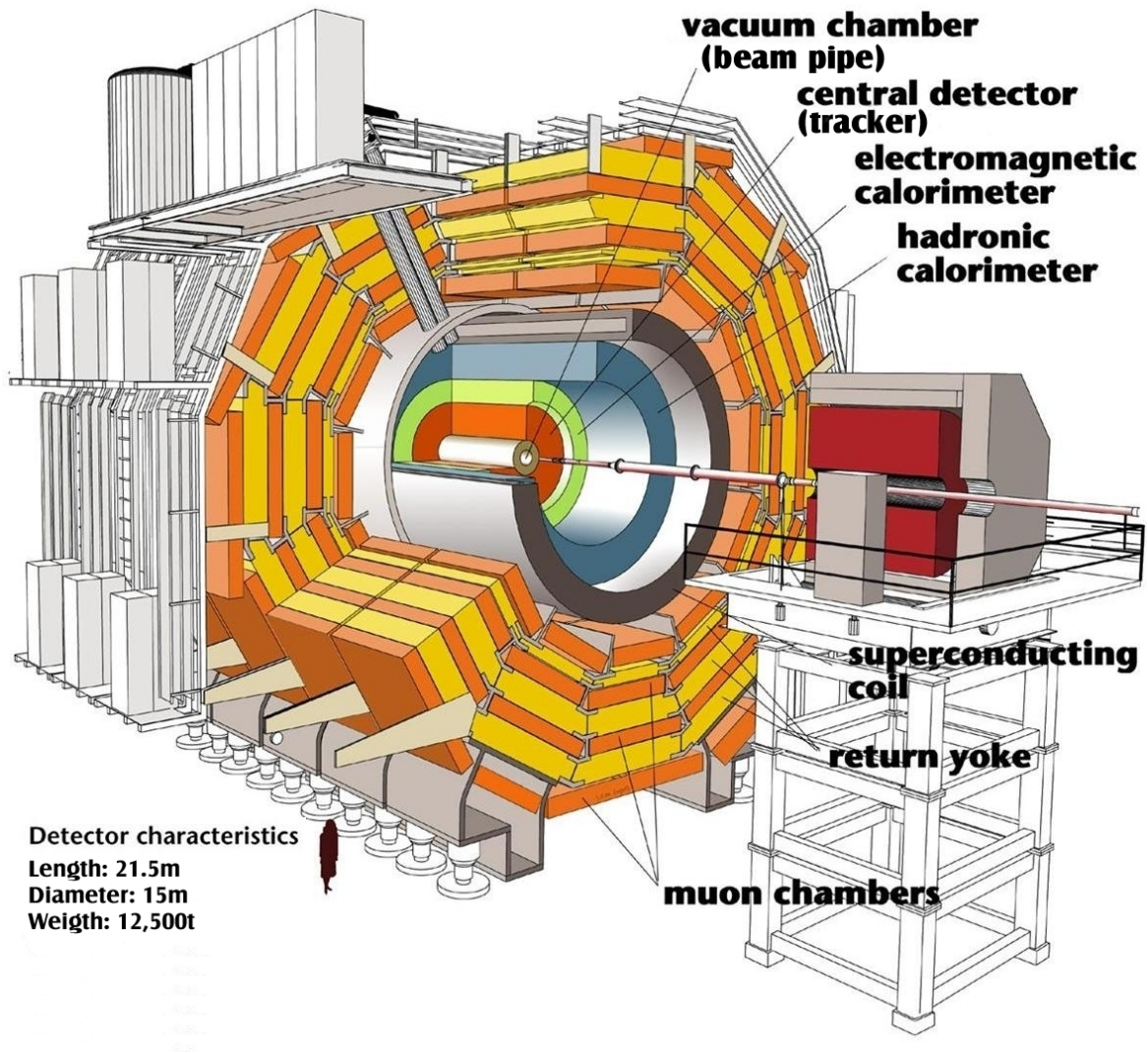


Figure 3.5.: The *Compact Muon Solenoid* (CMS) is one of two general purpose detectors at the LHC [21]. It consists of four classical detector subsystems: tracker, electromagnetic calorimeter, hadronic calorimeter and muon system. The large solenoid of CMS contains the tracker and the calorimeters, and produces a magnetic field of up to 4 T. The magnetic field is parallel to the beam axis and bends the particle tracks in the transverse plane, thus permitting to measure their transverse momentum.

layers and by nine endcap discs, as well as by three additional mini discs closer to the pixel detector. The tracker experiences a very high charged particle flux. Particles with p_T less than a few GeV do not reach the tracker diameter, their tracks rather end spirally due to particle absorption within the tracker or hit the endcap. Thus the tracker system has to be able to separate the tracks close to each other. The η -covering of the strip tracker is similar to the one of the pixel detector and reaches up to about $|\eta| = 2.5$. It is also operated at a temperature of -10°C .

The expected momentum resolution of the inner track in the central region is given by

$$\frac{\Delta p_T}{p_T} = 0.15 \frac{p_T}{\text{TeV}} \oplus 0.5\%, \quad (3.7)$$

for isolated charged particles. The expected efficiency is hereby higher than 98 %.

The electromagnetic calorimeter [33]

Particles, which are not absorbed in the tracker, penetrate the next CMS subdetector: the *electromagnetic calorimeter* (ECAL). Its task is to measure the energy and direction of particles participating mainly in electromagnetic interactions, like electrons and photons. The measurement occurs by absorbing these particles in scintillators. For this purpose lead-tungstate (PbWO₄) crystals are chosen. They are characterized by a high density, which results in a short *radiation length*¹ $X_0 = 8.9$ mm and a small *Moliere radius*² $R_M = 22$ mm. The PbWO₄ crystals are arranged in the barrel and the endcap systems of the ECAL.

The ECAL barrel is about 6 m long with an inner and an outer radius of 1.3 m and 1.8 m, respectively. It contains more than 60,000 crystals of length 230 mm (25.8 X_0) and cross section of 22 mm \times 22 mm. It corresponds to a granularity $\Delta\eta \times \Delta\phi = 0.0175$ mm \times 0.0175 mm. The barrel covers a range of $|\eta| < 1.5$.

The ECAL endcaps are positioned at a distance of 3.2 m from the interaction point. They consist of about 7300 crystals with a length of 220 mm and face cross section of 28.6 mm \times 28.6 mm. The endcaps enlarge the range covered by ECAL to $|\eta| < 3$. In front of each endcap a preshower detector is installed. It is built of a thin lead absorber for photon shower initiation and improves the π^0/γ , as well as the e^\pm/π^\pm separation. Its covering range is $1.65 < |\eta| < 2.6$.

The energy resolution obtained by the ECAL is given by

$$\frac{\Delta E}{E} = \frac{a}{\sqrt{E/\text{GeV}}} \oplus \frac{b}{E/\text{GeV}} \oplus c. \quad (3.8)$$

with $a = 2.7\%$ to 5.7% being a stochastic term, representing shower fluctuations, photon statistics and possible transverse leakage; $b < 250$ MeV corresponds to the electronic noise and $c \simeq 0.55\%$ results mostly from calibration errors and crystal non-uniformity.

The hadronic calorimeter [34]

The ECAL is surrounded by the next detector subsystem, the *hadronic calorimeter* (HCAL). The HCAL is used for measurements of hadronic jet components and other hadronic particles. They interact with the absorber, what results in the production of charged (generating light in scintillators) and neutral particles. The HCAL in common with the ECAL allows to calculate the transverse component of the energy loss, so that even neutrinos or other non-interacting particles can be detected. The HCAL consists of the following main sections:

- **The Barrel (HB) and Endcaps (HE) Calorimeter.** The absorber and scintillator are brass and plastic, respectively. The HB fraction consists of two cylindrical units, segmented in 16 wedges. The wedges are positioned parallel to the beam line and composed of alternating brass and plastic scintillator layers. The segmentation results in a granularity $\Delta\eta \times \Delta\phi = 0.087 \times 0.087$. The HB stability is provided by stainless steel. The HE consists also of brass/plastic modules with the same structure as the

¹ X_0 is an average distance which is passed by a high-energetic electron ($E \gg 1$ MeV), in which its energy is dropped to the 1/e part of the initial value.

² $R_M = \frac{21 \text{ MeV}}{E} \cdot X_0$ is a radius of a cylinder, in which about 95% of the energy of an electromagnetic shower energy is deposited.

3. New experiments for new particle search

barrel unit. The depth of HB and HE is at least 5.8 and 10 nuclear *interaction length*³ λ_I , respectively.

- **The Forward Calorimeter (HF).** It is located at a distance of ± 11 m from the interaction point and has a length of 1.65 m and a radius of 1.4 m. It is made of steel (absorber) and quartz fibers for Cherenkov light collection. This light can only be produced by electrons and positrons from showers of charged particles within the HF, providing thus a very clean signature. Due to its length of $9 \lambda_I$, its information is important to improve the detection of missing energy, and to tag forward jets by reducing the background signal in reactions without associated jet production in forward direction.
- **The Outer Calorimeter (HO).** Two layers of scintillators are positioned outside the solenoid to improve the shower containment if its energy is too high to be all deposited in the HB (e.g. 300 GeV pions). The HO extends the HB total depth up to $11.8 \lambda_I$.

The total energy resolution including both CMS calorimeters ECAL and HCAL is finally given by

$$\frac{\Delta E}{E} = \frac{100\%}{\sqrt{E [\text{GeV}]}} \oplus 4.5\% \quad (3.9)$$

for energies up to 1 TeV.

The solenoid [35]

The CMS tracker and calorimeters (except the HO) are enclosed by the superconducting solenoid, which provides a homogeneous axial magnetic field of 4 T. This field bends the tracks of charged particles and allows hereby the measurement of their transverse momentum. The coil measures 13 m in length and 5.9 m in diameter and is cooled with liquid helium. The energy stored in the system is about 2.7 GJ.

3.2.2. The CMS muon system [36]

A muon system of a general purpose detector like CMS has a particular importance for proton-proton colliders such as the LHC. The muons have very clear signature and they can be uniquely detected in the outer muon system, in contrast to other particles which largely are absorbed in the inner subsystems. Decay channels with muons in their final state, e.g. a Higgs boson, can then be analytically separated from the background data.

Muon system requirements and structure

To reach the demanded aims, e.g. the detection of the Higgs bosons, the CMS muon system should fulfill several requirements. Based on diverse simulation studies the following functionality and achievement features are needed:

- **Muon identification.** Up to $\eta = 2.4$ there are at least 16 interaction lengths of detector material, guaranteeing that muons are identified in the outer sections of the CMS detector. A combination of the muon tracking with the efficient trigger system in

³The nuclear interaction length λ_I is an average distance in which one hadronic interaction occurs.

this region ensures a unique assignment of the bunch crossing time and matching to a track segment in the inner tracker, as well as triggering on single and multi-muon events at defined p_T level, e.g. at 100 GeV for $\eta = 2.1$.

- **Track resolution.** The muons pass through the magnet return yoke where small angle multiscattering processes may occur. These processes limit the track resolution to about 100 μm for muons with $p_T \cong 200$ GeV. For lower momentum muons the value of 100 μm is sufficient to define the ultimate track resolution for the muons.
- **Momentum resolution.** The muon transverse momentum p_T is calculated by measurement of the track direction and the bending of the detected muons. The bending also depends on the angle between the muon track and the beam line. The resolution is limited at lower energies by the multiple scattering, while it worsens at very high energies (TeV) due to the smaller bending, the energy loss and secondary electromagnetic radiation. By matching the muon track segments with segments from the inner tracker, the p_T is generally improved. Table 3.1 provides some values of transverse momentum resolution $\frac{\Delta p_T}{p_T}$ for momenta of 100 GeV and 1 TeV. The more accurate the momentum measurement, the better the charge assignment of the detected muons – this is particularly important at high energies at the TeV scale, due to the very small bending of the particle tracks at these energies.
- **High rate operation.** The entire muon system is resistant against the high radiation background expected at the LHC. The largest particle flux occurs nearby the beam axis and in the endcap region and is rather non-threatening in the barrel region. In the barrel region the background consists mostly of diffusing neutrons with a hit rate of 1 to 10 Hz/cm². In the endcaps also background muons and hadrons pass the detector, so that the particle flux counts up to 1 kHz/cm² in this region.

Furthermore, for muons one has to take into account the angular resolution, which should be better than 1 mrad and the identification efficiency in the muon system being at least 99 %.

p_T	$\frac{\Delta p_T}{p_T}$ (muon stand-alone)		$\frac{\Delta p_T}{p_T}$ (muon and tracker)	
	$\eta = 0$	$\eta = 2.5$	$\eta = 0$	$\eta = 2.5$
10 GeV	8 %	15 %	1 %	1.5 %
1 TeV	20 %	40 %	6 %	17 %

Table 3.1.: Expected resolution of the muon transverse momentum measurement for muon $p_T = 10$ GeV and 1 TeV.

Based on these different requirements for different locations in the CMS detector it was decided to use three different technologies for the muon system. In the endcap region Cathode Strip Chambers (CSC) are installed to cope with the very inhomogeneous magnetic field and provide the high spatial resolution needed in this part of detector. They cover a range of $0.91 \leq |\eta| \leq 2.4$. In the muon barrel Drift Tubes (DT) chambers as an economic solution are covering the largest area of the CMS detector. The DTs are installed for muon detection in the range $|\eta| \leq 1.26$. CSCs and DTs provide both tracking and triggering. In both regions – barrel and endcap – the Resistive Plate Chambers (RPC) are used as special trigger detector.

3. New experiments for new particle search

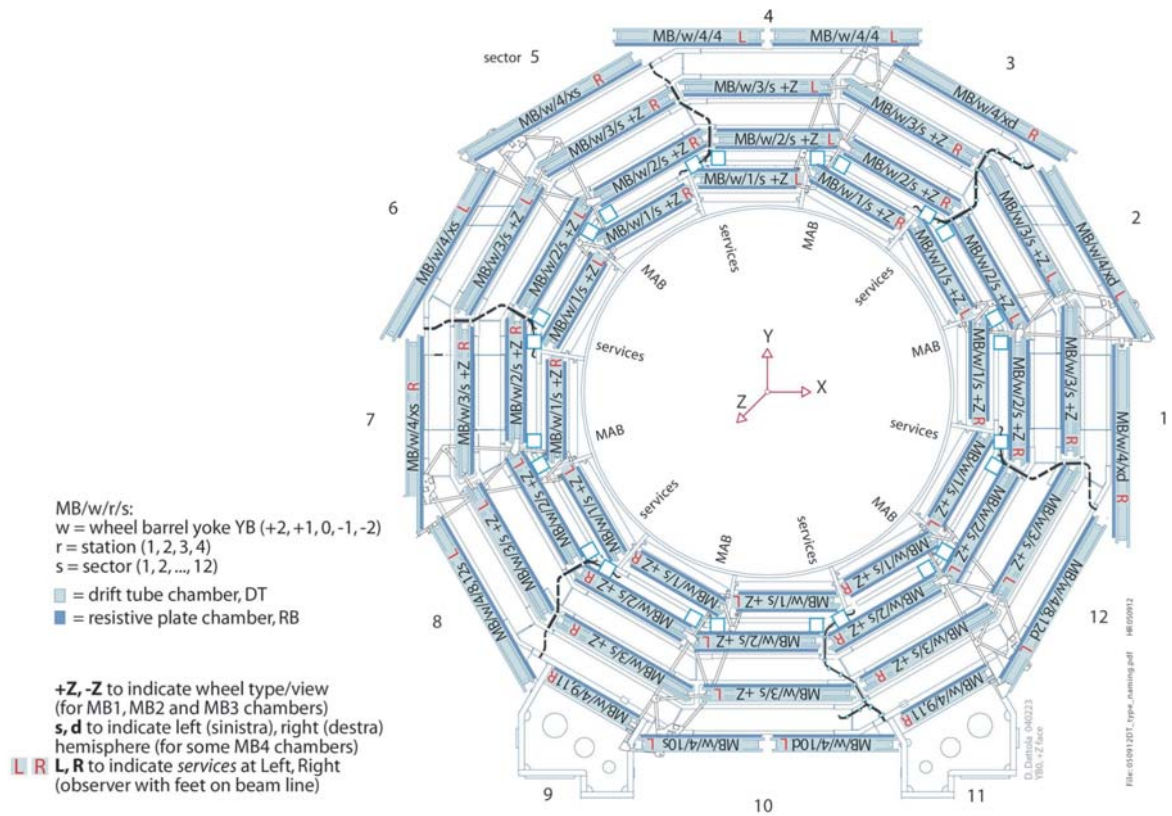


Figure 3.6.: Cross section through the CMS detector in the x - y plane [37]. A CMS DT muon chamber (presented here as blue box) is installed in one of the 12 radial sectors and in one of four cylindrical stations (except the sectors 4 and 10 in station 4, counting two chambers each).

Drift Tubes

As mentioned, in the barrel region the expected hit rate is 1 to 10 Hz/cm², which is much less than in the endcaps. Also the magnetic field is homogeneous with a strength up to 1.9 T. Therefore the muon detectors in this region do not need to have such a high granularity as in the endcaps and it was decided to use the *drift tube* (DT) technology here.

The muon DT system consists of four co-axial cylindrical stations with different diameter around the beam line as common axis, named MB1, MB2, MB3 and MB4⁴ which form 12 radial sectors in the x - y plane (Figure 3.6). Each of the five wheels of the CMS detector has one DT chamber per sector and station, except sectors 4 and 10 in station MB4 where the station is split in two chambers each. In the entire CMS detector a total of 250 DT muon chambers are installed. The detailed description of chamber design and function can be found in Section 3.3.

Cathode Strip Chambers

In the endcap region the *Cathode Strip Chambers* (CSC) are used for muon tracking and trigger. The application of CSCs considers the very high expected hit rate up to 1 kHz/cm²

⁴As abbreviation for Muon Barrel.

and an inhomogeneous magnetic field up to 3 T which does not affect the drift time in a CSC due to its very short drift distance.

The CSCs are multi-wire proportional chambers with plane of cathode strips aligned perpendicular to the wires (Figure 3.7 left). They are filled with a gas mixture (40% Ar, 50% CO₂ and 10% CF₄). The operating HV is about 4.1 kV. A muon passing the chamber ionizes the gas, what results in an avalanche at the wire. The moving charge induces signals on several cathode strips. The charge distribution on the strips is measured, so that the track position with a precision of about 100 μm in the ϕ direction can be determined by interpolation the amount of charge per strip (Figure 3.7 right). In addition, the fired wires provide a binary information about the second coordinate. Combining these two simultaneous and independent measurements, a 2-dimensional muon measurement (r by wires, ϕ by strips) is possible.

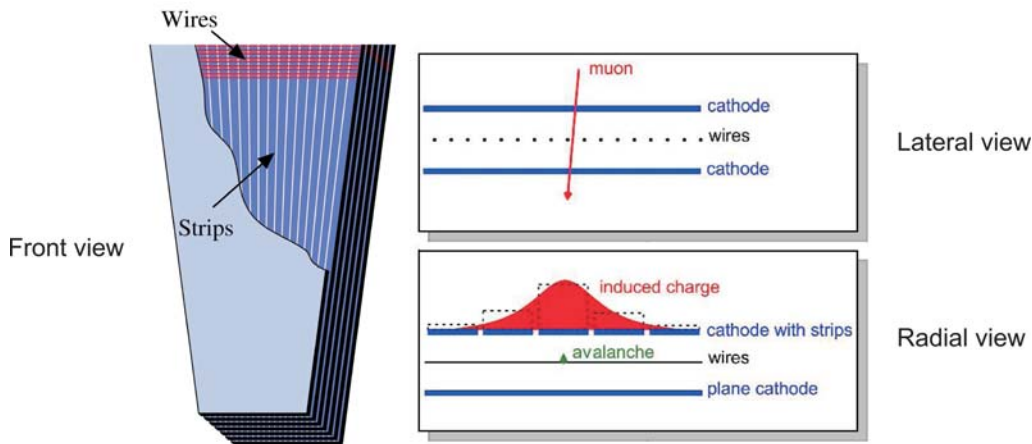


Figure 3.7.: The Cathode Strip Chamber (CSC, left) used for muon measurement in the endcap region of the CMS detector [36]. A muon passing the chamber causes gas ionization followed by an avalanche on the wire (right). This induces electric charge on several cathode strips. Interpolating the collected charge, one obtains a track measurement precision of about 100 μm in the r - ϕ coordinate.

The trapezoid-shaped CSC contains 6 sandwiched layers of cathode and wire planes. The CSCs are arranged along a ring around the beam axis, with overlapping chambers to avoid dead regions in the x - y plane. There are two or three concentric rings. These rings are then arranged in four discs, named ME1, ME2, ME3 and ME4⁵ which are separated by the iron yoke disks of the magnet. The ME1 contains a total of 216, the ME2 and ME3 108 each and ME4 36 CSCs.

In addition to the very precise measurement, the CSCs are also a fast working detector, thus being suitable for triggering. Due to the fact that the CSCs consist of 6 layers, they guarantee a broad pattern recognition able to eliminate the non-muonic background as well as to match the external muon tracks with the ones in the inner tracker.

Resistive Plate Chambers

The *Resistive Plate Chambers* (RPC) are fast gas detectors used for triggering events in the muon systems in both CMS barrel and endcap regions. By means of the RPCs the muon

⁵As abbreviation for Muon Endcap.

3. New experiments for new particle search

candidates are identified, their tracks assigned to the right event ID and the muon p_T is roughly estimated. Their satisfactory track resolution of a few mm is combined with a very precise time resolution of about 1 ns. In contrast to CSC and DT, in the RPC response is well within the time between two bunch crossings.

The RPC is a parallel plate counter (Figure 3.8). It consists of two bakelite plates with a very high resistivity of 10^8 – 10^{11} Ωcm , allowing to construct large and thin detectors with elimination of electrical flashovers. The plates are graphite-coated to connect a HV of about 9 kV. A charged particle passing the gas volume (96% $\text{C}_2\text{H}_4\text{F}_4$, 3.5% *iso* C_4H_{10} and 0.5% SF_6) ionizes the gas molecules and a gas amplification with an avalanche occurs. The plates, due to their resistivity, are discharged only in close vicinity to the particle track, the rest of the plate is not affected. The information about the discharge location is then obtained via the pulses induced in the external metallic read-out strips of 2–4 cm width. The electric charge is not evaluated, so that the measurement resolution is given by the strip position only. The strips are located parallel to the DT r - ϕ cells and CSC radial strips in the barrel region and endcaps, respectively. In practice the RPCs are realized as *double gap* version, i.e., as seen in Figure 3.8, using two active layers separated by the read-out strips. The RPCs can work at a particle hit rate of a few kHz/cm^2 .

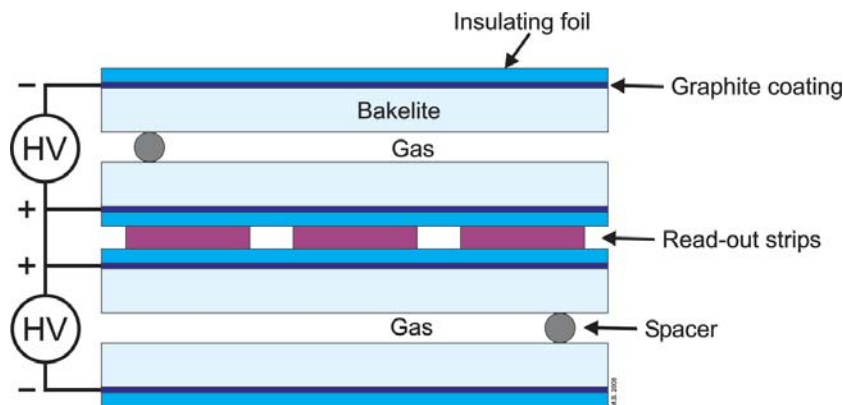


Figure 3.8.: Schematic cross section of the double gap Resistive Plate Chamber (RPC). The RPC consists of bakelite plates which are connected to a HV of about 9 kV. A muon crossing the chamber generates an avalanche in the gas volume, resulting in a local plate discharge due to the high bakelite resistivity. The RPCs respond very fast (ns range) and are used as trigger devices for barrel and endcap regions.

The RPC, as trigger planes for the muon detector, have the same planar form and coverage as the DT and the CSC chambers. For the barrel region the stations MB1 and MB2 have two RPCs each on both top and bottom side of the DT, the MB3 and MB4 have each only one RPC (see Figure 3.6). In the endcaps only one RPC plane is mounted on its outer (ME1, ME3 and ME4) or on its inner (ME2) side.

3.3. The Drift Tube muon chambers

For the CMS muon system in the barrel region chambers were chosen which work on the principle of a gas-filled drift detector. The decision for the use of these Drift Tube (DT) muon chambers was taken because of their measurement precision and the possibility of a cost-efficient production for a large area around the CMS detector. In the following sections the

chamber layout is described, their functionality is explained and an insight into the chamber production steps and test procedure is given.

3.3.1. Chamber layout

The basic unit of the CMS DT muon chamber (see Figure 3.9) is the *drift cell*. Each cell has a cross section of 42 mm (width) \times 13 mm (height), but its length is extended over the entire chamber dimension and can reach, depending on the chamber type, 2 m (MB1) to 3 m (MB3)⁶. In the center of the cell a gold plated steel anode wire is strained along the chamber length. The inner walls of the cell form the cathodes using two long aluminum strips located symmetrically on the left and the right side of the wire. To further shape the electric field within the cell, additional strip electrodes (field shaping strips) are fixed at the cell top and bottom. All these strips, like the wire, span over the entire cell length. The wire and the strips work under following nominal high voltage (HV): +3600 V (anode wire), -1200 V (cathode) and +1800 V (field forming).

The cells are at first arranged in a *layer*. A layer consists of multiple cells located in parallel along their length, which is the same for all cells in a layer. The total number of cells in a layer is dependent on the chamber station and its position in the CMS detector and can count up to about 100 (MB4) per layer. Two adjacent cells in a layer are separated by a common aluminum wall (named I-beam, due to its cross section shape), on which the mentioned cathode strips are glued. To insulate the strips from the grounded cell wall, a mylar film is located between them. The bottom and the top of the layer (and thus of the cells) consists of one aluminum sheet each (1 mm thick). The thin field shaping strips are glued on a mylar film which is glued directly on the sheets.

The next level in the cell arrangement is the *Super Layer* (SL). A SL consists of four layers which are located one on the top of the other; thus the sheet being top of the lower layer is the bottom of the upper one. The layers form the SL in such a way, that the cells of the next layer are shifted by a half-cell width (Figure 3.10). This shifting is important to obtain a clear muon track segments and avoid that a muon passes only through non-sensitive material. The four layers of each SL are then enclosed in a gas tight aluminum housing.

Finally a *CMS DT muon chamber* is composed of two or three SLs. One of the aims of the muon system is to measure the transverse momentum p_T of the muons in the outer region of the CMS detector. This is performed by measuring the track bending in the r - ϕ plane. Therefore the SLs are predominantly positioned with the tubes along the z axis (ϕ SL). Each muon chamber includes two ϕ SLs at a distance of about 30 cm from each other to increase the precision in the reconstructed track direction in a MB station. In addition, for 3-dimensional muon track reconstruction also information in the azimuthal direction is needed. For this purpose the chambers in all stations, except the MB4, have one SL (θ SL) whose cells are rotated by 90° with respect to those of the ϕ SL. The θ SL is located between the two ϕ SLs. The mentioned distance of about 30 cm between the inner⁷ ϕ SL (ϕ SL 1) and the θ SL for MB1, MB2 and MB3 or the outer ϕ SL (ϕ SL 2) for MB4 is in part given by an aluminum honeycomb panel. Beside the mentioned function as a "lever arm", it provides also an improved chamber rigidity and place for chamber ancillary equipment.

Each SL end is closed with an aluminum cover. At one end the cover has two connectors for HV supply to all electrodes in the cells (SL HV side). This side also contains a gas supply connector which can be used as input or output, depending on the chamber position in the

⁶Hence the name *drift tube*.

⁷I.e. being closer to the interaction point.

3. New experiments for new particle search

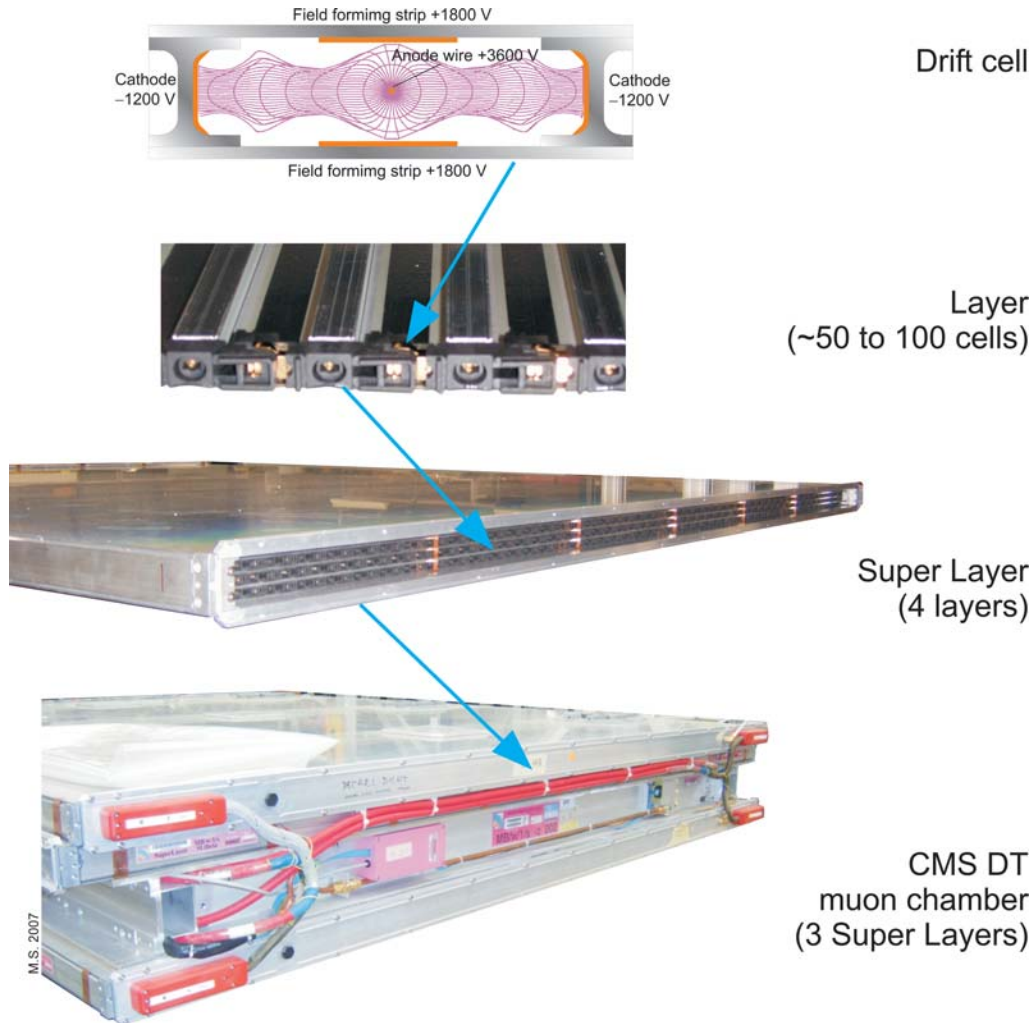


Figure 3.9.: The CMS Drift Tube muon chamber. The chamber basic unit, the drift cell, includes anode wire, cathode strips, as well as field forming electrodes. Multiple cells, arranged in parallel, form a layer; four layers compose a Super Layer (SL). For the MB1 (as presented here), MB2 and MB3 stations the chambers consists of two ϕ SL, for 2-dimensional measurement of the muon p_T , and one θ SL, 90°-rotated with respect to the two ϕ SLs, to allow 3-dimensional track reconstruction. The MB4 chambers do not have a θ SL.

CMS detector. On the opposite side the SL cover has Front End connectors for chamber output signals (SL FE side). In addition, on the FE cover an interface for the SL Detector Control System (see Section 5.1.2) and connectors for low voltage supply and chamber test signals are installed. The FE cover has also a gas supply connection as well as the water cooling pipe for the FE electronics.

On the ϕ SL FE side a box housing electronics for the chamber signal digitization and local trigger data, named *MiniCrate* (MC), is mounted along the honeycomb border (see Section 4.2.2). Its task is also to control and monitor the overall chamber work by means of the *Chamber Control Board* (CCB) inside the MC. On both ϕ SL sides, HV and FE, the gas manifolds for gas distribution and collection to/from the single SLs are installed. They include also two sensors for gas pressure measurement. The sensor analog signals are digitized

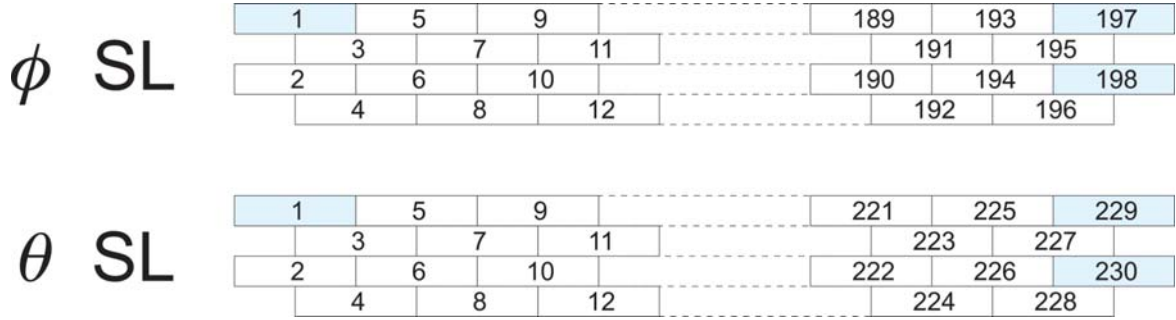


Figure 3.10.: ϕ SL and θ SL of an MB1 chamber with cell numbering. The layers are shifted by a half-cell width to resolve the inherent left/right ambiguity of a drift cell. Shaded cells have either no anode wire (cells number 1 of both SL type) or are not connected to read-out electronics (cells number 197 and 198 of ϕ SL and number 229 and 230 of θ SL).

by a Pressure Analog to Digital Converter (PADC),⁸ which is mounted on the ϕ SL HV side along the honeycomb border. On the left and right side of the chamber, viewed from the ϕ SL end, each two holders for the LEDs of the Barrel Muon Alignment System [38] are installed. The LED data as well as the PADC data are transferred to the CCB via a common I²C bus.

3.3.2. Chamber working principle

A muon passing through the cell ionizes an argon atom transferring an energy of 15.8 eV. Ionization occurs about each 0.3 mm along the muon track. The averaged charge released by these reactions is about 3 e . The free electrons (and also argon ions) experience the quasi-homogenous electric field \vec{E} resulting from the applied HV and being of about 2–2.5 kV/cm in a distance d of about 0.2–1.7 cm from the anode wire (Figure 3.11 right). The electrons, on one hand, are accelerated by the \vec{E} in the anode direction. On the other hand, they interact elastically in the collision process with other gas atoms and loose energy. They are then re-accelerated by the \vec{E} , then collide again etc. This interplay of acceleration and deceleration results macroscopically in a drifting movement of the electrons with a constant average velocity, described quantitatively by a *drift velocity* v_{drift} .

In the direct vicinity r of the anode wire the electric field rises rapidly and becomes proportional to $\frac{1}{r}$. In this region the drifting electrons get enough energy to be able to ionize further argon atoms, whose free electrons ionize the next atoms etc. An avalanche occurs and the resulting charge reaching the anode is about up to 50000 e (gas amplification factor). This process leads to a measurable potential drop on the anode, amplified by the Front End electronics and transformed into a logic LVDS signal (see Section 4.2.1).

Information about the v_{drift} is of particular interest in order to obtain the right distance d of the muon track to the anode wire. Knowing exactly the time of the muon passage through the cell one can measure the time needed by the electron to reach the wire (*drift time*, t_{drift}) and thus calculate

$$d = v_{drift} \cdot t_{drift}. \quad (3.10)$$

⁸The gas pressure measurement and read-out of the CMS DT muon chambers is described in detail in Chapter 5.

3. New experiments for new particle search

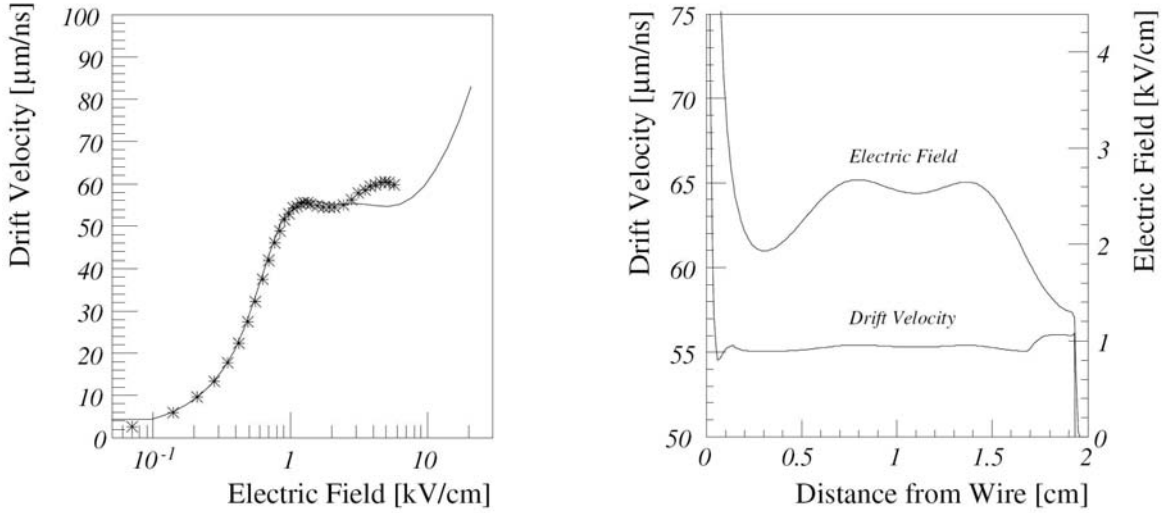


Figure 3.11.: The drift velocity v_{drift} as a function of the electric field \vec{E} for the used gas mixture of Ar/CO₂ in ratio 85%/15% (left). One can see a region from about 1 kV/cm to 10 kV/cm where the v_{drift} is nearly independent on \vec{E} and remains constant at about 55 μm/ns. The chamber cell design (geometry and \vec{E}) causes this value to remain constant over a large distance within the cell (right) [36].

As a result of repeating acceleration in the \vec{E} field and stopping by elastic scattering on the gas atoms, the electron drift velocity v_{drift} depends on the ratio $\frac{E}{N} \sim \frac{E}{p}$, where N means the density of the gas molecules and p is the gas pressure⁹ [39]. The most comfortable way is to find a region for a given gas mixture, where the v_{drift} remains constant even if $\frac{E}{p}$ varies somewhat. In fact, for the gas used in the CMS DT muon chambers the electric field in an interval of 1 kV/cm to 10 kV/cm does not affect significantly the v_{drift} value, which is

$$v_{drift} = 54.3 \text{ } \mu\text{m/ns},$$

as presented in Figure 3.11¹⁰.

The former studies on chamber cell geometry and \vec{E} field distribution allowed to design the chamber cells where the $v_{drift} = 54.3 \text{ } \mu\text{m/ns}$ is constant over a large section within the cell (Figure 3.11). Due to this constant value one can determinate the distance between the muon track and the anode wire and thus reconstruct the track segment registered by a chamber. The obtained precision is about 250 μm for a single cell and – assuming an average of four hits per muon event in a SL (Figure 3.12) – about 100 μm for an entire chamber.

Each track can be determined by these four measured drift times $t_{drift} = t_n$, $n = 1, 2, 3, 4$. The calculated *mean time*, t_{mean} , being the maximal drift time for an electron to be liberated at the cathode and traversing the maximal distance of half the cell width

$$t_{mean} = t_3 + \frac{t_2 + t_4}{2} = t_2 + \frac{t_1 + t_3}{2} \quad (3.11)$$

should have always the same value. Thus it can be used to check locally the quality of the chamber and of the drift time measurement.

⁹Assumed the Ideal Gas Law $pV = NkT$.

¹⁰A similar trend also shows the v_{drift} as function of $\frac{E}{p}$.

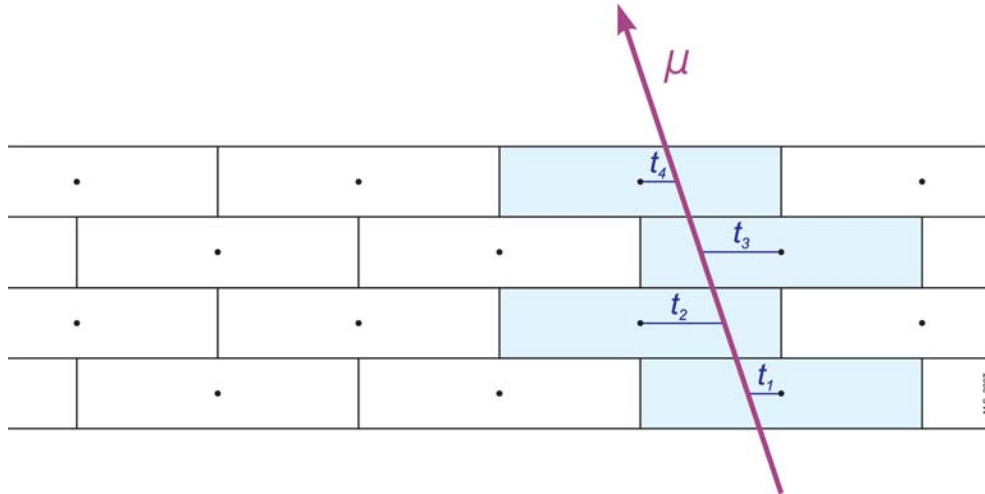


Figure 3.12.: The average number of hits per event is 4. The measured drift times in each hit cell can be used to check the *mean time*, which is the maximal drift time for an electron having to cover a distance of a half cell width (see Equation 3.11).

3.3.3. Chamber production and tests

The production of all 250 CMS DT muon chambers is shared by four collaborating institutes involved in the development of the CMS barrel muon system: Phys. Inst. III A of RWTH Aachen, CIEMAT Madrid, INFN Legnaro and INFN Turin. Also the chamber equipment is developed and produced by the CMS muon collaborators. For example, the chamber read-out electronics was developed by CIEMAT Madrid, the control and trigger electronics by INFN Legnaro, INFN Padua and INFN Bologna. The chamber alignment system was a project of the university Debrecen and the Institute of Nuclear Research, ATOMKI, Debrecen. The Aachen team was responsible for development, production and test of the chamber local gas supply and gas pressure read-out system (see Chapter 5).

Generally, the production of the muon chambers is performed in several steps. Each institute developed its own assembly tools which were individually adapted to the particular chamber size and to the specific resource environment. Nevertheless, the production steps are based on the same procedures without significant differences.

During the mechanical assembly of a chamber, prefabricated elements are glued together. For this purpose several assembling tables (e.g. four in Aachen) were especially made with very precise planarity. A layer was made in a first step by gluing the I-beams, which contained already glued cathode strips, on an aluminum sheet. This sheet, being thus the bottom of the layer cells, contained also the field shaping electrodes in form of glued aluminum strips on its surface. Between the I-beams the anode wires were placed, which were previously clamped in blocks by means of a special crimping machine. The wire ends were fit in holders between the ends of two adjacent I-beams. Such procedure was repeated three times. Each sheet with the glued I-beams and wires was then glued on the previous sheet, finally all four forming a SL. The uppermost layer was then covered (also glued) by a final aluminum sheet. The mechanical SL assembling was completed by gluing the walls at its edges and holding blocks at its corners, forming the SL housing.

The FE and HV sides remained at first open. In the next step the PCBs for the signal read-out (FE boards, see Section 4.2.1) on the FE and for the HV supply on the HV side were

3. New experiments for new particle search

mounted. They were then wired to the FE and HV connectors on the prepared FE and HV covers, respectively. Finally both the FE and HV covers closed the SL housing.

The SL could then be tested on its quality and function (see below). Three (or two in case of MB4) positively tested SLs were then glued together with the honeycomb to a complete muon chamber. In the last step the RPC holders were glued on the chamber surface. The finished chamber was tested once more on its functionality and, finally, together with other ones, transported to CERN. At CERN the chambers were finally equipped with the chamber electronics (MiniCrate, see Section 4.2.2), chamber local gas supply and read-out units (manifolds, sensors, PADC; see Section 5.2), as well as with the alignment system.

As mentioned above, the chambers should be tested practically after each production step to ensure the quality and, in case of defects, to be immediately repaired to guarantee an uninterrupted production cycle. The quality checks are focused on four main procedures: wire mechanical tension measurement, wire position measurement, HV tests and gas tightness.

Both, the wire tension and the wire position measurement, check for a potential deviation of the central anode wire location in the cells. The wire is strung along the cell with a force of 3 N. This is important, because in case of too low tension the wire has a sag resulting in too large sagitta. Such deviation leads to a wrong position measurement, deforms the electric field within the cell and the track reconstruction is imprecise. The same consideration is true for an incorrect wire positioning during the assembling process. The required precision is 35 μm for the wire sagitta and 250 μm in the lateral wire position [40]. For this purpose two measurement methods are used. The first of them, for tension measurement, is based on wire capacitive coupling, resulting in a resonance frequency, which can be measured by a specifically developed gauge WTM 64 (Purdue University and RWTH Aachen). The advantage of this method is its contact-free mechanism and the possibility to measure the frequency of all wires in a layer simultaneously. The second method, the measurement of the transverse wire position, is done optically by means of a system based on exact position measurement with a CCD camera observing the wire with respect to the chamber coordinate system. This measurement also took place on the tables in the chamber production chain, immediately when a layer had been finished.

The behavior of a SL (also of an entire chamber) must be tested at nominal HV, at first in air and then filled with the proper gas Ar/CO₂. One expects a couple of sparks caused by unavoidable pollution (dust, glue rests etc.), remaining from the production process. However, the longer a chamber is under HV, the more dust grains etc. are burned off and the spark rate decreases with time (chamber "training"). To test the chamber with HV a specific electronics and software system was developed in Aachen [41]. As a measure for a good HV behavior the current between cell electrodes and chamber body should then be below 10 nA.

Also the gas tightness of a SL (also of a chamber) is tested [42]. If a chamber is not gas tight, air can be sucked in. The oxygen can intercept the free electrons, which may not reach the anode wire. In addition, it delays the electron drift time. The measurement procedure for the gas tightness was also a project of the Aachen CMS team. As a measure of the tightness, the time constant τ of the drop of a small overpressure was used, which results from the exponential pressure drop in the SL or chamber vs. time. For example, a SL is called gas tight if $\tau > 140$ min. However, the typical values are $\tau > 3000$ min.

Finally, after all quality tests are passed, the complete SL and also chamber is tested on its functionality as a particle tracker by measuring the cosmic muons. The test procedure and environment is presented in Section 4.3.

4. Data taking with the CMS DT muon chambers

The 40 MHz collision rate at CMS causes very high rates of data which have to be written to a mass storage. The CMS and *Data Acquisition* (DAQ) System can store events at a rate of up to $O(10^2)$ Hz for further analysis. The raw event rate has therefore to be reduced. It is processed in two steps (Level-1 Trigger and High-Level Trigger) to reduce the accepted data volume and to provide the events to the offline analysis. In consequence, the DAQ system has to work with sufficient speed, storing all data without losses.

To study the functionality of the DAQ system, a large number of tests is required. At the Phys. Inst. III A of the RWTH Aachen the local DAQ system of the CMS DT muon chambers (called *MiniCrate*) is installed and can be operated in common with the "old" Aachen DAQ system, which was used for functionality tests of the muon chambers during the production period. The possibility to compare both DAQ systems is given by simultaneous data taking with *both* DAQ systems and subsequent comparison of the results. Also investigations of the noise behavior and its influence on the data quality during the data taking were performed. The present chapter describes concepts and test procedures, as well as the analysis of the data taken in different DAQ runs.

4.1. Detector triggering and data taking systems

4.1.1. CMS trigger system

General overview

The beam crossing frequency of $1/(25 \text{ ns}) = 40 \text{ MHz}$ at the nominal LHC luminosity of $10^{34} \text{ cm}^{-2}\text{s}^{-1}$ results in about 20 events in every bunch crossing. This implies an input rate of about 10^9 proton-proton interactions per second. Due to the technical requirements this rate must be reduced by a factor of about 10^7 to 100 Hz for data storage. It was decided to perform the rate reduction in two steps [43]:

- **Level-1 (L1) Trigger:** At this first level the data are stored for $3.2 \mu\text{s}$ with no dead time. L1 receives data from the calorimeters and the muon system, and holds them in pipeline registers of the front-end (FE) electronics. The L1 system relies on custom hardware.
- **High Level Trigger (HLT):** At the second trigger level the L1 data are handled with a rate of up to 100 kHz, before being passed to the online PC farm for complete processing. The HLT part of the trigger is based on commercial components.

The L1 time of $3.2 \mu\text{s}$ is needed to propagate the signals from the detector with its physical structure and its environment. In this time the trigger information must be collected from the FE electronics, it has to be decided, which data are of interest and which contain no relevant information. These decisions must be transmitted to the read-out buffers. As mentioned

4. Data taking with the CMS DT muon chambers

above, due to the bunch crossing period of 25 ns, which is too short to read out all data and receive trigger decisions, the data have to be stored in pipelines. That means, that every L1 trigger process is restarted after 25 ns and its maximal operation time (storage into the pipelines etc.) must be less than 25 ns. A mechanism able to handle overlapping triggers, is used to assign the interaction time (i.e. the proper bunch crossing ID). This is especially important for the CMS DT muon chambers, where the maximal drift time is about 400 ns, corresponding to 16 times the bunch crossing period.

The CMS L1 Trigger has to identify muons, electrons, photons, jets and missing transverse energy. All triggers should have a high efficiency even for a low energy threshold. It is required, that the trigger system is able to select photons and leptons for $|\eta| < 2.5$ and jets for $|\eta| < 5$ and a threshold of $p_T > 20$ GeV with an efficiency of $>95\%$ [44]. The trigger selects initially the electrons, muons, photons and jet events at the local level. Neutrinos, based on the sum of missing E_T , are triggered globally.

The L1 trigger system consists of three general parts: the L1 calorimeter trigger, the L1 muon trigger and the L1 global trigger (Figure 4.1).

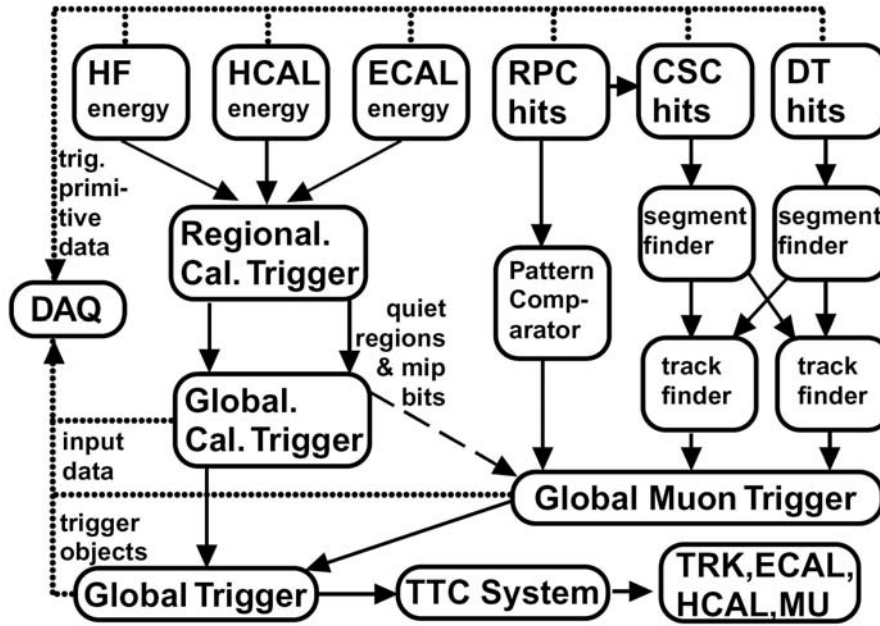


Figure 4.1.: The CMS Level-1 trigger system uses the data from the calorimeters and the muon system. The data are first selected by the local subsystem triggers (HF, HCal, ECal and RPC, CSC, DT) triggers. After the acceptance and selection by the system specific regional triggers, they are transmitted to the calorimeter and muon global triggers. All the information is then sent to the CMS Global Trigger which finally decides whether to trigger on a specific crossing. This decision is then transmitted via TTC to the subdetector read-out systems [43].

The calorimeter trigger obtains the energy from all channels of ECAL, HCal and HF and sends it to the *Regional Calorimeter Trigger* (RCT). Here the candidates for electrons, photons, taus and jets are selected, as well as the isolated and non-isolated electron/photon candidates. The candidates are then transmitted to the *Global Calorimeter Trigger* (GCT), where they are sorted. Afterwards the four best candidates of each type are propagated to the

Global Trigger (GT). Also the total transverse energy and total missing energy are calculated by GCT. Additionally the GCT provides information about (η, ϕ) regions to the global muon trigger for muon isolation cuts (for more information concerning the muon trigger system see next section).

The results from the calorimeter and muon triggers are then accepted by the GT. The L1 decisions are then distributed via the *Timing, Trigger and Control* (TTC) system to the sub-detectors to initiate the read-out. The TTC system provides L1 trigger information together with a precise 40 MHz clock signal via an optical fiber network. The signals are converted by active optical/electronic units TTCrx, where also additional functions (e.g. programmable course and fine compensation times, technical delays) are implemented [45].

Finally the HLT has access to all L1 data, the data mass storage and offline computing resources in the form of the HLT filter farm. The decision of event selection is made on a subset of the calorimeter and muon data. These data are then used to assemble complete events. They are filtered by using the physics reconstruction algorithms. The "problematic" events (e.g. events characterized by a large occupancy in the muon chambers) are not rejected but stored unprocessed for further investigations and analysis. HLT can also make other topological combinations and calculations using in addition the tracker data. The HLT output rate is about 100 Hz.

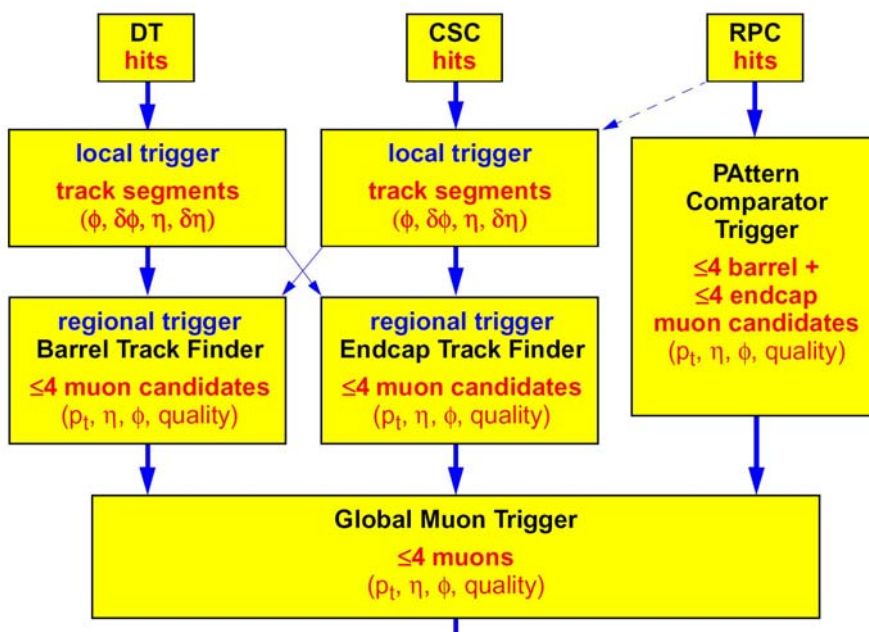


Figure 4.2.: The CMS L1 muon trigger is partitioned into local, regional and global units. In the DT/CSC local trigger the first primitive track segments are built in one station. The regional trigger selects 4 top muon candidates using the data from all stations, also by including the DT/CSC data in the CMS overlap region. Finally the Global Muon Trigger, supported by the RPC information, decides upon 4 muon candidates which have to be sent to the CMS Global Trigger [43].

4. Data taking with the CMS DT muon chambers

The L1 muon trigger

For the CMS L1 muon trigger all three muon subdetectors DT, CSC and RPC (see Section 3.2.2) are used. The DT and CSC systems provide precise spatial coordinates of the detected particle and the RPCs deliver the exact detection time. These complementary features provide independent information and eliminate ambiguities in the particle reconstruction. The muon candidate is then accepted in the cases, where it is either seen by both DT/CSC and RPC systems or by only one system, if the quality of the track is sufficiently high.

The architecture of the muon trigger is presented in Figure 4.2. It is formed by the local, regional and global muon triggers.

The task of the DT and CSC local triggers is to compose track segments based on the FE signals obtained directly at the chambers. The local trigger logic forms the segments and allocates the coordinates ϕ and η (track vector). For example, the *Bunch and Track Identifiers* (BTI) of the DTs use an algorithm to fit a straight line to the cells of a SL which show a hit, if, at least, three cells (track points) are available. For each found muon track the bunch crossing ID is assigned. The *Track Correlator* (TRACO) combines two such track segments, one from each ϕ SL and selects a possible candidate for the same particle. The *Trigger Server* (TS) filters these candidates and provides at most two track vectors to the regional trigger (Figure 4.3).

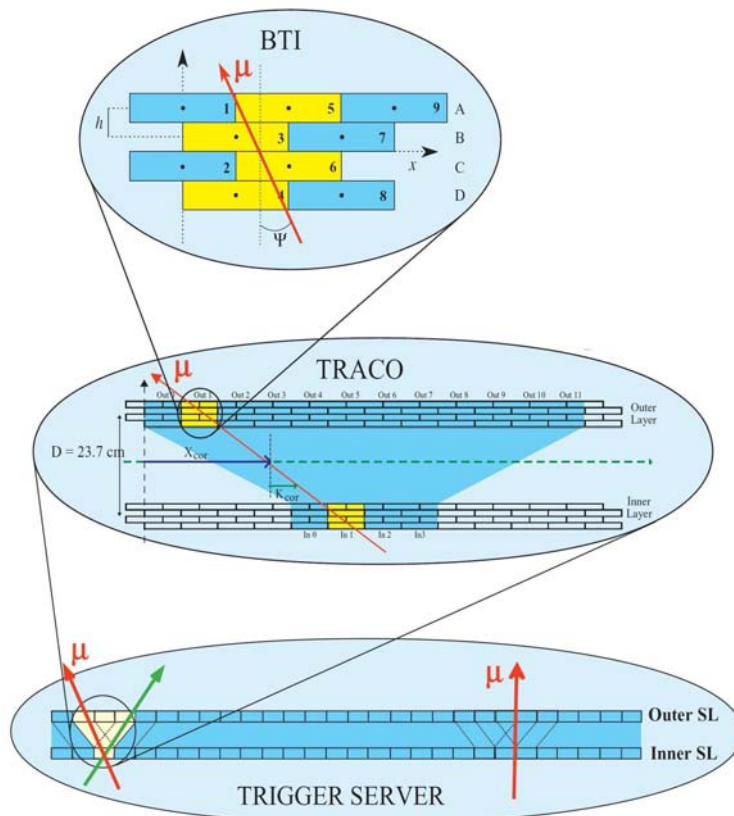


Figure 4.3.: In the DT local muon trigger at first primitive track segments are built by the Bunch and Track Identifier (BTI). Then the combination of two such segments from two ϕ SLs is performed by the Track Correlator (TRACO). Finally the Trigger Server (TS) filters the possible muon candidates and transmits them to the regional muon trigger [43].

The regional trigger builds the entire track on the basis of the track vectors from all stations and calculates the parameters ϕ , η and p_T . For $0.8 < \eta < 1.2$ (overlap DT/CSC region) the data from DT and CSC systems are exchanged for track building. Up to 4 top muon candidates, from DT and CSC each, are then transmitted to the Global Muon Trigger (GMT).

The RPCs do not process the events locally, they rather act as a synchronizer. The hits from all RPCs are collected by the *Pattern Comparator Trigger* (PACT).

All DT/CSC regional trigger data and PACT information are compared by the GMT, where an isolated muon trigger is formed. From here the 4 top muons with the highest p_T are propagated to the GT.

4.1.2. Data Acquisition System (DAQ)

DAQ requirements [46]

The general task of the *Data Acquisition* (DAQ) system of the CMS experiment is to record those events, which are selected by the Level-1 Trigger and prepare them for the offline analysis. Another crucial function of the DAQ is the co-operation with the Detector Control System (DCS, see Chapter 5) for the supervision of all detector components and its environment.

The DAQ system has to satisfy some technical and instrumental requirements to ensure that all interesting data are read out and stored for analysis. So, on the one hand, it is crucial for the FE electronics to store the read-out data for at least $3.2 \mu\text{s}$ awaiting the L1 trigger decision. The random-access memories, which provide data for the HLT, must have enough capacity for a storage period of about 1 s, which is the HLT processing time. On the other hand, the DAQ chain is optimized to manage the amount of the data and the data flow (see Table 4.1), which implies the right number and location of the DAQ modules in the detector. This is achieved by using a common interface to all the different detector FE modules (*Front End Drivers*, FED), which makes the global read-out possible [47].

DAQ architecture

The CMS DAQ system is factorized in four stages with different functionalities:

- **read-out:** collection and local storage of the FE event data;
- **event building:** grouping of data corresponding to one event from the read-out;
- **selection:** event processing by the HLT;
- **storage/analysis:** forwarding of those events selected by the HLT for storage and further analysis (also for monitoring and calibration).

These functions are performed by an electronics system, which is presented in the schematics of Figure 4.4. It is composed of the following parts:

- **Front-End (FE):** Interface between the subdetector and the DAQ system. It contains electronics modules for storing the data from the detector output channels upon the L1 Trigger accept. In the entire CMS DAQ system there are about 700 such modules.
- **Read-out System:** Modules for parallel reading of the data from the detector FE system. The data are stored in buffers until they are processed to analyze the event.

4. Data taking with the CMS DT muon chambers

Parameter	Value
Level-1 Trigger output rate	100 kHz
Event size	1 MB
Event Builder bandwidth	100 GB/s
Event Filter Computing Power	10^6 SI95
Data Production	10 TB/day
Number of Front-Ends	700

Table 4.1.: List of nominal data rates of the CMS DAQ system [43].

These about 500 so-called "Read-out Columns" contain a number of FEs and one *Read-out Unit* (RU), which ensure the proper buffering of the event data and connection to the switches¹.

- **Builder Network:** Network collection for interconnection between the Read-out and Filter Systems. It is composed of a switch facility working with sustained data throughput of 100 GB/s to exchange the partitioned event information from diverse Read-out Columns.
- **Filter Systems:** Processors, which execute the HLT algorithms to select the interesting events for offline analysis (about 500 entities, so-called "Filter Columns"). Each Filter Column contains one Builder Unit, which is responsible for receiving the incoming data fragments from an event and for building them into a full event. In the Builder Units are also Filter Units included that process the event elements for the HLT algorithms.
- **Event Manager:** Element for controlling the data flow. It was established to simplify the synchronization of the overall system.
- **Computing Systems:** Processors and controls responsible for receiving filtered events (but also fractions of rejected events) for storage and offline environment.
- **Controls:** Entities supporting DAQ user interfaces, configuration and monitoring.

Parts of the read-out subsystem, the switch fabric, parts of the computing farm and the Event Manager compose a common DAQ component called *Event Builder* (EB). Its task is to collect the data from the various read-out buffers and combine them into a single "event buffer", as well as their following transfer to the analysis processors. The event building procedure is presented in Figure 4.5. The data for the EB are obtained from the fragmented event data, stored in separate read-out units; their destination are the filter buffers, where the full event information is stored. The EB interconnects the data source and data destinations by emitting data packets of fixed size by using the maximal bandwidth. The right allocation of the event parts to the proper destinations is performed in a cyclical mode by switch network "barrel shifters".

¹The terms "Front-End" and "Read-out System" used in this section are declared for the global detector DAQ system. In the following sections describing the chamber *local* DAQ we also use the terms "Front-End board", "Read-out board" and "Read-out Server", which are different as mentioned here and can be easily distinguished if related to the context.

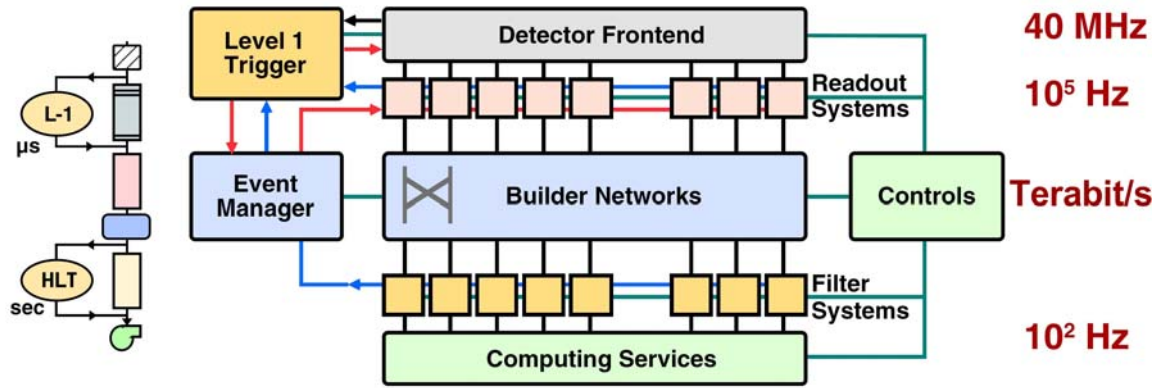


Figure 4.4.: The architecture of the CMS DAQ system. The detector Front-End electronics provide fragmented event data from all subdetectors which are then read-out and stored in deep buffers (Read-out Systems). The large switch network (Builder Network) merges these data by selecting parts belonging to a common event and transmits them to the Filter System. The interesting events are then forwarded to the Computing Services for mass storage and analysis. The DAQ process is managed, monitored and controlled by two complementary systems (Event Manager, Control and Monitor) [48].

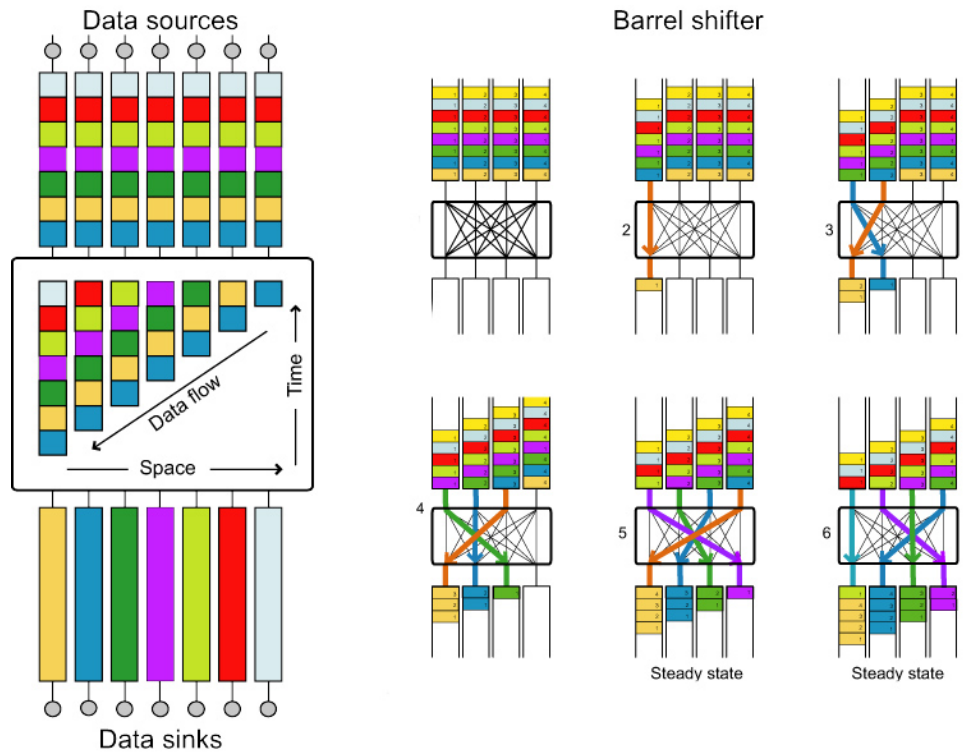


Figure 4.5.: CMS event building. The data of event fragments are stored in separate buffers (data sources). The barrel shifters extract cyclically the fragments and shift them to the proper filter buffers (data sinks) to obtain the full event information [49].

4.2. The local DAQ system for the CMS DT muon chambers

The main goal of the DAQ electronics for the CMS DT muon chambers is to digitize and store the drift time data from the chamber Front Ends. This local read-out system has to manage data arriving with a particle rate up to 2 kHz per cell by the Level-1 trigger (see Section 4.1). Therefore the local DAQ memories have to be large enough to store the data for $3.2 \mu\text{s}$ until the trigger matching is done. Additionally, a mechanism able to handle hits which belong to different triggers but match the same time search windows (trigger overlap) is used due to the maximum DT drift time of 400 ns being 16 times longer than the bunch crossing period. The present Section describes the main Front End and Read-Out Unit components, which were developed and are used locally in connection with the DT muon chambers to fulfill – among others – these requirements.

4.2.1. Chamber output signals

The cells of the CMS DT muon chambers provide fast analog signals caused by charged particles passing a cell. The processing of these analog signals is executed by the Front End (FE) electronics, which is the first stage of the local DAQ chain at the chambers. Their main tasks are:

- **Cell signal amplification.** The electron avalanche at the anode wire in the cell causes an anode voltage drop which is too small for the following processing. Also, the chamber should work at low gain to ensure the required reliability and lifetime. Therefore, this analog signal must be amplified, in order to make it usable for the downstream electronics.
- **Threshold comparison.** All electronic devices, also the muon chambers, produce undesirable noise signals, caused by random electron movement in the circuits. To eliminate most of this noise on the chamber input signals, the amplified ones have to be compared with a reference voltage (*threshold*), which presents a lower voltage limit for signal acceptance.
- **Logic signal creation.** The cell states (existence or non-existence of particle hit in a cell) can be represented as Boolean values (1 or 0, respectively). Therefore a digital signal is created by analyzing the discriminator output, and then transmitted to the next trigger and DAQ components.

To fulfill the mentioned requirements a special ASIC² chip, named MAD, containing all operation modules in integrated form, was developed by the Padua CMS DT team [50]. It was built using the $0.8 \mu\text{m}$ BiCMOS³ technology. It contains four analog input channels, which are initially preamplified with a gain of 3.3 mV/fC. The preamplification results in an output voltage signal of about -600 mV (see also Section 3.3.2). The signals are then transmitted to a low gain integrator (shaper), whose outputs are directly connected to one input of the fully differential discriminators. The other discriminator input is connected to the external threshold which is common to all channels and usually set to 15-20 mV during chamber operation. A buffer finally prevents switching noise propagation from the following

²Application Specific Integrated Circuit.

³Bipolar Complementary Metal-Oxide-Semiconductor.

4.2. The local DAQ system for the CMS DT muon chambers

sections to the previous sensitive circuits. The described analog sections use +5 V common supply.

When the discriminator is latched the pulses are stretched and sent to LVDS⁴ drivers [51]. The logic LVDS signals are then transmitted to the four chip outputs. The output sections are driven by a supply of +2.5 V.

Also some control and monitoring features were implemented in the MAD design. For example the channels can be disabled to mask a channel with high noise by a TTL⁵ high level. Also the temperature can be measured, based on the voltage difference between the base-emitter junctions when operated at different current densities. The voltage output is 7.5 mV/°C. A bias circuit is used to control the current generators and supply voltages.

Four MAD chips are placed on one PCB named *Front End Board* (FEB, see Figure 4.6 top). They are mounted directly at the cell ends at one SL side (Front End side). The FEB contains in the majority of cases four MADs in order to process signals from 16 SL cells. The FEB has also an I²C connector (PCF8577) for "slow control", i.e., among others, the temperature measurement and channel masking. Furthermore, it has a distribution connector for test pulses (one test pulse for all 16 channels).

The cells of an SL are connected consecutively to the FEB from left to right, each 16-number group to one board, independently of SL size and type (Figure 4.6 bottom). In some cases the last cells are connected to a special FEB type, which can process signals from more than 16 cells. The MAD and consequently the FEB outputs are then connected to the outer DAQ chain via a feedthrough board glued at the FE external cover.

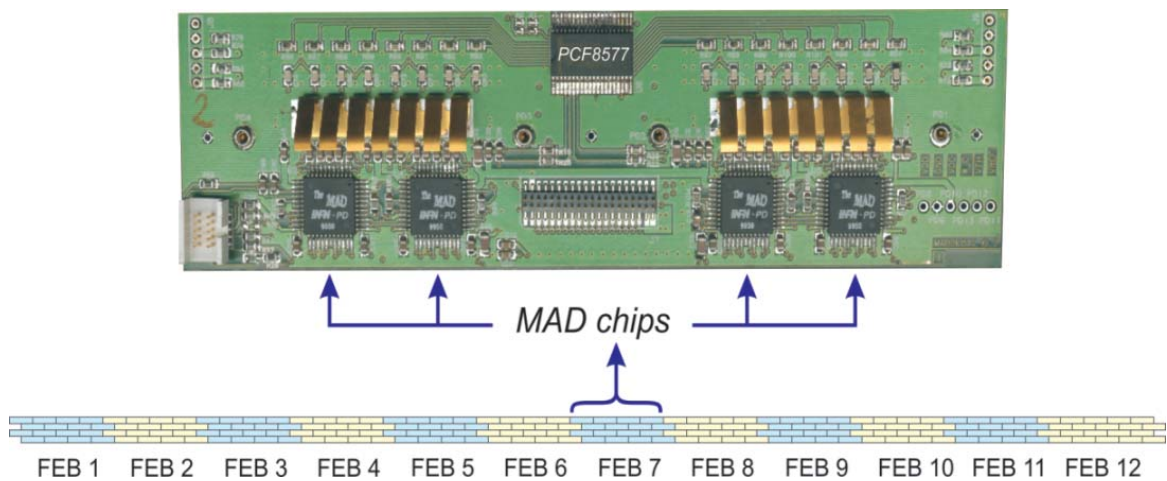


Figure 4.6.: A Front End Board (FEB) of the CMS DT muon chambers [52] (top). It contains four MAD chips, each with four analog inputs to collect the cell signals, compare them with a threshold and send an LVDS logic signal to the trigger and DAQ chain. Also other features like temperature measurement and channel masking are implemented. The signals of 16 SL cells are then processed in groups by the FEBs (bottom), here representatively presented for an MB1 ϕ SL. The last FEB 12 is a large version and can process 20 channels (5 MADs).

⁴Low Voltage Differential Signaling.

⁵Transistor-Transistor Logic.

4. Data taking with the CMS DT muon chambers

4.2.2. Drift time measurement

High Performance Time to Digital Converter

The FE output logic LVDS signals have to be converted into time units as quickly as possible, assigned to the proper event (muon passing the chamber), and the events must be allocated to the right bunch crossing. Therefore the signals must be locally compared with a time reference signal to obtain the drift times, which have then to be handled by an appropriate trigger mechanism.

All these tasks are managed by the *High Performance Time to Digital Converter* (HPTDC) [53], developed by the CERN/EP Microelectronics group. It is implemented in IBM 0.25 μm CMOS technology. As can be seen in Figure 4.7, it contains three main input types: one clock, 32 FE hits and one trigger channel.

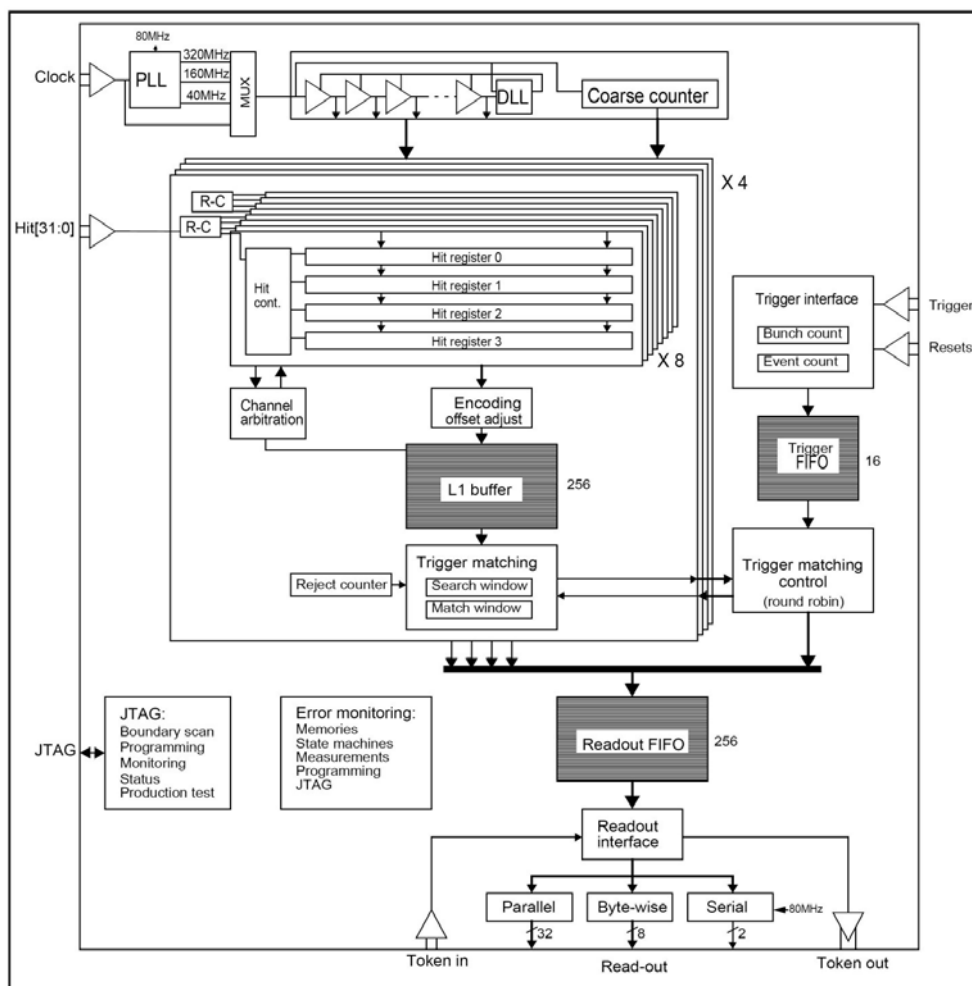


Figure 4.7.: Architecture of the *High Performance Time to Digital Converter* (HPTDC) [53]. The time base for the digitization is the *Delay Locked Loop* (DLL) with 32 delay elements. The incoming hits (32 channels) can be digitized with a resolution up to 25 ps. An overlapping trigger mechanism is implemented to ensure that all hits are assigned to the right events, even if the measured times are longer than the trigger period.

4.2. The local DAQ system for the CMS DT muon chambers

From the TTC system the HPTDC is provided with a clock signal of 40 MHz frequency, which is exactly the LHC bunch crossing frequency. This signal passes at first the *Phase Locked Loop* (PLL) [54]. In this unit the clock frequency f_{clock} can be multiplied from 40 MHz to 160 or 320 MHz, if it is required to obtain time measurements with higher resolution. Alternatively the PLL can act as a filter to remove jitter from the incoming signal. In this case it generates its own clock signal with one of the mentioned frequencies.

The clock signal with its final frequency f_{PLL} is then transmitted to the *Delay Locked Loop* (DLL) [55], the time base for the TDC measurements. It includes 32 delay elements, adjusted by control voltage. The delay elements divide the clock period into 32 intervals. The phase difference between the clock and the delayed clock is measured by the DLL phase detector. Afterwards the clock pulses are counted by a coarse counter. The actual DLL state and the clock count are used for the time measurement. For $f_{PLL} = 40/160/320$ MHz the possible HPTDC resolution is thus $1/(32f_{PLL}) = 0.78125/0.195/0.098$ ns, respectively. For example, the drift times of the CMS DT muon chambers are measured with a resolution of 0.78125 ns, which is sufficient to obtain the required muon track resolution of 250 μm (see Section 3.3.2). Using an implemented *R-C* delay one can run the HPTDC in a very high resolution (0.025 ns) mode.

When an FE signal reaches the HPTDC the actual DLL state and clock count is stored. Up to four such time measurements per channel can be buffered before being written into the L1 buffer, which is 256 words deep and shared by 8 hit channels. A special trigger matching function selects times related to a valid trigger.

The L1 trigger signals are also provided by the TTC system and contain the trigger time tag and the event ID. They are temporarily stored in the 16 words deep FIFO⁶. From this FIFO the trigger time tag is taken to perform trigger matching, i.e. the time match between trigger time and time measurements taken from the L1 buffer described above. The trigger matching occurs within a programmable time window (Figure 4.8). This window has to be smaller than the trigger latency to ensure that all hits matched by the trigger are already in the L1 buffer. The HPTDC trigger matching mechanism is able to assign measurements belonging to multiple triggers. This property is important, concerning the long drift times up to 400 ns with respect to the bunch crossing period of 25 ns. The data are then sent to the common read-out FIFO, shared by all 32 hit channels, and, after they are accepted, to the read-out interface. The data output proceeds in parallel, serial or byte-wise.

Read Out Boards and the MiniCrate

Since a CMS DT muon chamber contains up to about 900 drift cells (MB3), up to 28 HPTDC, each with 32 channels, are needed. The CIEMAT collaboration team developed, produced and tested the *Read Out Boards* (ROB, Figure 4.9) [56] including the HPTDCs to digitize the drift times of all 250 chambers. On each ROB four HPTDCs are mounted, resulting in 128 channels (ROB-128)⁷ In the ROBs, foreseen for the digitization of the ϕ SLs, both ϕ SLs share one HPTDC: 16 HPTDC channels are connected to the ϕ SL 1 and the remaining 16 channels of the same HPTDC are connected to the ϕ SL 2. The channels of the θ SL are connected to the ROBs with HPTDCs for the θ SL digitization only. The four HPTDCs on each ROB are connected in a token ring, working synchronously with the clock. One of them is defined as master to control the read-out chain on the ROB. If the read-out is

⁶First In, First Out: buffer mode, in which those data are first handled, which were stored first.

⁷The MB1 chambers, due to their size, have beside the usual ROBs-128 one small ROB version with only one HPTDC (ROB-32).

4. Data taking with the CMS DT muon chambers

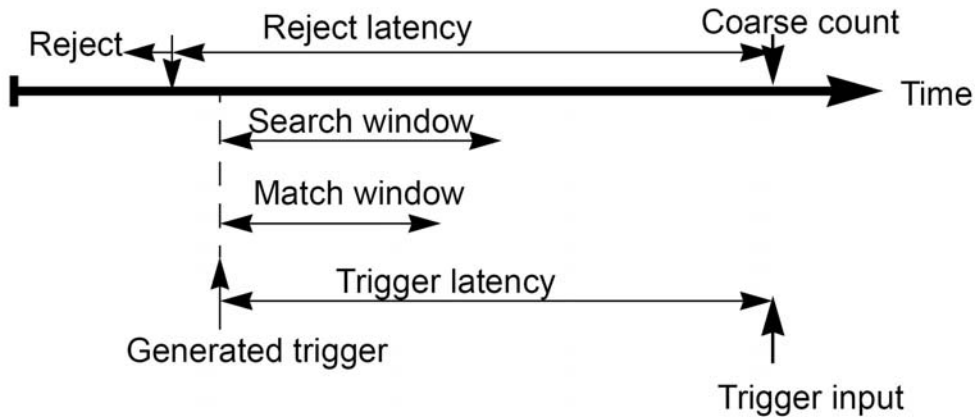


Figure 4.8.: Time windows for matching trigger hits in the HPTDC [53]. The programmable match window has to be smaller than the trigger latency to ensure that all data are in the L1 buffer before the trigger assignment.

performed the HPTDC having the token sends the data in a byte-wise mode to the serializer. The data processing on the ROB is managed by an Altera MAX 7000 CPLD⁸ [57], which slows down the read-out frequency to 20 MHz.

The ROBs are then directly installed at the chamber in an oblong sized local electronics device named *MiniCrate* (MC, Figure 4.10) [58]. It includes beside the ROBs also the *Trigger Boards* (TRB), designed and produced by the INFN Bologna team, with the local muon track finding mechanism *Bunch and Track Identifier* (BTI). The total amount of the ROBs (and also of TRBs) in an MC depends on the chamber size and its type (6 or 7 ROBs per MC) [59]. The read-out is managed by the *Chamber Control Board* (CCB; INFN Legnaro, INFN Padua) via an internal data bus (ROBUS). The CCB also controls the local chamber DCS elements (see Chapter 5), like gas pressure, alignment, low voltage distribution etc. The MC connection to the TTC and DCS system and the following DAQ chain occurs via two link boards, located at both ends of the MC.

4.2.3. Data transfer and storage

The HPTDC data are read out in 32-bit packets. These packets, obtained by each event are composed in groups (Figure 4.11) [53] [60], which contain information about the event, measured time and data sent. Each packet contains information about its type (header, trailer, time measurement etc.), encoded in its four most significant bits.

The data packet group begins with the group header which contains the number of the master TDC, event ID and bunch ID. All HPTDCs should have the same event ID and bunch ID at each L1 trigger if the system works properly. The group header is then followed by the leading measurement (i.e. by the time matching the leading edge of the hit signal, the signal width plays no role thereby) t_{lead} . This packet contains the HPTDC number, which digitizes the time, the HPTDC channel and measured time. Generally the HPTDCs are configured to measure the time of the hit's leading edge in low resolution mode, i.e. in steps of $(25 \text{ ns})/32 = 0.78125 \text{ ns}$. The bit-encoded information in t_{lead} has to be divided by 4,

⁸Complex Programmable Logic Device.

4.2. The local DAQ system for the CMS DT muon chambers

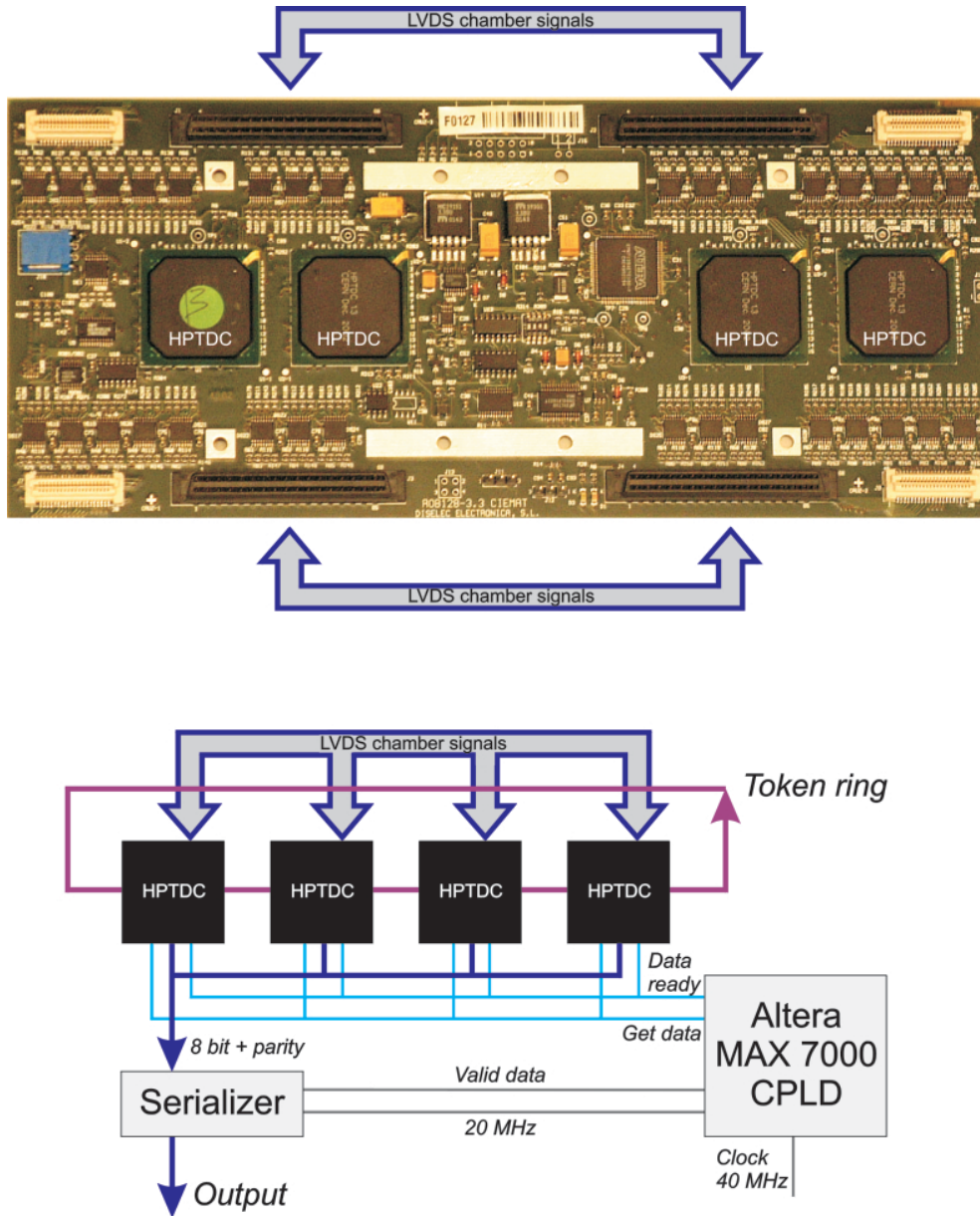


Figure 4.9.: Read Out Board (ROB) including four HPTDCs for drift time digitizing from up to 128 chamber cells (top). The HPTDCs are connected to a clock synchronous token ring. The byte-wise read-out on the ROB is controlled by an Altera MAX 7000 CPLD (bottom).

$$t_{drift} = \frac{t_{lead}}{4} \cdot \frac{25 \text{ ns}}{32} \quad (4.1)$$

due to the fact, that the two least significant bits in that sequence are reserved for higher resolution modes. The last data packet within a group is the group trailer. It contains the HPTDC number, the event ID and the number of the words in the corresponding group (incl. header and trailer).

If any error condition is detected by an HPTDC, e.g. buffer overflow, lost data etc., it signals this to the control system via the ROB error line; the error messages are also included

4. Data taking with the CMS DT muon chambers

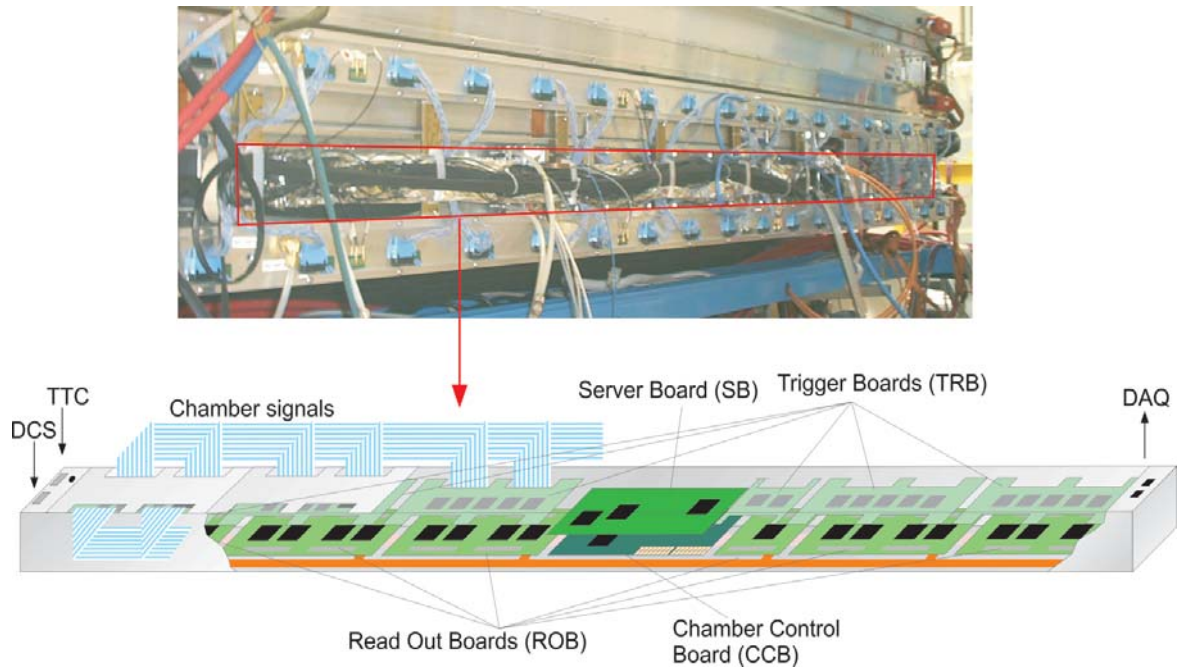


Figure 4.10.: The MiniCrate (MC) of the CMS DT muon chamber, installed at an MB3 chamber (top). It includes electronics for the drift time digitization (Read Out Boards), local trigger assignment (Trigger Boards), trigger server unit (Server Board), the chamber control (Chamber Control Board) and the connection to the outer TTC, DCS and DAQ systems (link boards), displayed here for an MB1 chamber (bottom).

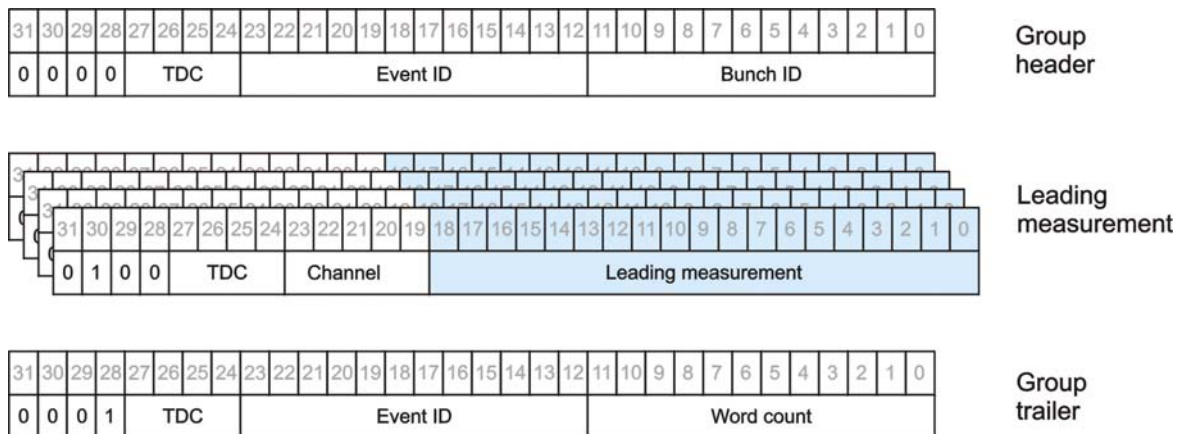


Figure 4.11.: Data group from a ROB in usual read-out mode. The data are composed in 32-bit packets (words). Each group begins with a header and ends with a trailer, containing the event and bunch IDs. The drift time measured is bit-encoded in the packets between header and trailer, one packet for one chamber hit, also containing the HPTDC number and HPTDC channel of the measured drift time.

in the ROB data flow. Some of them have only warning character, like hit or event loss, and the system is functioning properly. However, other ones can indicate an internal error. In this case the read-out system does not work well and it has to be re-configured and reset.

Optionally the HPTDC can be configured to obtain other measurement data in the 32-bit packets. In particular, the trailing or combined measurement of leading and trailing edge to obtain the width of the input pulses, the local HPTDC headers and trailers (beside the described master ones) and other debugging packets to obtain information about the FIFO occupancies in the HPTDCs.

The data from the ROBs are then merged and prepared for transmission out of the detector and its environment. For this purpose 9U VME modules named *Read Out Server* (ROS) boards [56] are developed, produced and tested by a CIEMAT (Madrid) team (Figure 4.12 top). They are located in the barrel tower rack close to the detector. One ROS collects data from 25 ROBs, installed in the MCs in approximately one sector. Thus 12 ROS boards are needed for one wheel, 60 ROS boards for the entire detector.

The encoded HPTDC data come to the ROS via eight RJ-45 connectors. Each of these inputs is dedicated for data from three different ROBs. In the following, the data are internally split into 25 channels, one channel for one ROB. The data in each channel are first equalized (high-speed data recovery) and serialized (Figure 4.12 bottom), afterwards they are locally buffered in a 16 kB deep FIFO per channel. A group of four FIFOs is managed by one CPLD processor, which performs a pooling search for reading next event data. These seven CPLDs are connected in a token ring controlled by an FPGA⁹. The FPGA selects the event number to be sent and the CPLDs fetch the corresponding data from their FIFOs in a parallel way. The 32-bit HPTDC data packets are split in two 16-bit words but the data format remains nearly unchanged. Depending on the read-out mode additional information about the ROB number, link status etc. can be implemented in the data packets.

For the data read-out from the ROS different modes can be used. At first, for general use for data transfer during the CMS operation, the data are transmitted through a *Gigabit Optical Link* (GOL) serializer, developed by the CERN/EP Microelectronics group [61], to the VCSEL¹⁰ output (850 nm wavelength, 62.5/125 μm fiber). The data, slightly modified for this kind of transmission [62], are then sent with the expected throughput rate of about 270 Mbs to the *Detector Dependent Unit* (DDU), being the global CMS DAQ interface (also called the DT FED, see Section 4.1.2) [63]. Another possibility for the ROS read-out is to send and control the data directly via the VME bus. This method is mostly preferred for ROS and environment test procedures (see Section 4.3.3), also during the commissioning and detector tests. The HPTDC data format remains in this case unchanged. Beside the two described methods it is also possible to save the data temporarily in an internal 516 kB RAM memory which can be read out via the mentioned serializer.

4.3. The Aachen CMS DT muon chamber test facility

At the Phys. Inst. III A of the RWTH Aachen equipment was developed and constructed to check the functionality of the CMS DT muon chambers assembled here (Figure 4.13). Using two independent DAQ systems it was also possible to validate these two systems (Section 4.4.1). The present section describes generally the two DAQ system setups, as a part of the chamber test facility and used for the data taking with the chambers produced in Aachen.

⁹Field-Programmable Gate Array.

¹⁰Vertical Cavity Surface Emitting Laser.

4. Data taking with the CMS DT muon chambers

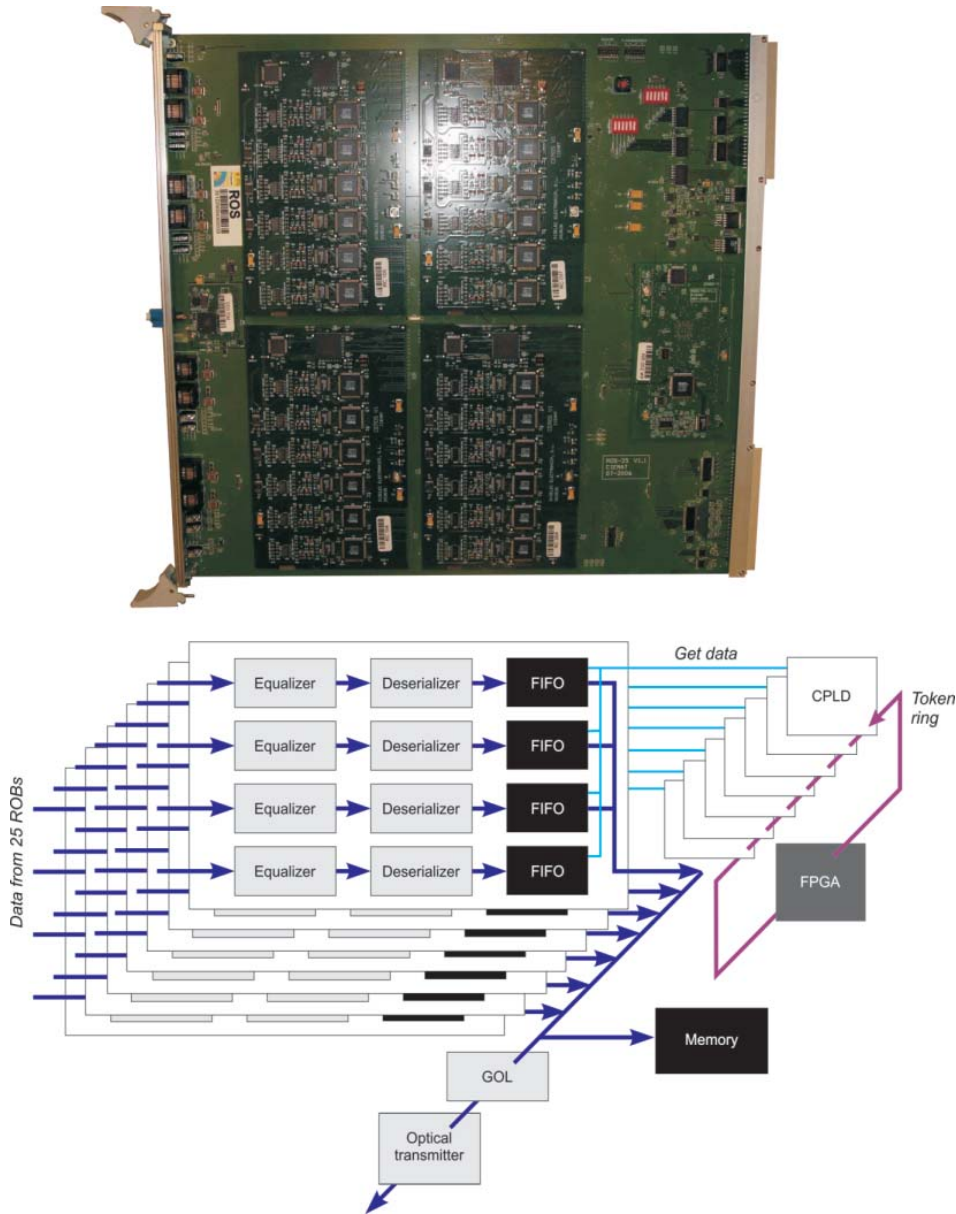


Figure 4.12.: Read Out Server (ROS) board for data merging and transfer (top). To one ROS data packets from up to 25 ROB can be connected, which are temporarily stored in FIFOs, and then, on demand and selected by event number, transferred via an optical link out of the CMS detector area (bottom).

4.3.1. Chamber function tests with cosmic muons

Each chamber has to undergo a large number of tests before its final installation and operation in the CMS detector. Besides the quality tests, which include the wire tension measurement, HV stability, gas tightness etc. (see Section 3.3.3), the chambers must be tested on their functionality, i.e. one has to make sure, that a charged particle passing the chamber can in fact be detected and measured properly. Therefore the chamber functionality was tested using cosmic ray muons as soon as the assembly phase had been completed and the quality tests had been done.

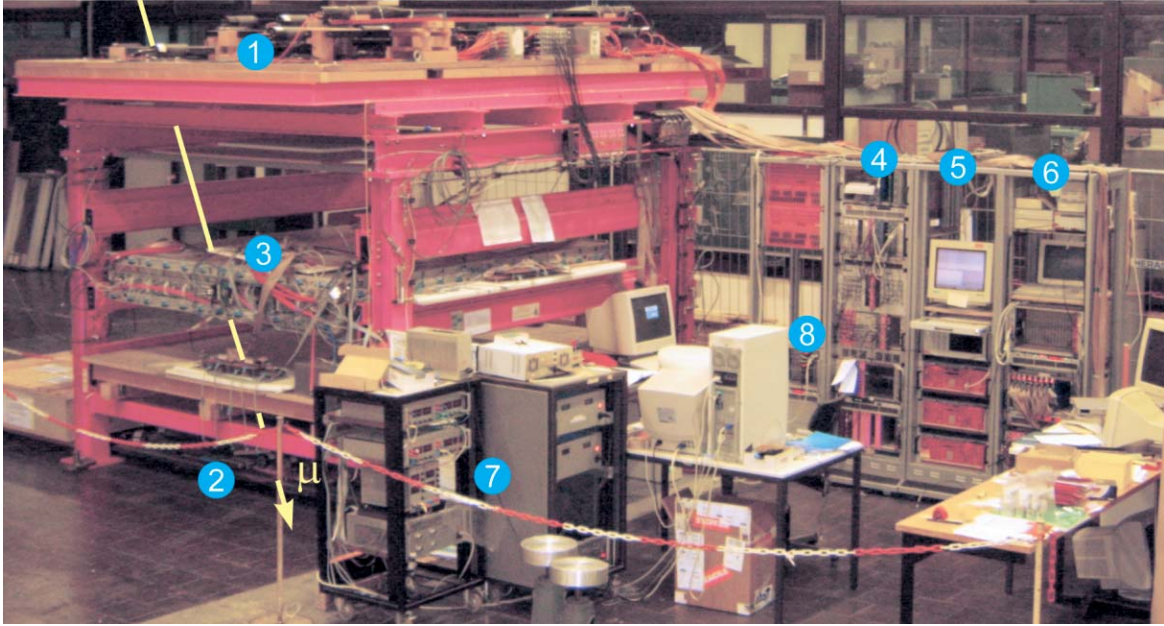


Figure 4.13.: The Aachen facility for CMS DT muon chamber function tests with cosmic muons. The muons (μ , yellow arrow) passed both scintillator triggers (1) and (2) and the chamber (3) being tested. The trigger logic (4), high voltage supply (5) and Aachen DAQ electronics (6), as well as the MiniCrate DAQ environment (8) are placed in racks set aside. The low voltage supply (7) is located in small racks in the front.

The passage of a cosmic muon, which has to be detected by a chamber, must be confirmed by an independent trigger system. Both, the tested chamber and the trigger are combined in the test facility (Figure 4.13 (1), (2) and (3)).

The trigger system for the cosmic ray chamber tests consists of two layers of plastic scintillators, on top and bottom of the test stand. The scintillator layers are made up of rectangular plates of different areas and forms. They are positioned in a way to cover the chamber surface as precisely as possible to obtain the optimal trigger rate. Each of the plates is connected to two or four photomultipliers (PM). The PMs are supplied with HV, which is optimized for each one (between 1850 and 2200 V). The HV supply is realized using two *CAEN Sy 127* crates connected to a common terminal [64].

All PM trigger signals are processed (threshold and pulse width) and transmitted via a set of meantimers and OR-level logic providing a coincidence signals of top and bottom. Finally, these two signals are connected to a coincidence unit, whose output signal is then provided to the DAQ system.

As mentioned before, the object to be tested is usually a muon chamber, but also single SLs can be tested in a similar manner. The test stand has place for up to three complete chambers or SLs. The chamber used for the tests of the DAQ systems was one of MB1 type, produced previously in Aachen as a spare unit. The chamber was not equipped with the complete final electronics environment used for the operation in CMS. For the test purposes in Aachen only the PADC (see next chapter) and the MiniCrate was installed on the chamber. The chamber was connected to HV, LV and gas; the connection to the water cooling system was not necessary, since only little heat is produced when operating only one chamber under the test conditions.

4. Data taking with the CMS DT muon chambers

4.3.2. The Aachen DAQ system

The Aachen DAQ system (AC-DAQ) was used in the years 2002–2006 for functionality tests on all MB DT muon chambers built in Aachen. For this purpose various commercial and custom-made hardware and software components were used, since the final read-out electronics and DAQ software was yet not completely developed and released during this chamber assembling period. The capacity of the AC-DAQ allows to handle only the signals from one SL.

The LVDS signals from the SL Frond Ends are at first connected to special electronic units *RFEB 16-V3* converting them into ECL logic signals. There are in total 15 such converter boards, developed and produced by the Aachen electronics group, each reading 16 channels of one FEB. A 30 m long flat ribbon cable, connected to the ECL output on each converter board, is used for the connection to the TDC.

As TDC eight *LeCroy Model 2277 Digital Counter* modules [65] are used. The model 2277 TDC is a CAMAC-based device designed especially for timing applications with high accuracy. Each TDC is connected to 32 SL channels (i.e. from two FEBs). The drift times are then measured with a resolution of 1 ns. The measurement occurs in the TDC mode COMMON STOP, provided by the delayed trigger signals: the input groups on several channels (chamber signals from a single muon event) precede the reference time mark generated by the trigger signal. The entire time range being at disposal for the time measurement is about 65 μs (it means the trigger delay has to be below this time limit). A FIFO attached to each channel allows to record up to 16 hits from one channel with respect to the same trigger signal. The digitized values are zero-suppressed at the chip level. Although the digitization is usually processed on the leading edge of the input signal, the TDC can also be operated in the trailing edge mode, as well as by a combination of leading/trailing edge measurement (pulse width measurement). During the entire DAQ process – CAMAC clear command, hit registration, time data processing and buffering – the TDC remains in the BUSY state and does not accept any new input. However, the read-out by the host computer can begin as soon as the first word has been sent to the FIFO which reduces the dead time and increases the data flow rate.

The data acquisition from the TDCs can only be performed via a VME application. For this purpose a CAMAC/VME interface (*Aachen DBCC/Wiener VC 16*) is used. The final data transfer connection to the PC is done by the VME controller *hp Model 747*.

The data read out from the TDCs are grouped in blocks of 32-bit (header and length of data group) and 16-bit (e.g. channel, drift time, trigger mode etc.) words. The software used for data taking [66] allows to enable or disable words containing additional information like test mode, crate ID etc, as well as to add new words being of interest for the user. The analysis software is hereby not affected.

The configured data, read out by the DAQ software, are at first stored in two different buffers. Two other subprograms responsible for data storage and online monitoring fetch the data from the mentioned buffers. They can also act autonomically, e.g. in the test periods; in this case the data from the TDCs are directly transferred to the mass storage unit and used for visualization on the PC monitor. The DAQ processes are controlled by a DAQ control program, maintained through a user interface.

4.3.3. The MiniCrate DAQ system

The chamber LVDS signals from the FEBs are directly transmitted to the MiniCrate (MC) via special twisted-pair cables. The MC, used for the tests in Aachen, is prepared for data

taking only, and does not include the Trigger Boards (TRB). Also the low voltage supplies are especially constructed in Aachen, but their technical design is equivalent to the original low voltage units used in the CMS experiment. Due to the fact that the MC includes no TRBs and thus the temperature inside the MC is permanently under 40 °C, no water cooling was connected to the MC.

The hardware environment for the MC DAQ system (MC-DAQ) is schematically presented in Figure 4.14. It mainly includes, beside the chamber with its MC, the TTC components and one ROS module, which are installed in a common VME crate, and the PC.

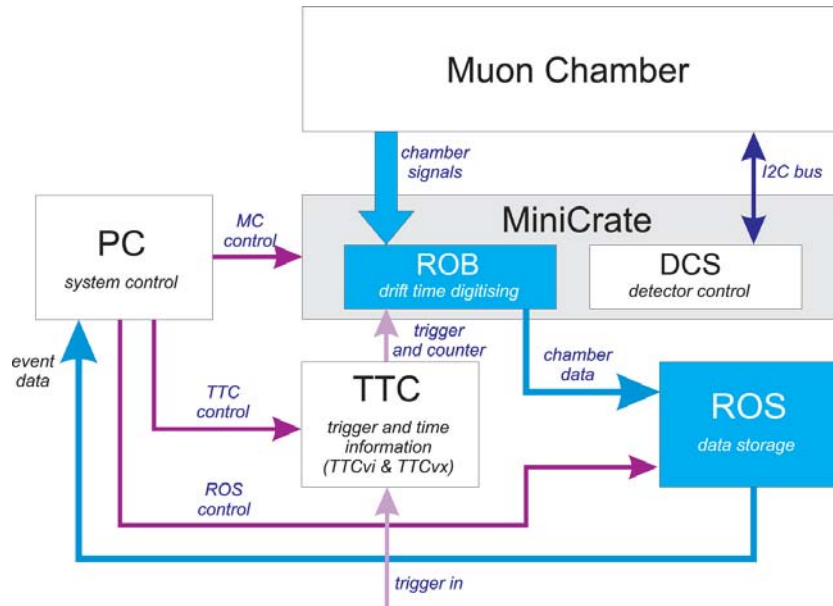


Figure 4.14.: The MiniCrate DAQ system environment for tests on the CMS DT muon chambers. The trigger and 40 MHz clock (counter) information is sent to the MiniCrate via TTC components. The chamber data matching the trigger with the event number are first stored in the ROS unit and then on the local PC. This PC also controls and monitors the operation of all system units, as well as the DCS data transfer.

The trigger signal from the scintillators is connected to the *TTC-VMEbus interface* (TTCvi, developed by CERN/EP group), becoming the LHC L1 format and, if needed, merged with other TTC commands [67]. From the TTCvi it is sent to the *TTC multiplexer, encoder and fiber-optics transmitter* (TTCvx, developed by CERN/EP group), where the signals are transformed into optical (1330 nm) pulses [68]. Also – generally used for DAQ tests – the 40 MHz clock is generated in the TTCvx. The L1 trigger and clock information are then encoded and sent commonly via one optical fiber to the MC.

The digitized drift times from the ROBs, matching the trigger with the event number (time mark) are then sent directly to the ROS-8, which is a smaller version of the ROS-25 module described earlier, developed for test purposes and capable to store data from up to 8 ROBs [69]. Then the ROS FIFO data are fetched via the VME backplane and stored locally on the PC, which also controls all mentioned DAQ components.

The MC operation is supported by software tools, which are used for the DAQ configuration, control and monitoring, as well as for data taking and storage. Some of the programs were

4. Data taking with the CMS DT muon chambers

developed by the collaboration team and adapted for the Aachen setup, others were developed in Aachen for the specific hardware environment. In the following a list of software used generally for the complete MC read-out system in Aachen is presented. In Appendix A two of the listed items, the main programs for the HPTDC configuration and MC data taking, are explained in some detail.

- *Measurement & Automation Explorer 4.0.0.3010* (National Instruments). It provides access to the modules installed in the VME crate, namely VME-MXI-2 controller, TTCvi, TTCvx and ROS-8. By means of this tool the VME devices are recognized and configured by providing them the VME logical addresses. It also handles possible errors occurring during the VME operation.
- *TTCvi_20041221.vi* (M.S., Aachen). It is used for the TTCvi configuration and control by using – among others – the count mode (orbit or bunch crossing), random trigger rate up to 100 kHz, selection of the time signal (external or internal) and trigger source (external, VME, random).
- *ROS-8_configuration_a_20050205.vi* (M.S., Aachen). This tool configures the ROS-8 via the VME bus. It enables and locks the FIFOs, resets the FIFOs and ROS-8 read-out, selects and loads the PAE and PAF values¹¹ for labeling the FIFO volume level and indicates the ROS-8 connection errors.
- *Monitor7* (L. Castellani, INFN Padua). This is the main software for maintaining and controlling the MC (Figure 4.15). It communicates with the CCB via a RS232 interface using specific CCB commands [70]. Among others it also controls the DCS chamber functions, like gas pressure. The communication with the MC is displayed on the Monitor7 message window independent of the software used, i.e. also if the chamber communication is performed by another software than the Monitor7, running synchronously with it.
- *Program_CCB_TCPIP.vi* (C. Fernandez, CIEMAT Madrid). This software performs the connection to the MiniCrate via the TCP¹² network. It is used for a quick initialization of the MiniCrate system.
- *MiniCrate_MB1_TDC_configuration_setup_ac20060127.vi* (M.S., Aachen, see Appendix A.1). Using this program the configuration setup file is created containing 647-bit long hexadecimal sequences for each HPTDC. It is then loaded in the HPTDCs by means of the *RO_MC_Configuration.vi* (see below).
- *RO_MC_Configuration.vi* (C. Fernandez, CIEMAT Madrid). This software reads the selected MC setup file (*MiniCrate_MB1_TDC_configuration_setup_ac20060127.vi*) and loads the configuration sequences from the file to the proper ROBs and their HPTDCs. It also signalizes errors when the configuration data transmission fails or the data are not accepted by the addressed chip.
- *Read_out_ROS-8_ac_DG5353setting_20070702.vi* (M.S., Aachen, see Appendix A.2). This is the main software for read-out of the digitized drift times stored in the ROS-8 FIFOs. It works by searching in each FIFO channel for a 32-bit word containing the

¹¹Programmed Almost Empty and Programmed Almost Full.

¹²Transmission Control Protocol.

same event ID. By matching the event ID the group of the data packets from each FIFO (see Section 4.2.3) are built into an event common block, formatted in accordance to the ones previously used for test beam analyses (see Appendix A.3) [71].

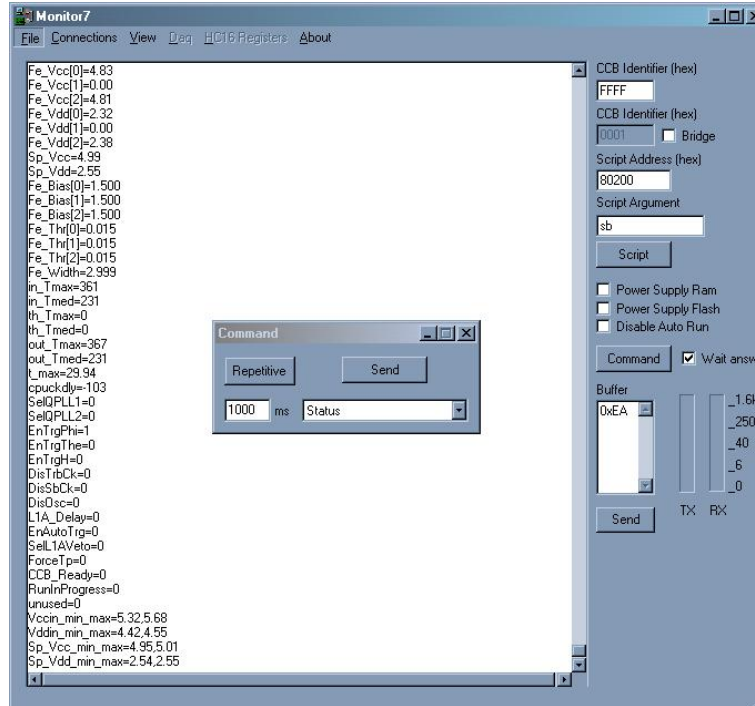


Figure 4.15.: The Monitor7 (developed by L. Castellani, INFN Padua) is the main software generally used for communication with the MiniCrate. It controls the chamber DAQ and DCS system using specific CCB commands. Any connection to the CCB within the MiniCrate is monitored by Monitor7, also when it is done by another software running synchronously with it.

4.3.4. DAQ data

By means of the measured data, the chamber functionality and quality can be tested under various operation conditions. For those purposes the DAQ raw data, stored at first in binary files (raw data), are converted using the software *testbeam-analysis* [72] into a root file. The root file, one for each SL, contains several subfields which handles the data by means of various statistical methods. It is possible to display the current data set directly as interactive diagrams. Depending on the software version they characterize the entire SL, cell groups (e.g. 16 cells in one FEB) or each SL cell individually. In detail, the data can be analyzed on the basis of the following characteristics:

- **Drift time spectrum** (Figure 4.16). It is presented as a histogram plotted with all hits registered by the HPTDCs within a programmable time window. The blue area is the so-called *time box* which contains the measured drift times. With enough statistics the hits within the time box of a maximal width of 380 ns (maximal electron drift time in the chamber cells), should be evenly spread over its entire width. The enhanced hit accumulation at the left box edge (i.e. very low drift times) is caused by avalanche

4. Data taking with the CMS DT muon chambers

electrons from gas amplification near the anode wire. The offset of the time box depends on the trigger latency and can be shifted by the HPTDC time window configuration (see Section 4.2.2). On the right side of the time box there are afterpulses caused by secondary electrons (a by-product of the gas ionization). The whole drift time spectrum is overlaid by noise. This phenomenon is unavoidable and evenly distributed over the entire spectrum. In the region left of the time box no entries from any electron drift related to the muon analysed can exist, so each registered hit here can be unambiguously identified as noise.

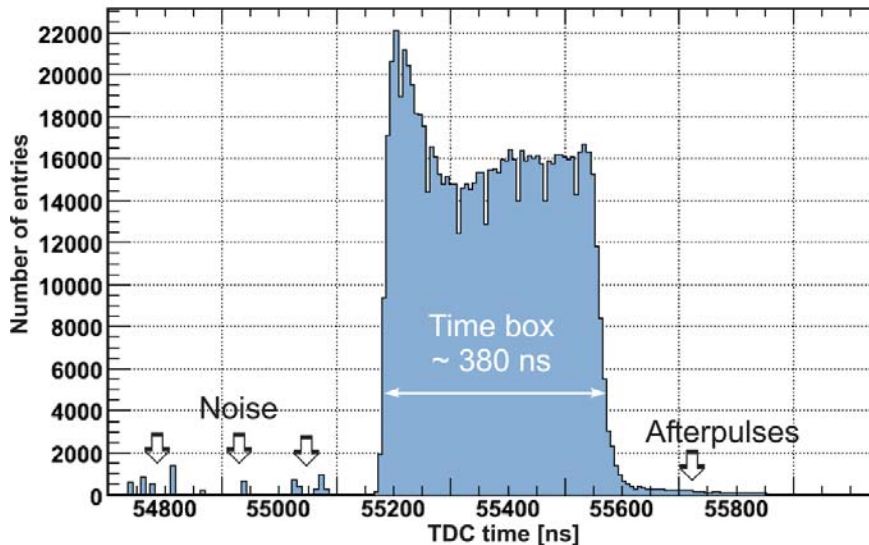


Figure 4.16.: The drift time spectrum of the cell hits. The regular drift times up to about 380 ns are nearly uniformly distributed within the time box in the middle of the plot. The peak at the left box edge is caused by electron hits close to the anode. Hits on the right side of the time box (afterpulses) are caused by secondary electrons which are a gas ionization by-product. Times on the left side of the time box represent only noise hits.

- **Cell occupancy** (Figure 4.17 left). This plot represents the illumination of all cells in a SL. The geometric shape is determined by the trigger acceptance: both scintillator layers (top and bottom) should register the muons passing through under a wide range of angles of incidence, so the cell occupancy is expected to be lower at the SL edge and higher in its middle¹³. The holes and spikes, seen in the smooth distribution, indicate dead and noisy cells, respectively.
- **Hits in the event** (Figure 4.17 right). This distribution peaks at a value of 4, in accordance to the average hit number per event in a SL (see Section 3.3.2). Occasionally, the number of the hits may be lower, if the muon passed through non-sensitive material. Additional hits are mainly due to noise. Strong inclined muons can fire more than one cell per layer.

¹³Muons hitting the edge cells of a SL in the test stand under a large angle of incidence cannot be registered by both scintillator levels top and bottom (see Figure 4.13). Thus for these cells only muons are triggered which almost vertically pass through the test facility

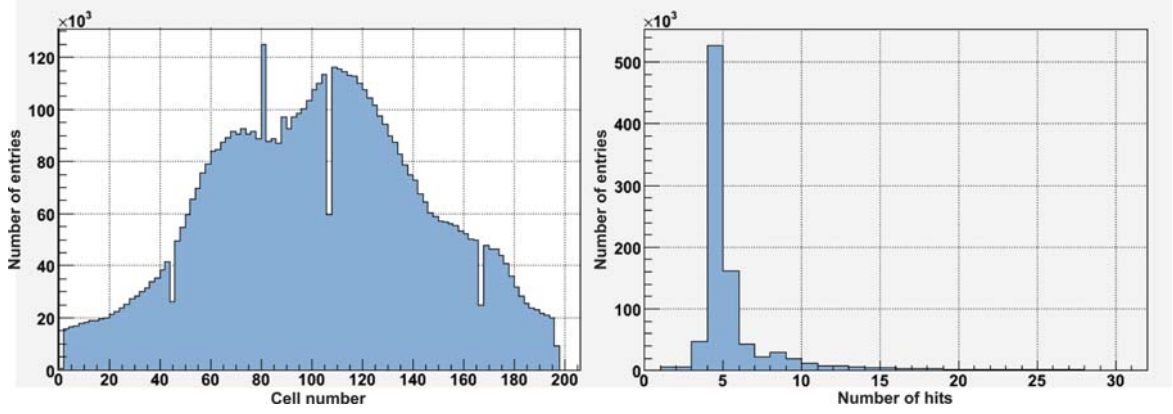


Figure 4.17.: The hit statistics in the DAQ runs. The cell occupancy (left) represents the total hit number in a cell during the run. The discontinuities and spikes in the distribution indicate dead and noisy cells, respectively (the bins in the presented diagram include the hit entries of two cells each; therefore the discontinuities in the diagram, which indicate the dead cells, have about a half of the entries from the adjacent bins). The event occupancy (right) shows the distribution of the number of hits per event. It has its maximum at 4 cells which are hit by the detected muon.

Noise definitions

As noise we define any signal generated in the cell or at the connection lines which is not caused by drifting electrons from gas ionization by transition of a muon, or such drift time signals from muon events which are not confirmed by any trigger (see also Section 4.4.2, page 80). This phenomenon, mostly caused by system electronics can in general not be distinguished from the "right hits". However, Figure 4.16 shows that one can recognize a time interval before the drift time box, where all registered hits should have a noise origin. Furthermore, it is observed that the noise hits are uniformly distributed over the entire time window, if the measurement time was long enough.

Qualitatively one can determine a cell to be or not to be "noisy" by comparing the number of hits in this cell with the number of hits in the adjacent cells during the same time, e.g. during the entire DAQ run. For detailed investigations a more exact measure characterizing the noise effects is required. Thus, for a DAQ run the absolute number of noise hits N_{noise} within a time window t (i.e. generally all noise hits on the left side of the drift time box like the example presented in Figure 4.16, $t \simeq 55100$ ns), should be "normalized" to the total number of events N_{events} (due to the fact, that all hits, including the noise, are registered during a very short time window, opened whenever for a trigger signal). This *noise rate per event*

$$f_{noise} = \frac{N_{noise}}{t \cdot N_{events}}, \quad (4.2)$$

measured in Hz, is independent of the different run durations and trigger rates, and can be used for further analysis. Based on earlier experiences, the cell performance is acceptable when $f_{noise} \simeq 30\text{--}40$ Hz.

4.4. Tests of the local DAQ system

To investigate the quality of the data transfer and to understand some unexpected properties (and, if possible, to eliminate or to use them) of the data taking processes some tests of the CMS DT muon chamber DAQ systems were done. These tests could be performed on a dedicated chamber, not installed in the CMS detector. The tests results can lead to possible re-adjustment and re-configuration of the local DAQ electronics, which can even be performed on the working chambers in the CMS detector during the LHC runs.

4.4.1. Comparison of two different DAQ systems

The functionality of the CMS DT muon chambers was tested with different DAQ systems. As mentioned in Chapter 4.3.1, during the production period in Aachen, chambers were tested with a test facility constructed especially for a direct functionality check and for the analysis of drift times. Before the final MiniCrates (MC, see Section 4.2.2) became available, each of the collaboration chamber assembly centers (Madrid, Legnaro, Turin and Aachen) has developed and used its own set for testing the muon chambers. The MC, as final local DAQ system for the drift time digitization, differs in features like time to digital conversion, data transfer mechanism, trigger response etc. A direct comparison of two DAQ systems – MC on the one hand (MC-DAQ) and e.g. Aachen test DAQ (AC-DAQ) on the other hand – by *simultaneous* recording of the *same* data can provide useful information about their efficiency, measurement precision etc.

Test procedure

For this tests a hardware unit, called *Splitter Board* (SB), was developed, constructed (H. Szczesny, RWTH Aachen) and used at the Aachen test facility (Figure 4.18). Its working principle is simple: the incoming LVDS chamber signals from front-end boards (FEB) are fanned out to three LVDS lines by a low-voltage differential driver (MC100EP210S [73]). Two of them end directly as LVDS output boxes. They can be directly connected to the MC-DAQ, or – via a converter board LVDS/ECL (see Section 4.3.3) – to the AC-DAQ. The third line has implemented a mini LVDS/ECL converter (including an MC100EL91 translator [74] and an MC100EP116 receiver [75]) on the SB, so that this output can be connected directly to the AC-DAQ. In this case no external LVDS/ECL converter is needed.

The SB is a prototype; due to the material costs and developing efforts it was decided to have only a small device for test activities. Therefore only 16 cells of one SL can be connected to the input of the SB. The SB was then mounted directly on the MC for the chamber MB1 002 (002 is the chamber ID) in the Aachen test facility.

Before the start of data taking, the SB input was connected to FEB 9 or FEB 8 of SL PHI 2, chamber MB1 002 at Aachen test facility. The used SB outputs were both LVDS connectors (see Figure 4.18): one directly to the MC-DAQ, and one via an external LVDS/ECL converter to the AC-DAQ. Also the chamber voltages (electrodes and threshold) were set differently for each run to obtain the DAQ quality under diverse voltage parameters (see below). Using cosmic muons (scintillator plates) a trigger rate up to 100 Hz was available. The trigger signal passed at first the AC-DAQ and was subsequently sent to the MC-DAQ. This method was chosen due to the unequal trigger acceptance of both DAQ systems (trigger rate about 100 Hz by MC-DAQ and about 40 Hz by AC-DAQ). The list of runs, the run parameters and the run duration is presented in Table 4.2.

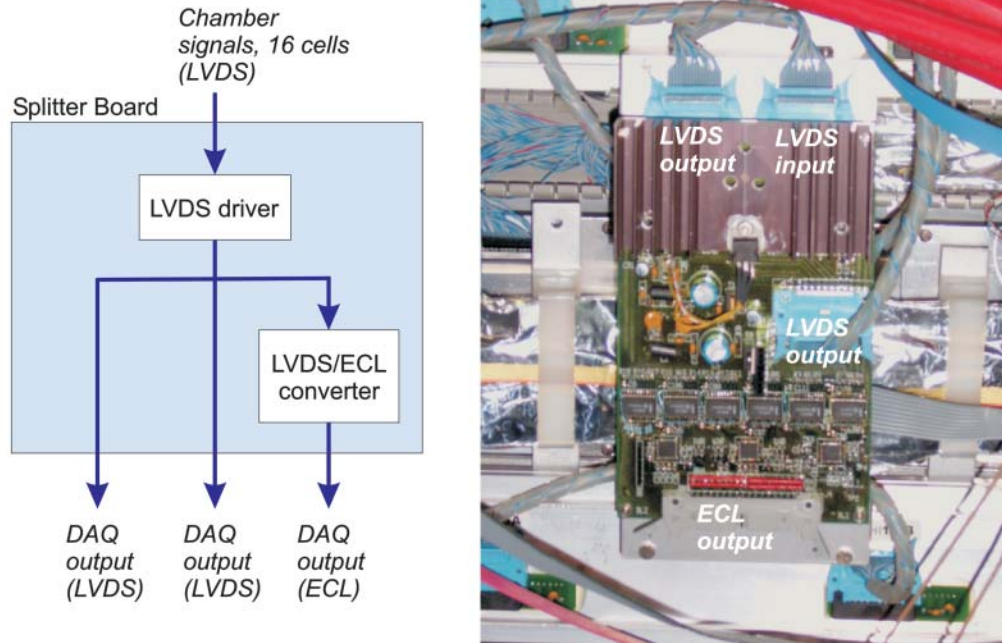


Figure 4.18.: On the Splitter Board (SB) the incoming LVDS chamber signals are branched out in three lines, two LVDS and one ECL. It is therefore possible to connect up to three different DAQ systems to its outputs and take the same FE data by these independent DAQ systems simultaneously.

Run number	Threshold	Voltage cathode	Voltage anode	FEB	Run duration
2006-11-13	+0.015 V	-1200 V	+3600 V	9	3h 18m
2006-12-20	+0.010 V	0 V	0 V	9	23h 34m
2007-02-02	+0.010 V	-1200 V	+3600 V	9	2d 19h 26m
2007-02-05	+0.020 V	-1200 V	+3600 V	9	1d 23h 56m
2007-04-11	+0.015 V	-1200 V	+3600 V	8	21h 57m

Table 4.2.: List of runs with different parameter sets and run duration for simultaneous data taking by the two different DAQ systems.

The read-out software was one of the *Read_out_ROS-8_ac_*.vi* series, the MiniCrate TDCs were default configured (software *MiniCrate_MBI_TDC_configuration_setup_ac*.vi*, configuration file with reject latency, search window and trigger latency 4095×25 ns); see Section 4.2.2 and Appendix A. The trigger signal was delayed by $20 \mu\text{s}$ to obtain the drift time box for both DAQ systems roughly in the same position within the registered drift time spectrum.

The runs were started in the following order: first MC-DAQ (awaiting trigger signals), then immediately the AC-DAQ. The data were taken during one to two days, then AC-DAQ was stopped, followed by MC-DAQ stop. Two binary output files, one for each DAQ system,

4. Data taking with the CMS DT muon chambers

were written in the usual data format. They were converted into two root files, then the root histories as two text files containing all interesting data (drift times, cell hits, trigger counts etc.) were created. The complete comparison of AC-DAQ and MC-DAQ is then executed by means of a *Perl* software, *DAQ_AC_MC_analysis.pl*, specifically developed for this kind of analysis.

To obtain a quality measure for comparison of both systems AC-DAQ and MC-DAQ, the following tests were done:

1. **Trigger counts:** If both DAQ systems work well, they "see" the same events, i.e. the same muons passing the chamber. The total number of registered triggers has to be equal for AC-DAQ and MC-DAQ which count them independently.
2. **Hits per event and number of hits per cell:** Each event, which is simultaneously and independently registered by AC-DAQ and MC-DAQ, must generate the same amount of hits for each cell.
3. **Drift times:** In one event, in the same cell the hits induce electron drifts with times measured simultaneously and independently by AC-DAQ and MC-DAQ. These times should be equal for both DAQ systems within a small tolerance for both systems (1 ns for AC-DAQ and about 0.8 ns for MC-DAQ).

DAQ data synchronization

Due to the fact that each DAQ system uses a different trigger delay and a different time window, the position of the registered hits is not the same in the drift time spectrum diagrams. Thus, before comparing DAQ systems, it was necessary to synchronize the data of the AC-DAQ and MC-DAQ represented in the respective diagrams. The procedure is simple and consists of the following steps (Figure 4.19):

1. Convert all registered drift times into one common time unit, e.g. 1 ns per bin (due to different TDC resolutions used).
2. Find in each diagram the lowest and the highest time bin (t_{\min}^{AC} , t_{\min}^{MC} and t_{\max}^{AC} , t_{\max}^{MC} , respectively, as well as one characteristic point easy to identify and common for both spectra, e.g. the time bin with the maximal number of registered hits, $t_{N_{\max}}^{\text{AC}}$ and $t_{N_{\max}}^{\text{MC}}$.
3. Align both diagrams matching both maximal hit bins $t_{N_{\max}}^{\text{AC}} = t_{N_{\max}}^{\text{MC}} = t_{N_{\max}}$.
4. "Cut" the diagrams at common points t_{\min} and t_{\max} , with the relations

$$\begin{aligned} t_{\min} &= \max(t_{\min}^{\text{AC}}, t_{\min}^{\text{MC}}) \\ t_{\max} &= \min(t_{\max}^{\text{AC}}, t_{\max}^{\text{MC}}). \end{aligned} \tag{4.3}$$

In all five runs t_{\min} was equal to zero and t_{\max} about 26 μs . The values t_{\min} and t_{\max} are then recalculated into the previous TDC resolution units. The hits of both DAQ systems in between these limits are then used for comparison analysis.

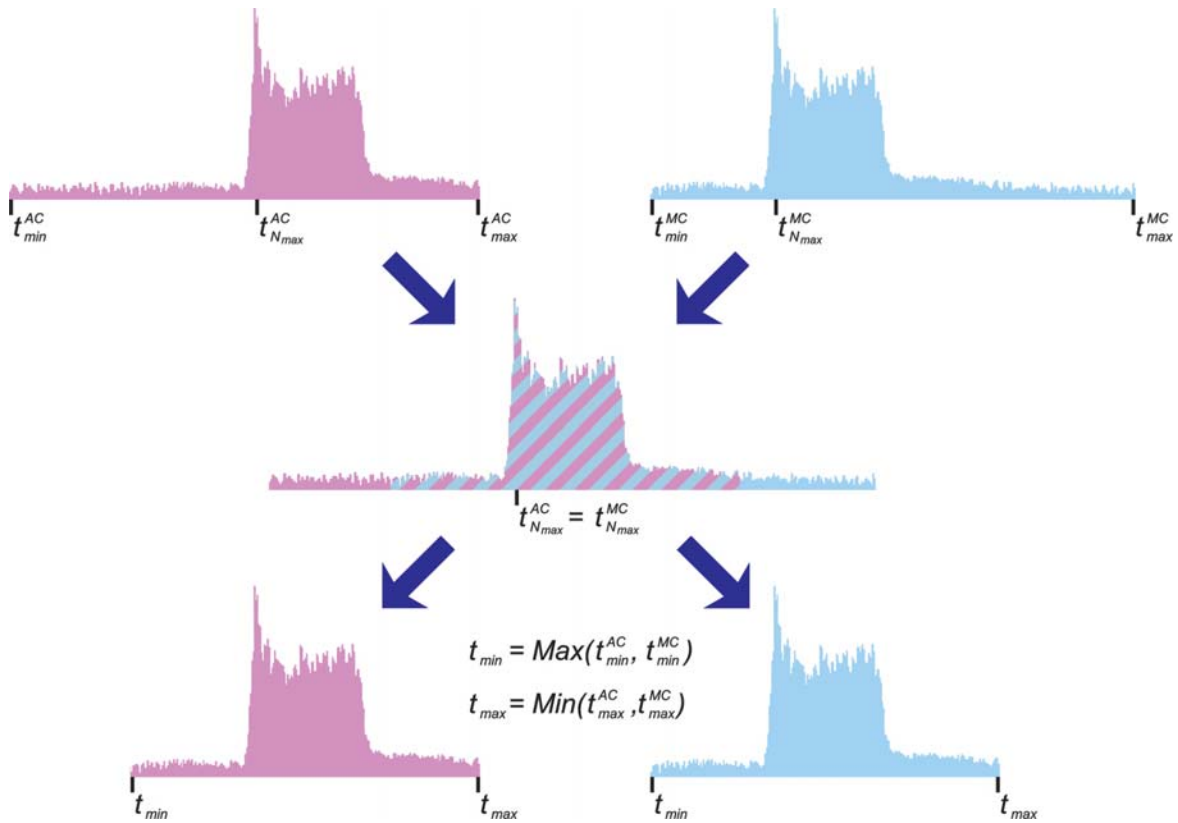


Figure 4.19.: The data of a large number of events, registered by both DAQ systems, must be aligned before analysis. This is achieved by matching a common characteristic point, e.g. the diagram bin with the maximal number of hits $t_{N_{max}}$. The data from both systems are then within the resulting interval $[t_{min}, t_{max}]$.

Event statistics

For the comparison of both DAQ systems five runs were taken (see Table 4.2). The event statistics of these runs is presented in Table 4.3. For the sake of clarity the columns were numbered. In the columns 2 and 3 there are the total event numbers, registered directly from the common trigger system by AC-DAQ and MC-DAQ, independently. The columns 4 and 5 include the total number of events, when for a trigger signal at least one of the 16 cells sent a hit registered by AC-DAQ and/or MC-DAQ. The next column (6) represents the total event numbers, registered by both DAQ systems in common, by matching the event ID. The entries in the column 7 represent the number of the same SB events registered in common by AC-DAQ and MC-DAQ, but with a different number of hits in event registered by different DAQ system. Finally, the last column (8) includes the number of the same SB events registered in common by AC-DAQ and MC-DAQ, with the same number of hits in the events, but these hits are registered for different cells by the different DAQ systems.

As mentioned before, the DAQ runs had different lengths in time (see Table 4.2). Therefore, to obtain a better overview for the run performance, it is recommended to regard the relative event statistics, i.e. the same information as in Table 4.3 but calculated as a ratio (in %) with respect to the total number of events being a proper reference, as shown in Table 4.3. For the columns 2 and 3 the entries are the total number of events registered by each DAQ system with respect to the average value of them. The number of the SB events (column 4 and 5 in

4. Data taking with the CMS DT muon chambers

Run	Event statistics						
	Trigger event count		SB event count		Identical SB events	Id. SB events, diff. hit number	Id. SB ev., diff. cells
	AC-DAQ	MC-DAQ	AC-DAQ	MC-DAQ			
1	2	3	4	5	6	7	8
2006-11-13	501202	501203	74104	74054	74045	18	0
2006-12-20	2106338	2105328	93864	92776	6245	2963	0
2007-02-02	5039936	5039958	446520	446558	427094	33872	0
2007-02-05	3798722	3788082	45945	52595	45928	4482	0
2007-04-11	2243776	2271506	29986	30335	29971	281	0

Table 4.3.: Event statistics for runs taken simultaneously and independently by two DAQ systems. If both systems work ideally the entries for the same run in the columns 4, 5 and 6 should have the same values and in the columns 7 and 8 should have zero entries.

Table 4.3) are presented with respect to the total number of events (columns 2 and 3). The number of identical events (column 6) registered by both DAQ systems is shown with respect to the average of both SB event numbers (columns 4 and 5). The ratio of identical events with different hit number and different cells (columns 7 and 8, respectively) is presented with respect to the total number of identical events (column 6).

Run	Relative event statistics, in %						
	Trigger event count		SB event count		Identical SB events	Id. SB events, diff. hit number	Id. SB ev., diff. cells
	AC-DAQ	MC-DAQ	AC-DAQ	MC-DAQ			
1	2	3	4	5	6	7	8
2006-11-13	100.0	100.0	14.8	14.8	100.0	0.0	0.0
2006-12-20	100.0	100.0	4.5	4.4	6.7	47.4	0.0
2007-02-02	100.0	100.0	8.9	8.9	95.6	7.9	0.0
2007-02-05	100.1	99.9	1.2	1.4	93.2	9.8	0.0
2007-04-11	99.4	100.6	1.3	1.3	99.4	0.9	0.0

Table 4.4.: Relative event statistics for runs taken simultaneously and independently by two DAQ systems. The data from the Table 4.3 are here presented with respect to the total number of events (columns 4 and 5), to the average of the SB event count from both DAQ systems (column 6) and to the total number of identical events (columns 7 and 8).

In addition Table 4.5 presents the calculated event rates (in Hz). The entries in the columns 2 and 3 represent the total trigger rate for the entire chamber, the entries in the columns 4 and 5 represent the trigger rate registered only for the 16 cells connected to the SB. The columns 6, 7 and 8 include rates of the selected events matching the criteria described above

Regarding the entries in Tables 4.3, 4.4 and 4.5 one can find:

- **For the columns 2 and 3:** If both AC-DAQ and MC-DAQ work well, the entries in both columns should be the same for the same run, due to the fact that each trigger signal has to be registered by the DAQ systems, even if a muon passing the SL causes no cell hits. Regarding the values, one can see a very good accordance in the entries

Run	Relative event statistics, in Hz						
	Trigger event count		SB event count		Identical SB events	Id. SB events, diff. hit number	Id. SB ev., diff. cells
	AC-DAQ	MC-DAQ	AC-DAQ	MC-DAQ			
1	2	3	4	5	6	7	8
2006-11-13	42.19	42.19	6.24	6.23	6.23	0.00	0.00
2006-12-20	24.83	24.82	1.11	1.09	0.07	0.03	0.00
2007-02-02	20.76	20.76	1.84	1.84	1.76	0.14	0.00
2007-02-05	22.01	21.95	0.27	0.30	0.27	0.03	0.00
2007-04-11	28.40	28.75	0.38	0.38	0.38	0.00	0.00

Table 4.5.: Event rates for runs taken simultaneously and independently by two DAQ systems. The data from the Table 4.3 are here presented with respect to the total run duration.

for runs 2006-11-13 and 2007-02-02 (event number difference $< 0.001\%$). Also the runs 2006-12-20 and 2007-02-05 show very small differences between the counted events, which are about 0.005% and 0.3% , respectively. The last run, most problematic of all, shows a difference of about 1.2% . Although the differences between the total trigger numbers counted by both DAQ systems in all runs are small, one would expect a better agreement, at least as for the first and third run. The SB event counts are much smaller than the trigger event counts, since only 16 cells are read out.

- **For the columns 4 and 5:** One realizes at first that the number of the SB events measured in common (i.e. with the same event ID) by AC-DAQ and MC-DAQ is approximately equal in each run for each DAQ system, but the relative event number with respect to all events registered by a given DAQ system varies from run to run.
- **For the column 6:** Here (total number of SB events measured separately by both DAQ systems) one can recognize again a good agreement in the data of run 2006-11-13 (event number difference about 0.07%). The next run 2006-12-20 (noise run, HV = 0 V) shows a big difference in the number of identical events. The relative number of identical events registered independently by the two systems during the runs 2007-02-02 and 2007-02-05 is high (about 96% and 93% , respectively), although for the run 2007-02-05 the entries in the columns 4 and 5 make up only about 1% of the total event number in the columns 2 and 3. The last run has also a very high rate of the commonly registered events (over 99%), although with very low ratio SB events vs. total number of trigger (about 1%).
- **For the column 7:** The values filling this column are fully satisfying only in the first and in the last row.
- **For the column 8:** Finally the entries of the last column inform that there are no identical events with the same hit number but with hits occurred in different cells. This last information is important for further analyses: although the DAQ process is affected by factors which should be afterwards investigated, **one can select identical events registered separately by AC-DAQ and MC-DAQ with the same hit number per event. These hits belong to the same cells and represent drift times (excepting the noise hits) in the DAQ-specific data blocks.**

4. Data taking with the CMS DT muon chambers

The reasons for the mentioned discrepancies presented in Tables 4.3 and 4.4 are different. On the one hand, the software used for the offline DAQ data processing ignores the "empty events", i.e. the events which are indicated by a proper trigger signal but with no chamber cell signal(s). This trigger information is then rejected and not used for the DAQ statistics. This results in the slight difference between the total number of registered events by the AC-DAQ and MC-DAQ (columns 2 and 3) if the registered number of the empty events is not the same for both DAQ systems.

On the other hand, the question, why the relative event numbers (columns 4 and 5) differ from run to run can be explained by the "missing events". However, it would be better to compare both systems by considering the real chronological process of each run, but unfortunately neither in the AC-DAQ nor in the MC-DAQ software a time-stamp was implemented in the data blocks. Instead one can analyze the event ID, which is attached to each event data block (see Appendix A.3) of the MC-DAQ. This MC-DAQ event ID is a 12 bit integer with an overflow following the value 4095. Nevertheless, if every event was registered and, which is more important, stored in all active ROS FIFOs (Section 4.2.3), there should have been a continuous event ID increment by 1 (overflow taken into account) for each next event data block in the DAQ data. Missing events are indicated by a non-continuous ID counting in the processed data. The observed number of the missing events for each run is presented in Table 4.6. The real number of missing events can be greater than the observed one by addition of a value $n \cdot 4096$, where n is the number of the overflows which cannot be estimated on the basis of the existing data. Unfortunately, it is not possible to obtain any information about the missing events from the AC-DAQ data, since the event ID assignment in the AC-DAQ data is made only during the offline data processing.

Run	Total number of events	Number (min) of missing events
2006-11-13	501203	0
2006-12-20	2105328	8218
2007-02-02	5039958	1
2007-02-05	3788082	3380
2007-04-11	2271506	275015

Table 4.6.: List of observed missing events in each run registered by the MC-DAQ system.

Therefore a quantitative analysis of the missing events' influence on the event statistics is not possible. For example, a view of the entries in all Tables can confirm the good quality of the first run 2006-11-13. Consequently, one can conclude, that **the events missing in the given runs can be treated as origin for the difference in the number of events between the two used DAQ systems.** In Section 4.4.2 on page 89 this phenomenon of missing events is described more explicitly. It is shown there that this behavior depends on the noise rate in the DAQ systems.

Hits in events and cell occupancy analysis

For the comparison of both DAQ systems then the hit number in a given event was analyzed. Therefore only events registered by both systems (Table 4.3 and Table 4.4, column 6) were considered. As measure for the analysis the hit difference

$$\Delta N_{hit} = N_{hit}^{MC} - N_{hit}^{AC} \quad (4.4)$$

for each registered event is used. N_{hit}^{MC} and N_{hit}^{AC} are the number of the hits in the same event which are registered by MC-DAQ and AC-DAQ, respectively. The analysis results are presented in Table 4.7.

Run	$\bar{\Delta}N_{hit}$	$\sigma_{\Delta N_{hit}}$	ΔN_{hit_min}	ΔN_{hit_max}
2006-11-13	0.00	0.03	-5	3
2006-12-20	-0.04	2.05	-16	12
2007-02-02	0.19	1.74	-31	35
2007-02-05	0.86	2.83	-1	28
2007-04-11	0.04	0.43	-1	11

Table 4.7.: Results of the analysis of the hits-in-event statistics. As measure the hit number difference according to Equation 4.4 for each event was chosen.

The mean value of the ΔN_{hit} distributions (aside from the run 2007-02-05) is about zero. But, the standard deviation (or RMS) is apparently non-zero. This, and also the asymmetrical position of maximal and minimal values in the last two runs, indicates – as mentioned before – an instable behavior of one DAQ system at least. Figure 4.20 shows the evolution of ΔN_{hit} with the irregularly progressing event ID for all five runs. These five charts can also be roughly treated as run time evolution. The structural changes in the diagram (i.e. ΔN_{hit} vs. event ID or time, also during one DAQ run) show an evident influence of the DAQ systems on the taken data. However, the averaged ΔN_{hit} for all 541667 events processed and all runs

$$\bar{\Delta}N_{all_hits} = 0.21, \sigma_{\bar{\Delta}N_{all_hits}} = 1.72$$

is relatively small, but the fluctuation (standard deviation) is too high, so that for further analysis only the events with the same hit number (93% of all events processed)¹⁴ must be selected.

To investigate the obvious noise influence the cell noise occupancy, i.e. the occupancy of the hits on the left side of the time-box in the drift time distribution (the noise hits, see Figure 4.16), is analyzed, which was independently registered by AC-DAQ and MC-DAQ. If the noise source is the chamber itself, both DAQ systems must register the same total number of noise hits occurring at the same cell. For a better comparison, the absolute noise rate f (Equation 4.2) is more suitable. So the difference

$$\Delta f_{noise_cell} = f_{noise_cell}^{MC} - f_{noise_cell}^{AC} \quad (4.5)$$

for each cell during the entire run is a measure of noise that is not produced in the chamber itself. $f_{noise_cell}^{MC}$ and $f_{noise_cell}^{AC}$ are the rates of the noise hits in the entire run registered by

¹⁴Due to a limited resolution of the plots in Figure 4.20 the distribution appear as though the most of the events had $\Delta N_{hit} \neq 0$. This is an illusion, the non-zero hit difference per event occurs rarely.

4. Data taking with the CMS DT muon chambers

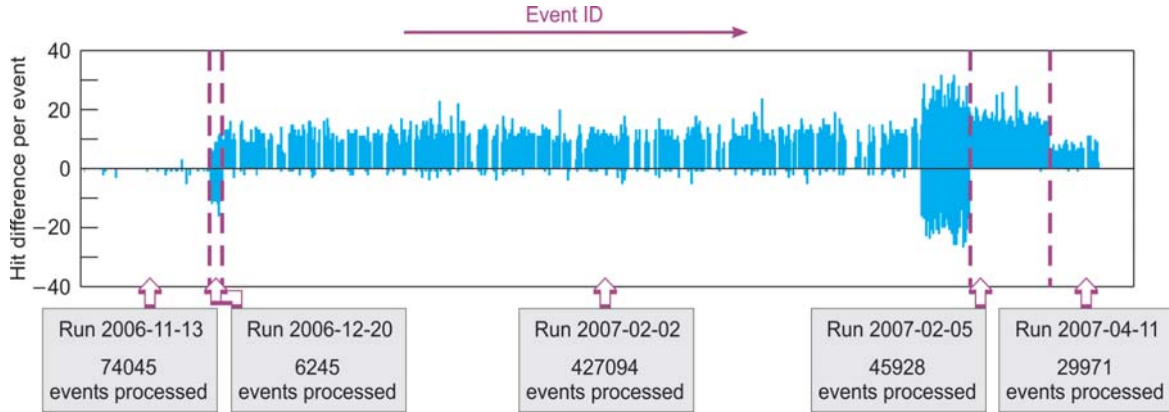


Figure 4.20.: The evolution of ΔN_{hit} with progressing event ID for all runs. One can recognize the irregular and asymmetric distribution, even during one run (2007-02-02). However, the average ΔN_{all_hits} is small, but the standard deviation is high (about 1.7).

MC-DAQ and AC-DAQ, respectively. Figure 4.21 represents the absolute value of Δf_{noise_cell} for hits from the noise area of the drift time spectrum (Figure 4.16) from the 16 cells of the FEB connected to both DAQ systems. One can see that only the first "good" run shows a good agreement for the noise hit measurement (Δf_{noise_cell} is about or below 0.1 Hz for each cell). The noise rate differences in the remaining runs are larger and can reach 230 Hz (cell 140, run 2006-12-20).

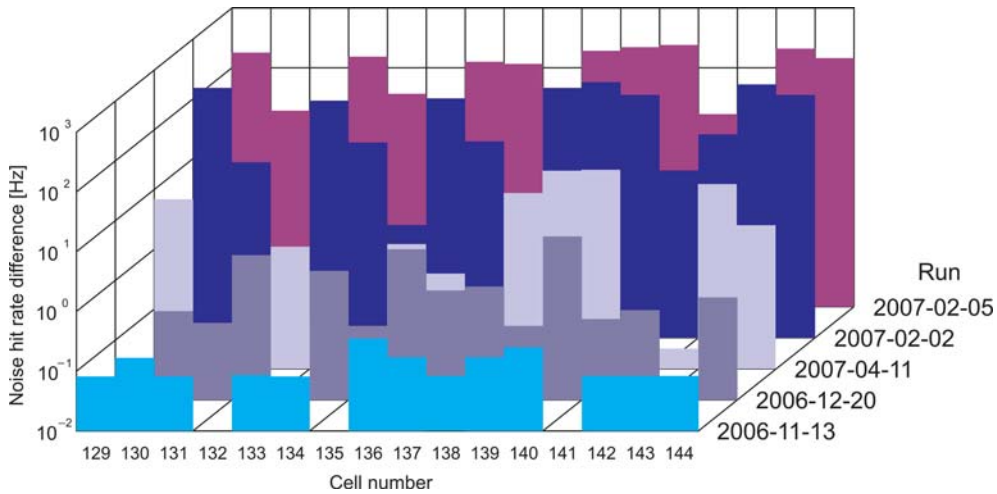


Figure 4.21.: Difference between cell noise rate at all 16 cells connected to one FEB and registered by two different DAQ systems. While the cells show no significant differences in the calculated noise rate during run 2006-11-13, the differences during the other runs are larger and reach 230 Hz (run 2007-02-05). This behavior indicates a noise source rather at the DAQ systems themselves than inside the chamber.

In Figure 4.22 the cell noise rate of the last two runs 2007-02-05 and 2007-04-11 is presented. These runs are particularly interesting due to the fact, that the SB was connected to different FEBs (and thus also to different cells). As one can recognize, in both runs both DAQ systems "see" a very noisy 8th cell (i.e. cell 136 for FEB 9 and cell 120 for FEB 8), which is also

observed by the other three runs. Moreover, the shape of the cell noise rate (especially the spikes at 8th and 12th cell) for AC-DAQ is almost the same as the one of the MC-DAQ. The MC-DAQ sees the noisy channels 8 and 12 but also a higher noise rate in the remaining cell channels (run 2007-02-05). Compared with run 2007-04-11 one can recognize the same step-like structure for the 10th, 11th and 12th channels, corresponding to the cells 138, 139, 140 (run 2007-02-05) and 122, 123, 124 (run 2007-04-11).

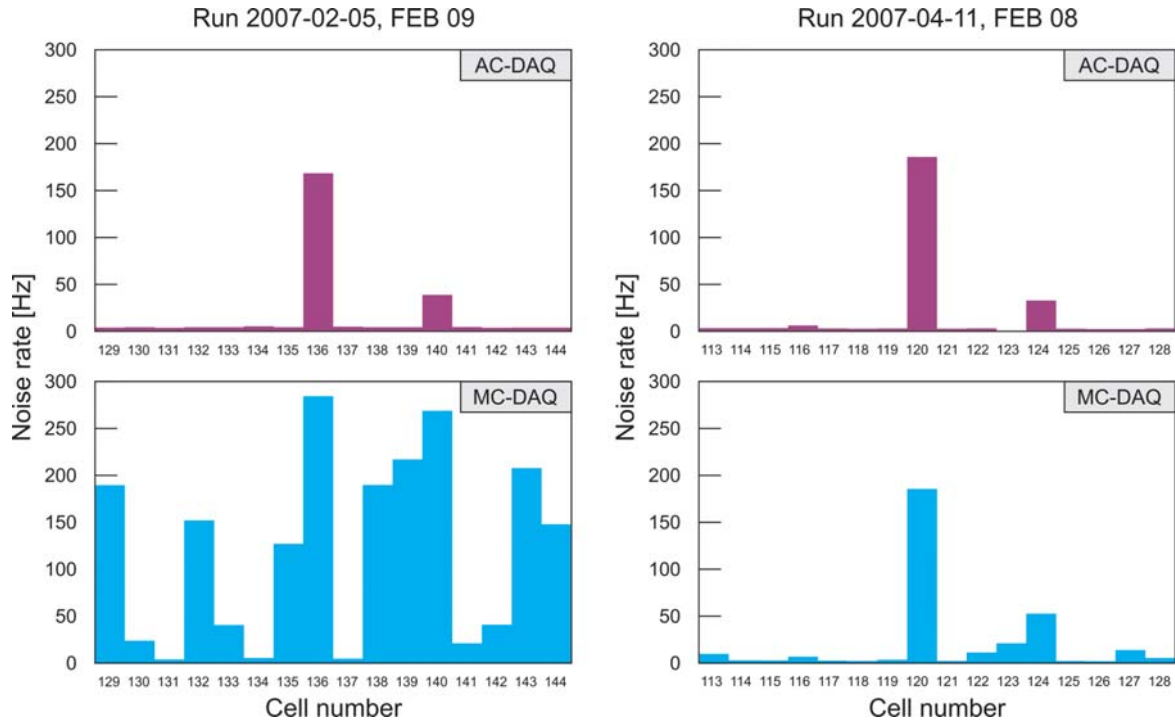


Figure 4.22.: Cell noise rate for the runs 2007-02-05 and 2007-04-11 with connected FEB 9 (cells 129-144) and FEB 8 (cells 113-128), respectively, and registered independently by two DAQ systems. There are the same noisy channels in both DAQ systems for both FEBs.

Regarding the plots in Figure 4.21 and 4.22 one can conclude that the SB itself produces noise. These disturbing signals occur at the common cell channels (evident is the noise at the 8th and 12th channels during all five runs). The noise rate in these channels is higher than in the other ones even after the FEB swap, and the cell noise rates are similar, independently of the connected FEB. The observed slightly higher noise rate (which is also manifest in the higher hit-per-event cell occupancy) registered by MC-DAQ is rather caused by the SB split signal lines, since in "good" runs with no significant noise both systems work well (see Figure 4.20 and 4.21). Such a disturbing feature occurring from time to time is observed only when the SB is in use. Therefore **the differences between the total number of hits per event and between the noise rate is not caused by a possible TDC mechanism, DAQ data transfer and/or storage procedure. The DAQ quality is thereby not affected.**

Analysis of drift times

The final test for both systems, AC-DAQ and MC-DAQ, compares the electron drift times for cosmic muon events. The drift times are digitized by these independent DAQ systems,

4. Data taking with the CMS DT muon chambers

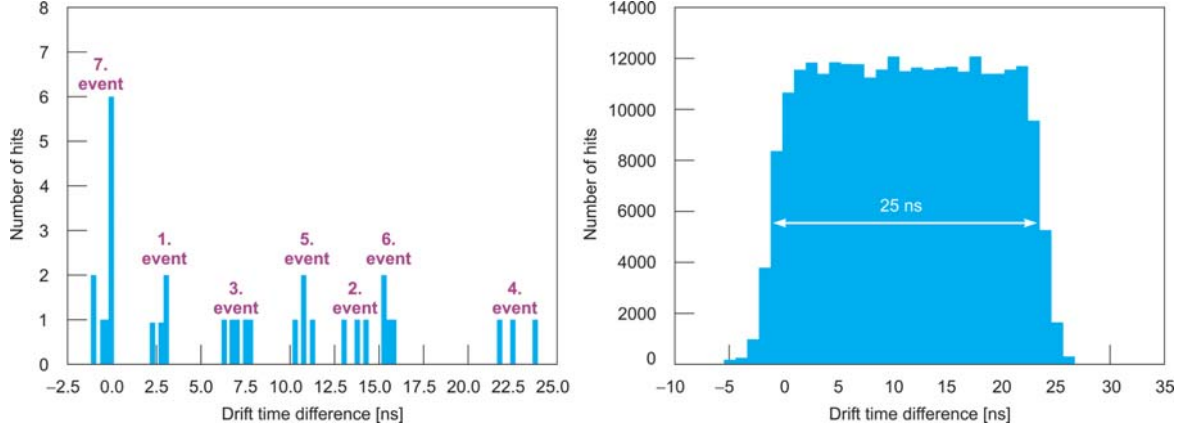


Figure 4.23.: Left: The calculated drift time differences measured for the first seven events of the run 2006-11-13. The drift time differences from hits belonging to an event are all grouped within very small time intervals of about 2 ns and these groups are all placed within a larger interval of about 10 to 20 ns. Right: The drift time differences of all hits of the entire run are flat distributed with a width of 25 ns.

with respect to a common trigger signal. If both systems work properly, the same drift time values should be measured by each DAQ system.

To perform a drift time analysis at first the "right" events must be selected. As shown above, the SB produces noise which results in events with different hit numbers. Also events with the same number of hits per event but in different cells must be eliminated. Furthermore, the analysis should not contain events of run 2006-12-20. This run was a special noise run, all chamber HV was switched off; thus no signals from drifting electrons are expected. In addition, we observed, that there were some peculiar events in all runs with an enormous number of hits (recorded by both systems) occurring in all cells (up to 41 hits in run 2007-02-02). These events (0.5% of total amount) were obviously caused rather by noise than by drifted electrons, so they were also eliminated for the analysis.

A direct comparison of the same drift times measured independently by the AC-DAQ and MC-DAQ is not possible. The trigger time resolution of the MC-DAQ is the clock period of 25 ns (Section 4.3.3). Only the AC-DAQ trigger mechanism allows to set the event time mark with the resolution of 1 ns (Section 4.3.2). This means, that the difference of the drift times from the same hit but measured by these two DAQ systems differs up to 25 ns. Figure 4.23 left shows the calculated drift time differences measured for the first seven events of the run 2006-11-13. As expected, the drift time differences from hits belonging to an event are all grouped within very small time intervals of about 2 ns and these groups are all placed within a larger interval of about 25 ns. For all hits of the entire run one finds a flat distribution of the drift time differences with a width of 25 ns (Figure 4.23 right).

Quantitatively the drift time analysis is therefore based on the comparison of the drift time differences of different hits from one event (similar to the mean time calculation, see Section 3.3.2). For each possible pair of different hits i, j ($i \neq j$) in the same event differences of their drift times t_i, t_j

$$\begin{aligned}\Delta t_{ij}^{\text{AC}} &= t_i^{\text{AC}} - t_j^{\text{AC}} \\ \Delta t_{ij}^{\text{MC}} &= t_i^{\text{MC}} - t_j^{\text{MC}},\end{aligned}\tag{4.6}$$

measured by AC-DAQ and MC-DAQ, respectively. The hits are labeled by cell number; for two and more hits in the same cell per event the hit identification for each DAQ system is guaranteed by a direct drift time comparison. Per event with n different hits, there are $\binom{n}{2} = \frac{n(n-1)}{2}$ pairs $\Delta t_{ij}^{\text{AC}}$ and $\Delta t_{ij}^{\text{MC}}$ constructed. Then the total difference

$$\Delta t_{ij} = \Delta t_{ij}^{\text{MC}} - \Delta t_{ij}^{\text{AC}} \quad (4.7)$$

is calculated.

This method is independent of the trigger latency, which is different for each DAQ system and can be different for each run for the MC-DAQ. Assuming, that all times are digitized with steps of about 1 ns (more precisely: 1 ns for AC-DAQ and 0.78125 ns for MC-DAQ) and the measurements were not correlated, the expected error of Δt_{ij} resulting only from digitization is about

$$\sigma_{\Delta t_{ij}}^{\text{dig}} = \sqrt{2} \cdot \sqrt{2} \cdot \frac{1 \text{ ns}}{\sqrt{12}} \simeq 0.6 \text{ ns}.$$

Table 4.8 presents the Δt_{ij} statistics of the four mentioned runs. The mean values of a large number of Δt_{ij} calculated for each run are about zero, however the standard deviations are greater than expected. Finally the statistics for all Δt_{ij} pairs from all four runs was calculated (Figure 4.24). The new average for Δt_{ij} is

$$\bar{\Delta t}_{ij_all} = 0.32 \text{ ns}, \quad \sigma_{\bar{\Delta t}_{ij_all}} = 1.55 \text{ ns}.$$

This value, although not exactly zero, is a satisfying result. However, the RMS is about 2.5 times greater than the expected one. It means that beyond of digitization also other factors (electronics, jitter etc.) play a role by affecting of the drift time measurement. Assuming that both DAQ systems contribute in equal measure to the error propagation, the average of a single drift time measurement has a true error of about 0.7 ns, independently of the used DAQ system. We call this *systematic error* σ_{sys} . The intrinsic drift time resolution in a cell is $\sigma_{DT} = 3.1 \text{ ns}$ [31]. Therefore the ratio

$$\sigma_{sys}^2 / \sigma_{DT}^2 = 0.05$$

is very small. Thus, **the digitization procedure does not affect the measured drift time precision.**

4.4.2. Noise analysis

The DAQ system of the CMS DT muon chambers is supposed to work reliably by digitizing and storing the drift time information of the cells hit by a muon traversing a chamber. These data should not be affected by any disturbing process, like e.g. noise production. Such unavoidable phenomena should therefore be known, in order to obtain information about its behavior and possible effects on the data taking and storage.

Although some analyses of the noise developing in the muon chambers were already done earlier, only a few DAQ runs were specifically performed to investigate the possible noise behavior [76]. Therefore a couple of runs were performed on the MB1 chamber in the Aachen test facility, which were dedicated to general noise studies. The results of these runs and their noise analysis are described in the present section.

4. Data taking with the CMS DT muon chambers

Run	$N_{\Delta t_{ij}}$	$\bar{\Delta t}_{ij}$ [ns]	$\sigma_{\Delta t_{ij}}$ [ns]
2006-11-13	493726	0.04	1.21
2007-02-02	3292277	0.36	2.03
2007-02-05	309625	0.11	1.24
2007-04-11	156286	0.10	1.21

Table 4.8.: Results of analysis for statistics of the TDC drift time differences. As measure the drift time difference calculated in accordance to Equation 4.7 for each possible drift time difference in registered hits of the same event was chosen.

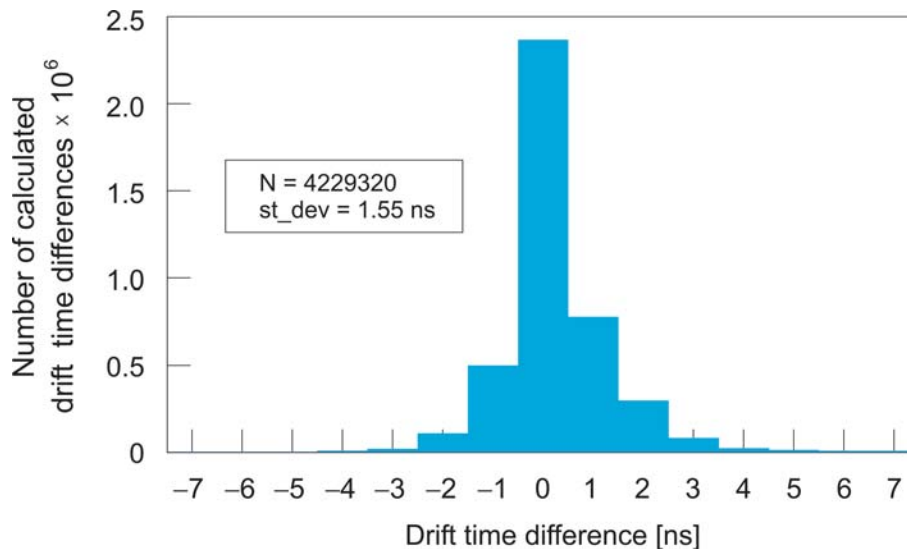


Figure 4.24.: Comparison of drift time differences measured by two different DAQ systems, in accordance to Equation 4.7. Both, the mean about zero and the standard deviation under 2 ns are satisfying results.

For the following noise study of a group of cells, i.e. for a FEB or SL, only cells with a noise rate within the interval $[\frac{1}{2}\bar{f}_{noise}, \frac{3}{2}\bar{f}_{noise}]$ are considered. This provision must be done to eliminate cells with the zero noise rate ("dead cells"), as well as the "noisy cells", whose noise rate can be higher by a factor 10^6 compared to other cells. Such values would falsify the following analysis of noise by studying its dependence of various parameters set.

Chamber HV and noise

Different kinds of noise can come from various sources, like for example on the contact surface at the connectors or being a result of a thermal fluctuation in the circuits (electronic noise). For the CMS DT muon chambers two additional noise effects (chamber noise) are important. On the one hand, microscopic dust particles adhere to the surface of the cells' electrodes, which are an undesirable but also unavoidable by-product of the chamber production. These particles are then gradually removed after the HV is supplied. On the other hand the supplied HV is not exactly constant, small deviation of the nominal value are always present. These signals are filtered out only on the HV distribution board inside the chamber,

but not directly at the HV connector on the SL cover, so that this distortion is transferred to the "antenna" anode wire inside the chamber [77]. In the muon chambers such noise generation can be directly correlated with the applied electrode voltage and should depend on the electrode length (i.e. cell length).

Also a part of the noise hits seen before the time box in Figure 4.16 can be caused by cosmic muons¹⁵. The particle (muon) flux ϕ in the hall of the Phys Inst. III. A is about $170 \text{ m}^{-2}\text{s}^{-1}$ [78]. Thus the tested MB1 chamber with its surface of about 4 m^2 experiences a muon rate of about 700 Hz. The trigger rate for a chamber under normal conditions (HV) "seen" by the test stand electronics and registered by the read-out software is only 30–40 Hz. Therefore a huge part of cosmic hits is not recognized as muon events, but rather as noise with a rate of 660–670 Hz. Concerning the fact that the number of the cells in a layer is about 50, the noise rate per cell is about 13 Hz, assuming a muon flux vertical to the chamber surface only. Regarding also inclined muons, this rate must be corrected by a factor 1.5:

$$\bar{f}_{\text{cosmic_noise}} \simeq 20 \text{ Hz.}$$

A couple of MC-DAQ runs were dedicated to study the noise in dependence on the electrode HV. The runs, each with 1 million events, were performed by different anode HV U_{anode} and cathode HV U_{cathode} ; the field forming strips HV U_{strips} were nominally set to +1800 V for all runs. The variation of U_{anode} and U_{cathode} should occur about their nominal values (+3600 V for U_{anode} and -1200 V for U_{cathode}) to ensure a correct functioning of the chambers during the run and to avoid a possible damage by a too high potential difference between anode and cathode. After all, the following HV values were chosen as parameters for the DAQ runs¹⁶ (all runs at the nominal threshold $U_{\text{thr}} = 15 \text{ mV}$):

- 5 runs with U_{anode} varied: +3300 V, +3400 V, +3500 V, +3600 V and +3700 V; $U_{\text{cathode}} = -1200 \text{ V}$ and $U_{\text{strips}} = +1800 \text{ V}$ (both nominal for all 5 runs).
- 4 runs with U_{cathode} varied: -1100 V, -1200 V, -1300 V, and -1400 V; $U_{\text{anode}} = +3600 \text{ V}$ and $U_{\text{strips}} = +1800 \text{ V}$ (both nominal for all 4 runs).

Figure 4.25 presents the obtained average noise rates \bar{f}_{noise} per cell for each SL at varied U_{anode} (left) and U_{cathode} (right). One can recognize a roughly linear correlation between \bar{f}_{noise} and U_{anode} , however the noise seems to be not or very weakly correlated to U_{cathode} with a \bar{f}_{noise} minimum at $U_{\text{cathode}} = -1200 \text{ V}$. The noise rate is lower for the θ SL than at both ϕ SLs by a constant factor of about 0.85. This corresponds to the MB1 SL cell length l ratio $\frac{l_{\theta}}{l_{\phi}} = 0.86$. Qualitatively one can infer as expected, that **the noise is scalable with the chamber HV (anode) and corresponds to the chamber geometry (cell length)**. Under nominal HV only 1/3 of the noise has a non-cosmic origin.

Front End threshold and noise

The amplitudes of the noise analog signals are more different than the ones of the signals caused by charge avalanche from drifted electrons. This noise can therefore be limited by setting the right threshold directly at the FEBs (see Section 4.2.1), so that substantially all output digital pulses represent the electron drift times. Empirically, the threshold voltage U_{thr} set for proper DAQ is about 15–20 mV. For all DAQ test runs described in this thesis

¹⁵During the CMS operation just the cosmic hits are undesirable and treated as noise.

¹⁶Approximately in accordance to the HV limit set for the former HV consistence tests [41].

4. Data taking with the CMS DT muon chambers

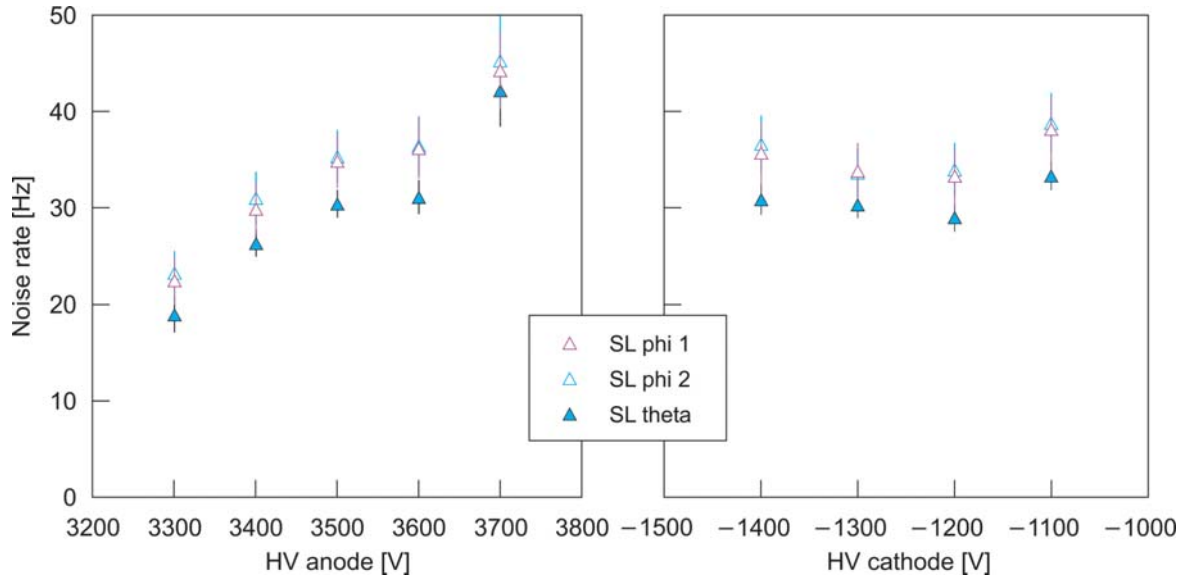


Figure 4.25.: Averaged noise rates per cell for varied anode HV and cathode HV for each SL, measured for a MB1 chamber. The noise increases with the higher anode HV, however no significant correlation between noise and cathode HV can be recognized. The noise on a θ SL is always lower by a factor of about 0.85 than on a ϕ SL, as expected, due to the different cell lengths in these two SL types.

$U_{thr} = 15$ mV (if threshold value is not mentioned explicitly). However, more precise information about the noise behavior in dependence on U_{thr} should be useful for understanding this kind of processes.

For this purpose several dedicated runs were performed with varying threshold. At the nominal electrode HV ($U_{anode} = +3600$ V, $U_{cathode} = -1200$ V and $U_{strips} = +1800$ V) 11 MC-DAQ runs with thresholds $U_{thr} = 5$ mV, 7 mV, 10 mV, 12 mV, 15 mV, 17 mV, 20 mV, 40 mV, 60 mV, 80 mV and 100 mV were performed. This parameter selection was preferred, due to a better investigation of the noise at $U_{thr} \leq 20$ mV (more steps in this range); usually at this threshold the CMS DT muon chambers are operated. All runs had 1 million events.

The average noise rates in dependence on the threshold are presented in Figure 4.26 (left: logarithmic scale for all U_{thr} ranges, right: linear scale for $U_{thr} > 10$ mV). One can recognize three significant ranges

- $U_{thr} \leq 10$ mV. The noise rate is very high, the magnitude is 10^2 – 10^5 Hz per cell.
- 10 mV $< U_{thr} \leq 20$ mV. The noise rate decreases with the increased threshold from about 40 Hz to about 30 Hz. **This range is chosen for the data taking.**
- $U_{thr} > 20$ mV. The noise remains low and is almost constant at about 30 Hz.

Also here one can see the expected differences in the noise rates for different SL types due to their different cell lengths.

Concerning the noise for each cell individually in the interesting threshold range of 10 mV $\leq U_{thr} \leq 100$ mV one can see a similar behavior as the measured SL average. As example f_{noise} in dependence on U_{thr} is shown in Figure 4.27, representatively for all cells of the outer ϕ SL (phi 2). One can recognize the same drop of f_{noise} for increasing U_{thr} as for the entire SL. However, the dead cells 44, 107, 166 as well as the noisy cell 81 are recognizable.

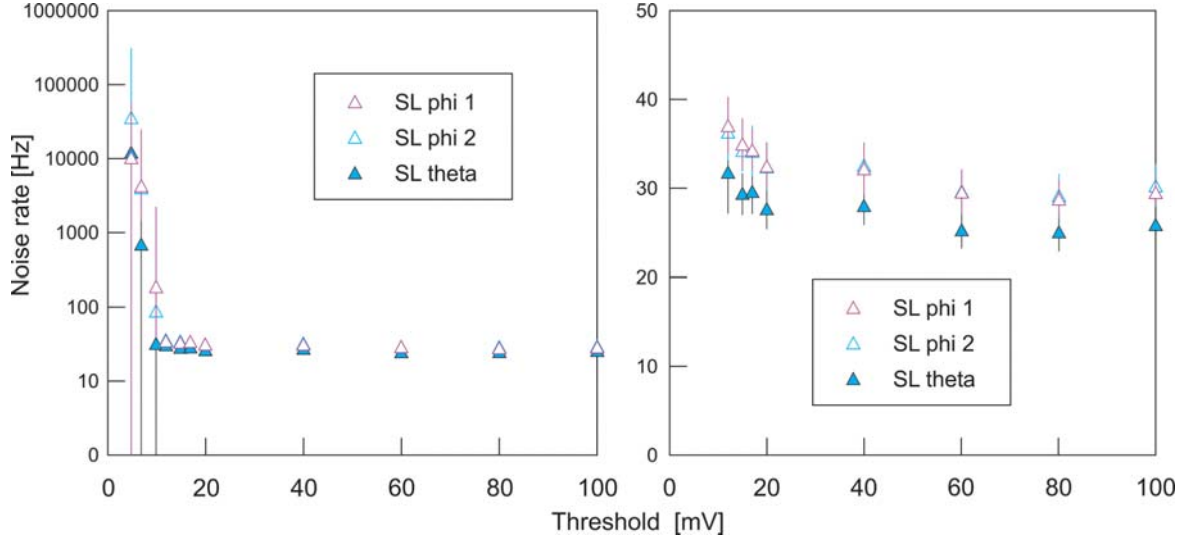


Figure 4.26.: Averaged noise rates per call in dependence on threshold, (left: logarithmic scale for all U_{thr} ranges, right: linear scale for $U_{thr} > 10$ mV). One can recognize very high noise rates up to 10^5 Hz for $U_{thr} \leq 10$ mV. For $U_{thr} > 10$ mV the noise rates are in the acceptable range of 30–40 Hz.

Another feature appearing in Figure 4.27 is the high f_{noise} at several outer cells. This concerns the three last cells 194, 195 and 196 of the SL phi 2 at $U_{thr} = 10$ mV and $U_{thr} = 12$ mV. This behavior is also observed earlier by the other two SLs (the other ϕ SL has also very noisy five first cells). This phenomenon was already observed and is explained by the proximity of the outer cells to the HV connector on the SL, because these cells are not sufficiently shielded from the outside influence (the HV connector is a non-metallic component part on the SL cover). As seen in the Figure 4.27, the noise rate for these cells drops to the usual values of about 30 Hz at higher threshold.

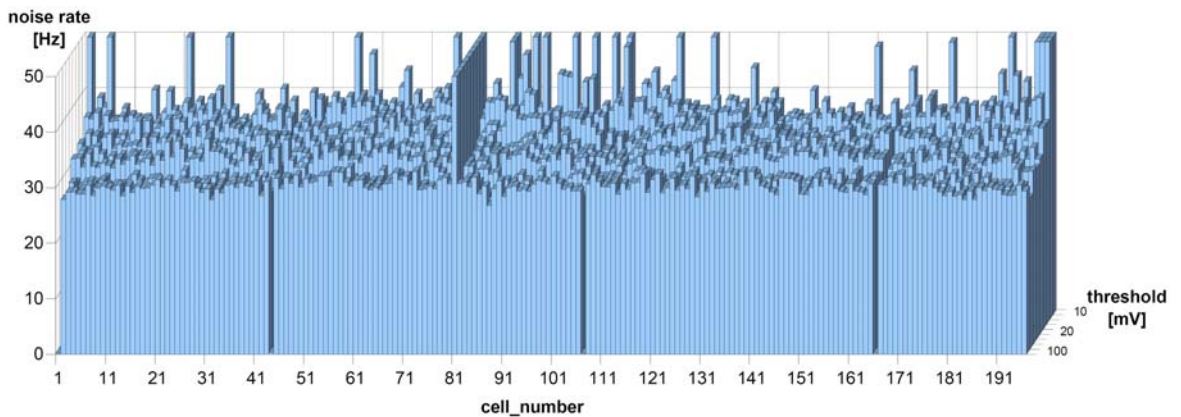


Figure 4.27.: The noise rates for each cell individually in dependence on the threshold for $10 \text{ mV} \leq U_{thr} \leq 100$ mV. The noise behavior of most cells corresponds to the SL average f_{noise} . Some outer cells (here cells 194, 195 and 196) show high f_{noise} due to their proximity to the HV connectors on the SL, because these cells are not sufficiently shielded from outside.

4. Data taking with the CMS DT muon chambers

For $U_{thr} = 7$ mV the individual cell noise rate f_{noise} is high, but its distribution over the entire SL is regular, although not as uniform as for $10 \text{ mV} \leq U_{thr} \leq 100$ mV, and shows no big variations. However, the f_{noise} distribution at $U_{thr} = 5$ mV shows an unexpected structure (Figure 4.28). At first appearance one can recognize a repetitive pattern in each 64 cells corresponding to the 64 read-out channels of a half ROB¹⁷, except the remaining 4 cells. Within a ROB one can then also see the noise occupancy coming from the four TDCs. The first 16 cells (TDC 0) registered the most noise hits, the next 16 cells (TDC 1) less than the first group and the remaining 32 cells (TDC 2 and TDC 3) registered almost no noise hits. The four last SL cells 193, 194, 195 and 196 are characterized by an enormous noise rate (see above). The noise hits from these cells had a large effect on the calculated f_{noise} , as presented in Figure 4.26 left. The θ SL noise distribution has no regular pattern.

An interpretation of these results can be found in the ROB read-out mechanism. It seems that at very high hit rate per event the FIFOs on the ROS-8, which are dedicated to store the data of the ROBs (see Section 4.2.3) lose a huge part of them. One expects the same noise rate f_{noise} of the ϕ SL cells as of the θ SL cells divided by a factor 0.85, but even the average f_{noise} measured by the first TDC 0 is at least by a factor 10 lower than expected. On the software side there is no distinction between handling the data from ϕ SLs and θ SL: all TDCs had the same configuration for these DAQ runs (see Section 4.2.2, and also Appendix A.1), there is no difference in the read-out procedure on FIFOs belonging to the ϕ SLs and θ SL channels. However, for an event on average there are twice as many hits (also noise hits) occurring in *both* ϕ SLs and digitized by *one* TDC than occurring in only *one* θ SL and digitized also by only *one* TDC (see Appendix A.3). Thus a ROS-8 FIFO, which stores data from one ϕ SL ROB, has twice as many words to store as a ROS-8 FIFO for the storing the θ SL data. Therefore it is conceivable, that at a very high hit number per event a data overflow occurs rather at the first mentioned FIFO than at the other one. This results in the missing hits belonging to the ϕ SL channels.

This discovered feature is interesting, but **has rather no influence on the data taking at nominal parameters at the LHC bias trigger rate**. At $U_{thr} = 15\text{--}20$ mV the noise hit rate is low and the read-out of about 12 hits per event (i.e. on average 4 hits per one SL) should be completely unproblematic. Nevertheless, based on the described experiences, **it is recommended to observe the cell hit rate to ensure a proper DAQ process**.

Dead and noisy cells

In addition to the investigation of noise behavior of "normal" cells, i.e. cells with a noise rate f_{noise} of about 30–40 Hz, it is advisable to analyze the f_{noise} development on the dead (i.e. cells with a very low hit rate about 0 Hz and no identifiable time box in the drift time spectrum presented in Figure 4.16) and noisy cells, to complete the noise analysis on all possible chamber cells. In the following, the noise of the dead and noisy cells of all three SLs is investigated in such a way as for the normally working ones, i.e. in dependence on threshold and anode and cathode HV. Also the shape of their time distributions is observed to understand their possible noise source.

According to the noise rate definition described before, in the three SLs the following dead and noisy cells (by number) were found¹⁸:

¹⁷Reminder: each TDC with its 32 channels on ROB 0, ROB 1, ROB 2 and ROB 3 is dedicated for read-out of 16 cells of ϕ SL 1 and 16 cells of ϕ SL 2 (see Section 4.2.2).

¹⁸The MB1 002 chamber, on which the tests were performed, is a one with a rather large number of dead and noisy cells. Normally the DT chambers are of good quality and contain – if indeed – only single dead

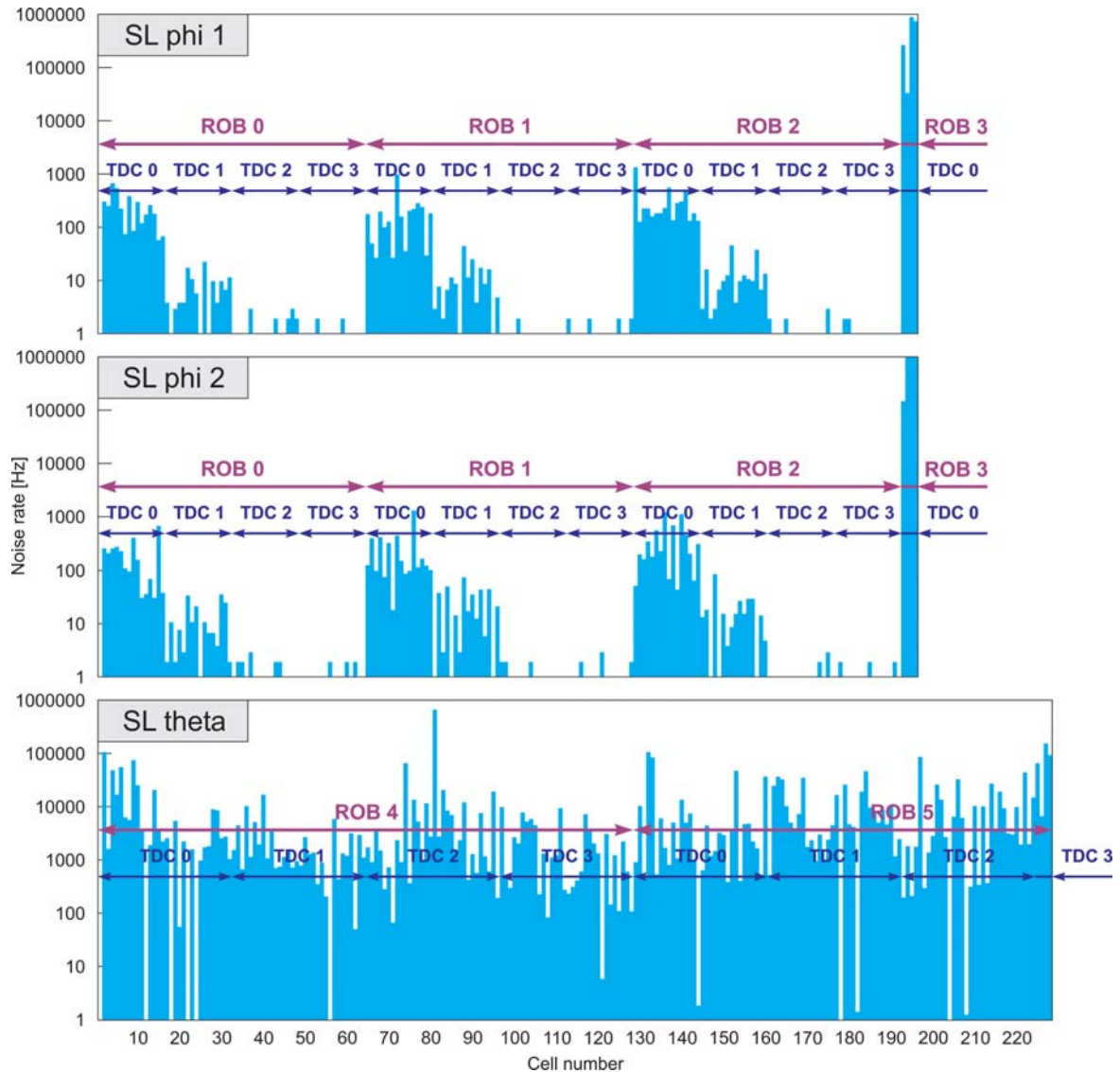


Figure 4.28.: The noise rates f_{noise} individually measured for cells of each SL at $U_{thr} = 5$ mV. The ϕ SL 1 and ϕ SL 2 show a regular pattern in the f_{noise} distribution, which is obviously depending on the TDC position on the ROBs. It suggests that this behavior is a feature of the read-out mechanism of the ROBs. The SL noise rate distribution shows no extraordinary structure.

- **Dead cells:** 1 (ϕ SL 1); 1, 44, 107, 166 (ϕ SL 2); 1, 12, 18, 22, 24, 56, 121, 144, 178, 182, 204, 208 (θ SL).
- **Noisy cells:** 81 (ϕ SL 2); 2, 6, 14 (θ SL).

In Figure 4.29 the noise rates f_{noise} of only four representative dead cells (due to clearness) and of all four noisy cells are shown in dependence on the mentioned parameters. The results can be interpreted in the following way:

- **For the dead cells:** f_{noise} of all cells is below 10 kHz at each threshold level U_{thr} .
-
- and/or noisy cells.

4. Data taking with the CMS DT muon chambers

However, qualitatively one recognizes a trend of the noise behavior like that for the observed normally working cells: f_{noise} is decreasing by increasing U_{thr} . For $U_{thr} > 20$ mV we find $f_{noise} \leq 1$ Hz for all observed cells. By varying anode and cathode HV one can also see a noise behavior being similar to the one of the normal cells. By increasing U_{anode} the f_{noise} smoothly rises but remains always below 10 Hz. The noise rate of about 10 Hz remains also constant by increasing $U_{cathode}$. **So one can distinguish between "cell noise" (about 25 Hz) and "electronic noise" (about 1 Hz).**

- **For the noisy cells:** All four cells, qualified as "noisy", are characterized by a high f_{noise} of about 100 Hz to 1 kHz at the nominal set $U_{thr} = 15$ mV, $U_{anode} = +3600$ V and $U_{cathode} = -1200$ V. For the variation of the threshold one can recognize a noise behavior like that for the normally working cells for $U_{thr} < 20$ mV. For $U_{thr} \geq 20$ mV the f_{noise} is nearly constant for all four cells and remains below 100 Hz (for the three noisy θ SL cells f_{noise} is even near the "good" value of 30–40 Hz). Variation of the anode HV shows no f_{noise} dependence on U_{anode} . Variation of the cathode HV shows again a weak f_{noise} dependence on $U_{cathode}$ with a minimum at $U_{cathode} = -1200$ V. **The threshold $U_{thr} = 20$ mV, together with the nominal cell HV $U_{anode} = +3600$ V and $U_{cathode} = -1200$ V, seems to be an optimal parameter set which results in a noise rate reduction in noisy cells and thus in a better drift time data quality.**

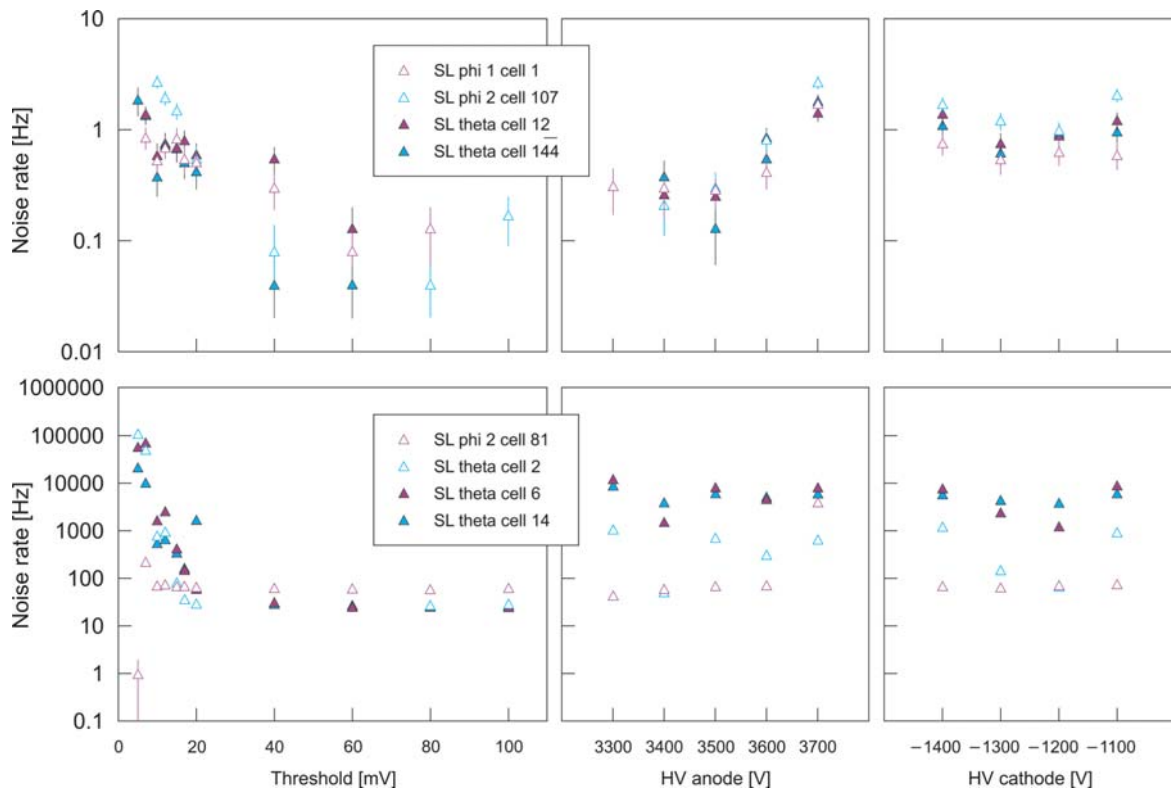


Figure 4.29.: The noise rates f_{noise} measured for dead (top, here only for four selected of all seventeen dead cells) and noisy (bottom) cells found at the SL of the chamber being tested. The noise behavior is very similar as for the normally working cells, i.e. cells with a noise rate of about 30–40 Hz. Missing entries for some dead cells by given parameters (threshold, HV) mean no hits registered (cell noise rate equal zero).

Finally an observation of the hits registered at channels belonging to the first cell (i.e. the cell numbered by "1", see Figure 3.10) at each SL is done. These cells are interesting because they have no anode wire due to the geometrical chamber layout. One expects therefore no signals from them. However, these cells are connected to the FEB channels and therefore to one of the TDC channels on the ROB.

As shown already in Figure 4.29 for the cell 1 of the ϕ SL 1 (the other two cells show an analog behavior), the channel provides signals. The noise rate is about 1 Hz, each; the trend is the same as for the other cells at varied threshold and HV. Interesting is also a comparison of the time spectrum registered for the first cells to the one of the adjacent cells 3 and 5 (Figure 4.30). The spectra of the cells 1 are intensified in a range corresponding to the time box of the cells 3 and 5, what indicates a possible crosstalk. This means that **the hits in adjacent cells bias each other**, although this interference effect is not very high (about 1% of the hits total number in the time box range of the cell 3 or 5).

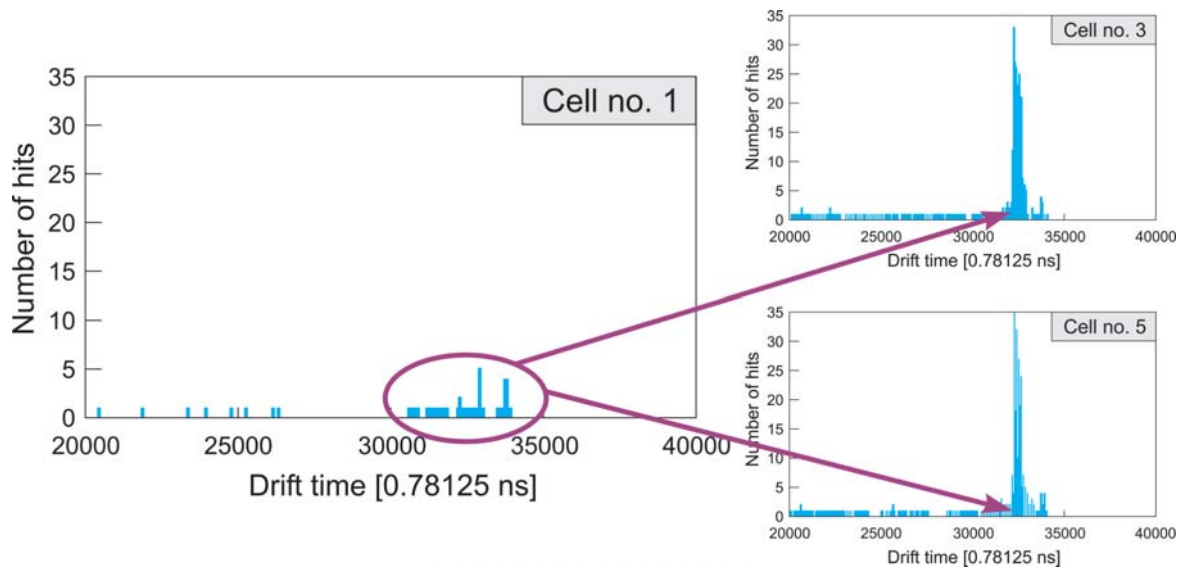


Figure 4.30.: The hit time distribution registered for a channel belonging to the cell 1 of the ϕ SL 2, which is connected to the DAQ system but has no anode wire. The distribution shows a concentration of the hits at the range corresponding to the drift time box of the adjacent cells 3 and 5, which can be explained by an interference effect (cross-talk).

Signal and threshold

Finally, the issue is investigated, whether the noise manipulation, as described in case of the threshold variation, also affects the "right" hits, i.e. the regular hits, which results from electron drift in the chamber cells. Knowing the DAQ mechanism one expects a similar statistical behavior of the hits filling the time box (see Figure 4.16) like that of the noise hits. This means that the total number of the time box hits should decrease by increasing threshold.

To see such possible dependence the absolute hit number matching the time window in the time box interval N_{drift} of each SL are investigated at given threshold U_{thr} . The data are from the DAQ runs as described before at varied U_{thr} and at nominally kept cell HV.

The results are shown in Figure 4.31 for each SL at threshold levels $U_{thr} = 12$ mV, 15 mV, 17 mV, 20 mV, 40 mV, 60 mV, 80 mV and 100 mV. As expected, N_{drift} decreases observably

4. Data taking with the CMS DT muon chambers

by increasing U_{thr} , which can be parametrised by a linear relation

$$N_{drift} = a' \cdot U_{thr} + b', \quad (4.8)$$

or, to calculate directly the efficiency ϵ_{thr} by a given threshold with respect to the one with nominal threshold set $U_{thr_nom} = 15$ mV, $\epsilon_{15\text{ mV}} := 1$

$$\epsilon_{thr} = a \cdot (U_{thr} - U_{thr_nom}) + b, \quad (4.9)$$

The measured parameters a (slope) and b (offset) are presented in Table 4.9 for each SL.

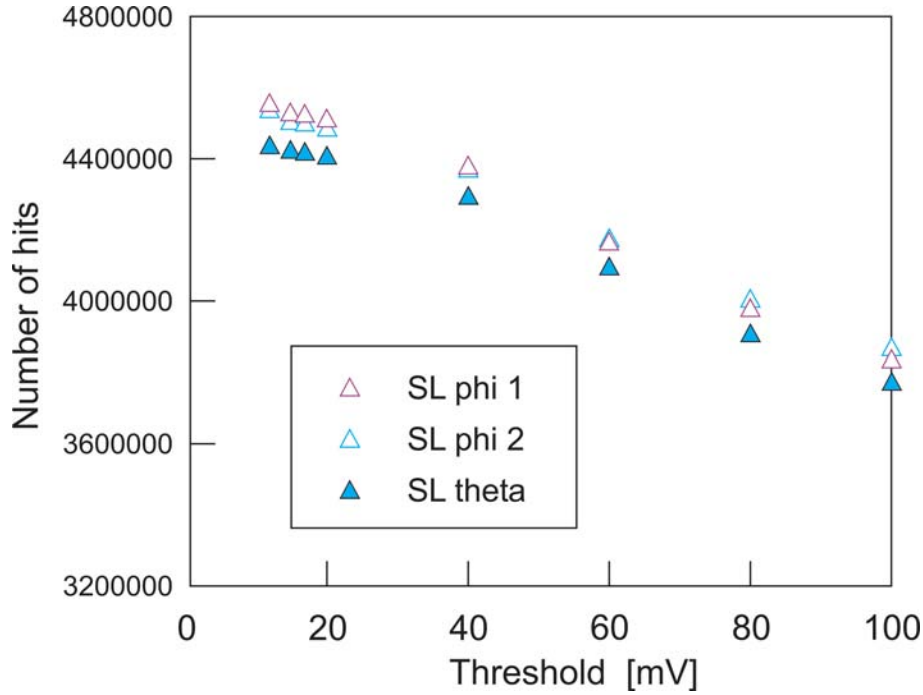


Figure 4.31.: The total number of registered drift hits N_{drift} for each SL shows a linear dependence on the threshold, as expected. By changing the threshold from 15 mV to 20 mV (usually set values) N_{drift} decreases only by about 0.5%.

	a [mV ⁻¹]	b
ϕ SL 1	$-1.85 \cdot 10^{-3}$	1.0033
ϕ SL 2	$-1.70 \cdot 10^{-3}$	1.0034
θ SL	$-1.75 \cdot 10^{-3}$	1.0032

Table 4.9.: The slope a and offset b measured for each SL by a linear regression describing the dependence between obtained hit efficiency and threshold (Equation 4.9).

With respect to the data taken at the nominal threshold of $U_{thr} = 15$ mV, about 1% of the data loss occurs at the higher threshold $U_{thr} = 20$ mV. The highest threshold level $U_{thr} = 100$ mV, set for these series of tests, causes that only about 85% of the data taken at the nominal U_{thr} are available. These results are valid for all three SLs.

Missing events and noise

As mentioned in Section 4.4.1 on page 74 one observes discontinuities in the event ID counting, which was included in the MC-DAQ data blocks (Appendix A.3) – the missing events. The experience obtained by the data analysis from the two different DAQ systems showed, that the data taking process was sometimes disturbed by an unexpected noise occurrence. Therefore, it could be interesting to see, whether this phenomenon of missing events depends on the noise in the DAQ system.

For this purpose the runs with varied run parameters U_{thr} , $U_{cathode}$ and U_{anode} are presented once more in Table 4.10 with the corresponding cell noise rate (averaged value of all three SLs) and the corresponding number of missing events calculated for each run. One can recognize the qualitative dependence between the noise and the missing events: the number of the missed events decreases with the decreasing noise rate. This is especially remarkable for the first three runs with varied U_{thr} , where the noise rate is very high. During the runs with a "normal" noise rate of 30–40 Hz mostly (except for two runs) no events were missed.

Run parameters			Noise rate [Hz]	Number of missing events
threshold [mV]	HV cathode [V]	HV anode [V]		
5	-1200	+3600	19303.5	879313
7	"	"	3066.0	58901
10	"	"	103.9	1329
12	"	"	35.1	0
15	"	"	32.8	1
17	"	"	32.7	0
20	"	"	30.9	0
40	"	"	31.0	0
60	"	"	28.2	106
80	"	"	27.7	0
100	"	"	28.6	0
15	-1200	+3300	21.5	0
"	"	+3400	29.0	0
"	"	+3500	33.4	0
"	"	+3600	34.5	0
"	"	+3700	43.9	0
15	-1400	+3600	36.7	0
"	-1300	"	32.0	0
"	-1200	"	32.6	5033
"	-1100	"	34.4	0

Table 4.10.: List of runs with varied run parameters, the averaged noise rate per cell of all three SLs and the number of missing events. All runs included 1 million events.

It is also interesting to observe the DAQ behavior during the run, which leads to the missing events. As example can serve the run with the parameter set $U_{thr} = 60$ mV, $U_{anode} = +3600$ V and $U_{cathode} = -1200$ V. This run is one of the "stable" runs, with a normal noise rate of about 30 Hz but it shows an accidental event ID discontinuity of 106 events. As presented in Figure 4.32 for the ϕ SL 2 up to event 3597 the data taking was not disturbed with about 4 hits per event. From event 3598 to event 3621 the number of hit per event rises rapidly (noise) until the event 3621. At the event 3622 the data information flow is abruptly terminated; for this and for the following 105 events there exist no data, the event data are lost. From the event 3728 up to the end of the run the data are available again; the number of hits per event

4. Data taking with the CMS DT muon chambers

is about 4, as expected.

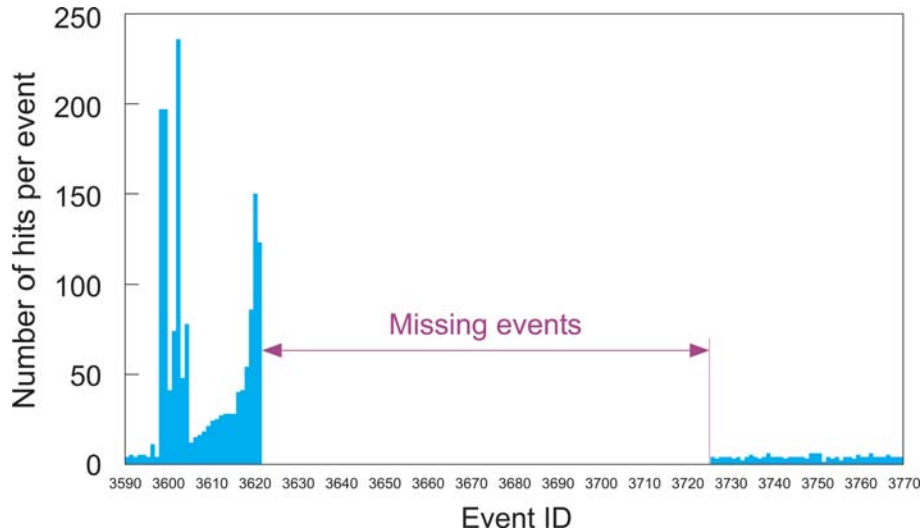


Figure 4.32.: Hit number in some events for the ϕ SL 2 in run with $U_{thr} = 60$ mV, $U_{anode} = +3600$ V and $U_{cathode} = -1200$ V. The observed interruption of the event data taking (106 missing events) was preceded by a very high hit rate (noise).

Assuming a good DAQ hardware and software functionality, such behavior can only be interpreted as event data loss by buffer overflow in the ROS FIFO(s). This can occur e.g if it is filled in with a huge number of noise data. **The noise in the DAQ system can therefore not only influence the data taking quality, but also cause the data loss.**

4.4.3. Conclusions on DAQ tests

The idea of direct comparison of data taken by AC-DAQ and MC-DAQ resulted in an attempt to perform a synchronous read-out of one CMS DT muon chamber by more than one DAQ system. Use of the Splitter Board for connection to 16 chamber cells and providing the chamber signals to different DAQ systems, has made this possible. Its design and architecture could be used for a potential future device for direct tests and adjustments on the applied chamber read-out systems. However, as seen in the described five DAQ runs, the stability of the SB must be improved to eliminate as much as possible any electronic noise source.

Nevertheless the data obtained by the common DAQ runs can be analyzed after applying a selection to reduce the undesirable influence of the hardware components. The "real" chamber information incoming as signals from the chamber cells are detected by both systems equally. The differences in the hit cells and cell occupancy per event are negligible. The measured drift times, caused by hits at the same cells in the same event, have the same value registered by both DAQ systems with respect to their TDC resolution of about 1 ns, as expected. Based on these analysis results one can realize that both systems – AC-DAQ and MC-DAQ – are suitable for drift time measurement of the CMS DT muon chambers.

The noise rate depends on the supplied anode HV but remains normally in the "save" range of 30–40 Hz. The cathode HV, however, has no influence on the noise rate. Thus, the HV values, chosen as being optimal for the \vec{E} field inside the cells, do not need to be changed due to noise arguments.

On the other hand the noise rate is lowered by increasing the threshold U_{thr} , as expected:

the higher the threshold level, the lower the noise rate. The best results are obtained for $U_{thr} > 10$ mV. Concerning also the noisy cells, i.e. cells with a noise rate $f_{noise} \gg 100$ Hz, one can reduce the noise rate below 100 Hz in these cells by increasing the threshold to 15 or 20 mV. The efficiency for hits registered by real muon events is hereby decreased by about 1%.

The threshold variation showed that more studies are needed to understand the read-out mechanism of the ROB. By increasing the hit rate per trigger (which is adequate to increased noise rate at low threshold) the read-out of ϕ SL data is affected, caused by data packet loss on ROS channels. Although this does not affect the DAQ process under nominal conditions (threshold, HV, trigger rate), this newly discovered feature should be of interest and undergo a broader investigation.

A specific investigation of the dead cell behavior shows that the noise origin is not inside the cells. Rather the noise is caused by the environment electronics (wire line, connectors), as previously seen by the use of the Splitter Board. Also cross-talk in the read-out channels occurs. It is also generally recommended to eliminate the noise as much as possible, due to the fact, that the noise can obviously cause the loss of event data (missing events).

5. Measurement of the gas pressure in the CMS DT muon chambers

The Compact Muon Solenoid is a complex detector containing $O(10^4)$ composite objects which need to be controlled continuously during the entire operation time. To provide an efficient detector run a reliable system must be able to monitor the detector performance. The *Run Control and Monitor System* (RCMS) consisting of hardware and software components monitors the CMS during the data taking. In this period it manages the *Detector Control System* (DCS), which is responsible for the overall status control of the detector and its environment.

One of the tasks at the Phys. Inst. III A of the RWTH Aachen is the development, production and test of the hardware system for the DCS gas pressure monitoring of the CMS DT muon chambers. To validate this system an interface to the DCS software framework is performed for gas pressure read-out at all times at each muon chamber in the CMS detector. The present chapter describes the strategy and successive steps leading to a reliable and safe gas pressure measurement at the CMS muon chambers. In addition, test procedures on this system are presented and their results analyzed.

5.1. Detector control and monitoring systems

5.1.1. Run Control and Monitor System (RCMS)

The Run Control and Monitor System (RCMS) of CMS is a set of hardware and software components to ensure reliable detector operation during the data taking periods. The software solution implemented in the RCMS allows to perform these activities from any place in the world by using commercial technologies. To meet these requirements the RCMS must interoperate with the DCS (see Section 5.1.2), as well as with the DAQ and trigger components [79]. During the data taking the RCMS acts as master controller of the CMS DAQ and gives instructions to the DCS and its other subsystems.

According to these specifications one can identify three main functions of the RCMS:

- guarantee the proper CMS work by controlling and monitoring it with support of DCS;
- allow for permanent control and monitoring of the CMS DAQ;
- provide a universal user interface and access system.

Each group of detector components, which can be configured and operated independently is defined *partition*. Concerning the mentioned three functions the RCMS treats the experiment as a set of partitions. Although several partitions can operate concurrently, they also can share resources, if necessary. A partition run is named *session*.

As presented in Figure 5.1 a session begins at the *User Interface* (UI) by connecting to the RCMS. Then the proper *Session Manager* (SMR), which is associated to the current session, coordinates all actions. SMR has to accept or reject commands coming from outside RCMS

5. Measurement of the gas pressure in the CMS DT muon chambers

and forward them, if accepted, via the *Sub-System Controller* (SSC) to the components being under control. It also takes advantage of diverse services for supporting the interaction with users. All three components of the logical RCMS layout – SMR, SSC and Services – can interact directly with each other.

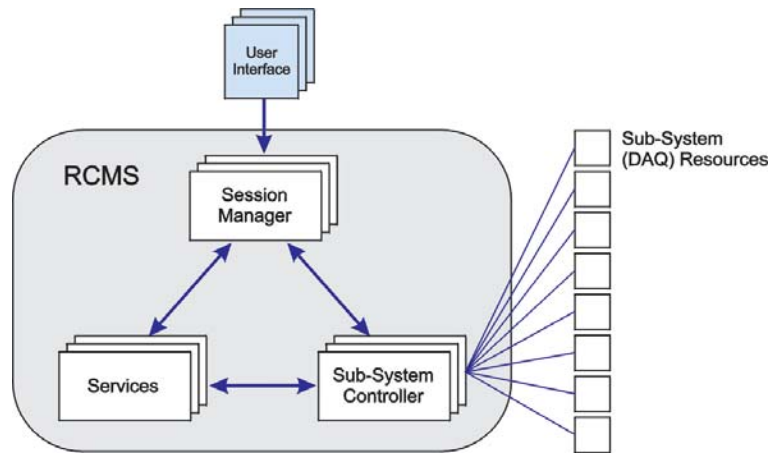


Figure 5.1.: The logical layout of the RCMS. It comprises the four element types User Interface, Session Manager, Sub-System Controller and Services, which all are responsible for functions like logging, security and resource handling.

The detector subsystems have direct connections to the SSC (Figure 5.1, 5.2). The sub-detectors like muon system and others represent natural partition area. Some DAQ systems like DCS deal directly with the detector and its environment. These systems can be partitioned according to the subdetector to which they are connected, for example DT gas pressure monitoring as an independent partition. After the commands initiated by users were interpreted and routed to the proper subsystem resources, the addressed subsystems respond asynchronously but the information resulting from the corresponding actions is logged and analyzed by RCMS. The RCMS has also to handle data messages of internal status, malfunctions etc. When required the RCMS shall monitor data sent by various DAQ systems.

The dialog to the subsystems is performed via *DAQ Service Network* (DSN) based on switched Ethernet. Each subsystem contains DAQ resources which are hardware or software components being able to be managed directly or indirectly through the DSN.

The interaction with users to manage subsystem resources is supported by a couple of services (Figure 5.3). Distribution of these services over a number of computing nodes is important to achieve their scalability and fault tolerance. The following services are defined in the RCMS:

- *Security Service* (SS): provides authorization and authentication modules, data encryption (if necessary) and manages profile and access rights data bases.
- *Resource Service* (RS): manages all DAQ resources by their identification and allocation. It also checks the resource availability and contention with other partitions if a resource is used in a DAQ session. It scans periodically the registered resources and updates the configuration data base.
- *Information and Monitor Service* (IMS): collects messages and the incoming data of different types from DAQ resources and RCMS components and stores them for sub-

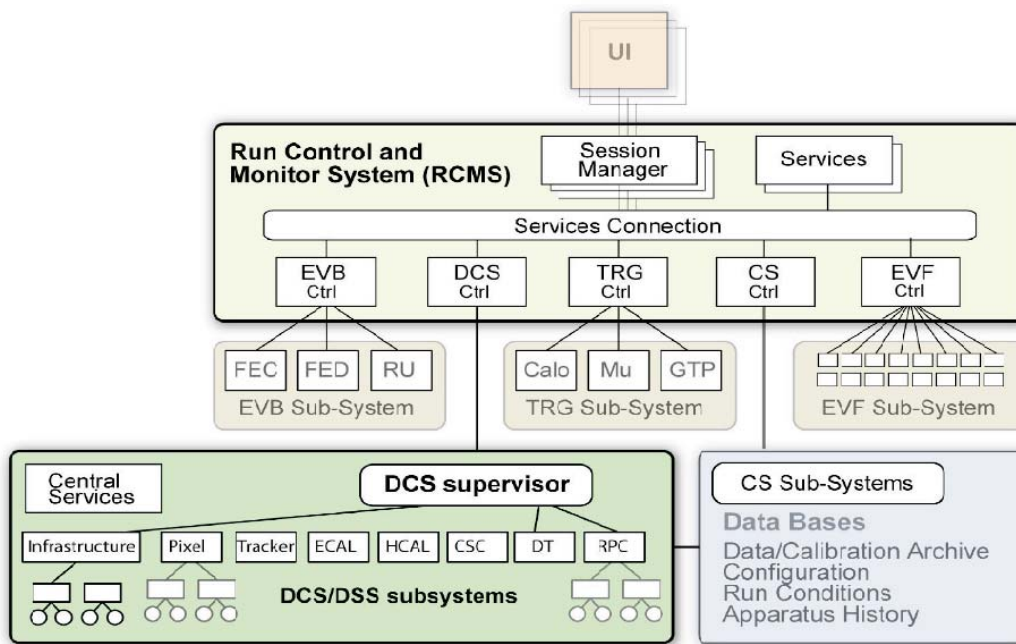


Figure 5.2.: Session Managers and subsystems of the RCMS [80]. Receiving commands from the User Interface (UI) the controllers for the corresponding detector subsystems, like Detector Control System (DCS), Trigger (TRG) and others, are addressed to perform demanded actions. In this manner the various subsystems can be configured and data taking sessions can be operated independently. This structure allows also monitoring of the data flow. For a detailed explanation of the acronyms used in this figure see Reference [80].

scribers. These informations are then registered and categorized by selection criteria like timestamp, information sources severity level etc.

- *Job Control (JC)*: allows remote control and supervision of DAQ processes, like start, stop, monitor etc., of the software infrastructure of the RCMS.
- *Problem Solver (PS)*: recognizes malfunctions by subscribing to the IMS and determines recovery procedures.

5.1.2. Detector Control System

General description

The *Detector Control System (DCS)* is responsible for the correct operation of the CMS experiment, providing data taking of high quality. When the data taking is executed, the DCS acts as slave of the RCMS which is responsible for the control and monitoring data taking operations (Section 5.1.1). Outside this period the DCS takes over the master function for all active detector components. Most DCS tasks are required to be executable at all times; this implies its 24/7 full operation during the entire year [82].

As mentioned above, the primary function of the DCS is to perform overall control of the detector and its periphery. The DCS range embraces all subsystems and other individual elements being involved in the detector control and monitor procedures, its active elements,

5. Measurement of the gas pressure in the CMS DT muon chambers

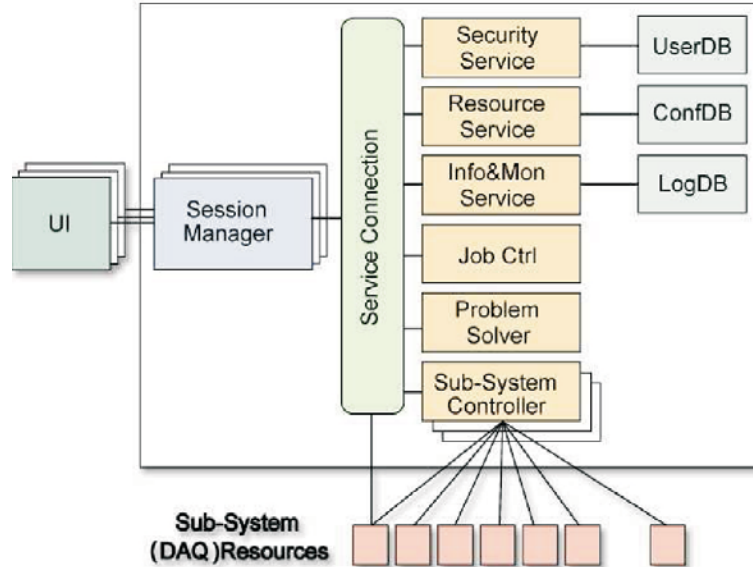


Figure 5.3.: A number of services is needed for the interaction with users to manage the resources of subsystems [81]. The services are distributed over a computing node system for scalability and fault tolerance reasons. Each subsystem has its own local instance of a service.

electronics and the experimental hall. In addition, the CMS communication to the external systems, like RCMS and accelerator, is performed via the DCS. Also the experiment protection against any events, which could affect its work, is attempted directly by the DCS tasks. Therefore the safety-related functions, like detector security (in common with *Detector Security System*, DSS), alarm handling and software access control are integrated into the DCS.

The major DCS facility consists in control and monitoring of the regulation systems on the detector and its environment, which was traditionally referred to as "slow controls". This includes especially:

- high and low voltage,
- detector electronics, e.g. calibration and read-out systems,
- cooling facilities,
- gas and fluid systems,
- racks and crates.

The detector control is ruled by hierarchically organized DCS supervision. The DCS of individual subdetectors, which is connected to the lower level to the central DCS supervisor, handles the electronics characteristic for each subdetector and partially based on standard components (e.g CAEN high voltage supply). The interfaces of all nodes in the hierarchical system are made in a way allowing to connect each node with any other one. This made the subsystems possible for independent development and facilitates their integration into the entire system. Some DCS subsystems, like low voltage and gas flow control, are common for all subdetectors; other ones, like cooling, are designed individually for each subdetector.

Some subdetectors have specific control particularities, e.g. both barrel alignment and DT gas pressure monitoring are parts of the muon system and use its control links in the barrel region of the CMS detector.

The supervisor at the top hierarchy level sends global commands like "start" and "stop" for the entire detector. Then they are propagated towards to the lower levels, at which the interpretation and translation for use at the subsystem units occurs. In the opposite direction the status information from the lower levels are summarized by the upper levels defining in this way the status of this upper level. Each action on the devices is transferred to the hardware, so the state of the devices represents generally the status of the hardware.

The partitioning concept of the CMS detector (see Section 5.1.1) is very important to handle the subsystems and its components independently. In the case that such subtree is cut off from the command hierarchy, it can be operated individually. This operation mode is very useful for maintenance, calibration, tests etc. During the data taking run there is only one partition which comprise all subdetectors.

For the supervising of the DCS a commercial *Supervisory Control And Data Acquisition* (SCADA) system PVSS II [83] was chosen by all LHC experiments. PVSS II is a development environment offering a large number of basic functionalities which satisfies the DCS demands mentioned above. The development and use of the PVSS II components is performed within the CERN internal *Joint Control Project* (JCOP) framework [84]. The JCOP provides tools and modules to construct partitionable control hierarchy and to implement the PVSS II into the hardware units. The JCOP also contains a prototype of the hierarchy mechanism as described above, thus the logical hierarchy structure is made exclusively in software. Also tools to handle the partition model exist in the JCOP framework, as well as the alarm handling mechanism designed in the PVSS II.

DCS of the DT muon system

Figure 5.4 represents the logical and physical architecture of the muon system DCS. The logical structure of the muon system DCS (similarly for the other subsystems) is detector based and is characterized by a hierarchical commands flow, beginning at the global DCS supervisor towards the muon subsystem component level chain and ends at the executing controlled DCS subsystem [85]. In the opposite direction – from controlled DCS subsystem to the supervisor – the status informations from each lower level are collected in the next higher level and forwarded up stepwise to the DCS supervisor. Analysis of these state data can induce new control actions which implies new commands etc.

Physically each action is executed by explicit commands created at the supervisor top level. At least four cardinal commands are defined by the DCS supervisor for each subsystem¹:

- ON: The DCS subsystems are instructed to be ready for data taking. This command contains configuration parameters, like tag or version key, which can be recognized by the configuration database.
- STANDBY: The DCS subsystems are instructed to be in a safer intermediated state, e.g. when preparing for data taking, due to the shorter time for changing from STANDBY into the ON-state than from the OFF-state. STANDBY can also contain the configuration parameters.

¹These commands are not specific to the muon system but rather similar in their design to all detector subsystems.

5. Measurement of the gas pressure in the CMS DT muon chambers

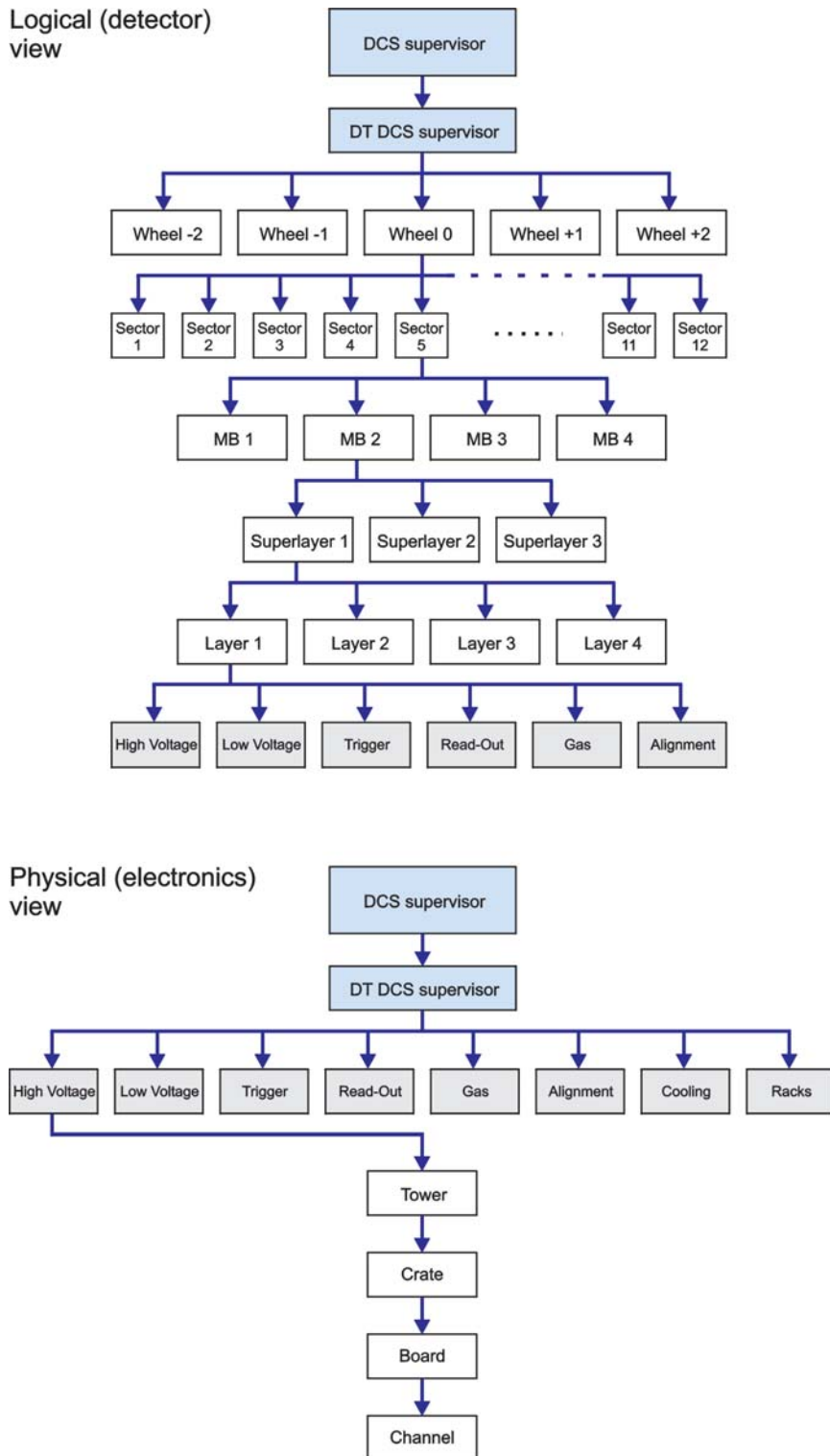


Figure 5.4.: The DCS hierarchy using the example of the muon system. The logical structure contains several levels beginning at the global DCS supervisor. From here the commands are distributed towards through the lower levels to the final executing device. Upwards the status informations are successive collected and lead to the supervisor. Physically the commands are linked to the subsystems, whose task is to provide the requested action via detector environment (tower, crates) to the chamber components (illustrated example: high voltage to the chamber channel).

5.2. Local DCS gas pressure monitoring and control for the CMS DT muon chambers

- OFF: The DCS subsystems are instructed to shut down and to complete the data taking.
- Commands for reconfiguration of the DCS: these commands draw on the ON and STANDBY commands using their different configuration parameters.

On the muon subdetector level there are also the commands ON, STANDBY and OFF, which set the DT muon system in the proper state. In addition, the DT muon system, like other CMS subdetectors, has to be able to handle an ERROR state from one or more of its subcomponents. Dependent on the importance and kind of this state the muon system tries to solve the problem. In case it remains unsolved, an alarm is sent to the alarm system by direct connection to the DSS. It has to initiate any recovery procedure and, in case it fails, to change its own state to ERROR. During the data taking time it is important to compute the detector inefficiency and transmit it as parameter of the ERROR state.

Following these commands from supervisor and subdetector levels the local control is executed directly at the DT muon chambers. The CCB inside the MiniCrate (see Section 4.2.2) is responsible for receiving and interpreting of the DCS commands, performing the monitoring and control at the chamber and sending the demanded data back to the DCS. The DT muon chamber control and monitoring processes in following sequences:

- OFF: No DCS subsystems are controlled.
- INITIALIZATION: Check of the DT environment systems (communication server, crates, LV), links to the MiniCrate, FEB read-out, MiniCrate boards (TRBs, ROBs) and chamber outer systems (alignment, gas pressure); booting the CCB and sending the status of the MiniCrate.
- CONFIGURATION: Loading and executing of all configuration files (Traco, TSM, BTI, TDC etc.; also if needed the mask files). Setting of the FE parameters (bias, threshold, pulse width). Selection of run mode (physics, test pulse, autotrigger). Configuration of L1A trigger, read-out configuration of alignment, gas pressure.
- RUN: Status check of CCB, CCB server and FE. Read-out of the TDCs.

5.2. Local DCS gas pressure monitoring and control for the CMS DT muon chambers

The CMS DT muon chambers are gas-filled detector components for the measurement of the drift time of the electrons from gas ionization caused by a charged particle (usually muon), which passed through a chamber cell (see Section 3.3.2). These times depend strongly on the gas pressure inside the chambers [39]. For high quality data taking the monitoring and control of the gas pressure in the chambers is indispensable as a part of the DCS. Also, due to the chamber security rules the gas pressure should be monitored to inform about a possible pressure increase.

The Ar/CO₂ gas mixture is supplied to the single chambers via a branched system of pipes, valves, manifolds etc. (Figure 5.5). Beginning at the gas mixing facility the gas is at first distributed to the five wheels (distribution ratio 1:5). From here the gas is provided to each of the five wheels via about 100 m long pipe to the instrumented gas distribution rack, located on a support platform at the side of the wheel. Here the next distribution to the chambers occurs (1:50) and the gas is separately lead to each chamber via up to 30 m long copper tubes.

5. Measurement of the gas pressure in the CMS DT muon chambers

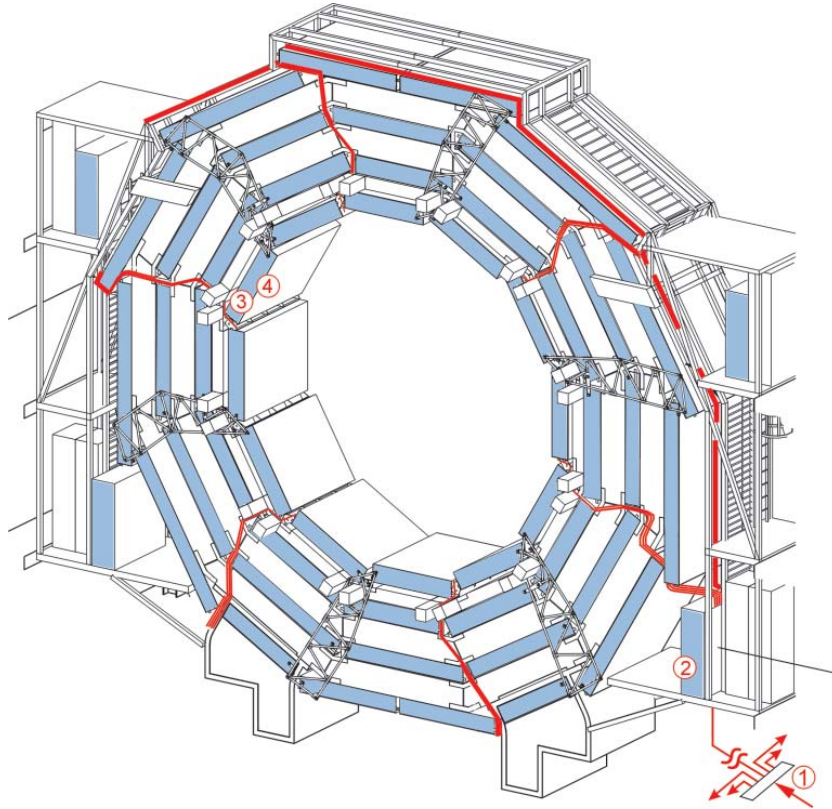


Figure 5.5.: Gas distribution at one wheel of the CMS detector. The gas tubes of the gas inlet side are marked red. The branching points are: 1 – wheel distribution (1:5), 2 – gas instrument rack (1:50), 3 – gas manifold at the chamber with distribution to the three or two SLs (1:3 or 1:2), 4 – distribution inside the SL to the single layers and cells. The gas outlet is implemented in a similar manner and is not represented here.

Then the gas outlets are reconnected stepwise analogically back to the gas source. In such closed loop the gas is cleaned up and reused; only about 10% of the gas is regenerated after each circulation.

The monitoring of the gas pressure within a DT muon chamber is presented in Figure 5.6²: In each manifold two sensors of different range are housed for measurement of the pressure of the incoming or incoming gas. The sensors measure the differential pressure, i.e. the gas pressure with respect to the ambient air pressure. In a manifold one of the sensors is able to measure the pressure within a range of ± 100 mbar (sensor 100). The other sensor, less sensitive than the previous one, has a measurement range of ± 500 mbar (sensor 500). The output of the sensor is an analog voltage signal, unique to the measured pressure, but can be different for different sensors of the same type. It also depends on the supplied manifold voltage and achieves a maximum value of about 4.5 V.

The sensor signals are digitized by means of a *Pressure Analog to Digital Converter* (PADC) board which is mounted directly on the HV chamber side. It is possible to connect up to 10 analog channel, which are digitized with a resolution of 10 bit. For the mentioned sensor types it means a resolution of about 0.3 mbar and 1 mbar for the sensors 100 and 500, respectively.

²More detailed informations about the gas pressure read-out hardware and software components, which are here shortly described, are given in the following parts of this chapter.

5.2. Local DCS gas pressure monitoring and control for the CMS DT muon chambers

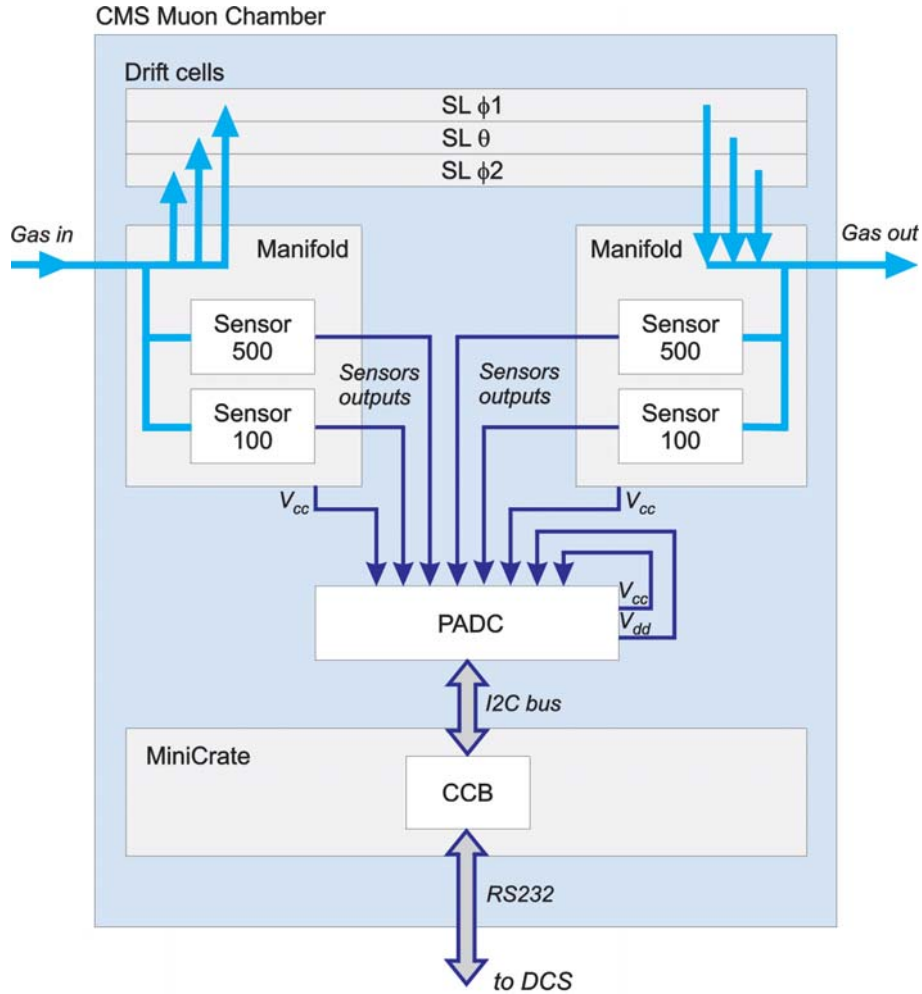


Figure 5.6.: Schematic diagram of the read-out of the gas pressure sensors on the CMS Muon Chambers. The sensors housed in the manifolds measure the relative pressure of the outcome and incoming gas. Their analog output signals are then digitized in the Pressure Analog to Digital Converter (PADC) in common with the different supply voltages. The digitized data are then transferred to the Chamber Control Board (CCB) from where they can be read out by the Detector Control System (DCS) software.

With the spare PADC input channel place we decided to read out each sensor 100 twice. Also, as well as the supply voltages V_{cc} of both manifolds, the voltages V_{cc} and V_{dd} of the PADC are connected to ensure more control over the local gas pressure read-out system of the CMS DT muon chambers.

The digitized values of each connected channel are then transferred on demand to the Chamber Control Board (CCB), which is housed in a electronic read-out and chamber control unit called MiniCrate. This is performed via an I2C bus shared by the read-out of the gas pressure and to drive the LEDs for alignment of the chamber. From outside the DCS can communicate with the chamber via a serial port. To obtain the current pressure value measured by a sensor the DCS software has to read out the actual counts of the corresponding PADC channel and convert it into the pressure value by using the appropriate *Look Up Table* (LUT) for this individual sensor.

5.3. Calibrated hardware components

For the measurement of the gas pressure within the CMS DT muon chambers the three hardware components used are: pressure sensors, PADC and CCB. In the following the properties, function and calibration of the sensors and PADC is presented. The CCB was described already in Section 4.2.2 and here only its DCS function is mentioned.

5.3.1. Why calibration?

The different hardware components used for the gas pressure measurement in the CMS DT muon chambers provide different physical values, which have to be interpreted correctly (Figure 5.7). At first the sensor, which directly experiences the gas pressure p (measured in mbar), convert it into an analog electric signal (voltage) V' . This signal, measured in mV, must generally be amplified to obtain a significant output signal V_{out} (up to several Volt). To make it possible for digital measurement V_{out} must be digitized by an ADC in n counts (here PADC with $n = 4096$). Each digitized value (count) corresponds then to one pressure value p_n , measured by the sensor. The conversion count/pressure is stored in the proper tables (Look Up Tables, LUT). The DCS software uses the LUT for the gas pressure monitoring and control during the CMS operation.

The relation between these converted values at two levels – the sensor (with applied sensor electronics, i.e. including the pre-amplifier³) on the one hand, and the PADC on the other hand – is generally provided by the hardware producer or developer. However, this information is always given within a tolerance limit. For example the simple relation p vs. V' of the sensors is expected to be linear with a precision of a few %, and – which is especially important – is not the same for different sensors. This in fact small effect can become larger when amplified. The error propagation results in different V_{out} for different sensors by measurement of the same p . Also some other factors, like e.g. temperature T , V_{cc} , can influence the output V_{out} . The same considerations concerning the linearity in the relation V_{out}/n are valid for the PADC: the slope and offset can be different for each PADC.

Therefore, to obtain a reliable conversion of the value pairs p/V' and V_{out}/n at first the individual calibration of all sensors (with electronics) and PADC is strictly recommended. Then, on the basis of the calibration data, the LUT can be created for each sensor/PADC combination used in the CMS detector, .

5.3.2. Pressure sensors

Sensor features, pre-tests and first calibrations [42]

For the right choice of the sensors used for the CMS Muon Chambers the following considerations had to be taken into account:

- The sensors should be very small. The fact that they are housed in the manifolds implies a volume of only few cm^3 (Figure 5.8 right).
- The gas pressure inside the chamber is relatively low (10 to 20 mbar overpressure). Thus the sensors should have a resolution of about 1 mbar. Besides this, one needs to register any unexpected overpressure exceeding 100 mbar.

³The sensor and its electronics form one hardware unit, so in the following the expressions "sensor output", "sensor signal" etc. mean always the *amplified* sensor output voltage V_{out} .

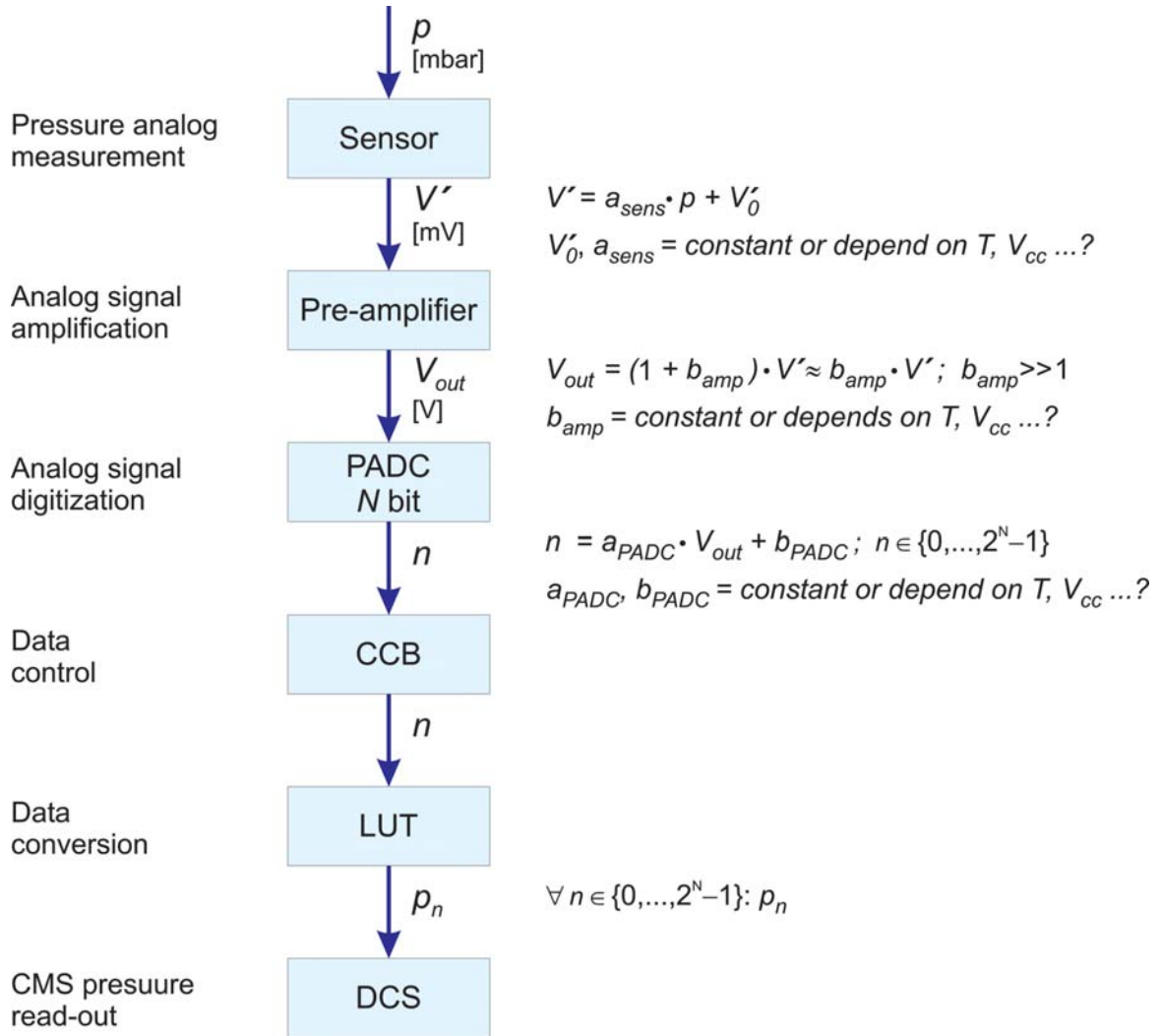


Figure 5.7.: The information about the gas pressure in the CMS DT muon chambers is provided by different physical values from different components in the measurement hardware chain. For right interpretation of these measured values the calibration of the pressure sensors and of the ADC (PADC) is needed. The final pressure read-out is performed by the DCS software which uses the conversion table (LUT).

- The sensors have to be adequate for electronic read-out and continuous gas pressure monitoring and should work reliably during the whole LHC run (about 10 years).
- The sensors should be resistant against high radiation (particle flow above 10^{11} neutrons/cm²) and the outer magnetic field up to 2 T should not affect their functionality.

Considering these requirements and after examination of several alternatives, two sensor types of *Motorola* were selected. They are MPX2010DP (sensor 100, [86]) and MPX2050DP (sensor 500, [87]) for measurement of the pressure differences (i.e. with respect to the ambient pressure). The pressure measurement is based on the piezo-resistive effect and provides an analog voltage output between 0 and 0.1 V when non-amplified.

The characteristic features of these models specified in the technical data sheets by the producer are:

5. Measurement of the gas pressure in the CMS DT muon chambers

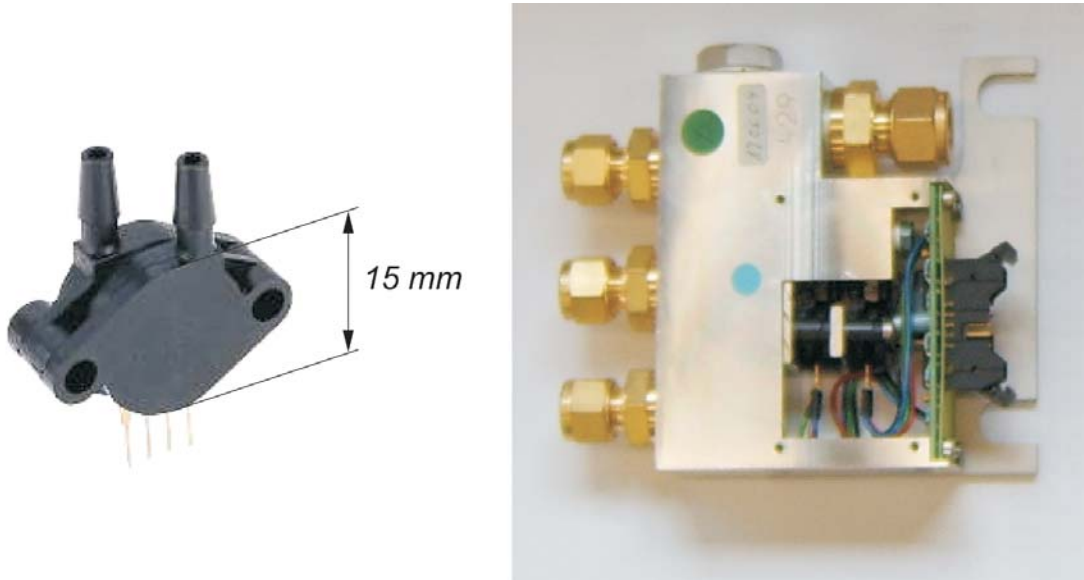


Figure 5.8.: Left: One of the *Motorola* sensors for the gas pressure measurement in the CMS DT muon chambers. Right: One of the gas manifolds for distributing the incoming gas to the SLs or for exhausting the outgoing gas from the SLs to the outer gas system. Each manifold contains two gas sensors of different measurement range each for a measurement of the chamber gas pressure with respect to the ambient pressure (measurement of the pressure difference).

- Storage and operating temperature $-40\text{ }^{\circ}\text{C}$ to $+125\text{ }^{\circ}\text{C}$ (temperature compensated).
- Response time 1 ms.
- Linear voltage output proportional to the applied pressure.
- Working range $\pm 100\text{ mbar}$ (sensor 100) and $\pm 500\text{ mbar}$ (sensor 500) differential pressure.

Before starting the mass calibration of the total amount of over 1000 sensors a couple of tests was performed to verify the last two items listed above. One measured the sensor outputs at different relative pressure values with an 8 bit ADC (as well negative as positive pressure values, Figure 5.9). These studies showed a nearly linear behavior of the response curve in the neighborhood of the offset (the range of interest for the CMS operating). Also the range information indicated by the producer is to be treated rather as guidance. The measurement range of the sensors 100 corresponds to their nominal value, whereas the range of the sensors 500 is shrunk to about $\pm 350\text{ mbar}$. This is designedly caused by using the pre-amplifier electronics (bipolar operational amplifier MC33272, [88]): high amplification implies reduction of the working range.

The measurement ranges vary for each sensor unit of the same type. So they will in fact affect the position of the offset and the slope in the linear range of the calibration curve. Corresponding to the technical data given by the producer, there are tolerances allowed, which could reach even 20% with respect to the entire range of the measurement for both sensor types. Also the testing of the linearity in the calibration curve shape has to be done to optimize the sensor operation in the interesting range around the zero point. Considering these aspects the individual calibrations of each of over 1000 sensors is indispensable before

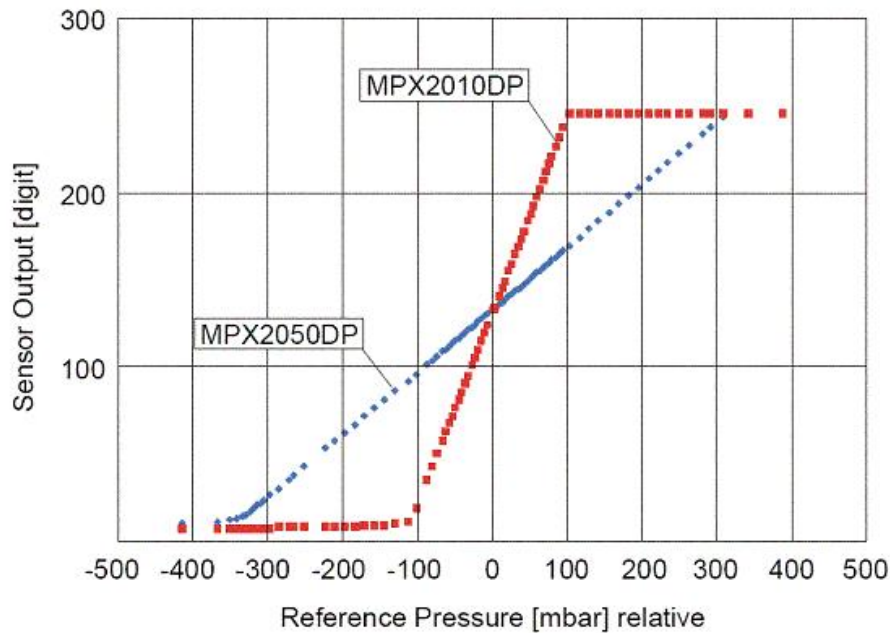


Figure 5.9.: The tentative calibration curves of the sensors 100 (MPX2010DP) and 500 (MPX2050DP) after 8 bit digitization used for test purposes. It shows a linear response. The working range of sensor 500 is limited to about ± 350 mbar by the pre-amplifier.

their usage for the measurement of the gas pressure in the CMS muon chambers, as well as for test purposes at the different sites producing and testing the chambers.

Besides that, some calibration measurements were done to obtain information about sensor operation under LHC conditions. Particularly the following was investigated: sensors under different supply voltages, in irradiated state and the influence of a magnetic field.

The outgoing sensor signal depends strictly on its supply voltage V_{cc} . If the V_{cc} is not stable the sensor signal is also not stable and one would interpret a wrong pressure value due to this fact. To investigate the possible correlation between the supply voltage V_{cc} and sensor signal, calibration curves of both sensor types were taken at different V_{cc} . As shown in the Figure 5.10 the sensors provide useful signals at V_{cc} between 3.0 V and 8.0 V and in this range the sensor signal increases proportionally to V_{cc} . To avoid a wrong interpretation of the taken data the supply voltage is measured simultaneously with the sensor signals, as shown in Figure 5.6.

The expected hit flux in the barrel muon system of CMS is up to 10 Hz/cm^2 (corresponding to 10^{11} neutrons/cm² of 10 years LHC at nominal luminosity). To test the sensors with this condition one sensor 100 and one sensor 500 were irradiated at the IRRAD2 facility at CERN [89], getting an energy spectrum and a radiation dose much higher than expected at the LHC. One day after irradiation calibration data for each of the irradiated sensors was taken (the activity of the sensors was about 48 Bq) [90]. The calibration of these sensors was repeated after one month when no significant activity of the sensors was ascertainable. The comparison of the full calibration data of the irradiated sensors with calibration data of the same sensors before irradiation shows no differences: the irradiation at the CMS does not affect the sensor work (Figure 5.11).

5. Measurement of the gas pressure in the CMS DT muon chambers

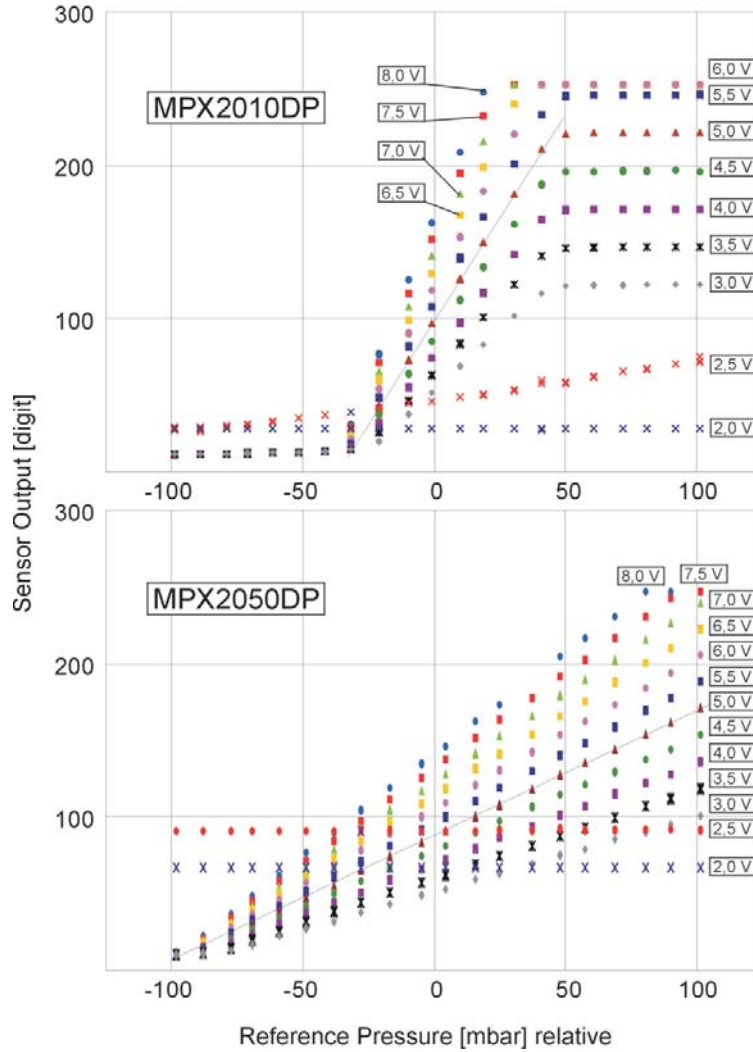


Figure 5.10.: Calibration curves of a pair of sensors 100 and 500 (MPX2010DP and MPX2050DP, respectively), recorded at different supply voltages V_{cc} . The gradient within the working range is proportional to V_{cc} for $V_{cc} > 2.5$ V. According to that, a calibration curve recorded at only one V_{cc} is sufficient to obtain new calibration values at another V_{cc} from the known conversion factor.

The magnetic field generated by the CMS solenoid will have a value up to 1.8 T in the regions where the sensors are mounted in the manifolds directly on the chambers. To study the behavior of the sensors in an outer magnetic field a sensor pair previously irradiated was placed between both poles of an electromagnet. The sensor membranes were oriented perpendicular to the magnetic field lines corresponding to the primary position planned for the sensor housed in the manifolds on the chamber. Then the calibrated curves were registered at different values of the magnetic field up to 2.0 T. A shift of the calibration data proportional to the field strength was observed: the intended orientation of the sensors on the chamber had to be revised (Figure 5.12 top). To test this, the sensors were rotated by 90° to bring their membranes in parallel with the field lines. The new calibration curves showed no shifts; the sensors are able to operate in this position in the CMS detector (Figure 5.12 bottom).

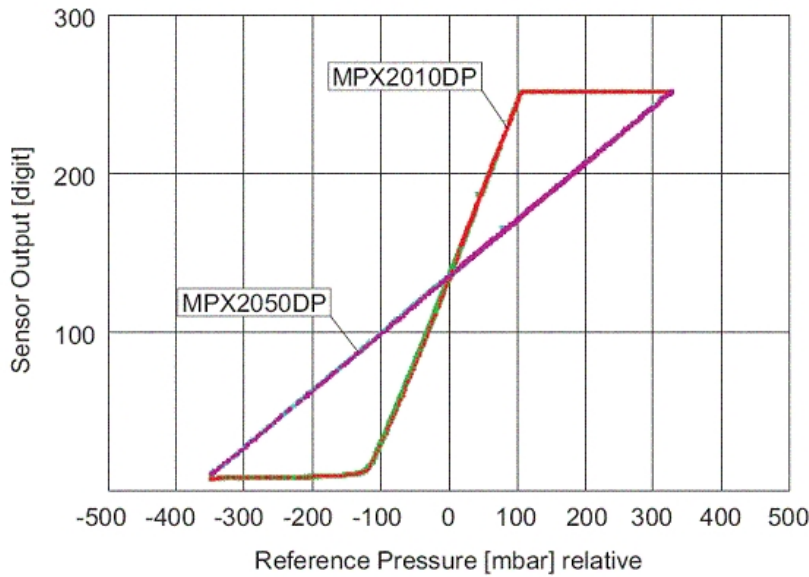


Figure 5.11.: Calibration curves of a pair of sensors (one 100 and one 500) recorded before (turquoise and green) and after (red and violet) irradiation with $1 \cdot 10^{11}$ neutrons/cm². There are no differences between the curves of the same sensors, i.e. the irradiation of the sensors at CMS will have no effect on them.

Sensor calibration

Calibration of the pressure sensors means to expose them to an outer pressure and measure simultaneously their output signal and the pressure by a reference manometer (Figure 5.13). Generally the outgoing electrical sensor signal is too small to provide a usable value, so it has to be amplified before being digitized. By these means, one obtains unique relations between the sensor output signals and the measured pressure. The sensors are calibrated when such value pairs are registered over the entire range of the sensors.

All pressure sensors for testing the muon chambers and for the final CMS operation period were calibrated in Aachen. Because of the total amount of sensors, which had to be calibrated (over 1000), and a relative short time for completing the calibrations (due to the fact, that the sensors with the manifolds had to be supplied continuously for chamber commissioning) a suitable calibration facility was developed and used in Aachen which allows a simultaneous calibration of 20 sensors (Figure 5.14). The sensors being calibrated were already mounted into the manifolds together with the final pre-amplifying as at the CMS. The monitored supply voltage of the sensors was regulated by a local voltage regulator at 5.0 ± 0.05 V.

Technically the calibration of each sequence of 20 sensors as shown in Figure 5.15 is performed in the following way: A negative pressure is generated in a large reservoir 4 by means of vacuum pump 11 and opened valves 17 and 18 (min. 0.5 mbar absolute). After the valves 17 and 18 are closed the valves 24 and 25 are opened. Now the other reservoir 5 is filled with Ar/CO₂ gas from the bottle 26 up to an overpressure of about 2.5 bar absolute. The valves 24 and 25 are then closed. The manometers 9 and 10 indicate the pressure in both reservoirs. When the valve 12 is open the sensors being calibrated 7 are subjected first to the negative pressure generated in reservoir 4. Opening the valve 13 or 14 causes gas to flow very slowly from the reservoir 5 via the leak valve 15 or 16, which is set to the necessary leak rate

5. Measurement of the gas pressure in the CMS DT muon chambers

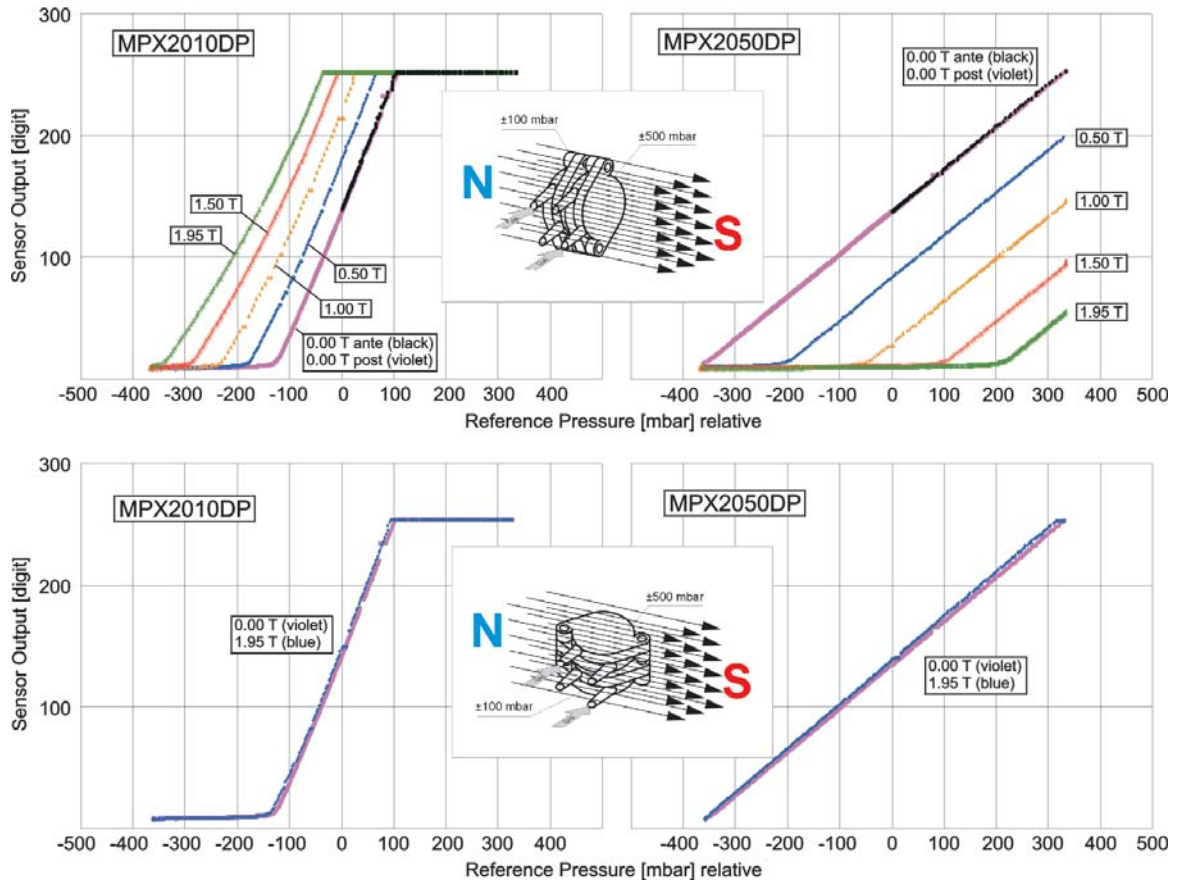


Figure 5.12.: Calibration curves of a pair of sensors 100 and 500 in membrane orientation perpendicular (above) and parallel (below) to the magnetic field lines. The magnetic field has no impact on reading of the sensors only if they are positioned parallel to the field lines (no shifts of the calibration curves).

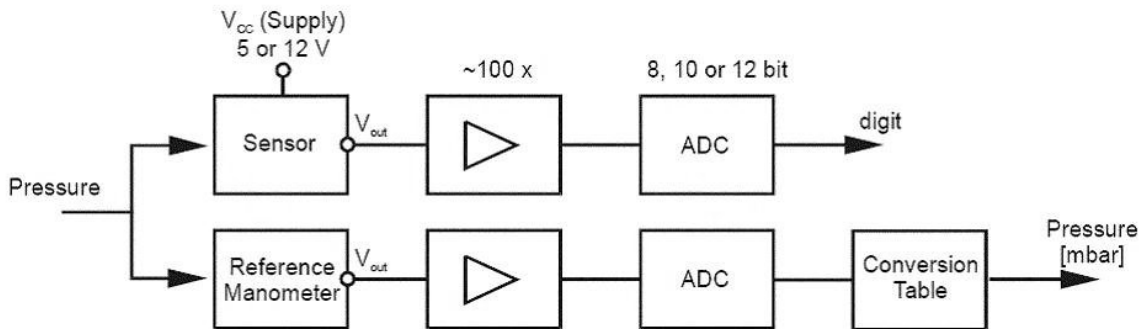


Figure 5.13.: Principle of the calibration of the pressure sensors. Before digitization (ADC) the output voltage of the sensors generally have to be amplified to match the ADC range.

(typically about 10% of gas per hour), into the reservoir 4 and to slowly vary the pressure at the sensors consequently. The current pressure at the sensors is indicated by a reference manometer 3 providing relative or – if needed – absolute pressure values. A second reference manometer 2 is used for the measurement of the atmospheric pressure. To avoid possible

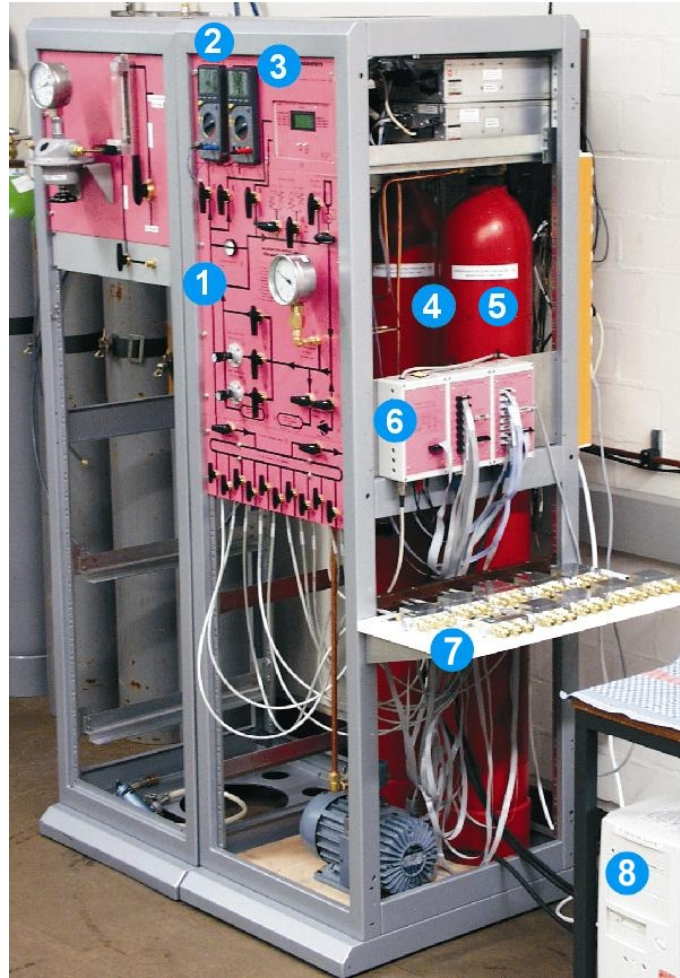


Figure 5.14.: The Aachen calibration facility for the pressure sensors (see also Figure 5.15). This system is mostly housed in a rack. All instruments can be controlled by manipulating the valves on the front panel (1). The pressure is monitored by the reference manometers (2). Inside the rack one can see the two reservoirs (3) for the positive and negative pressure. The sensors being calibrated are already in the manifolds (5) and are connected to the gas. The outputs of the sensors and manometers are plugged to the electronics boxes (4) which are connected to a PC (6) where the read-out at regular intervals, data check, averaging and generation of the data files is performed automatically via software.

damage of the sensors at too high or too low pressure safety valves for positive and negative pressure (19 and 20) are mounted. They act when the valves 21 or 22 are open. An outlet valve 23 is used to put the calibration system to ambient pressure.

For the measurement of the reference pressure two *MKS Baratron* manometers (baratrons) are used [91]. One of them measures only the ambient pressure, the other one provides the actual reference gas pressure at the point where the 20 sensors to be calibrated are connected. The system contains additionally another set of reference manometers PG4, which uses two sensors 100 and two sensors 500 calibrated in earlier tests. They could be used for coarse pressure information and serve to test long-term repeated calibration of themselves with a high-resolution ADC.

5. Measurement of the gas pressure in the CMS DT muon chambers

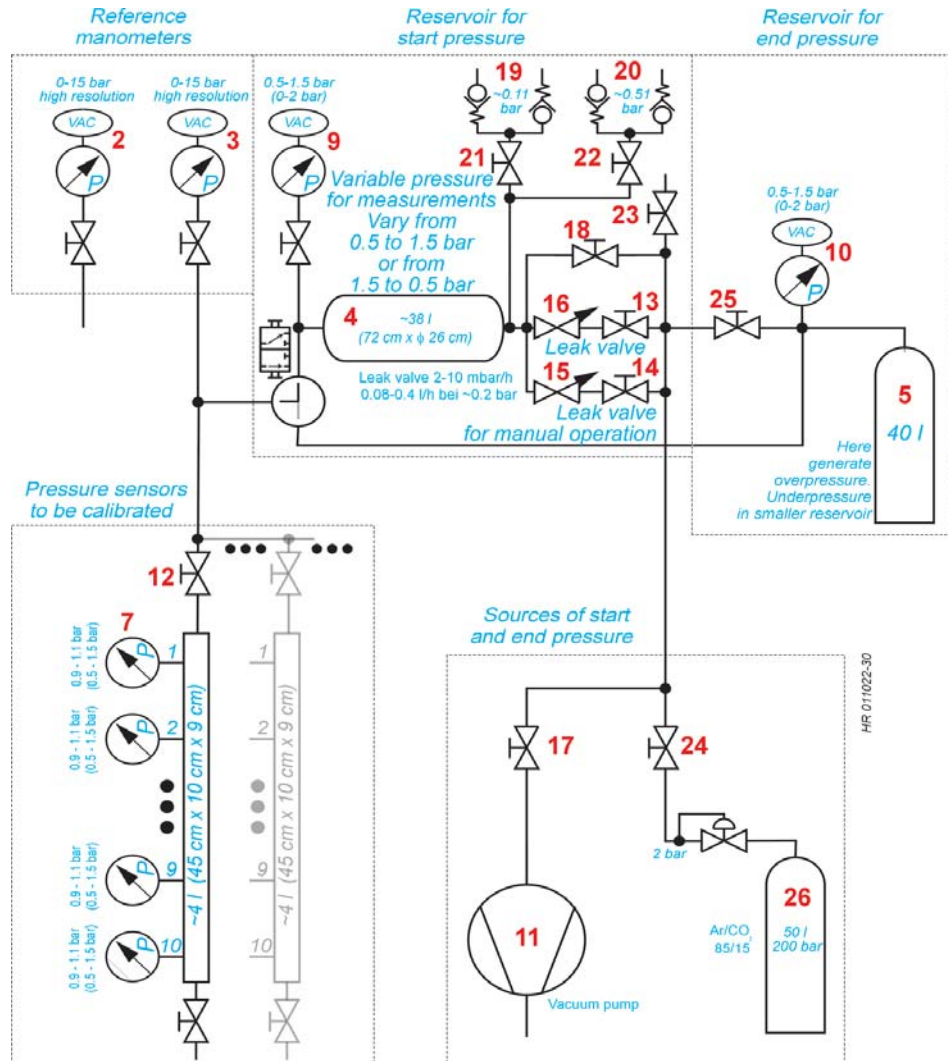


Figure 5.15.: Diagram of the calibration of the gas pressure sensors. The gas flows slowly from the reservoir where it was previously confined into the other one where a negative pressure was created passing by the point to which the pressure sensors are connected. The sensor outputs are registered in common with the outputs of the reference manometers by a PC (not pictured in the diagram) [93].

The outputs of all the manifolds with the sensors inside being calibrated, reference manometers outputs, as well as the actual supply voltage provided to the pre-amplifiers are connected via two link boxes to the analog channels of two *National Instruments* PCI modules NI6014 in a PC where they are digitized⁴ [92]. They are two multifunction DAQ featuring 16-bit resolution with 16 analog inputs and 10 digital input/output lines (and other features which are not essential for the sensor calibrations). An already existing *LabVIEW* environment based software (actually *kalibrationV1.5.vi*), especially developed for this purpose, is used to take and save the digitized data of the connected gauge (Figure 5.16) [94].

After the calibration system is prepared and before data taking can start, one has to choose

⁴This ADC with its high resolution is used for calibration purposes only, and is not the final PADC used in the CMS, which has 10 bit resolution. The smaller calibration errors should therefore have no impact on the final measurement errors while running CMS.

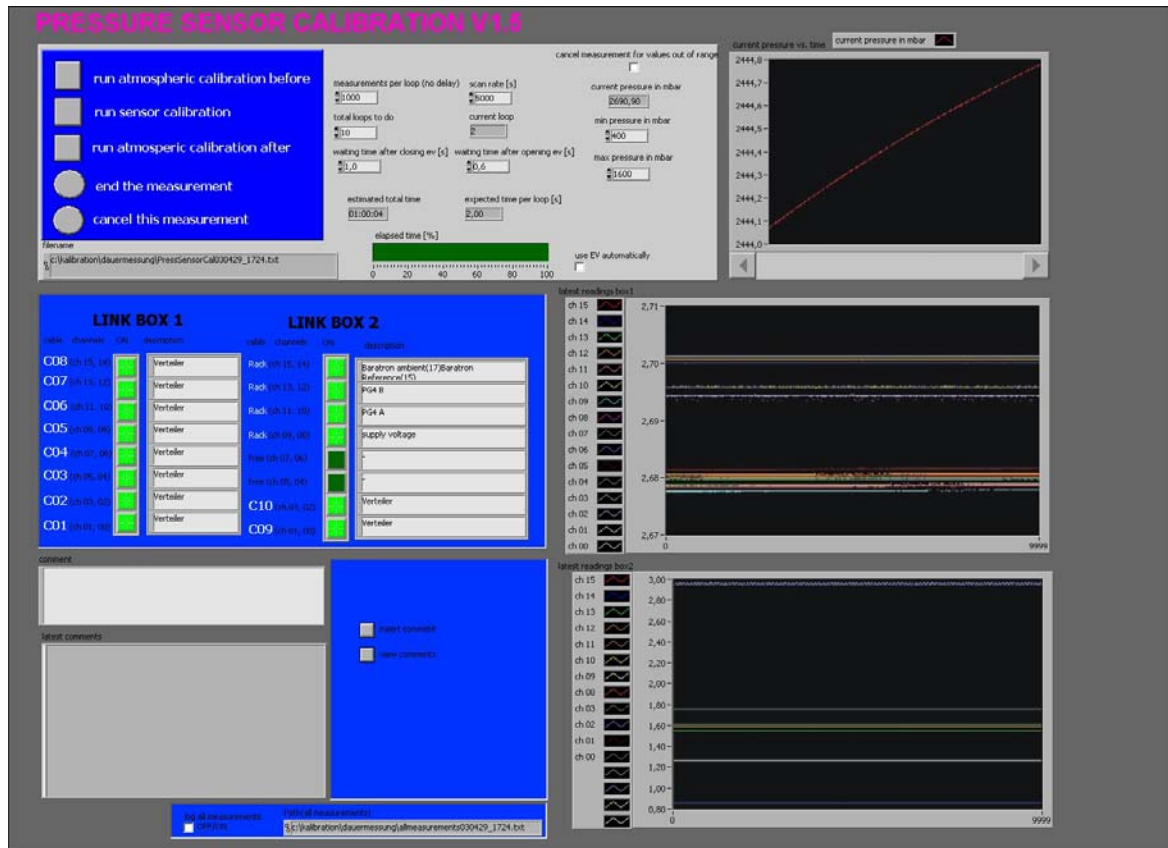


Figure 5.16.: User interface (front panel) of the software used for the calibration of the gas pressure sensors [94]. One can enable the channels which belong to the connected sensors being calibrated. The pressure and signal variation can be observed in the diagrams belonging to the enabled channels. The data taken during the calibration and other information and comments are then saved into a text file, whose path is also displayed in the front panel.

on the software panel (Figure 5.16) some options and conditions on which the data should be taken. Knowing the values of start pressure in the reservoirs for positive and negative pressure and the gas flow valve rate as described before one can estimate the entire time for the calibration and select accordingly the scan rate (the output sensor data are read not continuously but at given time intervals). Each measurement value (loop) is then registered as an average of a number of measurement points (default is 1000) and their standard deviation, as taken during a very short time (ms). It is recommended to execute a reference measurement at ambient pressure in this same way before and after the sensor calibration is done to check the behavior of a possible offset during the calibration. After about two hours, which is the time required for exposing the sensors to their entire pressure range (from about -500 mbar to $+500$ mbar), the calibration is completed and the raw data are saved in a text file for further analysis.

Calibration output data

During the calibration measurement a text file is created automatically containing all data taken (reference raw data file, see Appendix C.1). Experience showed that not always the

5. Measurement of the gas pressure in the CMS DT muon chambers

calibration measurement performed on a group of manifolds is valid for each manifold or sensor which has been calibrated in this run. Even the whole calibration run for all manifolds could be invalid because of wrong parameter set, electronic connection etc. Nevertheless the data of each calibration run are saved for possible further analysis. On that score it is important to have a list of all calibration runs with the ID of the calibrated devices (manifold serial numbers), with comments and the assignment of a reference run for each calibrated manifold. This information is saved in a spreadsheet file ([95], Appendix C.2).

On the basis of the data taken, a first quality analysis of the calibrated sensors as well as of the baratrons is done. For this purpose one considers for each measurement point k (1000 measurements) its average p_k , its standard deviations and the smoothness d_k defined as

$$d_k = \frac{p_{k-1} + p_{k+1}}{2} - p_k \quad (5.1)$$

where p_{k-1} , p_k and p_{k+1} are the following measurement points (loops). The typical sensor output with registered standard deviation for a sensor 100 during a calibration run is presented in Figure 5.17. For each calibration run a calibration report is created ([95], Appendix C.3).

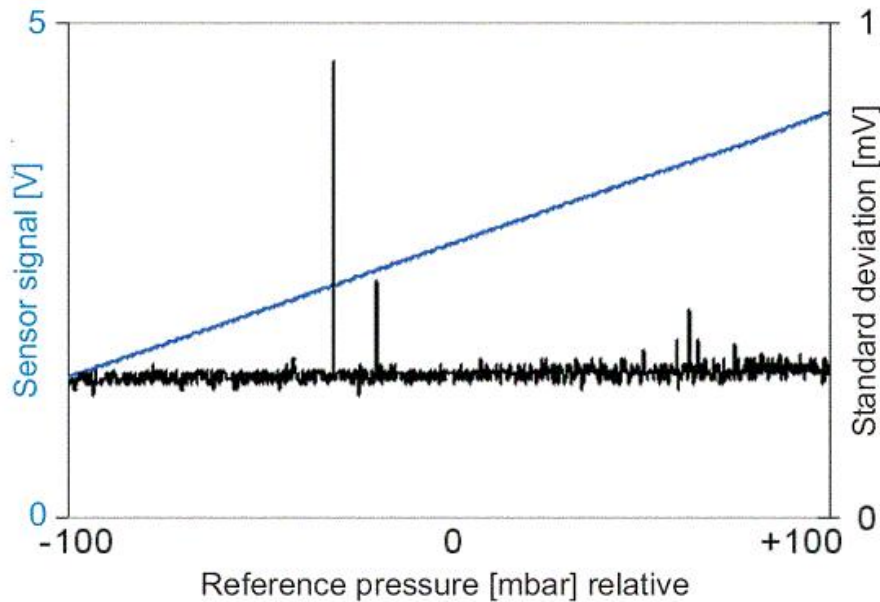


Figure 5.17.: Sensor output values (blue, left scale) in correlation with the reference pressure shows a precise linearity. Each point is the average of 1000 measurements. The standard deviation of each point (black, right scale) is below 1%. The data shown were registered with a 16 bit ADC for one sensor 100 and are representative for all sensor units and types [95].

As mentioned before, the data taken during a calibration run show indeed a time sequence of the device output values. Due to the fact that the data are taken at the constant time intervals and because of the non-linear pressure change in time by gas flowing from the reservoir with overpressure to the reservoir with negative pressure one obtains much more measurement points in the upper measurement sensor range than in the lower one. To obtain a very homogenous and sufficient distribution of the sensor output voltages vs. reference pressure the raw data have to be processed.

For this purpose another *LabVIEW* software, *SensCalV2.0.vi*, was developed (see Appendix B.1). When it runs the actual reference raw data file is then automatically extracted using the calibration run list for demanded manifolds previously selected. The raw data are then read and the user can check for each sensor data sequence whether the data taken show any irregularities and decide, if they are qualified for further use. If yes, the correct calibration range, visible as linear part of the curve, is specified and the procedure is accepted.

The max. possible complete range (voltage) of the raw data is then usually divided into 4096 intervals. Within this range a calibration range with nearly linear shape is selected, which contains usually $O(3000)$ of the mentioned 4096 intervals. In each of these selected intervals one average value is estimated by a local linear fit. This means that only several measurement points within the selected local intervals are fitted by a line. This method improves the quality of the processed data because the registered calibration curve based on the raw data is not exactly linear in the sensor measurement range. Moreover, an attempt to fit another function to the whole raw data curve was not useful. The global selection for 4096 values ($O(3000)$ and the rest outside the fitted area) is needed to ensure a very good approximation of the averaged value to the real measured points, what is shown in the very low values for standard deviations and smoothness calculated for each fit ($\%_0$ order).

When the data are accepted the program processes the raw data of the other sensor being in the same manifold. When also these recalculated data are accepted, a new text file is created automatically which includes the converted sensor calibration data. **These conversion files are finally used for creation of the Look Up Tables for the gas pressure read-out providing the relation between pressure and output voltage of each sensor mounted in the manifolds at the CMS DT muon chambers.** The procedure is then repeated for each manifold and sensor.

5.3.3. Pressure Analog to Digital Converter (PADC)

The outgoing analog sensor signal (voltage) depends strictly on differential pressure and should be digitized to obtain information about the pressure values. The digitization should occur locally, as close to the sensors as possible to reduce measurement uncertainties and ambiguities. Also the fact that the control unit CCB is placed directly on the chamber, was a further reason to make the digitization device small and suited for operation in the direct environment of the chamber. A board *Pressure Analog to Digital Converter* (PADC) [96] was developed, produced, tested and installed at the CMS DT muon chambers for these purposes.

PADC features and tests

First considerations led to the concept of a PADC which is able to digitize the analog signals and to immediately convert them into pressure values. The LUT (Look Up Tables, see Section 5.4) would have to be then saved directly inside the PADC. For this concept, beside a microcontroller and an ADC also an EEPROM⁵ would have been needed for storing the LUTs. However, the tests with the microcontrollers (e.g. AT90S8535 by *Atmel*) showed, that a lot of software efforts is needed to get a reliable version of a PADC with this equipment. Finally it was decided to develop a PADC board containing only one 10 bit ADC component (MAX1138 by *Maxim Integrated Products*) with 12 analog inputs [97]. This ADC has no additional functions like storage, control and data processing, so that the conversion of the counts into real pressure values by means of the LUTs must be done outside the PADC [98].

⁵Electrically Erasable Programmable Read-Only Memory

5. Measurement of the gas pressure in the CMS DT muon chambers

The following 10 of 12 analog channels are connected on the PADC (Figure 5.18): sensor 100 from manifold HV (twice), sensor 500 from manifold HV, sensor 100 from manifold FE (twice), sensor 500 from manifold FE, manifold HV supply voltage, manifold FE supply voltage, two PADC supply voltages (local down-stream and local up-stream stabilized). The remaining two channels are used for internal ADC checks. The simultaneous measurement of the gas pressure and the supply voltages allows to check in case of possible read-out instabilities if they are caused either by the supply voltages or in fact by the measured pressure (for right sensor read-out the supply voltage must always remain constant). Moreover, even during a possible drop of the sensor supply voltage one is able to reconstruct the true pressure values due to the linear relation between the sensor analog read-out and the supply voltage (Section 5.3.2).

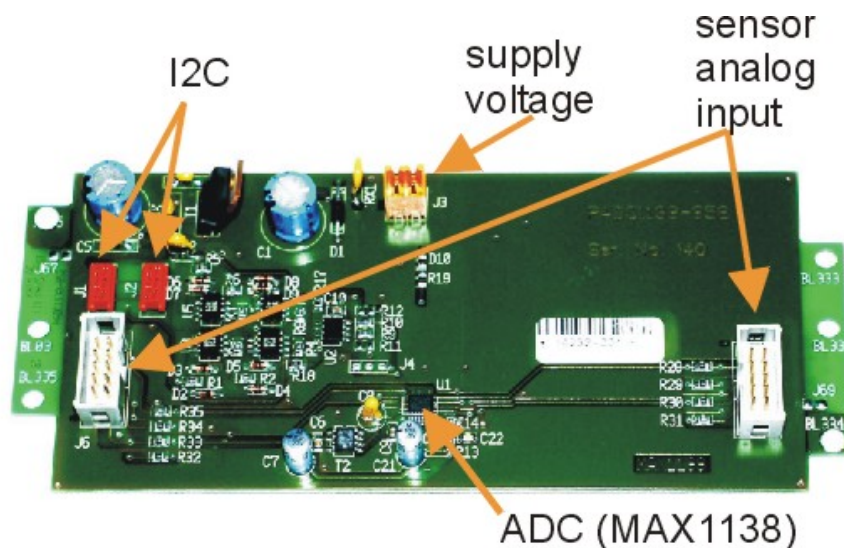


Figure 5.18.: The PADC for digitization of the pressure sensor output of the CMS Muon Chamber. The following channels are connected and digitized with 10 bit resolution: sensor 100 from manifold HV (twice), sensor 500 from manifold HV, sensor 100 from manifold FE (twice), sensor 500 from manifold FE, manifold HV supply voltage (local down-stream stabilized), manifold FE supply voltage (local down-stream stabilized), two PADC supply voltages (local down-stream and local up-stream stabilized). The read-out of the PADC is performed via an I²C bus.

For the transfer of the digitized data an I²C bus is used with a transmission frequency 1 kHz [99]. The I²C function is secured by an I²C driver U2 (P82B715). The interface to the PADC is accomplished by two optical couplers HCPL0701 which provide feedback-free data transmission and ensure, that the I²C bus operates even in case of a failure in the PADC unit. The PADC is installed in a standard aluminum housing and placed on the HV side on the CMS Muon Chamber. It uses I²C bus in common with the alignment diodes which are also placed on the chamber sides. The read-out and control of the PADC is performed via the mentioned CCB.

The sensors, the pre-amplifiers and the PADC must be tested under LHC conditions before mass production and installation. Therefore the operating PADC was tested in an irradiated state, in a magnetic field and at higher temperature.

To perform the irradiation tests several PADC boards were first irradiated by a proton beam

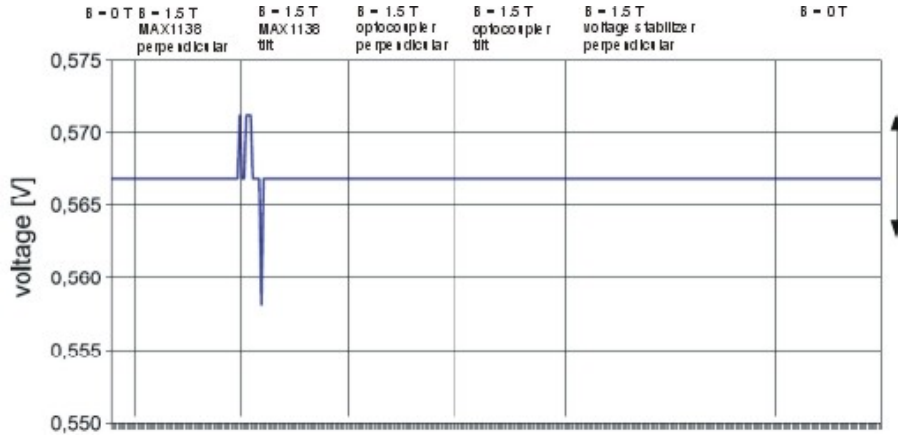


Figure 5.19.: The read-out values of the PADC working in a magnetic field. The region of the PADC with the strongest field value and the position relative to this field was changed during the test. Also a reference run at 0 T was done. The spikes within a range of about three counts in the voltage scale are caused by a contact the PADC with a magnet pole. Generally the magnetic field does not affect the functioning of the PADCs in the CMS experiment [98].

with energies up to 171 MeV. The total dose applied to the PADC was 1.4 krad. Then the neutron irradiation test was done with an average neutron energy of about 3.5 MeV (maximum around 20 MeV). The flux onto the PADCs was $1 \cdot 10^{11}$ neutrons/cm², which corresponds to about 10 years operation of LHC (see also Section 5.3.2). The PADCs passed all irradiation tests [100] without damage.

For the magnet test the PADC was placed between poles of an electromagnet, which provide a local magnetic field of about 1.5 T. Due to the limited size of the magnet, this field was homogenous only in a small area between the poles, one had to move the PADC in such a way that all PADC components encountered this value. Furthermore, one PADC was tested in an inclined position to investigate, if the possible influence of the magnetic field depends on the PADC orientation relative to it. Also the MAX1138 alone was prepared for tests in different orientations (parallel and perpendicular relative to the magnetic field). A reference run was done at the beginning and at the end of the magnet test. The output data taken at a constant pressure show a mostly constant behavior (Figure 5.19). The irregularities (spikes in an interval up to three counts) in the output data appeared for a very short time and are caused by an accidental electrical contact of the MAX1138 with a magnet pole.

Finally a temperature test was done. The data were taken first at the room temperature ($t = 25^\circ\text{C}$) and then repeated at $t = 45^\circ\text{C}$. Comparing the output data one finds no read-out differences (± 1 bit allowed) between both runs [98].

PADC calibration [98]

As mentioned above the following PADC channels are assigned to analog inputs:

- Channel 0: manifold HV side, sensor 100;
- Channel 1: manifold HV side, sensor 100;
- Channel 2: manifold HV side, sensor 500;
- Channel 3: manifold HV side, $V_{cc}/2$, preamplifier supply, downstream stabilizer;
- Channel 4: manifold FE side, sensor 100;

5. Measurement of the gas pressure in the CMS DT muon chambers

Channel 5: manifold FE side, sensor 100;
 Channel 6: manifold FE side, sensor 500;
 Channel 7: manifold FE side, $V_{cc}/2$, preamplifier supply, downstream stabilizer;
 Channel 8: PADC $V_{cc}/2$, downstream stabilizer;
 Channel 9: PADC and manifolds $V_{dd}/2$, upstream stabilizer.

The digitized values (counts) of each channel can be calculated for each input value using the technical data of the MAX1138 and cross-checked with the actual output of the ADC. One expects a linear relationship between the analog inputs and the corresponding digital counts on the PADC output channels. In fact, this calibration is a linearity check of the channels 0 to 7. For these channels the scaling factors and the offset are measured. The channels 8 and 9 measure the constant PADC supply voltages; for these channels it is only crucial to obtain a constant value during the whole measurement period. Their calibration is limited to the measurement of this one point which serves as offset check.

The schematic PADC calibration setup is presented in Figure 5.20: The analog signals are software generated by PC in two cards NI6014 (National Instruments). Each of these cards has two DACs (Digital to Analog Converter), thus two analog outputs. The four generated analog signals are at first filtered (Link Box, containing the filter electronics). Then each of them is split in two lines in such a way that the analog voltage can be connected to an analog input of the original NI6014 where it is re-digitized. These re-digitized values are used for monitoring and as reference of the PADC calibration. The main lines are connected to an AK (*AnschlussKarte*) box, where each of the analog signals is uniformly split and distributed to the ten PADC channel inputs which are to be finally used during the PADC operation. The counts of the PADC channels are then transferred via an I²C/RS232 bus to the PC. The re-digitized values from the NI6014 cards and the counts from the PADC are taken in parallel and stored in a text file which is generated automatically.

The *LabVIEW* software [101](version *040826_PADC_kalibrationV1.1.vi*) used for the PADC calibration controls the analog outputs, digital inputs on the NI6014 and the PADC read-out via RS232. The generated analog inputs start at 0 V and are incremented in steps of 1 mV up to 4.5 V (maximum voltage handled by the PADC). In every loop the NI6014s are read out 1000 times and their average value together with the standard deviation is sent to the PC via PCI. A text file with all measured data and calibration parameters is automatically created.

Comparing the counts of the same analog NI6014 channel re-digitized by NI6014 (nominal voltage, U_{nom}) and by the PADC (measured voltage, U_{meas}) using the resolution 16 bit and 10 bit for NI6014 and PADC, respectively, one expects in a diagram a homogenous dispersion of U_{nom} about U_{meas} for the 4500 measurement points. The average difference $U_{nom} - U_{meas}$ should then be 0. However, the electronics (mainly voltage dividing by resistors on the PADC) affects the signal amplitude and one finds in this case a distribution of the data which can be handled as a linear fit

$$U_{nom} - U_{meas} = a \cdot U_{nom} + b \quad (5.2)$$

where the parameters a (dimensionless) and b (in mV) are the slope and offset, respectively (Figure 5.21) and are calibrated by the present measurement.

The calculation of the parameters a and b by fitting the counts allows to correct the measured values. This corrected voltage U_{corr} is calculated for the PADC channels 0 to 7

$$U_{corr} = A \cdot U_{meas} - b \quad (5.3)$$

where $A = 1/(1 - a)$ is the scaling factor (Figure 5.22).

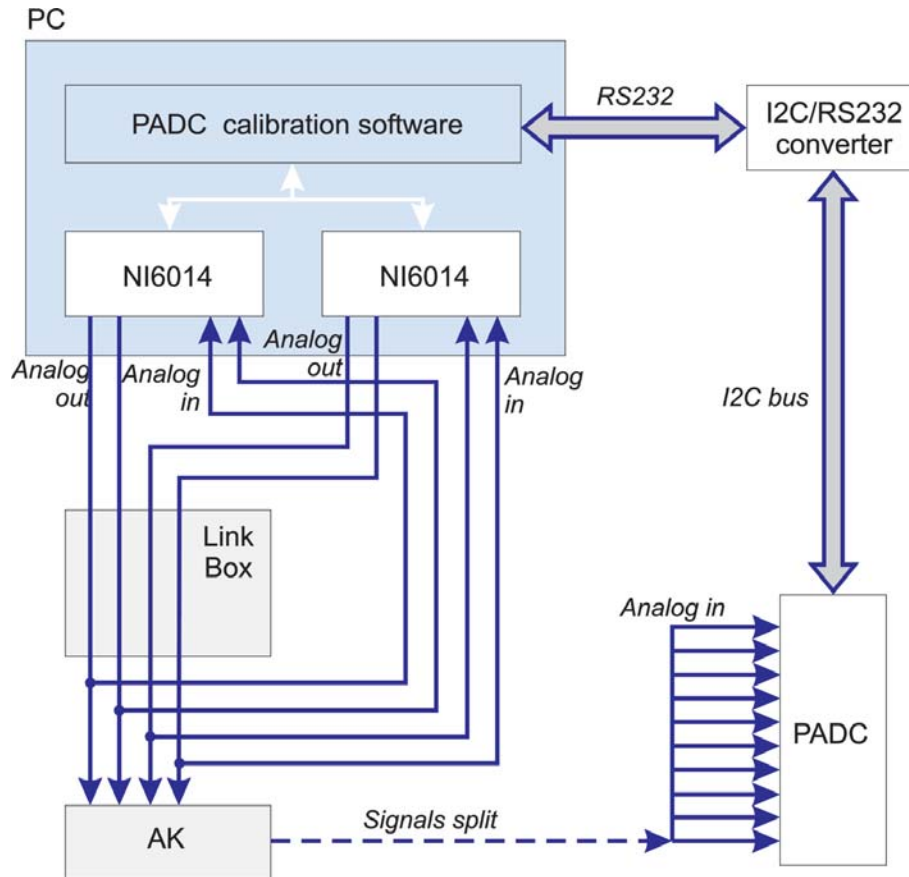


Figure 5.20.: The PADC calibration scheme. The analog signals are generated by two NI6014 DAQ cards. After passing the Link Box they are split: one of the lines is re-digitized by the NI6014 cards and the other one is used for signal distribution to ten PADC channels. The digitized values from NI6014 and PADC are simultaneously measured and stored in a file.

The typical values are: $A = 1.001$ (for channels 0, 1, 2, 4, 5 and 6), $A = 1.999$ (for channels 3 and 7) and $b = -0.001$ (for all channels). **These two values A and b are then the second source for creation of the Look Up Tables for the gas pressure read-out of the CMS Muon Chambers. They provide the correction for the digitized sensor output signals by the PADC.**

A quality measure for the PADC is the difference $U_{nom} - U_{corr}$ which should remain below a limit of ± 3 mV for all channels. This limit, whose the total width is about 1.5 PADC count was chosen in accordance to the final resolution of the gas pressure measurement (about 0.3 mbar for sensor 100 and about 1.3 mbar for sensor 500). A PADC is declared good if these error limits are crossed by less than five of the 4500 measurement points in each channel (under 1.1‰ in the entire measurement range). For channels 8 and 9 the offset is calculated which is the difference between the measured and expected voltage (2.5 V for channel 8, 3.0 V for channel 9).

Both the original PADC calibration data and the evaluation parameters A and b of each PADC channel are then saved in a file [101]. This file contains also the standard deviation, smoothness and other additional information and comments. The file is generated automatically at each calibration run.

5. Measurement of the gas pressure in the CMS DT muon chambers

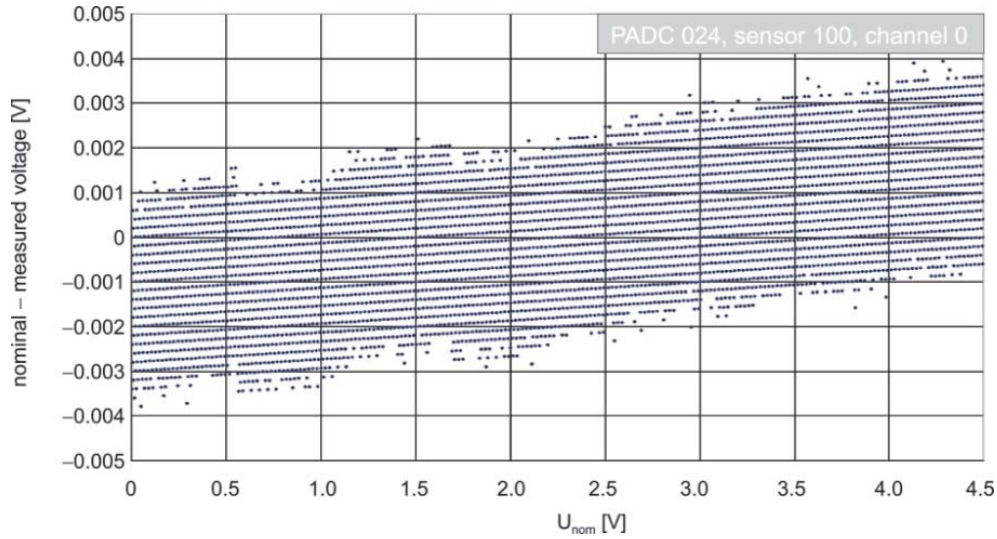


Figure 5.21.: The difference $U_{nom} - U_{meas}$ taken for 4500 measurement points (i.e. U_{nom} up to 4.5 V). Each of these points represents 1000 actual measurements. The distribution around the nominal voltages shows the expected behavior for the PADC resolution. A precise slope and offset are extracted from this diagram [98].

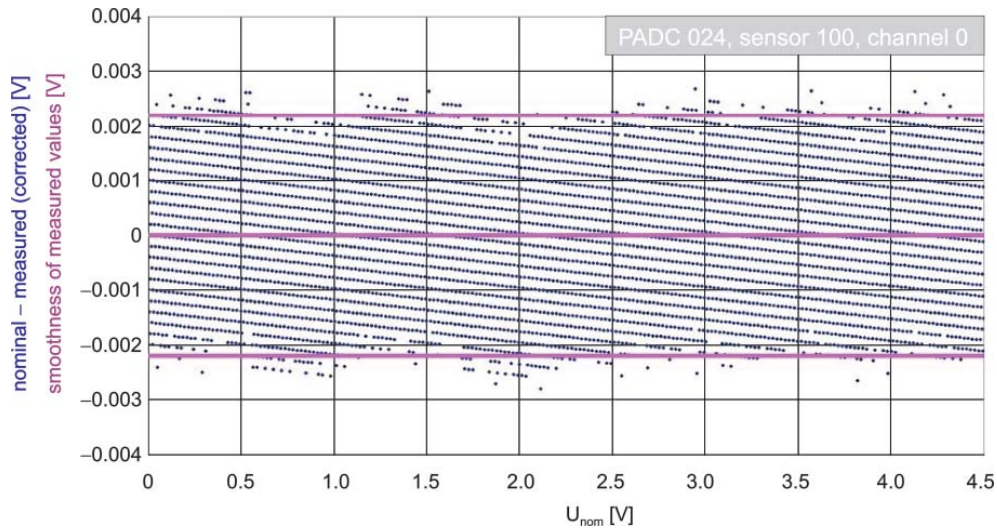


Figure 5.22.: The same distribution of Figure 5.21, after slope and offset are accounted for. Due to the different resolutions of the NI6014 and of the PADC, the smoothness of the data calculated as in Equation 5.1, should have only values -2.2 , 0 or $+2.2$ mV [98].

5.4. Look Up Tables (LUTs)

One CMS DT muon chamber is equipped with two manifolds, each with two gas pressure sensors of different range, and one PADC which digitizes the sensor output signals. The manifolds with their sensors inside and the PADC were calibrated separately, providing two different conversion tables: pressure to voltage (sensor calibration) and voltage to counts (PADC calibration). As already mentioned in Section 5.3.1, a final conversion table, *Look Up*

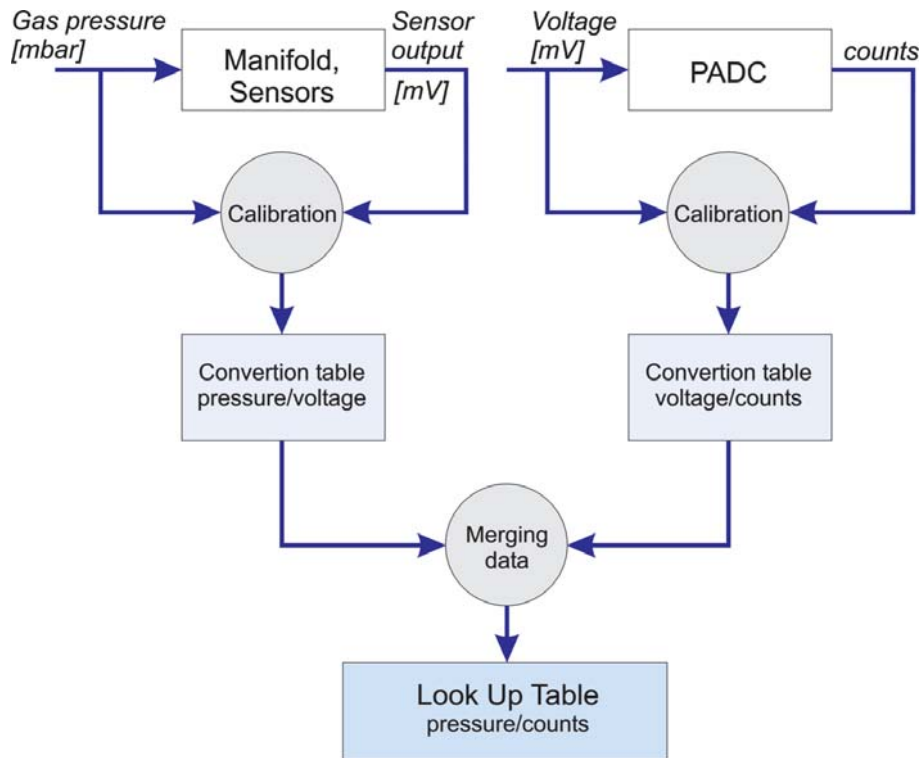


Figure 5.23.: A Look Up Table is created by merging the data of the calibrations of the gas sensors with the data of the calibration of the PADC. It contains the pressure values for direct conversion of the PADC counts.

Table (LUT), is needed which merges the data from both calibrations. This table contains a list of pressure values corresponding to the PADC counts (Figure 5.23).

The processing of the LUTs has to accurately take in account the unique assignment of the manifolds and PADCs, which all have their own serial numbers, to the 250 chambers in the CMS detector, as assigned by their CMS position and chamber type. For this assignment and merging of calibration data a reliable software system had to be developed to ensure the fully automatical creation of the 250 LUTs using the databases where the assignment and calibration data are stored.

5.4.1. Data for the LUTs

Chamber position data, manifold and PADC IDs

After the manifolds and PADCs are successively produced and calibrated in the Phys. Inst. III A in Aachen, they are shipped for installation to CERN. They are then mounted on the chamber together with other devices and the fully equipped chamber is finally installed in the CMS detector. The DCS software, which monitors – among other parameters – the gas pressure in the CMS muon system, needs to be provided with information about the exact place where the gas pressure is measured in the experiment and, of course, by which devices (manifolds and PADC) the pressure measurement is performed. Therefore a LUT for pressure read-out of a chamber has to contain the chamber identification data and ought to be created using the calibration data of exactly those devices, which are mounted on the chamber.

In detail, the following chamber and device information is required for the right assignment

5. Measurement of the gas pressure in the CMS DT muon chambers

of the LUT to a chamber:

- **Chamber position.** Three values characterize the position of a chamber in the CMS detector:
Wheel: +2, +1, 0, -1, -2.
Sector⁶: 1, 2, 3, 4 (4s, 4d), 5, 6, 7, 8, 9, 10, (10s, 10d), 11, 12.
Station: 1, 2, 3, 4.
- **Chamber ID.** This ID is a chamber serial number given to it at the production centers during the chamber production period. The number format of the ID is individually chosen and is represented mostly by two-digit integer up to 70. The IDs are not unique, they rather vary for each chamber type. Of course different chambers of the same type must have different IDs, but some chambers of different type could have the same IDs. This is particularly apparent for the MB4* chambers (chambers in station 4) where in almost all sectors chambers of different size (i.e. different type) are installed [37]. Also other chamber types, especially these of one type, which were produced in different production centers could be presented by the same ID.
- **Manifold and PADC IDs.** To each manifold and to each PADC, which all were produced in Aachen, a serial number was assigned. This number is represented by a three-digit integer.
- **Manifold position on a chamber.** Each CMS DT muon chamber is equipped with two manifolds, one on the HV side, the other on the FE side. Beside of the manifold ID an information about the manifold position on the chamber is needed for correct assignment of the sensor outputs to the PADC channels.

Several databases maintained on CERN servers contain all position data of each chamber installed in the CMS detector. Aside from the data of wheel, sector and station the databases contain also the chamber ID and the chamber type. The chamber type is rather not directly needed for creating the LUTs, but essential to prevent ambiguities in using the chamber ID. An example for such a database is presented in Appendix C.8 [102]. The information being stored there is actually used for the creation of the LUTs.

A further database is used for tracking the assignment of manifolds and PADCs to chambers [103] (see Appendix C.9). It includes the IDs of the manifolds and PADCs, belonging to a chamber whose ID and type are also listed in this spreadsheet; also the manifold position (HV or FE side) on the chamber is given there. This file is successively updated by the operator doing maintenance when replacing or adding new components.

Due to the fact that both mentioned databases contain information about the chamber ID and type these two last values are the interface to merge the database contents. **The finally obtained set of seven numbers: wheel, sector, station, chamber ID, PADC ID, manifold HV side ID and manifold FE side ID is unique and used for the right assignment of the created LUTs.**

⁶In station 4 (chambers of type MB4*) the muon chambers in sector 4 and 10 are partitioned in two, due to some technical requirements. They are additionally assigned by *s* and *d* corresponding to their relative FE side position, left (*sinistra*) and right (*dextra*).

Manifold and PADC calibration data

The sensors used for gas pressure measurements in the CMS Muon Chambers provide an output signal, which is simply a voltage. Its value depends on gas pressure and ranges from 0 up to +5.0 V. This voltage is then digitized by 10 bit PADC providing 1024 counts each corresponding to a pressure value. The right value pairs pressure/count can be found by means of the Look Up Tables.

For the LUT creation the following data are needed:

- **Sensor calibration data.** As mentioned in Section 5.3.2 the raw data of sensor measurement runs are stored in calibration raw data files (Appendix C.1). Then they are checked offline and one can decide, whether the sensor calibration was done well and the sensor is good. The values are then recalculated, filtered and smoothed by a local linear fit and stored in the conversion files (Appendix C.4) for the LUT creation.
- **PADC conversion factor.** The MAX1138 component installed on the PADC board digitizes the analog signals with 10 bit resolution. To obtain the voltage on the input of the PADC one has to multiply the read out count with a factor $(4.5 \text{ V})/1023 = 4.3988 \text{ mV}$, where 4.5 V is the PADC reference voltage. This factor is used for the analog input (voltage) conversion for each PADC channel.
- **Scaling factor and offset (PADC calibration data).** To correct the PADC read-out a scaling factor and offset shift of the sensor outputs is needed (Equation 5.3). These two parameters can be found in the PADC calibration header file (Appendix C.5).

5.4.2. LUT creation

LUT processing

A *LabVIEW* based software *LUT_PADC.vi* was developed, which creates the Look Up Tables (see Appendix B.3). This software runs fully automatically loading first chamber and device identification data from external databases (see Section 5.4.1) or optionally from a table edited by the operator. Then the proper calibration files of the manifolds and PADC stored in the local PC are loaded. The processing of the calibration data occurs then in the following steps:

1. **For all PADC channels 0 to 9:** The PADC counts n from 0 to 1023 are converted into the voltage values, using the multiplying factor 4.3988 mV/count (channel 0, 1, 2, 4, 5 and 6) or 8,7976 mV/count (channel 3, 7, 8 and 9).
2. **For channels 0 to 7:** The calculated voltage values in step 1 are now corrected with the scaling factor A and offset b which are read from the conversion file (Appendix C.4) for each channel using the Equation 5.3. The corrected values $U_{n, \text{corr}}$ of channel 3 and 7 are finally ready for the LUT.
3. **For channels 0, 1, 2, 4, 5 and 6:** The corrected voltage values in step 2 are now converted into the pressure values. For this purpose, the calibration data of both sensors in a manifold are taken from the conversion file (Appendix C.4). For the manifold mounted on the HV chamber side the data are used for the PADC channels 0,1 (sensor 100) and 2 (sensor 500); for the manifold mounted on the FE chamber side the data are used for the PADC channels 4,5 (sensor 100) and 6 (sensor 500).

5. Measurement of the gas pressure in the CMS DT muon chambers

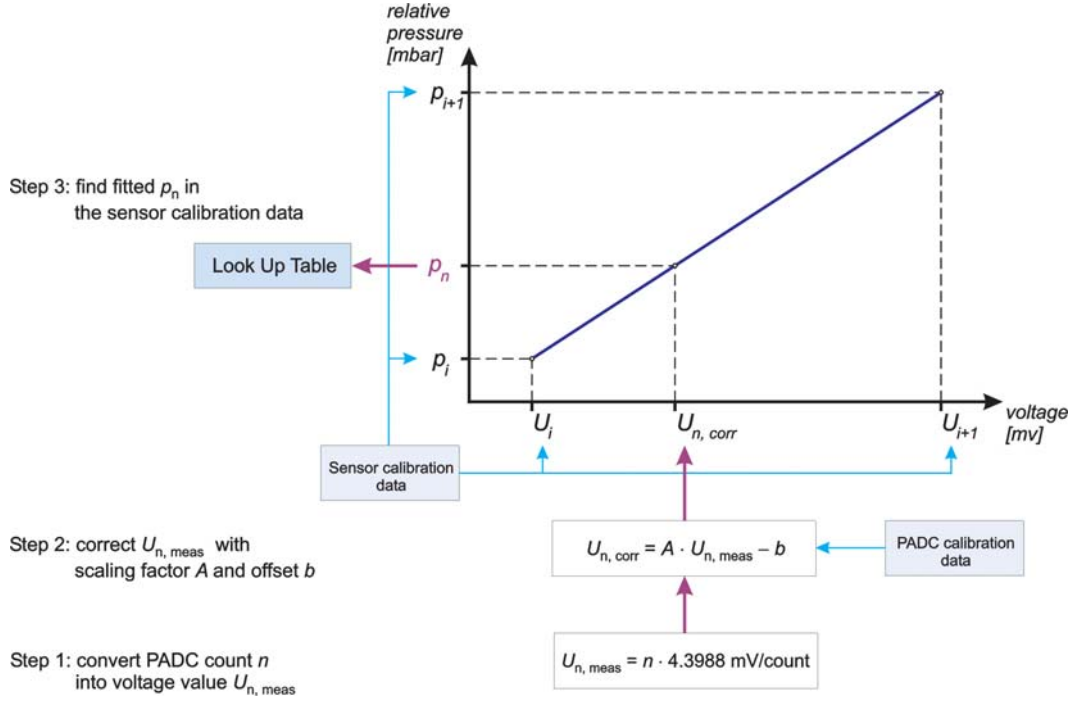


Figure 5.24.: The pressure values p_n for Look Up Tables are found by three steps. First the PADC counts n are converted into the voltage values by the known conversion factor. Then they are corrected by scaling factor A and offset b which are estimated in the PADC calibration. Finally the corrected voltages $U_{n, \text{corr}}$ for each n are fitted into the sensor calibration data and the interpolated values p_n are written into the LUT.

For the corrected voltages $U_{n, \text{corr}}$ from step 2 two sensor output values U_i and U_{i+1} as entries following each other in the conversion file should be found, which form an interval where the $U_{n, \text{corr}}$ can be local fitted by a linear approximation. For this fitted $U_{n, \text{corr}}$ the pressure p_n can be estimated

$$p_n = \frac{U_{n, \text{corr}} - U_i}{U_{i+1} - U_i} \cdot (p_{i+1} - p_i) + p_i, \quad (5.4)$$

where p_i , p_{i+1} are the corresponding pressure values for U_i , U_{i+1} , respectively in the tables in the conversion files (Figure 5.24).

During the data processing one Look Up Table per one PADC (i.e. per one chamber) is created and saved in a text file (Appendix C.6). When all LUTs have been created, a summary report is written (Appendix C.7). Both the LUT files and the summary file are then placed in the Aachen database (Appendix C.10).

5.5. Gas pressure system tests

The DCS pressure system of the CMS DT muon chambers has to be tested for its functionality and correctness before use in the regular LHC run. Regarding the procedures described in the previous parts of the current section, to ensure a reliable gas pressure system, tests concerning two principal aspects should be done. On the one hand, it is important to be sure

that the calibration data are valid and reproducible for each sensor/manifold/PADC combination. On the other hand the read-out of the sensors during the usual detector run must be verified to make sure, that the sensors and PADCs always provide correct data of the pressure measured inside the chamber.

5.5.1. Verification of the sensor calibration

Sensor stability

During the sensor calibration measurement the output signals of the sensors and baratrons (reference manometers) were taken also at the ambient pressure in two independent sequences (zero-sequences, see also Section 5.3.2). The first sequence, consisting of ten measurement points⁷, was taken at the beginning of the measurement run before the main sequence (i.e. the sequence with varied pressure). The second one, consisting also of ten measurement points was always taken at the end of the run after the main sequence. The time difference between these both zero-sequences was usually about 2–3 hours. In the ideal case one sensor should provide the same output value in both zero-sequences and in each measurement point, due to the fact that the sensors measure the pressure relative to the ambient pressure. Thus the output, measured in mV, of every sensor in these zero-sequences should correspond to the relative pressure value 0 (mbar). Note, that for this data point no reference manometer is needed.

Independent of the real pressure value, by assuming a sensor works well, its voltage output should have the same value in both zero-sequences (labeled from now as *before* and *after*). Thus the output difference

$$\Delta_{Output} = Output_{before} - Output_{after}, \quad (5.5)$$

which can be expressed in mbar, mV etc. should always be zero, and it measures the stability of the sensors. Furthermore it also serves as proof that the sensor has not been damaged during its use, e.g. during the calibration.

To explore the stability of all calibrated sensors their calibration data were analyzed. For this purpose at first the mean value of the ten measurements in the *before* zero-sequence of one sensor was calculated. Also its standard deviation σ was estimated. The analog operation was then repeated for the *after* zero-sequence of the same sensor. Finally the *before–after* difference Δ (Equation 5.5) between these two values was calculated, together with its error $\sigma_{\Delta} = \sqrt{\sigma_{before}^2 + \sigma_{after}^2}$. The procedure was then repeated for the second sensor in the same manifold, then for the sensors in the next manifold etc. Also the zero-sequence differences of the reference pressure sensors (baratron and four PG4 [104] sensors) being involved in the calibration measurement runs were calculated.

To obtain a quantitative information about the stability of the sensors the mentioned output differences of all calibrated sensors 100 and sensors 500 (in total 512 sensors of each type) are compared (Figure 5.25 top). The calculated differences are given here in pressure units (mbar), due to the fact, that the pressure measured by different sensors for the same relative pressure can provide a different voltage value, even by sensors of the same type (see Section 5.3.2). The conversion factor voltage/pressure is obtained from the calibration table contained in *CalTabMan***_yymmdd_HHMM.txt*. This method allows direct comparisons of a large

⁷Reminder: each measurement point is the average of a large number of single measurements (usually 1000), which are executed in a very short time interval (about 1 second).

5. Measurement of the gas pressure in the CMS DT muon chambers

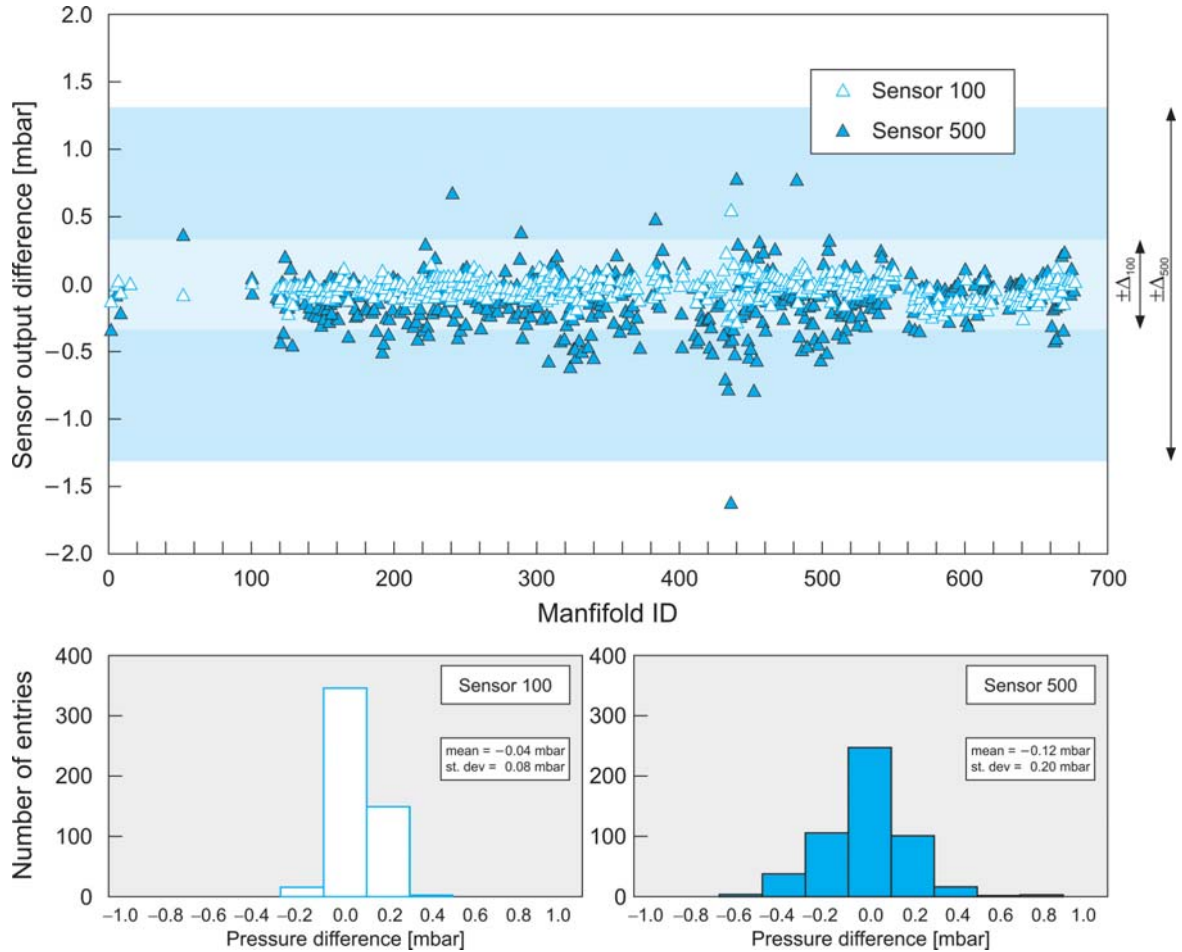


Figure 5.25.: Top: The sensor output differences at the ambient pressure taken during the calibration measurements at the beginning and at the end of the calibration measurements for each sensor type, labeled here by the manifold number. The statistical errors at the single diagram points are too small to be presented here. The read-out precision corresponding to the number of the PADC bits is indicated here by a marked region for each sensor type. Bottom: The frequency of the output differences of all calibrated sensors for each sensor type. The mean value is in both cases about zero, the standard deviation is clearly under 0.3 mbar for sensor 100 and 1.0 mbar for sensor 500, which matches the expected 10-bit resolution of the PADC used in the CMS pressure measurement.

amount of sensors, when the sensor output difference Δ is not exactly zero. By means of the presented data the Δp mean value of all sensors of both types is calculated with its standard deviation (Figure 5.25 bottom).

During the calibration measurements the fluctuations in one measurement point (i.e. 1000 separate measurements, taken with 16-bit resolution) are very small, within ± 1 count interval in the calibration sensor output sensitivity. The standard deviation obtained from such distributions has a typical value

$$\sigma_{point} = 0.2 \text{ mV},$$

which translates into

$$\sigma_{point} = 0.015 \text{ mbar (sensor 100) and } \sigma_{point} = 0.04 \text{ mbar (sensor 500).}$$

This error can thus be neglected in the analysis of the sensor output stability.

The mean value of the output difference of all sensors in their zero-sequences is nearly zero for both sensor types (Figure 5.25). The standard deviations obtained from these distributions are both

$$\sigma_{100} = 0.08 \text{ mbar} \quad \text{and} \quad \sigma_{500} = 0.20 \text{ mbar}.$$

The sensors should work at the CMS with a resolution of about 0.3 mbar (sensor 100) and 1.0 mbar (sensor 500). This means that **the sensors remain very stable during the calibration runs, so the calibration measurement data are reliable and can be used for the successive read-out conversion.**

To investigate any correlation between the measured variables, which are the output differences of the sensors 100, sensors 500 and baratron (reference pressure), the pairwise output data of sensor 100/sensor 500, baratron/sensor 100 and baratron/sensor 500 are presented in diagrams (Figure 5.26). By means of the presented data the *Pearson product-moment correlation coefficient*⁸ (PMCC) r is calculated as measure of the correlation of the analysed variables. The average values are

$$\begin{aligned} r_{100/500} &= 0.05 \pm 0.04 \\ r_{100/Baratron} &= 0.20 \pm 0.04 \\ r_{500/Baratron} &= 0.15 \pm 0.04. \end{aligned}$$

The very small values r point that there is no correlation in the mentioned differences of sensors and baratron. **The observed fluctuations in the sensor outputs are mostly of statistical origin.**

As mentioned before, the usual sensor calibration measurement takes about 2 to 3 hours. Apart from those short measurements it is desirable to study the sensor outputs during a long-term measurement of several days and more.

For this purpose an atmospheric pressure measurement, running for about 2.5 days (weekend run from Friday to Monday) was performed, in which 20 sensors were exposed to the ambient pressure only. The connected manifold series was 371, 372, 373, 374, 375, 376, 377, 378, 379 and 380. Apart from the other usually connected devices like PG4 and baratron, also involved in this run, in addition the supply voltages V_{cc} were measured directly at two channels of one of two supply boxes. The data were taken in about 5000 measurement points, distributed within the total run time of about 55 hours. The data of some sensors and V_{cc} are presented in Figure 5.27. To study the sensor stability a linear regression on the output data of each device was done with time and its slope declared as stability measure for this run (Table 5.1). To check the possible correlation of different output channels, the PMCC was estimated for all possible output channel variable pairs (Figure 5.28). For this kind of considerations it was not necessary to convert the sensor outputs into the pressure units, so the data comparison was performed by using the voltage units (mV), in common for all devices.

The atmospheric pressure run shows a sensor output drop for almost all 20 sensors (Figure 5.27 and Table 5.1). Apart from the sensors contained in the PG4 device, which have a very

⁸The PMCC of two variables x and y (with their expected values \bar{x} and \bar{y}) is defined as

$$r_{xy} = \frac{\text{Cov}(x, y)}{\sigma_x \sigma_y}, \quad (5.6)$$

where $\text{Cov}(x, y) = \frac{1}{n} \sum_{j=1}^n (x_j - \bar{x})(y_j - \bar{y})$ is the covariance of x and y , and σ_x, σ_y their standard deviations.

5. Measurement of the gas pressure in the CMS DT muon chambers

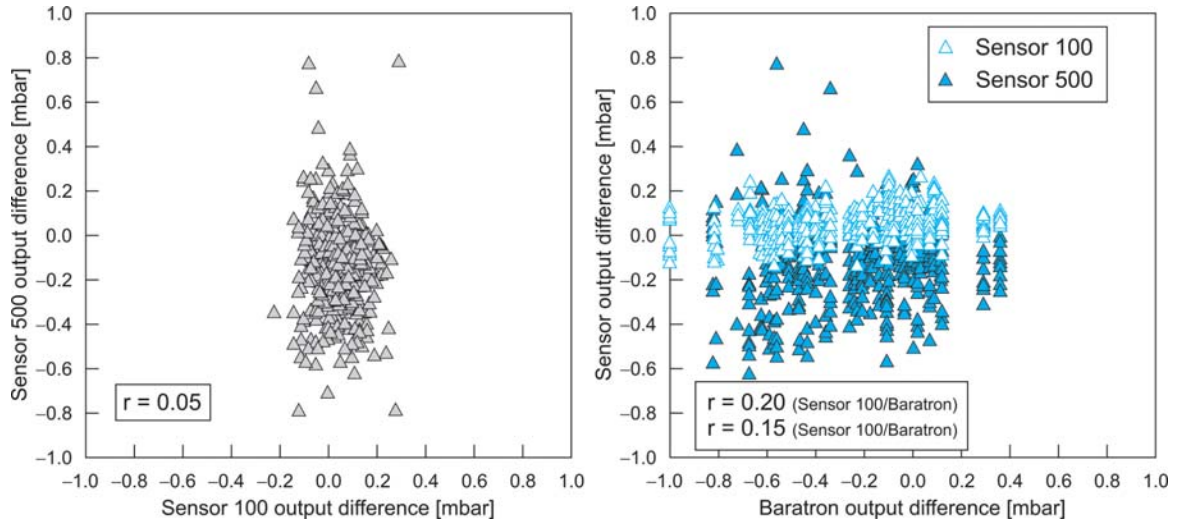


Figure 5.26.: The correlation between the output differences in the zero-sequences of the sensor 100 and sensor 500 (left) and between those of each sensor type and the baratron (right). The estimated correlation coefficients r point to a very small correlation among all considered variables. Thus the origin of the measured output differences in the zero-sequences is an intrinsic feature of the sensors. The elongated cluster (left) is caused by the different resolutions of sensor 100 and 500; the asymmetric distribution in the right diagram is caused by the fluctuations of the baratrons, which are larger than those of the calibrated sensors

small slope a'_V (maximal 0.1 mV/day), the outputs of all sensors drop slightly with time. The average slope for all sensor outputs is about $a'_V = -1.0$ mV/day. The supply voltage, measured simultaneously, is stable: the external one shows only inessential fluctuations within an interval of 1 mV; this does not affect the V_{cc} of the sensors, which remains constant for the entire atmospheric pressure run.

Additionally, the calculated PMCCs for all possible output values in the atmospheric pressure run (Figure 5.28) point at very distinctive correlation in the manifold sensor outputs ("blue triangle" in Figure 5.28):

$$|r| \geq 0.7 \text{ for } 94\% \text{ observed sensor output pairs.}$$

However, there is no correlation between the manifold sensor outputs and V_{cc} or PG4 sensors. It means, that the differences in the calibrated sensor outputs are caused by a common external property. One could conjecture i.e. sensor output dependence on temperature, especially as the observed diagram shape in Figure 5.27 is very similar for the sensor outputs and the ambient temperature.

To investigate a possible influence of the ambient factors on the sensor output in this weekend run also the ambient temperature data, measured continuously in the sensor calibration room (Halle 008) [105], are compared with the mentioned sensor and voltage data. The temperature data are also presented in Figure 5.27 and the corresponding PMCCs in Figure 5.28.

The PMCCs for the value pairs sensors/temperature (Figure 5.28) indicate a dependence of sensor outputs on the temperature. However, the PMCCs calculated for the sensor/temperature pairs are lower than for the corresponding sensor/sensor pairs. This is caused by different

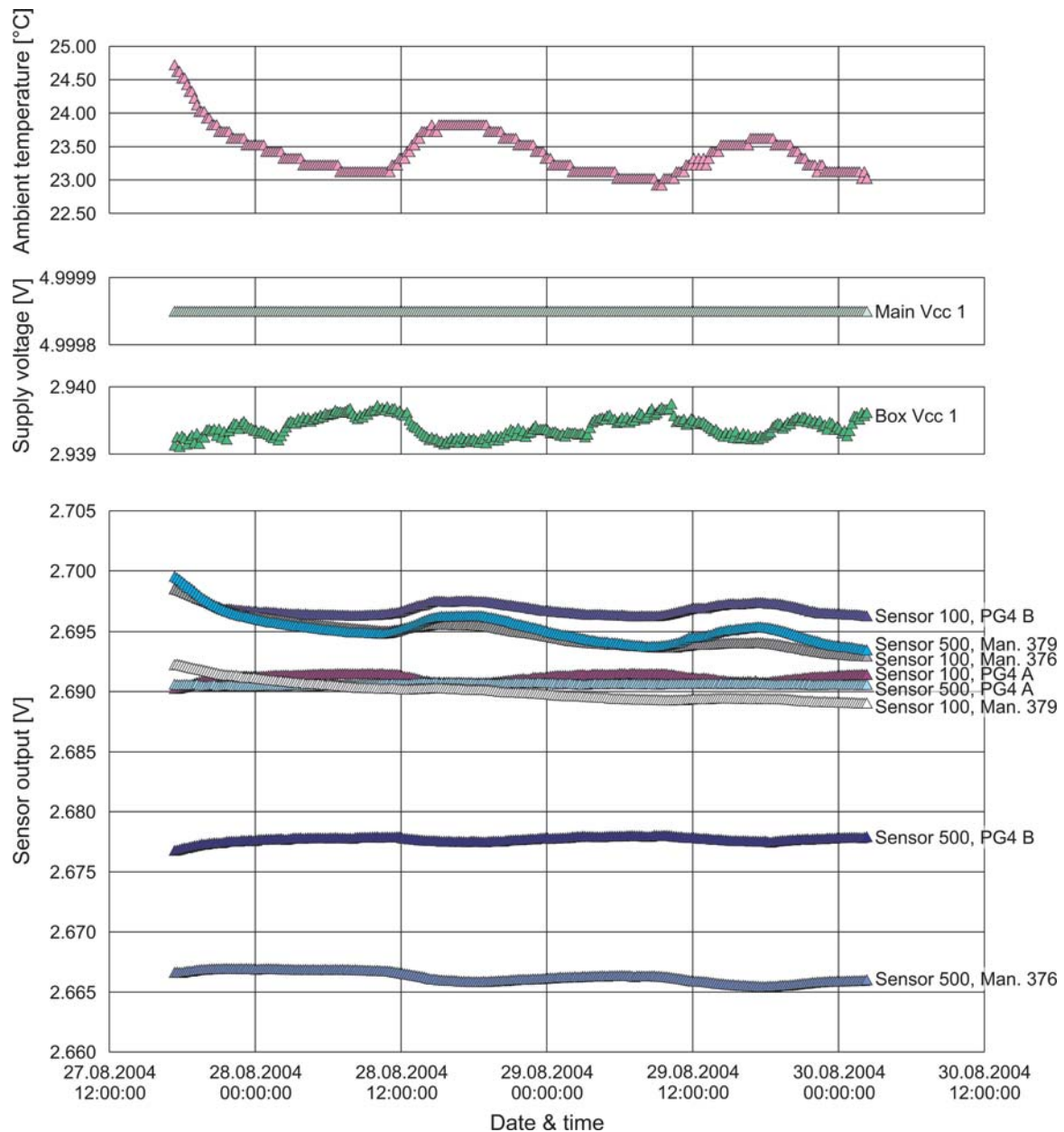


Figure 5.27.: The outputs of some calibrated sensors (manifold 376 and 379), PG4 sensors and V_{cc} continuously taken during the atmospheric run within about 2.5 days. Because the relative pressure difference is invariably zero and the global supply voltage $Main_V_{cc}$ is constant, each output should show a constant value during this period. However, the sensor outputs have a slight tendency to shift in time. Also the sensor outputs seem to depend on daytime. By comparing the sensors output data with the simultaneously measured ambient temperature one (top) one can recognize a correlation. Thus the temperature dependence can explain the non-constant sensor behavior in time.

resolutions in the measurement of the pressure and of the temperature⁹. The *temperature*

⁹The correlation differences between the measured values (pressure, voltage) of different devices can be originated by several factors:

- the temperature sensor is positioned in a distance of about 4 m from the calibration facility;

5. Measurement of the gas pressure in the CMS DT muon chambers

	Sensor 100	Sensor 500		
PG4 A	0.02	0.05		
PG4 B	-0.1	0.1		
Manifold 371	-1.2	-0.7		
Manifold 372	-1.1	-0.9		
Manifold 373	-0.9	-0.7		
Manifold 374	-0.9	-1.1		
Manifold 375	-0.8	-0.7		
Manifold 376	-1.7	-0.6		
Manifold 377	-1.4	-0.9		
Manifold 378	-0.9	-0.7		
Manifold 379	-1.1	-1.2		
Manifold 380	-0.8	-0.4		
			<i>Main_VCC</i>	0.0
			<i>VCC 1</i>	0.05
			<i>VCC 2</i>	0.05

Table 5.1.: Slope of regression line in mV/day units for sensor outputs (left) and supply voltage (right), measured during the atmospheric pressure run. Besides the PG4 sensors, which are better thermally insulated, all calibrated sensors have a negative slope. It indicates indirectly a correlation with the ambient temperature drop during the weekend run (see also Figure 5.27).

correction factor is then calculated as

$$a_V = \frac{a'_V}{\Delta T}, \quad (5.7)$$

where ΔT is the temperature change in time [$^{\circ}\text{C}/\text{day}$]. Remarkable is the fact that the sign and the magnitude of the PMCC varies from sensor to sensor. Its averaged value for all sensors in the weekend run is

$$a_V = -2 \text{ mV}/^{\circ}\text{C}.$$

This value is below the technical tolerance of the sensor output in dependence on temperature [86] [87]. However, for $\Delta T \simeq 1^{\circ}\text{C}$ it is of the order of sensor output digitization in the CMS detector (about 4.3 mV/count). Knowing the corresponding conversion factors voltage/pressure (LUT), **it is possible to obtain the temperature correction factor for each calibrated sensor.**

In addition, to observe the sensor functioning during a time period much longer than several days, the PG4 sensor outputs were analyzed. These sensors, which are of the same types like the usually calibrated ones, were neither removed nor replaced from the PG4s for all calibration measurement runs and their outputs were registered in each run. They are

- the pressure sensors are partially thermally insulated within the manifold;
- the PG4 sensors are better insulated (plastic box) than the calibrated sensors in the aluminum manifold;
- baratron sensors are specifically insulated and thermally compensated.

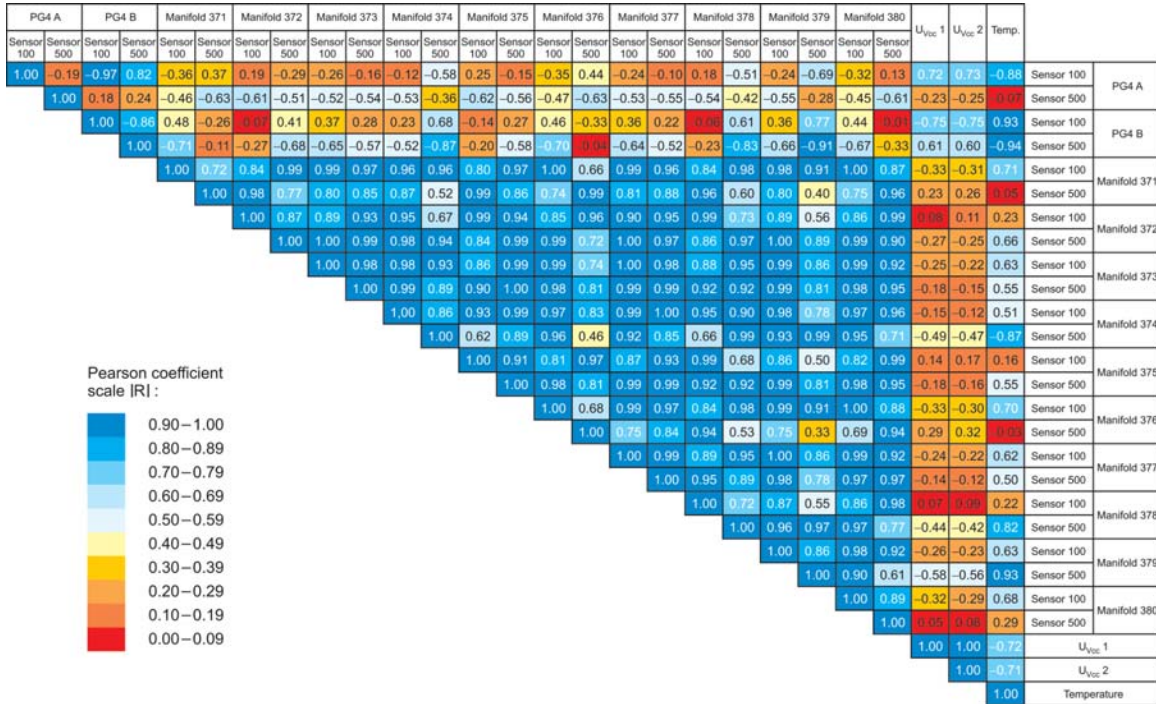


Figure 5.28.: The correlation in the atmospheric run of all possible value pairs (various sensor outputs and supply voltages) at room temperature expressed as Pearson product-moment correlation coefficients (PMCC). To obtain a broad view of them, the intervals of absolute PMCC values are in colored boxes according to the presented scale. One can clearly recognize correlations in the outputs of the sensors in the manifolds. Also the PG4 sensors on the one hand and the two measured supply voltages V_{cc} on the other hand are well correlated. One can also recognize a sensor output dependence on temperature (see also Figure 5.27).

not dedicated to be applied in the CMS DT muon chamber, but their behavior during the mentioned time can provide very useful conclusions about the sensor properties during the LHC operation of about 10 years.

Therefore the zero-sequence data of the four PG4 sensors, taken in 64 calibration runs from 24.08.2003 to 13.09.2006 were used to calculate the output differences according to the Equation 5.5. The results are presented in Figure 5.29 in common with ambient temperature data measured for this time. Based on these data, the PMCCs for each PG4 sensor and temperature were then calculated (Table 5.2).

PG4 A		PG4 B	
Sensor 100	Sensor 500	Sensor 100	Sensor 500
-0.57 ± 0.08	0.21 ± 0.12	0.57 ± 0.08	-0.34 ± 0.11

Table 5.2.: PMCCs for each PG4 sensor zero-sequence output with the temperature based on the data taken in 101 calibration runs from 24.08.2003 to 13.09.2006. One can recognize a good correlation of the sensor 100 output with the temperature (high PMCC values).

5. Measurement of the gas pressure in the CMS DT muon chambers

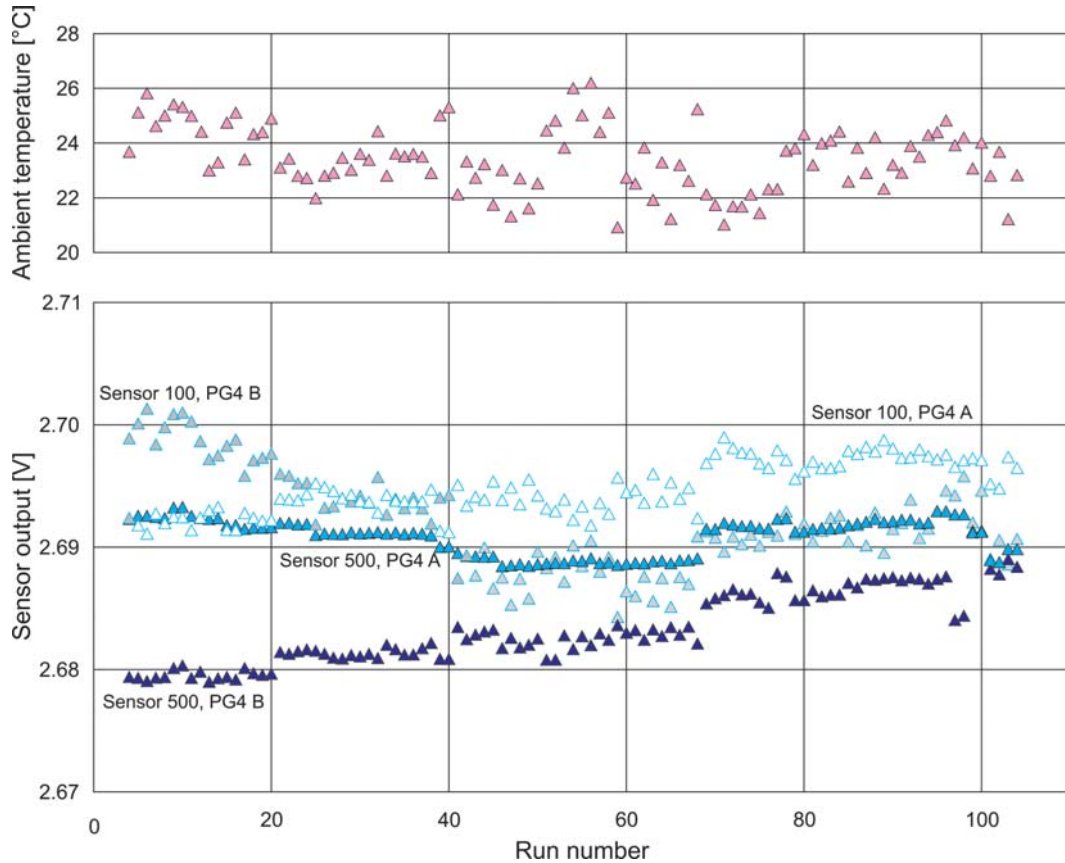


Figure 5.29.: PG4 sensor zero-sequence outputs taken in 101 calibration runs from 24.08.2003 to 13.09.2006 (bottom) and the corresponding ambient temperature (resolution 0.1 °C) measured in this time interval (top). Due to the fact that the measurement scales and resolutions in both cases are different the sensor output dependence on the temperature is only vaguely perceptible. The PCMMs (Table 5.2) provide more information about their correlations.

The PG4 sensor zero-sequence data taken in all calibration measurement runs (time interval about 3.5 years, Figure 5.29) show a good overall stability of these sensors, the mean difference values are about zero. However the sensors 100 seem to be correlated with the temperature (somewhat more than sensors 500, Table 5.2), their PMCCs have also here different sign, as seen before (Table 5.1 and Figure 5.28). Based on this measurement and the calibration data, the temperature correction factors referring to the atmospheric pressure a_p were calculated for almost all calibrated sensors¹⁰ (Figure 5.30). An ASCII file *Temperature_Correction_SensorReadOut_at_ZeroPoint.txt* with sensor list and their corresponding temperature correction factors is created and placed in the Aachen database http://wwwdbac.physik.rwth-aachen.de/LUT_PADC for use in the CMS DT muon chamber gas pressure read-out.

¹⁰Within the time interval of interest (about 3.5 years) there were periods of interrupted temperature measurement (which run independently from the sensor calibration), so for some calibration runs no ambient temperature data are available. However, the air conditioning of the laboratory room has at all times have ensured that temperature variations were small.

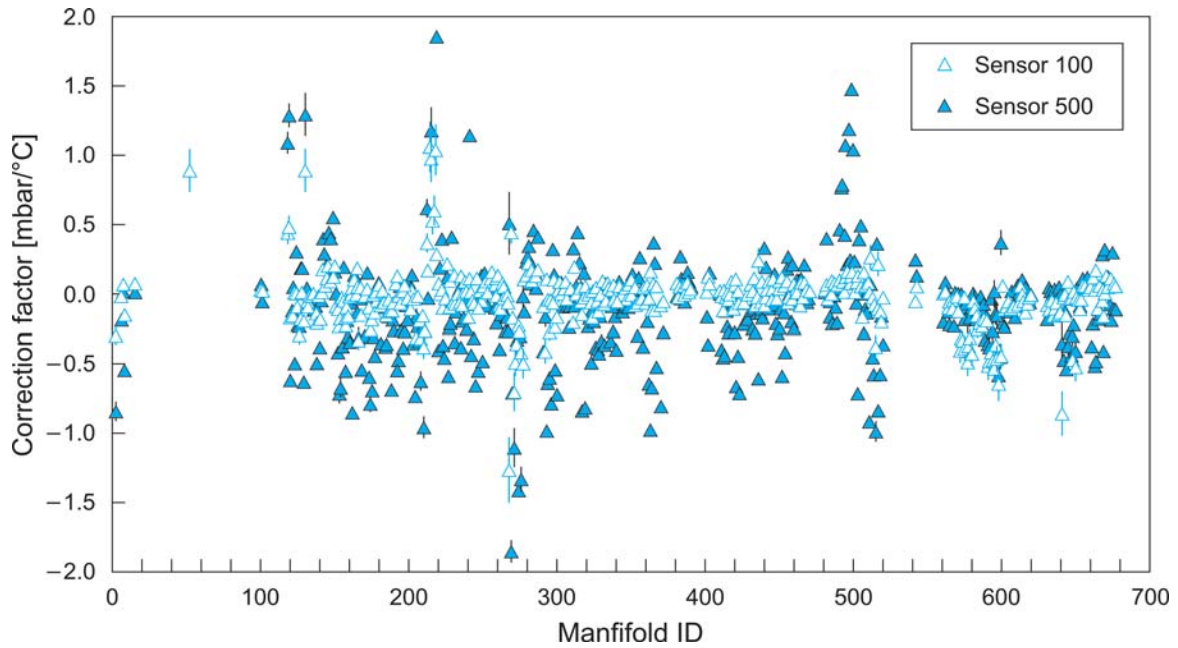


Figure 5.30.: Temperature correction factors for almost all calibrated sensors. The errors result mainly from temperature measurements.

Temperature run

The analysis of data taken in the weekend run suggested, that the sensor outputs are dependent on the ambient temperature. The hints obtained in that run need to be confirmed by more precise data. On the one hand, the temperature varied by only a few degrees in the weekend run. On the other hand, the temperature measurement was imprecise, due to the different locations of the temperature sensor and manifolds in the calibration room. An additional test was therefore needed to investigate the sensor's behavior at different temperatures.

For this purpose five manifolds (551, 552, 555, 556 and 557) were set in a MELAG autoclave [110]. Their electronics was connected to the calibration set, as described in Section 5.3.2. They were not connected to gas and thus at atmospheric pressure. For cross check, five other manifolds (104, 105, 106, 107 and 108) were connected the same way but placed outside the autoclave. The usual calibration run was then started, all sensors provided data for ambient pressure (relative pressure was always zero). During the run the air in the autoclave was progressively heated up from ambient temperature to about 80 °C and then cooled back to the ambient value (Figure 5.31 top).

The data of all sensors in ten manifolds were registered as during a usual calibration measurement run (Section 5.3.2; see Figure 5.31 bottom) in common with data from other devices usually involved in the sensor calibration run (baratrons, PG4, supply voltage), also date and time of each measurement point. Simultaneously and independently of the gas pressure sensor measurement the temperature was measured directly at the manifolds inside and outside the autoclave, using temperature sensors DS1820 [111] with a resolution of about 0.1 °C. The temperature data, as well as the date and time of measurement points, were taken by a LabVIEW software *temperature.vi*, which was developed especially for this purpose [112] and stored in a text file *temperature_PRESSURE_SENSORS_20071004_1459.txt*. On the basis of this file and of the usual sensor calibration file the sensor output data and temperature were merged by matching the date and time of the measurement points. Then the PMCC

5. Measurement of the gas pressure in the CMS DT muon chambers

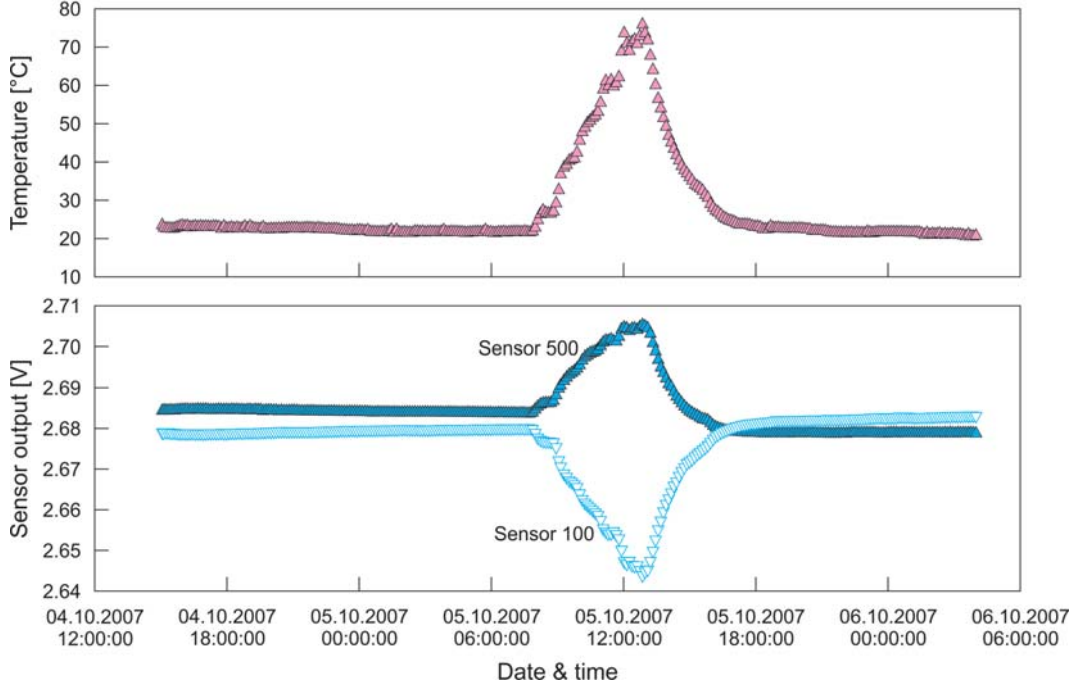


Figure 5.31.: The course of temperature (top), which was created to investigate the sensor functionality (five manifolds) dependence on it. The temperature here was measured at the location of the manifolds. The outputs of these sensors, here representatively displayed for manifold 556 (bottom), show a very pronounced correlation with the temperature. The other sensors involved in this run show a similar temperature dependence.

as measure for possible correlations was calculated for each sensor/temperature pair (also for each sensor/sensor pair).

The comparison of the sensor output data and temperature during the temperature run shows a very similar common tendency (Figure 5.31). The sensor output signal is linearly correlated with the temperature (Figure 5.32). However, one can realize a hysteresis in the characteristic lines for each sensor type. Nevertheless the divergences in the sensor signals measured for the same temperature but at different times (during the temperature rise and during the temperature drop) are smaller than the CMS sensor read-out resolution. The calculated PMCCs for each sensor/temperature pair and sensor/sensor pair (Figure 5.33) quantifies this temperature dependence of the sensor outputs. Regarding the ten PMCCs for the sensor/temperature pairs (excepting sensor 100, manifold 551) one finds

$$|r| \geq 0.9 \text{ for all observed sensor/temperature pairs.}$$

However, also here one can see that r has a different sign for different value pairs. This effect was not expected, the reason for this behavior can be the residuum of the temperature compensation mechanism in the sensors [86] [87].

The averaged variation in the sensor outputs of all five sensors of each type is

$$a_{V_{100}} = 0.8 \text{ mV}/^\circ\text{C} \quad \text{and} \quad a_{V_{500}} = 1.1 \text{ mV}/^\circ\text{C}.$$

For a temperature difference from about 20 °C to about 45 °C (electronics temperature at the chamber FE-side) and PADC counts about 14.3 mV/mbar (sensor 100) and about 4.3 mV/mbar (sensor 500) one expects a sensor read-out difference of the order

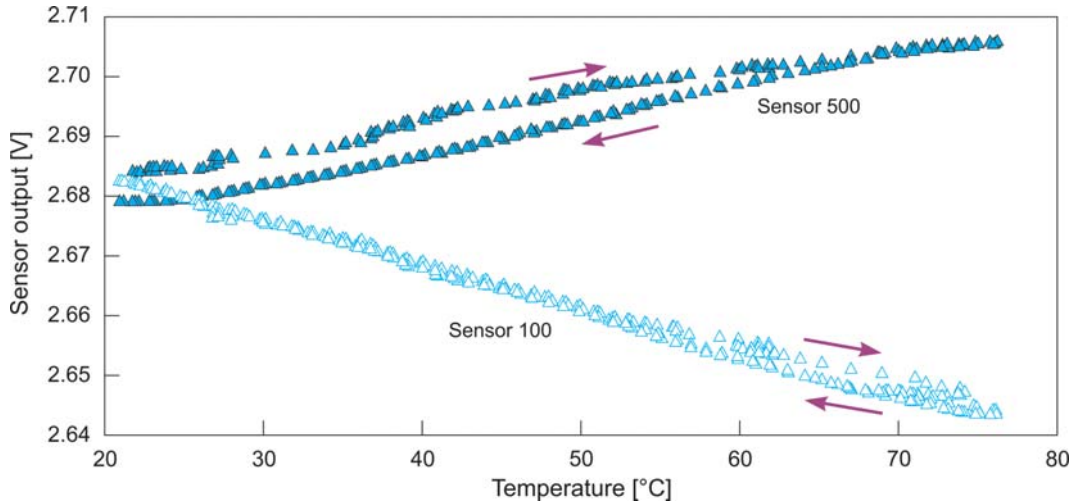


Figure 5.32.: The output signals of all sensors (here presented for manifold 556) show a linear dependence on the temperature. The characteristic lines are smooth hysteresis curves; the violet arrows indicate the data taken during the temperature rise and drop. The sensor read-out differences occurred by this feature are smaller than the CMS read-out resolution.

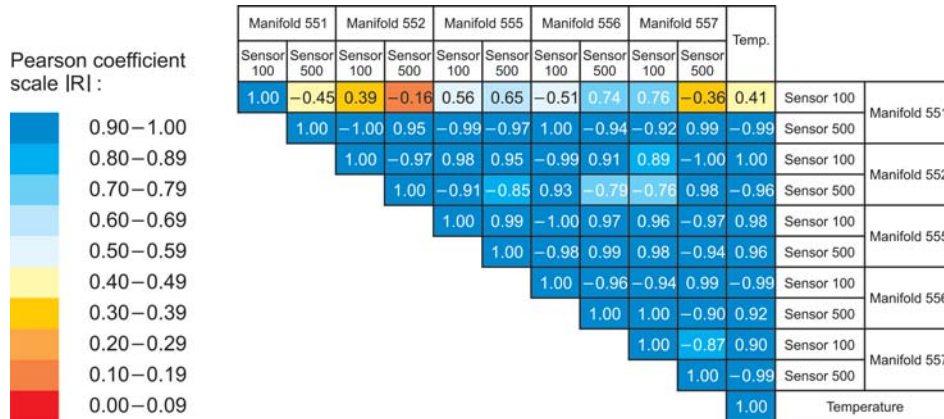


Figure 5.33.: The correlation in the temperature run of all possible value pairs (various sensor outputs and temperature) expressed as Pearson product-moment correlation coefficients (PMCC). With the exception of sensor 100 in manifold 551, all other sensors show a strong dependence on the temperature (blue boxes), which is also manifest in Figure 5.31.

$$\Delta_{p_{100}}(25^{\circ}\text{C}) = 1.4 \text{ mbar} \quad \text{and} \quad \Delta_{p_{500}}(25^{\circ}\text{C}) = 6.4 \text{ mbar}.$$

These calculated values are benchmarks, estimated on the basis of temperature run data of only five sensors of each type. Furthermore, it is not possible to measure temperature at all 500 various manifold positions at the CMS detector. A possible solution is to perform pedestal measurements at specific time intervals during the CMS DAQ runs, when the local detector temperature is stable and remains constant. The sensor read-out at this temperature and at the ambient pressure can then be compared with the ambient pressure read-out at normal temperature as used for the LUTs. **These read-out differences can be then used for**

5. Measurement of the gas pressure in the CMS DT muon chambers

temperature correction of the sensor read-out of all CMS DT muon chambers. The temperature correction factors stored in the mentioned database should serve as an orientation help for the sensor behavior in dependence on temperature; the zero-point measurement (pedestal) at CMS remains essential.

Calibration reproducibility

The sensor outputs were registered in common with the reference pressure for the sensor calibration in various runs (Section 5.3.2). Once a single calibration run was certified as good for a sensor, there was no requirement for its iteration. However, in some cases the sensor calibration measurements were repeated, e.g. when one of the manifolds in the calibration run showed a malfunction etc., it was exchanged or repaired and set back in the same manifold group for a new run. In this case the outputs of the "good" sensors contained in this group were measured more than once. Based on the comparison of two such independent sensor measurement data, one can validate (or reject) the calibration results.

During the entire calibration period 86 manifolds (86 sensors 100 and 86 sensors 500) were measured more than once, each with satisfactory results. For each run the measurement data are calculated using the same range for the local linear fits (Section 5.3.2). The data from this range, representative for only one sensor (sensor 100, manifold 307; other sensors show similar behavior) are presented in Figure 5.34 (top). The differences are not significant, but for the sensor use in the CMS detector the difference Δp in the sensor output about the zero-point is relevant, due to the small typical working range. These differences about the zero-point of all 172 sensors are presented at the bottom of Figure 5.34. The estimated mean values for each sensor type and their standard deviations are listed in Table 5.3.

Sensors 100		Sensors 500	
mean [mbar]	σ [mbar]	mean [mbar]	σ [mbar]
-0.02	0.26	0.22	0.78

Table 5.3.: The mean values and their standard deviations of differences at zero point for each sensor type presented at the bottom of Figure 5.34.

All analyzed sensors, which were measured more than once in various valid calibration runs show similar calculated calibration data. The most important difference between data obtained by these different runs in the sensor working area about zero-point is small for each sensor and each sensor type: the data mean values are nearly zero and the difference Δp of about 80% of all sensors is below the expected sensor output precision (about 0.3 mbar for sensor 100 and 1.3 mbar for sensor 500; see Table 5.3). **The sensor calibrations are reproducible.**

5.5.2. Gas pressure read-out tests.

Before the main CMS runs in the LHC operation start it is crucial to test the whole gas pressure read-out system of the CMS DT muon chambers. An available facility for this was especially the *Magnet Test and Cosmic Challenge* (MTCC) [106]. From August 2006 to November 2006 14 fully equipped muon chambers of all types, installed in three sectors of the

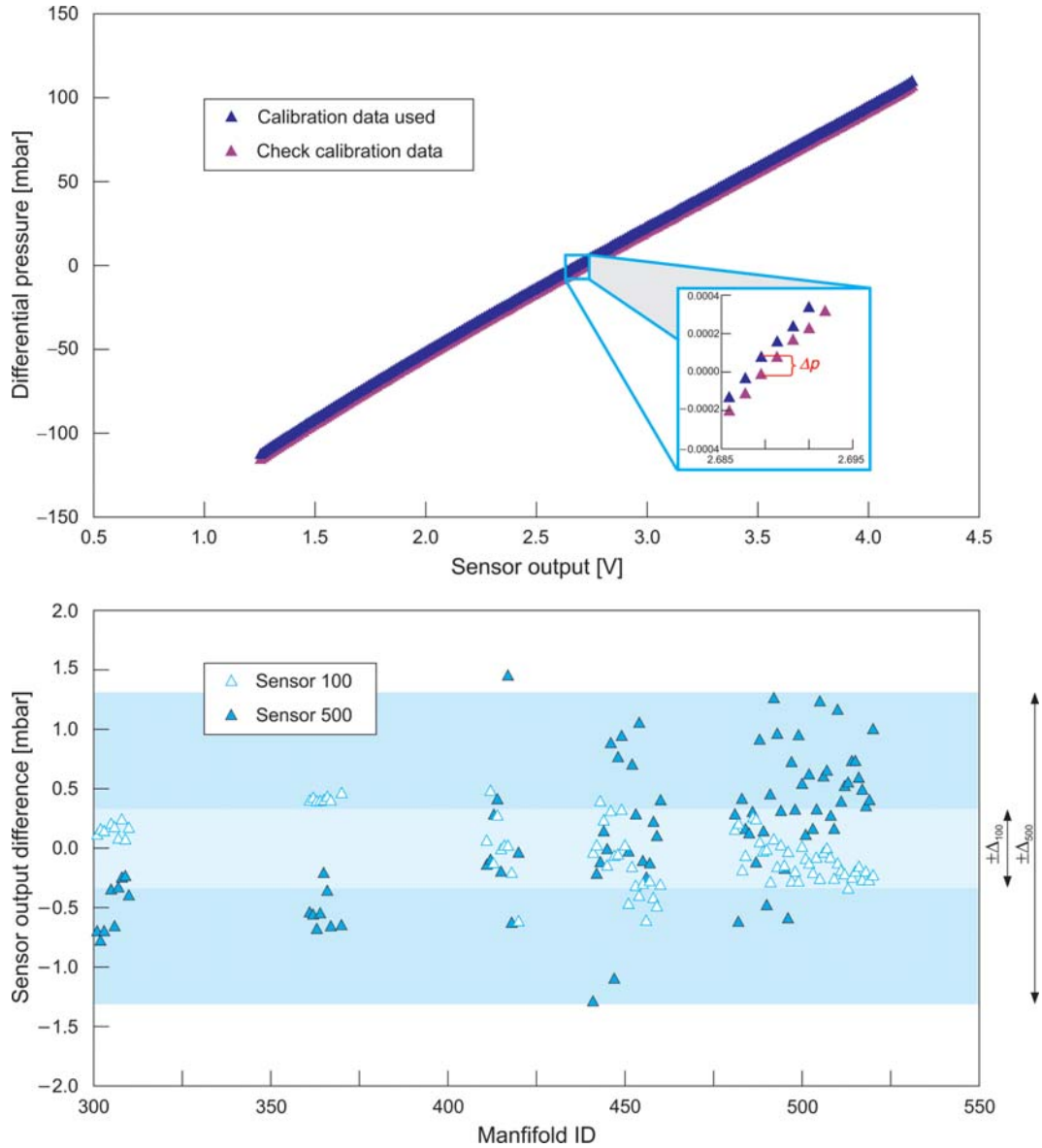


Figure 5.34.: Data of two different calibration runs of one sensor (here sensor 100, manifold 307), taken at different times (top). One can see no significant difference between both data sets; an analog behavior is shown by all other sensors. For the work range of the sensors, which will typically be around 10 mbar, the difference Δp at zero-point is important. These differences for all 86 sensors 100 and 86 sensors 500, for which more than one valid calibration runs were performed, are also presented (bottom). The read-out precision corresponding to the number of the PADC bits is indicated here by a marked region for each sensor type

CMS detector, were tested on their functionality by detecting cosmic muons, also affected by the detector magnetic field of up to 3.8 T [107]. Besides the DAQ system tests of different subdetector parts working simultaneously also the DCS functionality was partially checked during the MTCC period.

The MTCC allows to test the gas pressure system for the first time at several chambers simultaneously. It means that the data of 56 sensors (28 sensors 100 and 28 sensors 500),

5. Measurement of the gas pressure in the CMS DT muon chambers

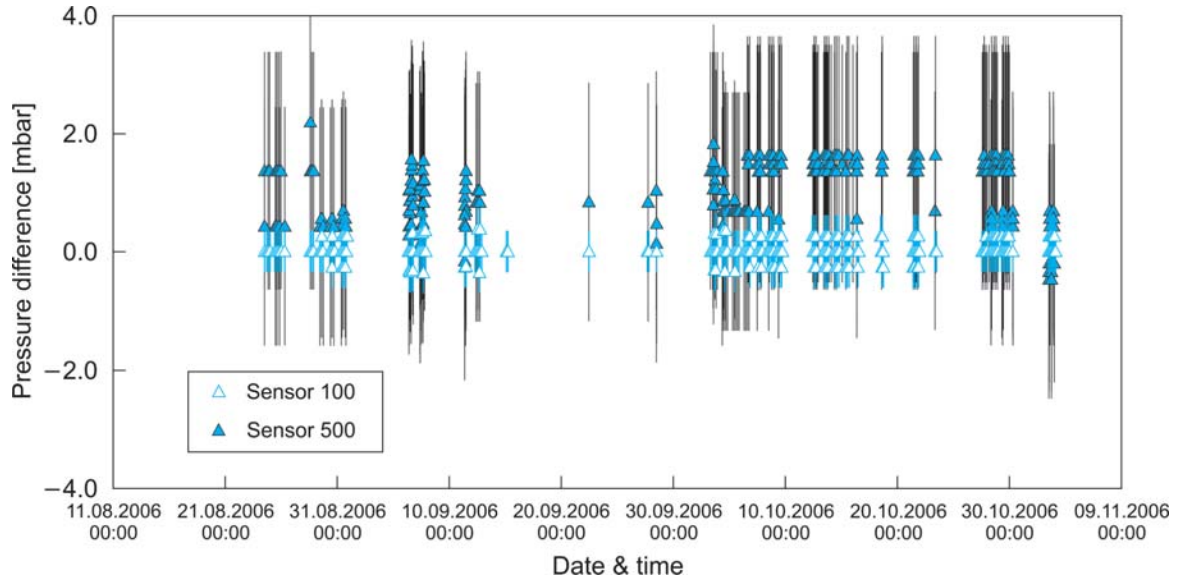


Figure 5.35.: Sensor read-out differences at the same CMS location for one sensor pair (here representatively for MB/+1/1/10, PADC 263, FE-side manifold; the other sensor pairs show similar behavior) by measurement of the same pressure without magnetic field: between two different PADC digitization channels of the same sensor 100 and between sensor 100 (average from the PADC channels for one sensor 100) and sensor 500. The differences are small (about 0 mbar) and within expected tolerance (about 0.35 mbar for $\Delta p_{100/100}$ and 2.0 mbar for $\Delta p_{100/500}$), which results from digitization only.

taken at the same time can be compared to study the pressure system behavior at different places of the detector. Also the influence of the magnetic field, which is variable and possibly affects the work of the sensors [108], could be investigated. The test procedure is therefore the analysis of the sensor outputs at the same CMS location, fluctuation measurement of the supply voltage (which is simultaneously measured by the PADC) and the effects of the magnetic field.

The first test provides information about the gas pressure measurement correctness at various locations in the detector: As described above (Section 5.2), each chamber is equipped with two manifolds, one on the FE-side and one on the HV-side. Each manifold contains one sensor 100 and one sensor 500. Thus, both sensors in one manifold – assumed, they work properly and are not affected by outer factors; also the sensor signals are digitized correctly – should provide the same pressure values every time, due to the fact, that both sensors measure the same pressure at the same place.

To investigate the gas pressure read-out in such a manner in the absence of a magnetic field ($B = 0$ T), two similar procedures were performed. On the one hand the differences of the pressure values from the same sensor 100 digitized by two different PADC channels (Section 5.2, Figure 5.6) $\Delta p_{100/100}$ were measured. On the other hand the differences were measured between the pressure values obtained from sensor 100 (averaged from both PADC channels for the sensor 100) and sensor 500, $\Delta p_{100/500}$, contained in the same manifold¹¹. The data taken during the "non-magnetic" runs of the MTCC allow to compare about 2000 pressure

¹¹During the MTCC no zero measurement, i.e. sensor read-out at ambient pressure as reference, was done. Instead of this for the presented analysis the pedestal correction was performed: the Δs were calculated with respect to the averaged value of the first 30% sensor output measurements.

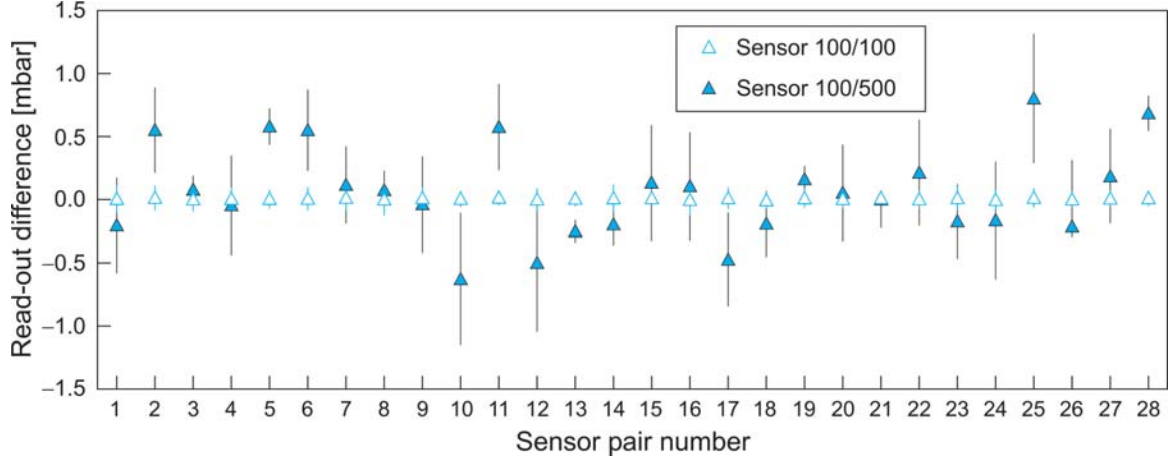


Figure 5.36.: Averaged read-out differences of all 28 sensor pairs operated in the MTCC. All differences are small with respect to the expected accuracy (about 0.3 mbar for sensor 100 and 1.3 mbar for sensor 500 read-out).

value pairs $\Delta p_{100/100}$ and $\Delta p_{100/500}$ for each of the 28 manifolds. The representative read-out differences with their statistical errors (standard deviations) of chamber MB/+1/1/10, PADC 263, FE-side manifold are presented in Figure 5.35. The mean values $\bar{\Delta p}_{100/100}$ and $\bar{\Delta p}_{100/500}$ were calculated for each sensor read-out difference. These data with their statistical errors are presented in Figure 5.36.

The averaged read-out difference of the same sensor 100 but digitized by two different PADC channels and its standard deviation obtained for all sensor 100 read-out pairs is

$$\Delta p_{100/100} = 0.01 \text{ mbar}, \quad \sigma_{\Delta p_{100/100}} = 0.08 \text{ mbar}.$$

The expected digitization difference between these two sensor read-outs at the same time is

$$\Delta p_{100/100}(exp) = 0 \pm \sqrt{2}\Delta_{100} \simeq 0 \pm 0.5 \text{ mbar},$$

with sensor 100 digitization count $\Delta_{100} \simeq 0.35$ mbar. The digitization differences are clearly within the expected limit. **The digitization of the sensor 100 output works very well; sensors 100 are suitable for gas pressure measurement at the CMS DT muon chamber with their resolution of about 0.35 mbar.**

The read-out difference between sensor 100 and sensor 500 at the same location in the detector, averaged over all 28 sensor pairs and its standard deviation after the pedestal correction is

$$\Delta p_{100/500} = 0.03 \text{ mbar}, \quad \sigma_{\Delta p_{100/500}} = 0.52 \text{ mbar}.$$

The expected digitization difference between these two sensor read-outs (at the same time) is

$$\Delta p_{100/500}(exp) = 0 \pm \sqrt{\Delta_{100}^2 + \Delta_{500}^2} \simeq 0 \pm 1.5 \text{ mbar},$$

5. Measurement of the gas pressure in the CMS DT muon chambers

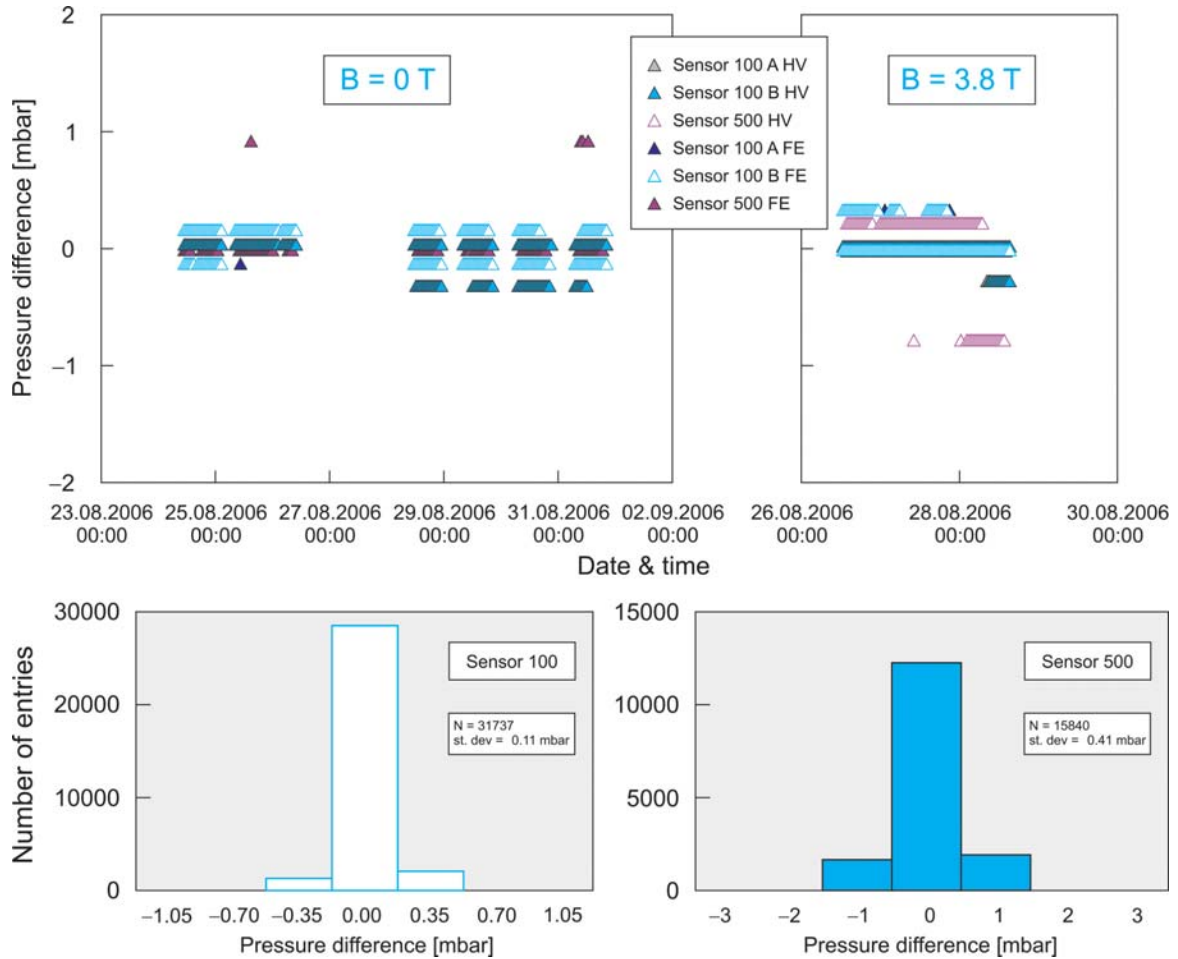


Figure 5.37.: Sensor read-out differences with respect to the mean value of the measured pressure at periods with constant gas flow and magnetic field (top), representatively for MB/+2/4/10(10R), PADC 14. The plots show good read-out system stability in both cases; the sensor read-out fluctuations are compatible with the read-out resolution. The calculated mean of these differences for all 56 sensors (bottom) are about 0 with standard deviations being within expected accuracy (about 0.3 mbar for sensor 100 and 1.0 mbar for sensor 500).

with sensor 500 digitization count $\Delta_{500} \approx 1.3\text{ mbar}$. Also here the digitization differences are within expected limit. However, for all sensors the difference $\Delta p_{500/500}$ is systematically higher or lower than $\Delta p_{100/500}$ in the order of about 1 mbar (see Figure 5.35). This smooth offset shift can be explained with the mentioned temperature influence. Working with less resolution but wider range than the sensor 100, **the sensor 500 is also suitable for gas pressure measurements at the CMS DT muon chambers.**

The second test investigates the stability of the read-out system: At constant gas flow one expects no significant variance of the pressure values, the fluctuations should be at most $\pm\Delta_{100}$ or $\pm\Delta_{500}$ (digitization counts) for each sensor type. In addition, as described in Section 5.3.2, the sensor output depends on the sensor supply voltage which is stabilized locally at the manifolds. It is slightly different for each manifold, but should remain stable with time, independently from outer factors (i.e. magnetic field). The sensor read-out fluctuations should

therefore result from digitization only.

As a measure for the read-out stability the deviation from the mean read-out value was chosen. Therefore the read-out differences with respect to the mean read-out value for all 56 sensors in MTCC periods with constant gas flow and various magnetic fields were considered. Representatively, all sensors read-outs of the chamber MB/+2/4/10(10R), PADC 14 at magnetic field $B = 0\text{T}$ and $B = 3.8\text{T}$ are presented in Figure 5.37 (top). The fluctuation distribution, based on all read-outs of the 56 sensors working during the "non-magnetic" MTCC runs was calculated, the results are shown in Figure 5.37 (bottom) for both sensor types.

The standard deviations as measure of read-out differences with respect to the mean measured pressure values ($\Delta_{p_{100}} = \Delta_{p_{500}} \simeq 0$ mbar) during MTCC periods with magnetic field, averaged over all 28 sensors 100 (31 737 read-outs) and 28 sensors 500 (15 840 read-outs) are

$$\begin{aligned}\sigma_{\Delta_{p_{100}}} &= 0.11 \text{ mbar} \simeq \frac{1}{2}\Delta_{100} \\ \sigma_{\Delta_{p_{500}}} &= 0.41 \text{ mbar} \simeq \frac{1}{3}\Delta_{500}.\end{aligned}$$

There is no significant read-out difference and the statistical errors are within the digitization counts Δ_{100} and Δ_{500} . Hence **the gas pressure read-out system of the CMS DT muon chambers works in a stable way.**

In addition the behavior of the sensor read-out system supply voltage V_{cc} and V_{dd} (see Section 5.3.3) during the entire MTCC period (also at variable magnetic field) was analyzed. As example the supply voltages measured by PADC 14 at MB/+2/4/10(10R) is presented in Figure 5.38 (top). Then the mean values of the internal supply V_{cc} of all manifolds and their statistical errors (standard deviations) were calculated (Figure 5.38, bottom).

As seen in Figure 5.38 the external supply voltage V_{dd} is dependent on low voltage supply hardware and can vary, but remains always above 5.5 V. The internally regulated supply voltages V_{cc} of PADC and manifolds with their sensors remains constant, always at the required value of 5.0 V. The averaged sensor supply voltage of all 28 manifolds is

$$V_{cc} = 5.007 \pm 0.020 \text{ (stat.) V.}$$

These V_{cc} are all above 4.95 V which is a safe limit for right work of the sensor voltage regulator [109] at the manifold. Hence **no voltage correction for the sensor read-out system is needed.**

5.5.3. Conclusions on gas pressure tests

The gas pressure sensors show a stable behavior. The comparison of the zero-sequences, measured at the beginning and at the end of the calibration run, show no significant differences between these sensor outputs at different times. The observed sensor fluctuations during the calibration runs are not correlated with the fluctuations of the PG4 reference sensors or baratrns. No indication could be found for any bias caused by the calibration facility.

The repeated calibration runs for the same sensors, done at different times, show a good reproducibility of the calibration measurement. This also indicates good sensor stability in their working range.

Long term measurements (weekend run, PG4 sensors in all runs during 3.5 years) show an evident influence of the ambient temperature on the sensor output, and thus on the calibration results. This behavior was confirmed by a dedicated temperature run with sensors of both types. The observed sensor output changes proportionally to the temperature change, but the proportionality factor is different for each sensor and can be positive or negative. However,

5. Measurement of the gas pressure in the CMS DT muon chambers

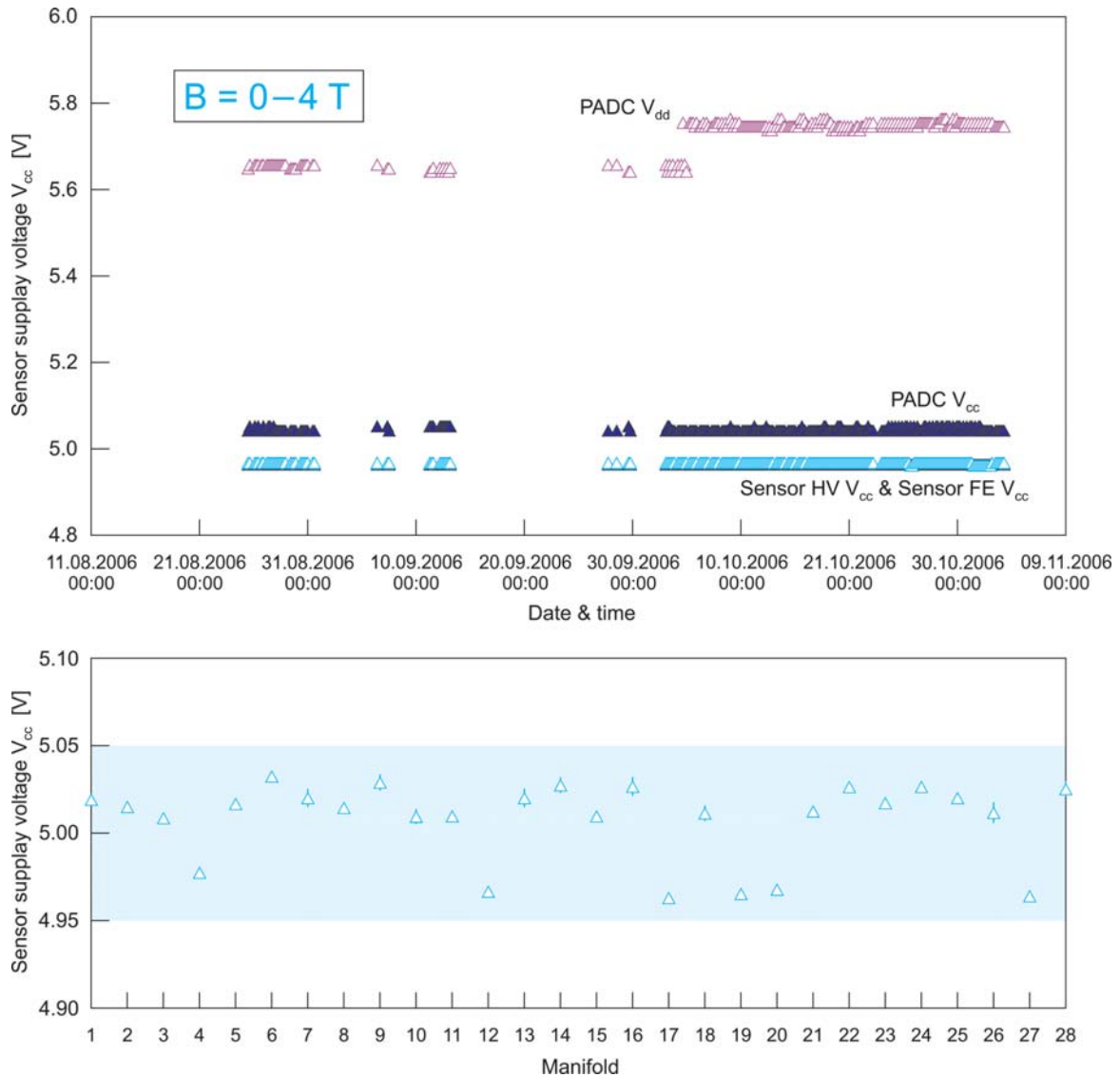


Figure 5.38.: Supply voltage stability check during entire MTTC time interval, here representatively for chamber MB/+2/4/10(10R), PADC 14 (top). Although the external supply voltage V_{dd} varies (the data jump in the first decade of October 2006 is due to the replacement of the low voltage supply at the detector), the stabilized internal voltages V_{cc} remain constant. The average supply voltage is different for each manifold (bottom) but is always within the demanded interval of 5.00 ± 0.05 V. The voltage fluctuations are very small (error bars); some of the data have no error bars that means exactly constant voltage during the entire MTCC time (standard deviation is zero).

the time for a usual calibration run was relatively short (2 to 3 hours), so the temperature changes within this period were not significant. Therefore the sensor output differences caused by the temperature change remained below the CMS read-out resolution. Nevertheless, the ambient temperature during the calibration run was not accurately known. This implies that the CMS gas pressure read-out values could be shifted when the local ambient temperature at the manifold is not the same as the ambient temperature during the calibration. The need for such a temperature measurement at the CMS detector for all 500 manifold positions was

not foreseen and hence this measurement has not been implemented. Therefore, pedestal measurements in situ are recommended, to obtain the temperature correction for the gas pressure measurement of the CMS DT muon chambers. During the long data taking runs the temperature in the CMS cavern is expected to remain very constant and therefore only a very small drift of the zero point of the sensors is expected.

During the MTCC the sensors of different types, which are placed at the same position in the chamber gas system, measured the same pressure value. Also the read-out of the same sensor 100 by two different PADC channels provided the same pressure values. In addition there were no significant fluctuations in the read-out data at constant gas flow and magnetic field.

Also the supply voltage of the PADC and sensors remained constant at nominal value, during the entire MTCC time. It means that the ambient magnetic field, which was varied for the MTCC does not affect the supplies. Under these conditions the voltage read-out correction seems not to be needed for the entire LHC operation.

6. Summary

The LHC project with its four main experiments will either confirm or exclude the existence of the Higgs boson in the interesting mass range of about 200 GeV. It can also validate the Standard Model or discover one of its proposal extending, e.g. Supersymmetry.

The search for very rare events, like Higgs production, implies the use of a very sophisticated DAQ system to detect and measure its decay products. The tests of the CMS DT muon chamber showed, that this system works as expected. The local DAQ system (MiniCrate) works well. The drift times measured by this system were compared with drift times measured by another system. The obtained differences were about 1 ns. This result is fully satisfying for the demanded muon track resolution of about 100 μm . However, it is shown, that the chamber noise can affect the quality of the data taking. Under normal conditions the chamber DAQ system has the capacity to manage the enormous volume of data used for the decision on the L1 trigger level.

To guarantee an efficient data taking process, the entire CMS apparatus must be monitored and controlled by the DCS (Detector Control System) during LHC operation. Especially for the muon chambers, which are gas-filled detectors, the control of the gas pressure – among others – plays an important role. By means of a data system (Look Up Tables), which was specifically developed in Aachen and contains the conversion factors analog/digital for each gas pressure read-out unit, the gas pressure system passed all tests concerning its precision, stability and general behavior under different CMS conditions (e.g. magnetic field). The calculated statistical errors remain always below the required gas pressure measurement resolution of 1 mbar. The systematical uncertainties are caused by the temperature influence, but they are minimalized by the pedestal correction based on the offset measurement at atmospheric pressure. The analysis of test results qualifies this system as being very reliable and appropriate for gas pressure measurements on the CMS DT muon chambers. The measurement sequence, in common with a specific gas pressure read-out software, is implemented in the general DCS monitoring procedures.

The LHC and in particular the CMS experiment are ready to explore the physics of proton-proton collisions at 14 TeV, and will hopefully discover new phenomena.

A. MiniCrate DAQ configuration and readout software

For the MiniCrate operation a couple of software was developed which is needed for connection, initializing, configuration and data read-out. In the following, two main programs are presented which are important for proper TDC configuration and efficient data taking by reading the ROS-8 channels (see Section 4.3.2). Information for use and details of the other ones can be obtained by contacting the author.

A.1. *MiniCrate_MB1_TDC_configuration_setup_ac.vi*

The configuration setup occurs by clicking the demanded field (Figure A.1), whose detailed description can be found in the HPTDC manual [53]. The selection fields are segmented in following groups:

- **Data format.** Here the format and transmission mode of the 32-bit data packet is chosen. For example, the leading resolution of the drift time measurement (also by using the RC components) and signal width can be determined; further the use of local or global trailer in the data packets, as well as the measurement mode (trailing and/or leading signal edges). In addition, the source of the test signal can also be selected here.
- **Time windows & offsets [clock cycles].** This is very important part of the configuration which sets the width of the time windows as described in Section 4.2.2 (see also Figure 4.8). The time unit set depends on the selected clock cycle (default: 25 ns, i.e. 40 MHz). For the right selection of the time windows remind that different time windows depends on each other and on the time offset selected (detailed informations can be found in the manual [60]).
- **Clock.** For different purposes and time resolutions different clock sources can be used. The fine clock adjustment can be done by right clock delay selection.
- **Read out control.** In this part of VI the speed of the read-out can be controlled, as well as the various read-out mode and read-out interface operation. Also the dynamic HPTDC FIFO size can be set and some reject functions can be enabled.
- **Enable error mark.** The user has the option to set some errors alerts that occur by read-out and HPTDC operation. It is recommended to enable all possible error options but the **Enable error bypass**. If this option is selected, the HPTDC having any error is bypassed and no information (also error messages) from this chip is available.
- **TDC control.** These fields control the HPTDC operation. They includes many options for input and output delays, diverse reset enabling, power and test modes etc.

A. MiniCrate DAQ configuration and readout software

Figure A.1.: The HPTDC configuration setup software. The demanded read-out parameters have to be selected and the enabling function set by clicking the proper fields. By execution the software creates a simple text file which includes lines of hexadecimal values (647 bits lines), which are then loaded to the proper HPTDC.

- **TDC control.** In some cases, e.g. by use of higher resolution modes, it is useful to perform a fine time adjustment to reduce any effects occurring by the real time differences in the electronics etc. For these purposes times up to 80 ps can be corrected in all 32 HPTDC channels at their offsets and DLL taps. Also for the very high resolution mode the adjustment of the RC elements is possible.

When all settings are done, the program execution creates a simple text file *MB1_MiniCrate_TDC_configuration_data_ro****_tl****_sw****_yymmdd_HHMM.txt*¹ (file path in the indicator **Configuration file path**:), including lines with hexadecimal values for 647-bit sequence each, where the configuration setup is encoded. Each line corresponds to one HPTDC. This setup file is then used to load the configuration data to the HPTDCs. In addition, an image of the front panel is written to the file *MB1_MiniCrate_TDC_configuration_data_ro****_tl****_sw****_yymmdd_HHMM.jpg* (**Panel image (jpg) path**:), which can be treated as a comfortable configuration overview.

¹The abbreviations *ro*****, *tl***** and *sw***** mean the roll over, trigger latency and search window, respectively, in bunch cross units (usually 25 ns, see also Section 4.2.2), expressed as ****** in the file name.

A.2. Read_out_ROS-8_DG535_ac.vi

Before running the software (Figure A.2) some important parameters should be set, allowing right data reading process, output data assignment and automatic control during the DAQ. The fields for the settings are located in the left region of the VI panel.

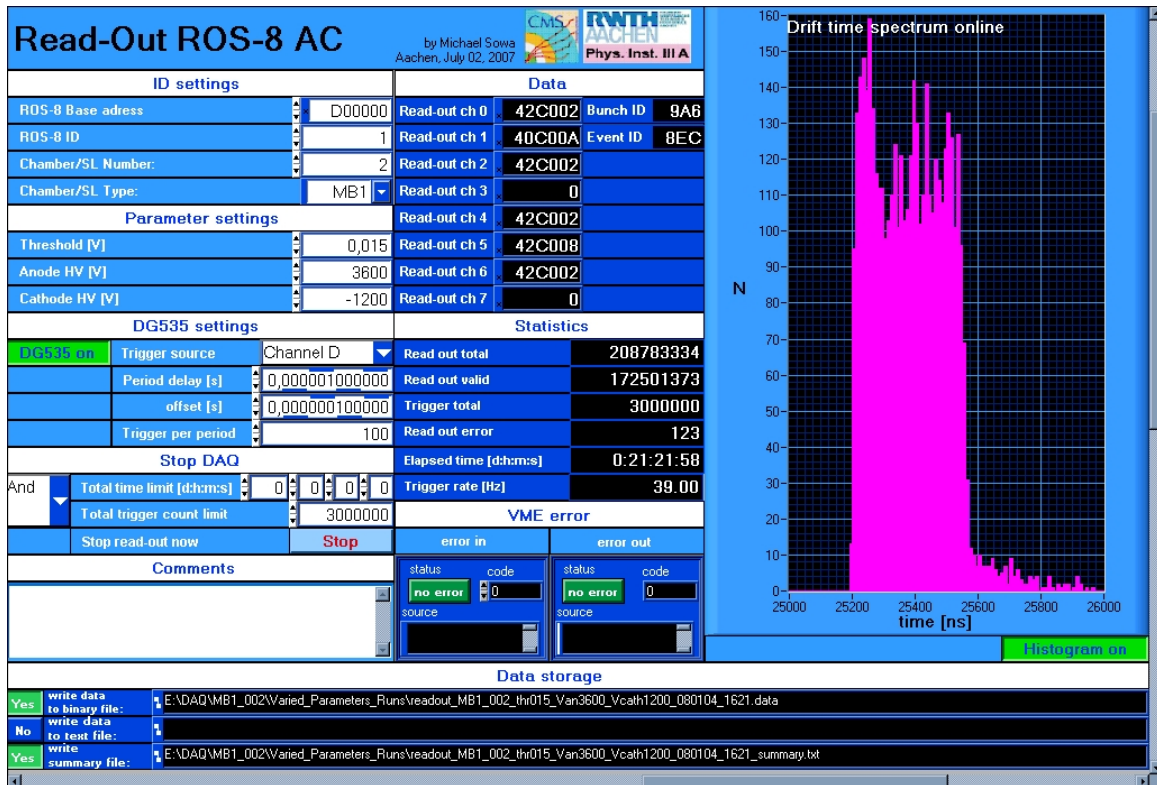


Figure A.2.: The front panel of the software *Read_out_ROS-8_DG535_ac.vi* for the DAQ via the MiniCrate. It includes four segments: parameters to be set like ROS-8 and chamber IDs, DAQ duration and limits (left), current monitoring of data taken and DAQ statistics as well as of possible connection errors (middle), online monitoring of the drift time spectrum (right, optionally used) and options for storage of the data taken and writing the run summary report (bottom).

At first it is needed to set the ROS address (ROS-8 Base address) and ID (ROS-8 ID) which can be found either in the ROS-8 PCB (jumper) or set automatically by VME configuration. The chamber ID and type (Chamber/SL Number and Chamber/SL Type) are to be selected for right allocation of the data read and file storage. Also the three next parameters Threshold [V], Anode HV [V] and Cathode HV [V] are to be set for assignment of the data in file name by executing the DAQ under various chamber voltages set.

The fields within DG535 settings, namely Trigger source, Period delay [s], offset [s] and Trigger per period, are used only in an expert test modus by the *Digital Delay and Pulse Generator DG535* [113] support and are not essential for usual DAQ. The connection of the DG535 in the DAQ is performed only by previous click on DG535 on.

The DAQ is running uninterrupted, if it is not stopped. Several stop options are implemented to limit the DAQ time or the recorded data amount. For this purpose one select the

A. MiniCrate DAQ configuration and readout software

Total time limit [d:h:m:s], in order to determine the DAQ duration in days, hours, minutes and seconds, or/and the **Total trigger count limit** to specify the total number of events in the DAQ run. It is possible to combine the both limits set by clicking the **And/Or/No limit** optional field. The DAQ can be stopped every time by clicking the **Stop** button at **Stop read-out now**.

Finally the operator has also the option to add any supplemental comments and annotations (also during the DAQ run) typing them into the field **Comments**. These entries are then attached to the run summary report (see below).

The DAQ can be monitored in the middle part of the front panel. It contains indicators for the actual data taken, run statistics and error messages.

In the data fields one can observe the 32-bit data sequences currently read out from each ROS-8 channel as hexadecimal value **Read-out ch0 ... 7**. Also the actual event and bunch number (**Bunch ID** and **Event ID**) are displayed, which are assigned by the clock to the trigger signal and extracted from the HPTDC data.

The current DAQ state is displayed during the run in six statistics indicators: the total amount of read-out steps via VME from the ROS-8 **Read out total**, the total number of valid read-out steps, i.e. read-out steps by non-empty ROS-8 FIFOs **Read out valid**, the total number of events registered by the DAQ **Trigger total**, the total number of VME read-out errors **Read out error**, run duration **Elapsed time** [d:h:m:s] and the trigger rate, which is the actual event total number divided by the run duration in seconds **Trigger rate** [Hz]. Also any possible VME input and output errors are displayed by means of their specific LabVIEW code and source description, as far as known (**error in** and **error out**).

The right part of the front panel consists of a histogram with the actual drift time spectrum. It is activated by clicking the button **Histogram on**. This option is useful for online observation of the data taking quality, but slows down noticeably the DAQ speed. Therefore it is recommended to use this function if no data are written into a file, although the quality of data taken is not affected in this case.

The read data are continuously written to a file. The user has the option for storing the data in a binary file (**write data to binary file**, recommended) `readout_MB1_002_thr***_Van****_Vcath****_yymmdd_HHMM.data` or in a text file (**write data to text file**) `readout_MB1_002_thr***_Van****_Vcath****_yymmdd_HHMM.txt`². The format of the data written into the file is the same as described in the Section 4.3.2. After the data taking is completed the summary report `readout_MB1_002_thr***_Van****_Vcath****_yymmdd_HHMM_summary.txt` (option **write summary file**) is written. It includes all final statistics data and comments displayed, as well as the file paths, DAQ software, run date and time. Also the parameters set and DG535 settings are attached to this file.

²The abbreviations `thr***`, `Van****` and `Vcath****` mean the threshold, anode HV and cathode HV, respectively, in millivolt (threshold) or Volt (HV), expressed as `***` or `****` in the file name.

A.3. Event data block

An example for a formatted data block read out from all six active ROS-8 channels is presented. The 32-bit words containing the measured drift times are marked blue and mean detected 8 hits by the HPTDC 0 on ROB 1 (4 hits from the ϕ SL 1 and 4 hits from the ϕ SL 2) and 4 hits by HPTDC 1 on ROB 4 (from the θ SL) in the same event 621.

2A	<i>Number of words in the event data block</i>
0	<i>Run number</i>
0	<i>Spill number</i>
26D	<i>Event number</i>
0	<i>Reserved</i>
9	<i>ROS data offset</i>
FFFFFFFF	<i>Reserved</i>
FFFFFFFF	<i>Reserved</i>
FFFFFFFF	<i>Reserved</i>
20	<i>Total number of ROS data words</i>
EF428877	<i>ROS ID, ROS channels enabled</i>
FF001000	<i>ROS channel 0 (ROB 0) data begin</i>
326DCE7	<i>ROB 0 group header</i>
1326D002	<i>ROB 0 group trailer</i>
FF001001	<i>ROS channel 1 (ROB 1) data begin</i>
326DCE7	<i>ROB 1 group header</i>
4011FA2C	
4091F890	
4019F9E0	
4099FBF0	<i>ROB 1 data, here from HPTDC 0 only,</i>
4001FB44	<i>with encoded drift time measurements</i>
40A9FD80	
4009FF58	
4081FE70	
1326D00A	<i>ROB 1 group trailer</i>
FF001002	<i>ROS channel 2 (ROB 2) data begin</i>
326DCE7	<i>ROB 2 group header</i>
1326D002	<i>ROB 2 group trailer</i>
FF001004	<i>ROS channel 4 (ROB 3) data begin</i>
26DCE7	<i>ROB 3 group header</i>
1026D002	<i>ROB 3 group trailer</i>
FF001005	<i>ROS channel 5 (ROB 4) data begin</i>
326DCE7	<i>ROB 4 group header</i>
4131FBDC	
4139FBE0	<i>ROB 4 data, here from HPTDC 1 only,</i>
4121FCAC	<i>with encoded drift time measurements</i>
4129FC8C	
1326D006	<i>ROB 4 group trailer</i>
FF001006	<i>ROS channel 6 (ROB 5) data begin</i>
326DCE7	<i>ROB 5 group header</i>
1326D002	<i>ROB 5 group trailer</i>
2A	<i>Number of words in the event data block (repeated)</i>

B. DCS gas pressure sensor calibration and LUT software

For the preparation of the sensor calibration data and creation of the Look Up Tables (LUTs), as described in this thesis, a couple of *LabVIEW* software application was developed. The following unit describes only those ones which are directly used for mentioned purposes. All other auxiliary programs which are also useful for e.g. comparing the created data files, control the calculation parameters etc. are not presented here; for any information concerning this please contact the author.

B.1. *SensCalV2.0.vi*

Starting the *SensCalV2.0.vi* (Figure B.1) at first the sub-VI *Select_Manifold.vi* (see section B.2) is executed, which ought find and list the calibration measurement data files of the sensors in the selected manifolds via *SensCal_Global.vi*. After the manifolds are listed, the *SensCalV2.0.vi* extracts the measurement data contained in the files in three tables, corresponding to the offset measurements (ambient pressure) in the beginning and in the end of the measurement run and the main data sequence taken for the whole calibration pressure interval. Also additional information, like connected device names (listed in field **selected device**), measurement parameters, comments (**comment of source file**) etc. are read and displayed on the front panel. On the basis of the listed device the software allocates after that the value columns in the tables to the proper sensors and manifolds.

The data taken from the baratron sensors are calculated to obtain a mean difference of the same baratron taken during the offset measurement before and after the main measurement and the difference between the both baratron sensors taken at the same time (one of the baratron sensors measures always the ambient pressure and the other one measures the reference pressure, which is simultaneously measured by the calibrated sensors). These values are displayed in the **info panel**.

These baratron values and the sensor output data are then investigated, if there are any outlier or anomalies in their data set. They are then filtered, if needed, by selection of the filter parameters (**Filter**). Such filtered data are displayed in the graphs **Baratron15-Baratron17** (baratron data vs. measurement point), **Sensor** (sensor data vs. measurement point) and **diff baratron vs. sensor** (merged data of the previous two data sets). The user must check the proper calibration limits (**initial calibration limits [V]**) and – if needed – change them by moving the interactive cursor in the graph **Sensor**.

Such determined limit calibration interval is then divided into a constant number of uniform interval units. On each of these small intervals a local linear fit is performed. Also the smoothness (Equation 5.1) and standard deviation is calculated and displayed (indicator group with **ref av smooth**, **sensor av st dev** etc.). The result for each sensor is then presented in the graph **Calibration Curve**. This is the main information source for classification the present calibration as good or bad (see also Section 5.3.2). It presents the relation rel. pressure/voltage but also the difference between calibration and linear fit of all raw data measured in this fit

B. DCS gas pressure sensor calibration and LUT software

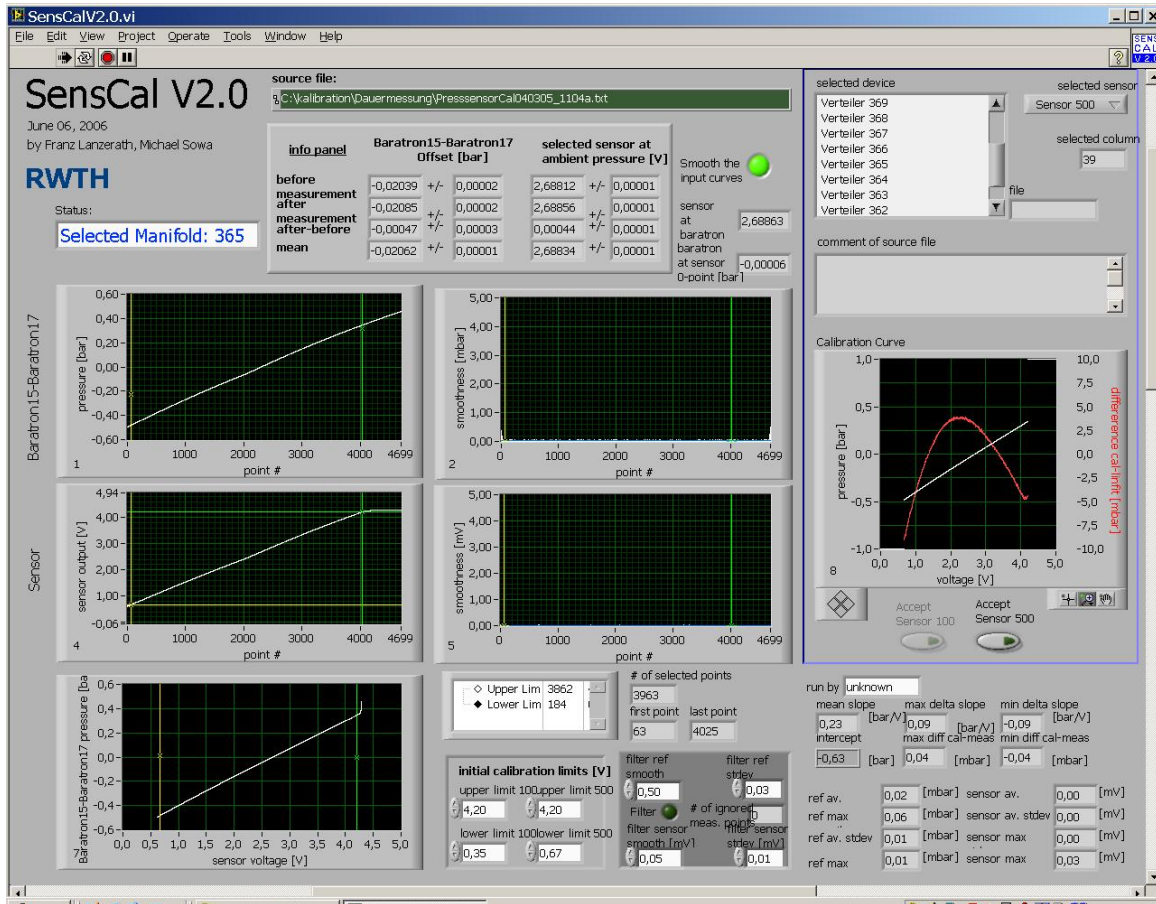


Figure B.1.: The front panel of the calibration software *SensCalV2.0.vi*. It recalculates the raw data of the sensors mounted in the selected manifolds by means of the local linear fit. For this purpose one select the fit range for each sensor (is proposed automatically by the software). In this range the local linear fits are done. The output file contains then the two tables with the converted data (pressure to sensor output) and is used for creation of the Look Up Tables for the gas pressure read-out.

interval. If there is no objection, the calibration for given sensor has to be accepted (clicking **Accept Sensor 100** or **Accept Sensor 500** for corresponding sensor). The procedure is then repeated for the other sensor in the same manifold.

After both sensors are calibrated, two files are created (for the decryption file name refer to Section 5.17):

- *CalTabMan***_yymmdd_HHMM.txt*: Converted calibration data text file (see Appendix C.4).
- *CalTabMan***_yymmdd_HHMM.jpg*: Screenshot of the *SensCalV2.0.vi* front panel. It is useful for additional documentation, especially for quick view on the calibration data and the graphs.

The process is repeated for all manifold listed in the **selected device** and in the reference manifold list obtained from *Select_Manifold.vi*. The current status during the *SensCalV2.0.vi* run is indicated in field **Status**:. After the calibration of all selected manifolds is done the *SensCalV2.0.vi* stops and a calibration summary report is created.

B.2. Select_Manifold.vi

This application runs as sub-VI of the mean calibration software *SensCalV2.0.vi* (see Section B.1). When the front panel was opened (Figure B.2), the measurement data files of the sensors in the manifolds have to be selected for calibration by clicking on proper manifold number. After all needed manifolds are selected by their numbers, the selection has to be confirmed (clicking "OK" on **Manifold selected?**). Then the software contacts the actual reference list *Gasverteiler_Uebersymmdd.xls* (indicated in **Reference path**) containing the file names with the measurement data of the sensors in the corresponding manifolds. These file names in common with the corresponding manifold numbers are then listed in a table (**Selected manifolds/corresponding raw data files**) and exported as a global variable (in *SensCal_Global.vi*) for use by *SensCalV2.0.vi*. Also current status can be observed in the front panel (**Status**), which is also exported as global variable to the *SensCal_Global.vi*.

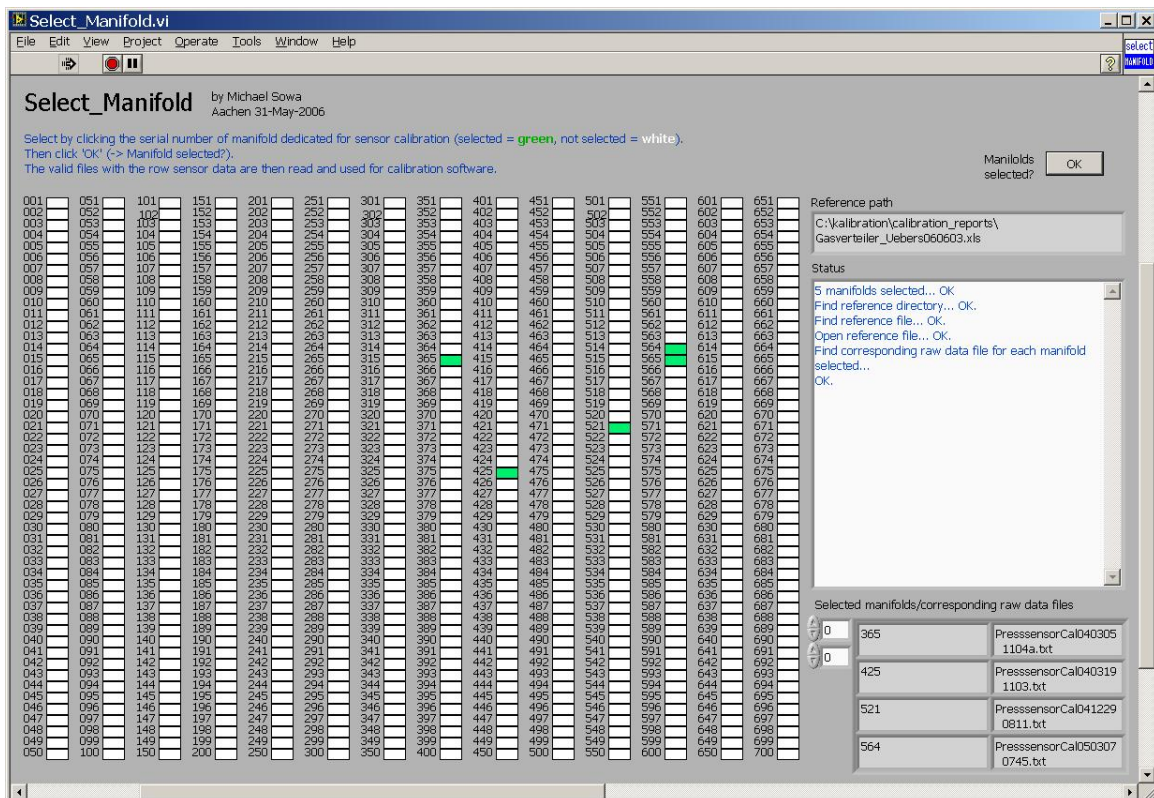


Figure B.2.: The front panel of the software *Select_Manifold.vi*. By clicking on the serial numbers of the manifolds the files with the sensor output data taken by *kalibrationV1.5.vi* are selected and the data can be transferred to the another one *SensCalV2.0.vi* for recalculate them for use in a converted form (pressure to sensor output).

If no manifold is selected, the execution of *Select_Manifold.vi* and *SensCalV2.0.vi* is stopped. If no measurement file list is found or any measurement files are not existing at the expecting place, a dialog window appears and the user is asked, whether to find the proper files manually – the execution is then continued if the search succeeded, or aborted. In each case the action is registered (**Status**) and sent to *SensCal_Global.vi*.

B. DCS gas pressure sensor calibration and LUT software

B.3. *LUT_PADC.vi*

By loading the *LUT_PADC.vi* (Figure B.3) the operator has the option to select the source for the seven chamber identification and pressure device data (wheel, section, sector, chamber ID, PADC ID, manifold HV ID and manifold FE ID; MB Items). This could be realized either by connection to an external databases (recommended, by selecting from **DataBase**, see Appendix B.5) or by manual editing (by selecting **manual input**, see Appendix B.4). For this and all following operation steps the status is displayed in **Status**.

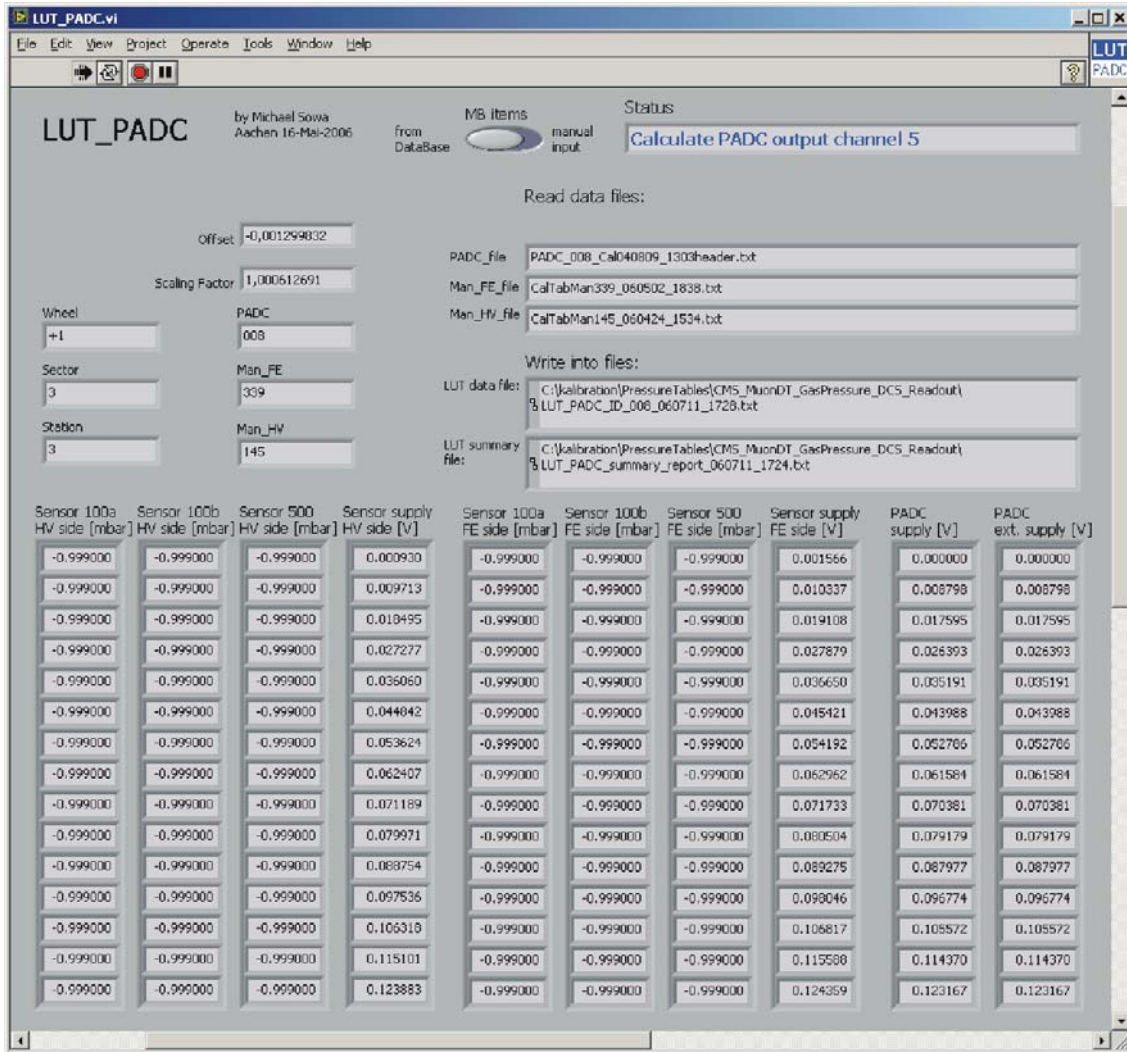


Figure B.3.: The main software used for creation of the Look Up Tables *LUT_PADC.vi*. This *LabVIEW*-based program runs automatically loading chamber and device identification data from external databases or from a table edited by operator, loading then the appropriate calibration files of the manifolds and PADC stored in the local PC, processing the calibration data and creating LUT output files and summary report files.

Once these data of all 250 chambers are loaded in a 7x250 table the software searches first for the PADC and manifolds calibration files of the first chamber (actual chamber position data in **Wheel**, **Sector** and **Station**; device IDs in **PADC**, **Man_FE** and **Man_HV**), whose data

filled the table in the first row. By finding these three files (names appear in *Read data files*: for *PADC_file*, *Man_FE_file* and *Man_HV_file*) their data are processed as described in Section 5.4.2. For each PADC channel the already converted data appear then in the one of the ten 1x1024 arrays (from *Sensor 100a HV side [mbar]* to *PADC ext. supply [V]*). These ten arrays form together one 10x1024 Look Up Table (LUT), which is then directly written into an ASCII file (*Write into files*: under *LUT data file*:) (see Appendix C.6) being the ultimate source for the gas pressure read-out values of the actual chamber.

If the LUT creation for the first chamber is complete, the same procedure begins for the next one, etc., until the data for all 250 chambers are processed for the LUTs. If the LUT processing run is complete as described, the summary report is written (*Write into files*: under *LUT summary file*:; see Appendix C.7).

B.4. *MB_item_for_LUT_PADC.vi*

An optional way to create the identification data, which are needed to create the LUTs (*LUT_PADC.vi*, see Section B.3), is to write them manually in the prepared spreadsheet *MB_item_for_LUT_PADC.vi* (Figure B.4). This file contains an editable 7x250 table *MB Items*, where the entries in the first three columns (wheel, section and sector) are already pre-filled. One has only to fill in the remained ones by numbers in accordance with the other identification data for all chambers of which the LUTs have to be created. By clicking OK the values edited in the spreadsheet are then read by *LUT_PADC.vi* and used for creation of the LUTs.

This method is not recommended, due to the possibility of making errors in the cell editing. Nevertheless, it can be used optionally every time, for example also in a moment, when the connection to the external databases is failed.

B.5. *Read_mbID_mbposition_URL.vi* and *Read_mbtype_mbID_padcID_manifoldID_URL.vi*

The recommended case to obtain the CMS DT muon chamber position and IDs, as well as the gas pressure read-out device IDs (PADC and two manifolds), is performed via a direct connection to the data bases. For this purpose two programs were developed, which act as subprogram of *LUT_PADC.vi* (Section B.3). They can also be executed independently as main software to check the chamber position and ID data.

Once the *LUT_PADC.vi* is running at first the *Read_mbID_mbposition_URL.vi* is executed (Figure B.5 left). It reads the actual data of the chamber position in the CMS detector directly from the database by connecting to it via <http://isr-muon.web.cern.ch/isr-muon/cgi-bin/>. The data are taken over for each of the 250 chambers and saved in a two-dimensional 4x250 array, whose each row is represented by one chamber, each column by the identification data wheel, station, sector and chamber ID. The read data array is then saved temporarily as a global variable in an additional *LabVIEW* subroutine *Global_read_mbitems.vi*.

The another subprogram *Read_mbtype_mbID_padcID_manifoldID_URL.vi* (Figure B.5 right) runs after the previous one is closed. It loads the array saved in *Global_read_mbitems.vi* which includes the four chamber identification data. Then it connects the another database via http://cmsdoc.cern.ch/~fetchenh/DT_PADC_Manifolds.xls, which includes, among others, the PADC and manifold IDs, manifold position on the chamber, chamber ID and chamber

B. DCS gas pressure sensor calibration and LUT software

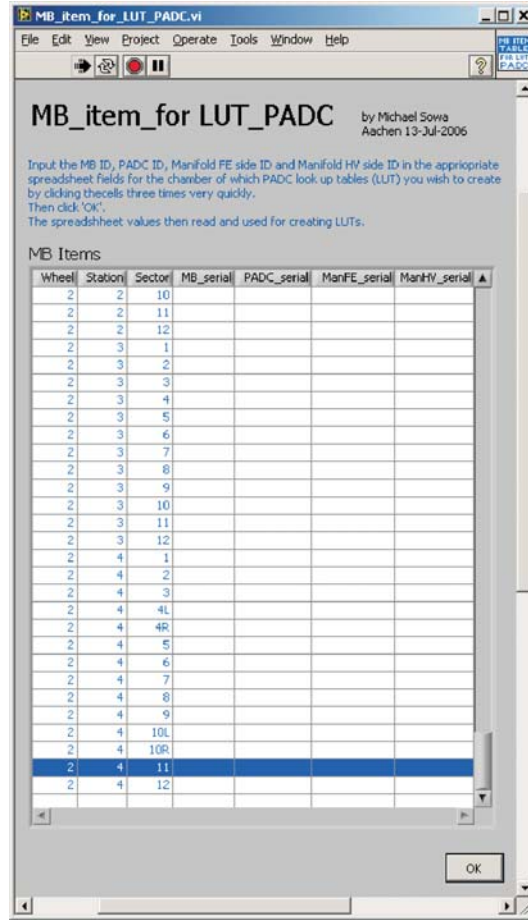


Figure B.4.: Beside the extern databases one can optionally create the source for the chamber identification data by manual editing a spreadsheet. Although this method is not recommended, it could be used in cases, when the connection to the databases is failed.

type. The software recognizes automatically the corresponding chamber type by given chamber position in the CMS detector. Reading the chamber position data (wheel, station and sector) from the data array a chamber type is assigned to them. This assigned chamber type in common with the fourth array row entry (chamber ID), is tried to be matched in the *DT_PADC_Manifolds.xls*. By matching these two values, the corresponding PADC ID, manifold ID and manifold position are then read from this file. The seven numbers assigning the 250 CMS DT muon chambers – wheel, station, sector, chamber ID, PADC ID, manifold FE side ID and manifold HV side ID – are then written in a new two-dimensional 7x250 array, which is temporarily saved as a global variable in the *Global_read_mbitems.vi*. The creation of the chamber identification sequence by seven values is repeated for each of the 250 chambers. Also the report containing the both array data and other summary informations, is saved for further usage in the *Global_read_mbitems.vi*.

B.5. *Read_mbID_mbposition_URL.vi* and *Read_mbtype_mbID_padcID_manifoldID_URL.vi*

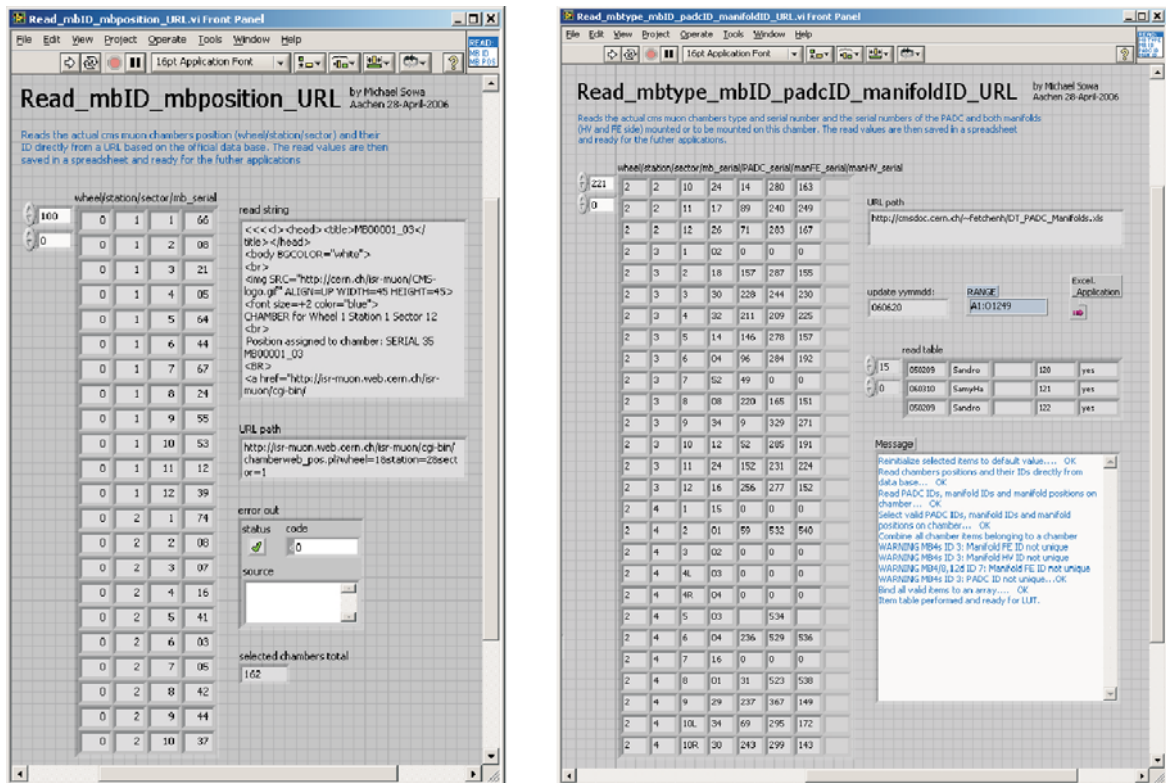


Figure B.5.: The subprograms of the *LUT_PADC.vi* used for assignment of the LUT data to the appropriate chamber in the CMS detector by automatical connection to the external data bases. Left: *Read_mbID_mbposition_URL.vi* reads the actual data of the chamber position in the CMS detector and their IDs. Right: *Read_mbtype_mbID_padcID_manifoldID_URL.vi* reads the device IDs, chamber type and chamber ID. Merging the data of the both databases one obtains a unique sequence characterizing the chamber for which the LUT is then created.

C. DCS gas pressure sensor calibration and LUT files and databases

The data of the different calibration runs, the LUTs etc. made in different steps for the final gas pressure measurement at the CMS DT muon chambers are stored mostly in text files. The name of the files contains the date and time of the file creation for easy retrieval and identification of the actual data storing place. The date and time coding is `yymmdd_HHMM` within the file name and means **y**ear, **m**onth, **d**ay, **H**our and **M**inute; all two-digit. The item ID (manifold, PADC, LUT etc.) is also included in the file name indicated below as `****`.

The databases contain some of the mentioned files or include informations, which are directly needed for the LUT creation. The databases are accessible worldwide via the usual data transfer protocols (e.g `http`).

C.1. *PressSensorCal*yymmdd_HHMM.txt

This reference raw data file is created automatically by executing the sensor calibration program (see Section 5.3.2). It contains average data values (reference pressure and voltage) and their standard deviations, read from each channel at each loop. One table line contains all values registered at one measured loop. The values in one column correspond to the output of the same device (manifolds, baratrons etc.) connected to the PC, averaged over the 1000 measurements making up a single data point and their calculated standard deviation for each loop (read pressure values of reference manometers and voltage values of the sensors and connected supply voltage). The total number of loops and of the measurements per loop are set at the beginning of the calibration run as parameters (Figure 5.16). Usually there are also data from the atmospheric calibration done at the beginning and at the end of the calibration run (zero-sequences). Additional information, like date and time measurement, used software version, calibration parameters and comments etc. are also written into the file. Also information about devices connected to the PC (manifold serial numbers, baratrons, supply voltages etc.) and their channel configuration can be found there.

C.2. *Gasverteiler_Uebersymmdd.xls*

This *Excel* file [95] contains mainly the ID of each manifold whose sensors were at least once calibrated (one column) and the name of the corresponding reference raw data file(s) (Appendix C.1), where the calibration data are stored (following columns). If a calibration run for a given manifold was done well, the name of the reference raw data file is properly labeled in this list. This spreadsheet is maintained manually, it is filled in with new entries after each sensor calibration run.

C.3. *yymmdd_HHMMcal.pdf*

In this report one can find diagrams with plotted sensor output and the corresponding standard deviations based on the multiple measurement loop and smoothness based on Equation 5.1. This was separately plotted for each sensor being calibrated, as well as for the reference PG4 sensors and baratrons. In addition, the file contains also a list of the connected devices, comments etc.

C.4. *CalTabMan***_yymmdd_HHMM.txt*

This file contain the converted calibration data from two sensors belonging to one manifold with an ID *** (three-digit). It is automatically created by using the software *SensCalV2.0.vi* (see Section 5.3.2, Appendix B.1). Particularly, the file includes two tables, one for each sensor. Each table has 4096 lines and three columns. Each line corresponds to one average sensor output value, as fitted locally by *SensCalV2.0.vi*. The three columns are composed of the values of reference pressure, sensor output and standard deviation calculated by the local fit, respectively. Additional information about source file, date, time and other parameters set for the calculation of the raw data are also included in this file and labeled by keywords.

C.5. *PADC***Cal_yymmdd_HHMMheader.txt*

Due to the large size of the PADC output files (up to 30 MB, see Section 5.3.3) the headers were extracted from it and this new text files were made out of them. The scaling factor A and offset b (see Equation 5.3) are listed in a table for the PADC channels 0 to 7. For the channels 8 and 9 only an offset value is given. These channels were not calibrated and should give only information about a possible instability of the read-out, which should measure permanently constant supply voltages.

C.6. *LUT_PADC_ID***_yymmdd_HHMM.txt*

This file is automatically created by executing the software *LUT_PADC.vi* (see Section 5.4.2, Appendix B.3). It contains the Look Up Table (LUT) which is a spreadsheet consisting of 10 columns representing the 10 PADC channels as mentioned on the page 115 and 1024 rows, each row for each PADC count read out. The entries in the LUTs are converted pressure values (channels 0, 1, 2, 4, 5 and 6) or voltages (channels 3, 7, 8 and 9). All of them are six-digit precision numbers and can be positive or negative (pressure) or only positive (voltage). In the header of the LUT file one can find useful information, like source calibration file names used for creating the LUT, PADC and manifold IDs, chamber ID and chamber type, chamber position in the detector, among others. All these parameters are there labeled by keywords, so that a simple access to these data can be performed.

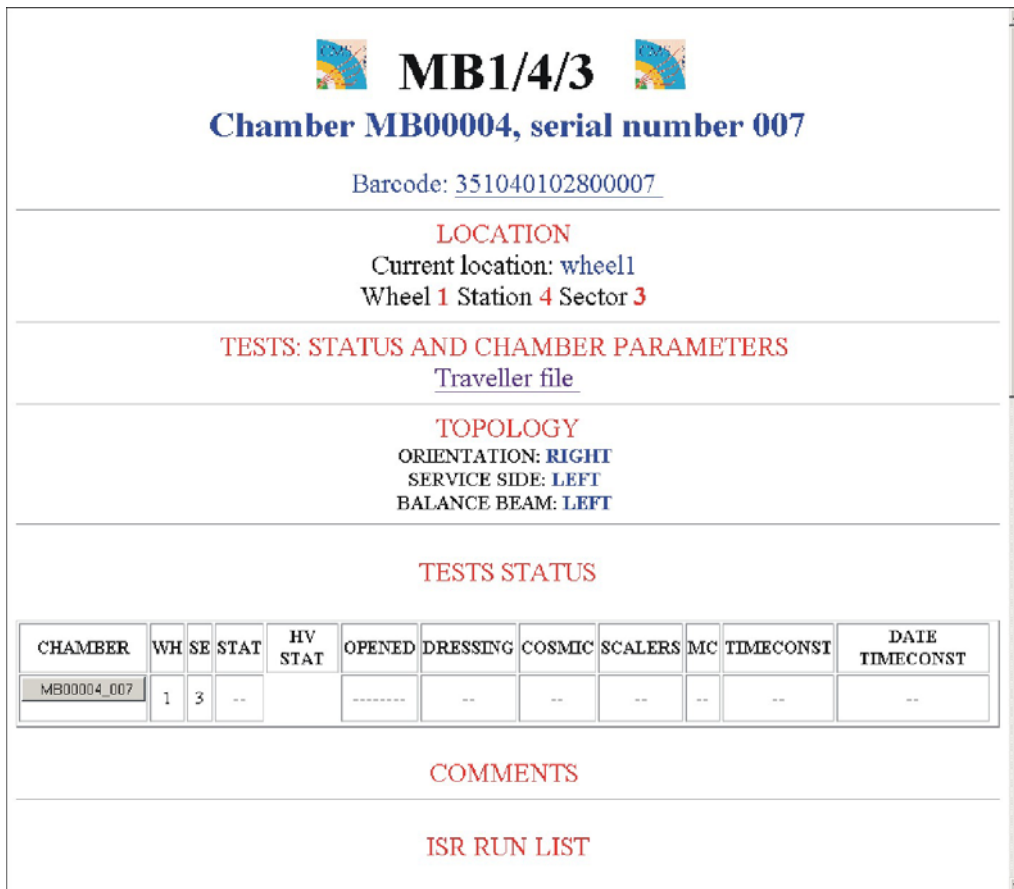
C.7. *LUT_PADC_summary_report_yymmdd_HHMM.txt*

This summary report can be treated as minutes of the *LUT_PADC.vi* run (see Section 5.4.2, Appendix B.3). Also data read from the external databases (chamber identification data, see Appendix C.8 and C.9), as well as the contacted URLs are recorded there. All steps by which the connection and data reading process were done and all eventual failure messages

are also listed in the file. Finally a list with the LUT file names and their corresponding chamber identification data is attached to the file.

C.8. DT chambers positions and ID database

This *html* database contains the position data of the chambers. Aside from these informations one can find here the chamber ID, chamber type, chamber position and other details. The contact with this database can be done usually via *http* protocol under *http://isr-muon.web.cern.ch* [102].



MB1/4/3

Chamber MB00004, serial number 007

Barcode: [351040102800007](#)

LOCATION
Current location: **wheel1**
Wheel **1** Station **4** Sector **3**

TESTS: STATUS AND CHAMBER PARAMETERS
[Traveller file](#)

TOPOLOGY
ORIENTATION: **RIGHT**
SERVICE SIDE: **LEFT**
BALANCE BEAM: **LEFT**

TESTS STATUS

CHAMBER	WH	SE	STAT	HV STAT	OPENED	DRESSING	COSMIC	SCALERS	MC	TIMECONST	DATE TIMECONST
MB00004_007	1	3	--		-----	--	--	--	--	--	--

COMMENTS

ISR RUN LIST

C.9. PADC and Manifold database

This *Excel* spreadsheet http://cmsdoc.cern.ch/~sfetchenh/DT_PADC_Manifolds.xls contains data like manifold IDs, PADC IDs and IDs and type of the muon chamber they belong to. Also the manifold position in the chamber is listed there. Along with the registered date of each intervention, the status of the system at any earlier time can also be reconstructed. The chamber ID and type are the interface to the other database containing the chamber position data so that a unique number sequence characterizing a complete chamber can be used for the LUT creation [103].

C. DCS gas pressure sensor calibration and LUT files and databases

Microsoft Excel - DT_PADC_Manifolds_071205.xls

Frage hier eingeben

Charcoal 16

DT Gas Pressure Measurement Items

1 Lists which PADC board and manifolds have been installed WHEN on WHICH CHAMBER.
 2 On a single line enter data for ONLY ONE gas item (PADC or manifold).
 3 Do NOT delete previous installation entries - they remain in use, to reconstruct earlier data.
 4 If the entries are by serial numbers, find the latest status by sorting by date (column
 5 or the status of a given chamber by sorting by "MB" (columns H, I). Warning: select the whole block under the header line prior to sorting!
 6 Remark on gas connection (NOT included in this table): as inlet take the lowest manifold of the chamber; for horizontal chambers the front one.
 7 List maintained by Gerd.Fetchenhauer@cern.ch, tel. +41 76 487 3443

8

9

10 Last update (yyymmdd) **071205**

11 **These columns might be obsolete**
(refer to Installation data file)

DATE	Info from (name)	PADC serial	Manifold serial	ManifPlug blue plug	ManifFE at FE side	ManifHV at HV side	MB type	MB serial	Installed / Remove	"G.F." yyymmdd	COMMENT	Service chamber Position Left/Right	MB wheel / sector	COMMENT2
DATE	Info from	PADC serial	Manifold serial	ManifPlug	ManifFE	ManifHV	MB type	MB serial	Installed /	"G.F."	COMMENT	Service chamber Position	COMMENT2	
050213	ISR all		387	yes	X		MB1+	53		070118		L +0/10		
050213	Sandro		355	yes		X	MB1+	53		070118		L +0/10		
060317	CN Girls	44					MB1+	53		070118		L +0/10		
050213	ISR all		508	yes	X		MB2+	37		070118		L +0/10		
050209	Sandro		257	yes		X	MB2+	37		070118		L +0/10		
041111	CN Girls	231					MB2+	37		070118		L +0/10		
050213	Sandro		369	yes	X		MB3+	44		070118		L +0/10		
050311	Gerd		150	yes		X	MB3+	44		070118		L +0/10		

Verteiler+PADC / Manual D / Manual E /

Bereit NF

C.10. LUT database

In this database both the LUT files (Appendix C.6) and the LUT creation reports (Appendix C.7) are stored. They can be accessed via http://wwwdac.physik.rwth-aachen.de/LUT_PADC each time for the online (or offline) pressure data conversion, or to obtain other useful data concerning the LUT processing.

Bibliography

- [1] LEP Higgs Working Group; R. Barate *et al.*: *Search for the Standard Model Higgs Boson at LEP*. Phys. Lett. **B365**, 61 (2003).
- [2] S. F. Novaes: *Standard Model: An Introduction*. hep-ph/0001283 v1, 2000.
- [3] S. P. Martin: *A Supersymmetry Primer*. hep-ph/9709356 v4, 2006.
- [4] Emmy Noether: *Gesammelte Abhandlungen/Collected Papers*. Springer-Verlag, Berlin-Heidelberg, 1983.
- [5] W. M. Yao *et al.*: *Review of Particle Physics*. Journal of Physics G **33**, (2006).
- [6] R. N. Mohapatra *et al.*: *Theory of Neutrinos: A White Paper*. hep-ph/0510213 v2, 2005.
- [7] S. L. Glashow: *Partial-Symmetries of Weak Interactions*. Nucl. Phys. **22**, 579 (1961);
A. Salam: *Elementary Particle Theory*. Ed. N. Svartholm "Almqvist & Wiksell", 367, Stockholm, 1968;
S. Weinberg: *A Model of Leptons*. Phys. Rev. Lett. **19**, 1264 (1967).
- [8] C. N. Yang, R. L. Mills: *Conservation of Isotopic Spin and Isotopic Gauge Invariance*. Phys. Rev. **96**, 191 (1954).
- [9] P. W. Higgs: *Broken Symmetries, Massless Particles and Gauge Fields*. Phys. Lett. **12**, 132 (1964);
F. Englert, R. Brout: *Broken Symmetry and the Mass of Gauge Vector Mesons*. Phys. Rev. Lett. **13**, 321 (1964).
- [10] J. Goldstone, A. Salam, S. Weinberg: *Broken Symmetries*. Phys. Rev. **127**, 965 (1962).
- [11] D. I. Kazakov: *Beyond the Standard Model*. hep-ph/0611279 v1, 2006.
- [12] S. Willenbrock: *Triplicated Trinification*. hep-ph/0302168 v2, 2003.
- [13] G. Shaughnessy: *Review of Lightest Neutralino in Extensions of the MSSM*. hep-ph/0508027, 2005.
- [14] R. N. Mohapatra: *Unification and Supersymmetry, The Frontiers of Quark-Lepton Physics*. Springer-Verlag, Berlin-Heidelberg, 2003.
- [15] A. Zee: *Unity of Forces in the Universe, vol. I and II*. World Scientific, Singapore, 1982.
- [16] P. Nath, S. Reucroft (editors): *Particles, Strings and Cosmology*. Symposium Proceedings, Northeastern University Boston, USA, 27-31 March 1990. World Scientific, Singapore, 1991.

Bibliography

- [17] C. Efthimiou, B. Greene: *Fields, Strings and Duality*. TASI 96. World Scientific, Singapore, 1997.
- [18] K. Lane: *Lectures on Technicolor*. Boston University.
http://cyclo.mit.edu/~schol/8.811/TC_trans_2002.ps
- [19] H. Goldberg, M. E. Gomez: *How Georgi-Jarlskog and SUSY-SO(10) imply a measurable rate for $\mu \rightarrow e\gamma$* . hep-ph/9606446 v1, 1996.
- [20] LHC - The Large Hadron Collider.
<http://lhc.web.cern.ch/lhc/>.
- [21] CERN Multimedia gallery.
http://multimedia-gallery.web.cern.ch/multimedia-gallery/PhotoGallery_Main.aspx.
- [22] S. Catani: *Aspects of QCD, from the Tevatron to the LHC*. hep-ph/0005233 v1, 2000.
- [23] M. Spira *et al.*: *Electroweak Symmetry Breaking and Higgs Physics*. hep-ph/9803257v2, 1997.
- [24] N.V.Krasnikov, V.A.Matveev: *Search for Standard Higgs Boson at Supercolliders*. hep-ph/9909490 v1, 1999.
- [25] TOTEM Total Cross Section, Elastic Scattering and Diffraction Dissociation at the LHC.
<http://totem.web.cern.ch/Totem/>.
- [26] LHCf Verification of interaction model for very high energy cosmic ray at 10^{17} eV.
<http://www.stelab.nagoya-u.ac.jp/LHCf/>.
- [27] FP420 R&D Project.
<http://www.fp420.com/>.
- [28] The ATLAS experiment.
<http://atlas.web.cern.ch/Atlas/index.html>.
- [29] ALICE A Large Ion Collider Experiment at CERN LHC.
<http://aliceinfo.cern.ch/>.
- [30] The Large Hadron Collider beauty experiment.
<http://lhcb.web.cern.ch/lhcb/>.
- [31] The CMS Collaboration: *The CMS experiment at the CERN LHC*. CERN 2008, submitted to the Journal of Instrumentation (JINST).
- [32] The CMS Collaboration: *The Tracker System Project – Technical Design Report*. **CERN/LHCC 94-38**, December 1994.
- [33] The CMS Collaboration: *The Electromagnetic Calorimeter Project – Technical Design Report*. **CERN/LHCC 97-33**, December 1997.
- [34] The CMS Collaboration: *The Hadron Calorimeter Project – Technical Design Report*. **CERN/LHCC 97-31**, December 1997.

- [35] The CMS Collaboration: *The Magnet Project – Technical Design Report*. **CERN/LHCC 97-10**, December 1997.
- [36] The CMS Collaboration: *The Muon Project – Technical Design Report*. **CERN/LHCC 97-32**, December 1997.
- [37] H. Reithler: *CMS DT Type Naming*. Aachen, 2005.
http://www.physik.rwth-aachen.de/~reithler/050912DT_type_naming.pdf.
- [38] G. Bencze: *Overview of the Barrel Muon Alignment Project*. Barrel Muon Workshop, Aachen, 30 April 2004.
- [39] W. Blum, L. Rolandi: *Particle Detection with Drift Chambers*. Springer-Verlag, Berlin-Heidelberg, 1993.
- [40] H. Schwarthoff: *Simulationen in Konzeption und Bau der zentralen Myondriftkammern am CMS-Detektor*. PhD thesis, RWTH Aachen, 1997.
- [41] C. Autermann: *Funktionstests von CMS-Myon-Kammern*. Diploma thesis, RWTH Aachen, 2002.
http://web.physik.rwth-aachen.de/~hebbeker/theses/autermann_diploma.pdf.
- [42] M. S.: *Aufbau, Kalibration und Anwendung einer Messapparatur zur Überwachung des Gasdrucks in den CMS-Myonkammern*. Diploma thesis, RWTH Aachen, 2003.
<http://web.physik.rwth-aachen.de/~sowa/Dipl/Diplomarbeit.pdf>.
- [43] The CMS Collaboration: *The TriDAS Project Technical Design Report, Volume 1: The Trigger Systems*. **CERN/LHCC 2000-38 CMS TDR 6.1**, 15 December 2000.
- [44] N. Ellis: *Triggering in the LHC Environment*. Seminar DESY, 12-13 December 2006.
<http://www.desy.de/f/seminar/NEllis.ppt>
- [45] Timing, Trigger and Control (TTC) Systems for the LHC.
<http://ttc.web.cern.ch/TTC/intro.html>.
- [46] The CMS Collaboration: *The TriDAS Project Technical Design Report, Volume 2: Data Acquisition and High-Level Trigger*. **CERN/LHCC 02-26 CMS TDR 6**, 15 December 2002.
- [47] E. Cano *et al.*: *FED-Kit design for CMS DAQ system*. 2002.
http://dgigi.web.cern.ch/dgigi/fed_kit/lecc_2002.pdf
- [48] S. Cittolin: *DAQ baseline and main parameters*. CMS-TriDAS 1999.
<http://bosman.home.cern.ch/bosman/Filters.pdf>
- [49] A. Oh: *The CMS Data Acquisition and Trigger System*. DPG Frühjahrstagung, Berlin, 5 March 2005.
<http://berners-lee.physik.uni-dortmund.de/~behrendt/dpg2005/oh.ppt>
- [50] F. Gonella and M. Pegoraro: *”The MAD”, a Full Custom ASIC for the CMS Barrel Muon Chambers Front End Electronics*. Padova 2001.
<http://wwweda.pd.infn.it/cms/DTFB/electronics/frontend/documenti/leb2001proc.pdf>

Bibliography

- [51] *Low Voltage Differential Signalling (LVDS)*. National Semiconductor, 2007.
<http://www.national.com/appinfo/lvds/0,1798,100,00.html>.
- [52] Front End Board Homepage.
<http://www.pd.infn.it/cms/DTFB/electronics/frontend/feb/feb.html>.
- [53] J. Christiansen: *HPTDC High Performance Time to Digital Converter, Version 2.2*. CERN, March 2004.
- [54] P. Moreira: *Quartz Crystal Based Phase-Locked Loop for Jitter Filtering Application in LHC, Version 1.1*. CERN, 10 January 2005.
<http://proj-qp11.web.cern.ch/proj-qp11/images/qp11Manual.pdf>.
- [55] M. Mota, J. Christiansen: *A high-resolution time interpolator based on a delay locked loop and an RC delay line*. IEEE Journal of Solid-State Circuits **34**, Issue 10, 1360-1366 (1999).
- [56] C. Fernandez-Bedoya *et al.*: *Overview of the Read-Out System for the CMS Drift Tube Chambers*. CIEMAT Madrid, 2003.
<http://lhc-electronics-workshop.web.cern.ch/LHC-electronics-workshop/2003/sessionsPDF/Quality/BEDOYA.PDF>.
- [57] *MAX 7000 Programmable Logic Device Family*. Altera Corporation, September 2005.
<http://www.altera.com/literature/ds/m7000.pdf>.
- [58] C. Fernandez-Bedoya *et al.*: *Electronics for the CMS Muon Drift Tube Chambers: The Read-Out Minicrate*. IEEE Transactions on Nuclear Science, **52**, Issue 4, 944-949 (2005).
- [59] *Minicrate layout*. November 2002.
http://www.pd.infn.it/~caste/pub/minicrate_layout.pdf.
- [60] C. Fernandez-Bedoya *et al.*: *Read-Out Minicrate User Manual*. CIEMAT Madrid, 2005.
- [61] P. Moreira *et al.*: *A Radiation Tolerant Gigabit Serializer for LHC Data Transmission*. Proceedings of the 7th Workshop on Electronics for LHC Experiments (LEB 2001), 10-14 September 2001, Stockholm.
- [62] J. M. Cela *et al.*: *ROS-25 User Manual, Version 0.1*. CIEMAT Madrid, 2005.
http://cmsevf.web.cern.ch/cmsevf/pub/DT_ROS_25_Manual.pdf.
- [63] F. Benotto *et al.*: *The CMS DT Muon DDU: a PMC based interface between frontend and data-acquisition..* INFN Torino.
http://ph-collectif-lecc-workshops.web.cern.ch/ph-collectif-lecc-workshops/LEB00_Book/daq/cirio.pdf.
- [64] T. Stapelberg: *Der Trigger*. Aachen, 2002.
- [65] *2277 Digital Counter Time-to-Digital Converter*. LeCroy Corporation
<http://www-f9.ijs.si/~rok/sola/praktikum4/electronics/doc/2277.ps>.
- [66] B. Fehr: *Entwicklung eines schnellen und flexiblen Datennahme- und Monitoring-Systems für einen Myonkammerteststand*. Diploma thesis, Aachen, 1996.

- [67] Ph. Farthouat, P. Gällnö: *TTC-VMEbus Interface TTCvi-MkII, Rev 1.6*. CERN, May 2000.
<http://bonner-ntserver.rice.edu/cms/ttcvi.pdf>.
- [68] P. Gällnö: *TTCvx, Technical description and users manual*. CERN, May 1999.
<http://bonner-ntserver.rice.edu/cms/ttcvx.pdf>.
- [69] C. Fernandez, C. Willmott: *ROS-8 User Manual*. CIEMAT Madrid, 2004.
- [70] L. Castellani: *CCB Commands description V3.3*. INFN Padova, 2005.
- [71] M. Bontenackels, private communication, 2005.
- [72] M. Bontenackels, software, 2003.
- [73] *MC100EP210S 2.5V 1:5 Dual Differential LVDS Compatible Clock Driver*. Semiconductor Components Industries, LLC, 2002.
<http://pdf1.alldatasheet.co.kr/datasheet-pdf/view/103476/ONSEMI/MC100EP210S.html>.
- [74] *Motorola Semiconductor Technical Data MC100LVEL91 MC100EL91*. Motorola Inc., 1997.
<http://pdf1.alldatasheet.co.kr/datasheet-pdf/view/11729/ONSEMI/MC100EL91.html>.
- [75] *MC10EP116, MC100EP116 3.3 V / 5 V Hex Differential Line Receiver/Driver*. Semiconductor Components Industries, LLC, 2006.
<http://pdf1.alldatasheet.co.kr/datasheet-pdf/view/172428/ONSEMI/MC100EP116.html>.
- [76] K. Hoepfner, private communication, 2002.
- [77] G. Hilgers, private communication, 2008.
- [78] H. Dembinski: *Aufbau einer Detektorstation aus Szintillatoren zum Nachweis von kosmischen Teilenschauern, Simulation und Messung*. Diploma thesis, RWTH Aachen, 2005.
http://web.physik.rwth-aachen.de/~hebbeker/theses/dembinski_diploma.pdf.
- [79] J. Gutleber et al.: *Clustered Data Acquisition for the CMS Experiment*. Computing in High Energy and Nuclear Physics, Beijing, China, 03-07 September 2001. Science press, 601.
- [80] S. Cittolin: *Data Acquisition, Control and Monitor*. JCOP workshop, 05-06 June 2002.
<http://itcofe.web.cern.ch/itco/Projects-Services/JCOP/Workshops/JCOPworkshop3/Presentations/sergio.pdf>
- [81] V. Brigljevic et al.: *Run Control and Monitor System*. Computing in High Energy and Nuclear Physics, 24-28 March 2003, La Jolla, USA.
<http://arxiv.org/ftp/cs/papers/0306/0306110.pdf>
- [82] F. Glege et al.: *CMS DCS Integration Guidelines, Version 3.0, MTCC phase 1 corrections*. October 2006.
http://cms.cern.ch/iCMS/jsp/page.jsp?mode=cms&action=url&urlkey=CMS_DCS

Bibliography

- [83] ETM professional control PVSS.
http://www.pvss.com/index_e.asp?id=2&sb1=&sb2=&sb3=&sname=&sid=&seite_id=6
- [84] ITCO: JCOP.
<http://itco.web.cern.ch/itco/Projects-Services/JCOP/>
- [85] M. Passaseo *et al.*: *Stato e prospettive del DAQ & DCS*. Padova, 16 December 2004.
<http://cms.pd.infn.it/riunioni/16-12-2004/Marina041216.ppt>
- [86] *Motorola Semiconductor Technical Data MPX2010 MPXV2010G Series*. Motorola Inc., 2000.
<http://pdf1.alldatasheet.co.kr/datasheet-pdf/view/86195/MOTOROLA/MPX2010DP.html>.
- [87] *Motorola Semiconductor Technical Data MPX2050 Series*. Motorola Inc., 2002.
<http://pdf1.alldatasheet.co.kr/datasheet-pdf/view/83239/MOTOROLA/MPX2050DP.html>.
- [88] *MC33272 data sheet*. Motorola Inc., 1996.
http://www.datasheetcatalog.com/datasheets_pdf/M/C/3/3/MC33272.shtml.
- [89] M. Huhtinen: *Recommendation for Irradiation of CMS Components in the IRRAD2 Facility at PS*. **CMS IN-2001/012**, 2 April 2001.
- [90] H. Reithler, private communication, 2002.
- [91] MKS Instruments.
<http://www.mkinst.com>.
- [92] *DAQ NI 6013/6014 User Manual*. National Instruments, 2002.
<http://www.ni.com/pdf/manuals/370636a.pdf>.
- [93] H. Reithler, files, 2001.
- [94] F. Lanzerath, D. Schulte, software, 2003.
- [95] H. Reithler, files, 2004.
- [96] H. Szczesny: *PADC1138 Nr. 852 Drucksensoren-Meßsystem mit ADC*. Aachen, 2004.
- [97] *MAXIM 2.7V to 3.6V and 4.5V to 5.5V, Low-Power, 4-/12-Channel, 2-Wire Serial 10-Bit ADCs*. Maxim Integrated Products, 2006;
<http://datasheets.maxim-ic.com/en/ds/MAX1136-MAX1139M.pdf>.
- [98] P. Rütten: *Development, tests and calibration of electronic modules for measuring and monitoring the gas pressure in CMS muon chambers*. Diploma thesis, RWTH Aachen, 2005.
- [99] *The I²C-Bus Specification, Version 2.1*. Philips Semiconductors, 2000.
http://www.nxp.com/acrobat_download/literature/9398/39340011.pdf.

- [100] D. Novák et al.: *Pressure monitoring system of the CMS muon chambers*. 10th Workshop on Electronics for LHC Experiments and Future Experiments, 13-17 September 2004, Boston, USA.
http://lhc-workshop-2004.web.cern.ch/lhc-workshop-2004/5-Posters/70-novak_proceedings.pdf
- [101] P. Rütten, software, 2004.
- [102] ISR Data Base (maintained by J. Puerta-Pelayo), 2006.
<http://isr-muon.web.cern.ch>.
- [103] DT Gas Pressure Measurement Items (maintained by G. Fetchenhauer), 2006.
http://cmsdoc.cern.ch/~fetchenh/DT_PADC_Manifolds.xls.
- [104] M. S.: *Gas pressure sensors*. Aachen, 2006.
<http://web.physik.rwth-aachen.de/~sowa/Gas/sensors.html>.
- [105] *PC Wetterstation, Version 2.41*. 2000.
<http://www.teledata-update.de/info2.htm>.
- [106] *MTCC*. 2006.
<http://cms.cern.ch/MTCC.html>.
- [107] The CMS Collaboration: *The CMS Magnet Test and Cosmic Challenge (MTCC Phase I and II), Operational Experience and Lessons Learnt*. **CMS Note 2007/005**, 7 March 2007.
- [108] H. Reithler: *Pressure Sensors and B-Field*. CMS Week, Barrel Muon DT Session, 19 September 2006, CERN.
<http://indico.cern.ch/getFile.py/access?contribId=10&resId=0&materialId=slides&confId=6338>.
- [109] *LP2950/LP2951 Series of Adjustable Micropower Voltage Regulators*. National Semiconductor, 2003.
<http://www.national.com/an/AN/AN-1148.pdf>.
- [110] MELAG medical technology.
<http://melag.de/englisch/autoklaven/index.html>.
- [111] *DS1820 1-WireTM Digital Thermometer*. Dallas Semiconductor, 1995.
<http://www.systonix.com/Resource/ds1820.pdf>.
- [112] J. Frangenheim, software, 2007.
- [113] *DG535 – Digital delay / pulse generator (4 ch.)*. Stanford Research Systems Inc., 2003.
<http://www.thinksrs.com/products/DG535.htm>.

Acknowledgments

I would like to thank my supervisor Prof. Dr. Thomas Hebbeker for the opportunity to work on an interesting topic and thereby to allow me to participate in a one of the most important physics experiment. Many thanks also to Prof. Dr. Achim Stahl for agreeing to be my second referee.

I am very thankful to Dr. Hans Reithler for long inspiring discussions over a large variety of topics, for different perspectives and much more. He was always willing to listen my problems and advised me during my entire PhD studies.

A special thanks to my collaboration colleagues Cristina Fernandez-Bedoya, Carlos Willmott (CIEMAT Madrid), Lorenzo Castellani, Matteo Pegoraro, Marco Bellato (INFN Padua, INFN Legnaro) and Marco Dallavalle (INFN Bologna), and many others for providing me with the diverse CMS DT read-out hardware and answering a lot of questions concerning the right installation of the chamber electronics and the data taking for the chamber tests. I always enjoyed the many visits at their institutes and laboratories which gave me an experience in MiniCrate functioning and in the CMS read-out procedure. Also thanks to Marcus Joos from the CERN E-Pool, who organized the TTC modules. I would like to thank all colleagues from the CERN commissioning and 2004 test beam for very good times I could spend with them, extending my experiences in the DAQ system and the DCS of the CMS DT chambers.

It would have been impossible to perform the tests described in this thesis without an enormous support of the entire Aachen mechanics and electronics team. I am very thankful to Henry Szczesny for the developing and construction of the PADC and the Splitter Board and explaining to me their functions. Thanks to Günther Hilgers, Rüdiger Lampe and Franz Adamczyk for their help in MiniCrate installation and realization of various hardware tests; thanks also for the preparation of the facility for the calibration of the gas pressure sensors and PADCs. For the performance of the sensor and PADC calibration it is also thanks to Dr. Hans Reithler, Rüdiger Lampe, Franz Lanzerath and Pim Rütten.

Michael Bontenackels and Oleg Tsigenov helped me by the developing of the software for the MiniCrate DAQ, Dr. Hans Reithler gave me maybe a million useful hints to make the software for the LUT creation efficient – thank You all very much! Michael Bontenackels discussed with me the usage of the existing software for the Aachen test stand data taking and explained to me the right conversion of the data into the test beam format, and subsequently the root file creation – thanks Michael once more. Thanks also to Jens Frangenheim for his software for the temperature measurement.

A big "thak you" goes to the entire CMS Aachen group: Emanuel, Georg, Michael, Clemens, Philipp, Jens, Carsten, Oleg... the list is long and I want to come to an end with my thesis... so thank You all for a great time and a great working atmosphere.

Prof. Dr. Lalit Sehgal, Dr. Kerstin Hoepfner and Dr. Hans Reithler many thanks for reading my manuscript, thus being correctors and gaving me a lot of hints helping me finally to upgrade the layout of this thesis.

I am happy that I have You, Kasia – I do not know, if it would have been possible to complete this thesis without You (and Dora, of course...) besides me, dziękuję kochanie za wszystko!

Curriculum Vitae

Personal Data:

Name: Michael Sowa
Address: Reimser Str. 45, D-52074 Aachen
Date of Birth: December 22, 1964
Place of Birth: Groß Strehlitz (Strzelce Opolskie, Poland)
Nationality: German
Marital status: married, no children

School Education:

Sept. 1971 – Jun. 1979 Primary school in Strzelce Opolskie (Poland)
Sept. 1979 – Jun. 1984 Technical high school in Strzelce Opolskie (Poland)
Jun. 1984 Abitur (Polish)
Dec. 1985 – Jun. 1987 GfbA language school and college
in Anrath and Geilenkirchen (Germany)
Dec. 1987 Abitur (German)

University Education:

Oct. 1984 – Sept. 1985 Study of mechanical engineering at the Silesian University of
Technology (Politechnika Śląska) in Gliwice (Poland)
Mar. 1985 – Mar. 2003 Study of physics at Rheinisch Westphälische Technische
Hochschule (RWTH) in Aachen (Germany)
Sept. 1992 – May 2003 Study of philosophy and psychology at Rheinisch Westphälische
Technische Hochschule (RWTH) in Aachen (Germany)

Research:

Sept. 2001 – Mar. 2003 Diploma thesis *Aufbau, Kalibration und Anwendung einer
Messapparatur zur Überwachung des Gasdrucks in den CMS-
Myonkammern* at the III. Phys. Inst. A, RWTH Aachen;
Supervisor: Prof. Dr. T. Hebbeker
Mar. 2003 Undergraduate Degree: Diplom-Physiker
May 2003 – Apr. 2008 Research Assistant at the III. Phys. Inst. A, RWTH Aachen;
Study and work visitations in CERN (Swiss), INFN Padua,
INFN Legnaro (Italy) and CIEMAT Madrid (Spain);
Student adviser for the laboratory course experiment
"Cosmic Muons"
since May 2003 Dissertation at the III. Phys. Inst. A, RWTH Aachen